UNIVERSITÄT
OSNABRÜCK

Department of Physics

From Magnetite to Cobalt Ferrite Thin Films: New Perspectives for the Growth of Thin Ferrite Films for their Application in Spintronics

Jannis Thien, M.Sc.

Dissertation (kumulativ)

zur Erlangung des Doktorgrades (Dr. rer. nat.)
vorgelegt am Fachbereich Physik der Universität Osnabrück

Osnabrück, March 8, 2022

Examiners:

Prof. Dr. Joachim Wollschläger
Dr. Karsten Küpper

Contents

1 Introduction 1

2 Theoretical background and experimental methods 5
- 2.1 Periodic structures - Single crystals . . . 5
  - 2.1.1 Classification of crystal lattices - The cubic crystal system . . . 6
  - 2.1.2 Lattice planes, directions, and Miller indices . . . 6
  - 2.1.3 Reciprocal lattice . . . 7
- 2.2 Growth of epitaxial (ultra)thin films . . . 8
  - 2.2.1 Growth modes in epitaxy . . . 8
  - 2.2.2 Substrate-induced strain effects . . . 9
- 2.3 Matter in external magnetic fields and collective magnetism . . . 11
  - 2.3.1 Collective magnetic ordering . . . 13
  - 2.3.2 Domain formation and magnetization curves . . . 17
- 2.4 Superconducting quantum interference device - SQUID . . . 19
  - 2.4.1 Flux quantization . . . 20
  - 2.4.2 Josephson effect . . . 20
  - 2.4.3 SQUID sensor . . . 21
- 2.5 Core-level spectroscopy - XPS, XAS, and XMCD . . . 22
  - 2.5.1 X-ray photoelectron spectroscopy - XPS . . . 23
  - 2.5.2 X-ray absorption spectroscopy - XAS . . . 29
  - 2.5.3 X-ray magnetic circular dichroism - XMCD . . . 30
  - 2.5.4 Sum rules . . . 32
  - 2.5.5 Charge-transfer multiplet theory . . . 33
- 2.6 X-ray diffraction - XRD . . . 35
  - 2.6.1 Bragg condition and Laue condition . . . 36
  - 2.6.2 Kinematic diffraction theory . . . 37
- 2.7 Low-energy electron diffraction - LEED . . . 44
- 2.8 X-ray reflectivity - XRR . . . 45
- 2.9 Direct imaging of structures . . . 48
  - 2.9.1 Atomic force microscopy - AFM . . . 49
  - 2.9.2 (High-resolution) transmission electron microscopy - (HR)TEM . . . 50

3 Investigated materials 53
- 3.1 Materials used as substrates . . . 53
  - 3.1.1 Magnesium oxide - MgO . . . 53
  - 3.1.2 Strontium titanate - $SrTiO_3$ . . . 54
- 3.2 Film materials . . . 54
  - 3.2.1 Cobalt(II) oxide - CoO . . . 54
  - 3.2.2 Magnetite - Fe_3O_4 . . . 55
  - 3.2.3 Cobalt ferrite - $CoFe_2O_4$ . . . 56
  - 3.2.4 Electronic structure of ferrites . . . 56
  - 3.2.5 Magnetism of ferrites . . . 58
  - 3.2.6 Antiphase boundaries - APB . . . 59

4 Experimental setups 61

4.1 Sample preparation 61
4.2 Surface characterization 62
  4.2.1 XPS - Experimental setup 62
  4.2.2 LEED - Experimental setup 63
4.3 Experimental setups at synchrotron radiation facilities 64
  4.3.1 Generation of synchrotron radiation 65
  4.3.2 (GI)XRD and XRR - Experimental setup 66
  4.3.3 Processing and analysis of (GI)XRD and XRR data 67
  4.3.4 (AR-)HAXPES - Experimental setup 68
  4.3.5 XAS and XMCD - Experimental setup and data analysis 69
4.4 AFM - Experimental setup 70
4.5 HRTEM - Sample preparation 71
4.6 SQUID magnetometer - Experimental setup and data processing 71

5 Anomalously Strained Fe_3O_4 Thin Films on $SrTiO_3$(001) Resolved by HRTEM and X-ray Diffraction 75
J. Thien, T. Niermann, M. Lehmann, J. Bahlmann, J. Rodewald, and J. Wollschläger

5.1 Introduction 75
5.2 Experimental details 76
5.3 Results and discussion 76
  5.3.1 Surface characterization by means of XPS and LEED 76
  5.3.2 XRD and GIXRD 77
  5.3.3 HRTEM 79
5.4 Summary and conclusions 81
5.5 Acknowledgements 81

6 Effects of Post-deposition Annealing on Epitaxial CoO/Fe_3O_4 Bilayers on $SrTiO_3$(001) and Formation of Thin High-Quality Cobalt Ferrite-like Films, *PREPRINT* **83**
J. Thien, J. Bahlmann, A. Alexander, M. Hoppe, T. Pohlmann, K. Ruwisch, C. Meyer, F. Bertram, K. Küpper, and J. Wollschläger
*The Journal of Physical Chemistry C **124**, 23895-23904 (2020)*

7 Cationic Ordering and Its Influence on the Magnetic Properties of Co-Rich Cobalt Ferrite Thin Films Prepared by Reactive Solid Phase Epitaxy on Nb-Doped $SrTiO_3$(001), *PREPRINT* **85**
J. Thien, J. Bahlmann, A. Alexander, K. Ruwisch, J. Rodewald, T. Pohlmann, M. Hoppe, F. Alarslan, M. Steinhart, B. Altuncevahir, P. Shafer, C. Meyer, F. Bertram, J. Wollschläger, and K. Küpper
*Materials **15**, 46 (2022)*

7.1 Introduction 85
7.2 Materials and methods 87
7.3 Results and discussion 88
  7.3.1 AR-HAXPES 88
  7.3.2 AFM 90
  7.3.3 XAS/XMCD 90
  7.3.4 SQUID 94
7.4 Conclusions 97

7.5 Acknowledgments 97

8 Co Depending Strain Accumulation and Relief during Growth of Ultrathin $Co_xFe_{3-x}O_4$ Films 99

J. Thien, J. Rodewald, T. Pohlmann, K. Ruwisch, R. Fan, P. Steadman, F. Bertram, K. Küpper, and J. Wollschläger

8.1 Introduction 99
8.2 Experimental details 100
8.3 Results and discussion 101
    8.3.1 XRD 101
    8.3.2 LEED 103
    8.3.3 XRR 104
    8.3.4 HAXPES 105
    8.3.5 SQUID 106
8.4 Summary and conclusions 107
8.5 Acknowledgements 107

9 Summary and outlook 109

10 List of publications 113

Literature 115

1 Introduction

Our modern world is bursting with information and social networks, in which enormous amounts of data are generated by high-performance electronic devices and need to be stored [1]. Satisfying the world's increasing demand for more and more computing power to process such volume of data while simultaneously reducing energy costs is the incentive for the ever-growing research field of spin-transport electronics (spintronics) [2, 3]. Unlike conventional (semiconductor) electronics, spintronics strives to exploit not only the fundamental charge property of electrons but also their spin nature for transmission of information [2, 4, 5]. Successfully established technologies that already incorporate the intrinsic spin property of electrons include, for example, magnetoresistive read heads in hard disk drives (HDDs) and non-volatile magnetoresistive random-access memory (MRAM) [1–3]. In the not-too-distant future, the spin property is expected to find application also in other current research areas such as artificial intelligence, in which spintronic devices might be able to enable low-power adaptive artificial neural networks operating at high performance [3, 6].

The seeds for the research field of spintronics were sown with the discovery of the giant magnetoresistance (GMR) effect in the late 1980s by the groups of Albert Fert and Peter Grünberg [7, 8], which occurs in multilayer structures where a thin non-magnetic conductive spacer is sandwiched between two ferromagnetic layers. This effect arises from the strongly spin-dependent scattering of electrons carrying the electric current as they travel from one ferromagnetic layer to the other, which causes a large variation in the electrical resistance dependent on the magnetization alignment (parallel or antiparallel) of the two ferromagnets relative to each other.

Back then, the scientific world and industry recognized right away that the discovery of the GMR effect could have significant technological implications and might even represent a milestone for electronic storage of information. By simply switching the magnetization of just one ferromagnetic layer, one was able to create two different resistance states, which could correspond to the logic digital states (0,1) in a typical data storage device [9]. As a result, it took less than a dozen years for the first GMR-based hard disks to enter the market and quickly supersede the previously established technologies [9].

Almost simultaneously, reports began to accumulate of a very similar magnetoresistance phenomenon, known as tunneling magnetoresistance (TMR) [10, 11], which had originally been discovered a few years earlier by Jullière [12]. Unlike the GMR effect, the TMR effect occurs in so-called magnetic tunnel junctions (MTJs) – multilayer structures with an ultrathin layer of insulating material between two ferromagnetic layers. Many critical and important features that constitute the TMR effect are similar to those of the GMR effect [13]. Yet, the key difference between both effects is that instead of classical conduction, the TMR effect relies on the spin-dependent quantum-mechanical tunneling of electrons through a barrier from one ferromagnetic layer to another, which leads to the characteristic large change in electrical resistance upon a variation of magnetization direction of one ferromagnet relative to the other [14].

Up to now, only transition metals and their alloys have been employed for magnetoresistive devices. However, these have already reached their theoretical limits, with their performance still lagging severely behind that of semiconductor switches and transistors by multiple orders of magnitude [13]. Consequently, new and more promising materials with a higher degree of spin-polarization, capable of much higher performance, are required in order to be able to compete with the conventional electronic representatives. For that matter, ferromagnetic and ferrimagnetic half-metals such as Fe_3O_4 (magnetite) are believed to provide a potential remedy since they exhibit maximum spin asymmetry around the Fermi level, allowing for a theoretical spin-polarization of up to 100 % at the Fermi edge. But even spintronic prototype devices based on Fe_3O_4 layers have not been convincing either, and their performance leaves much to be desired [15–17]. It is suspected that the origin of the problem lies in interface effects such as surface modifications [13, 18] that limit the efficiency of such devices. Therefore, further as well as in-depth knowledge of the growth process and especially of the interface of these promising half-metals is inevitable before they can even come close to delivering their full potential in spintronic applications.

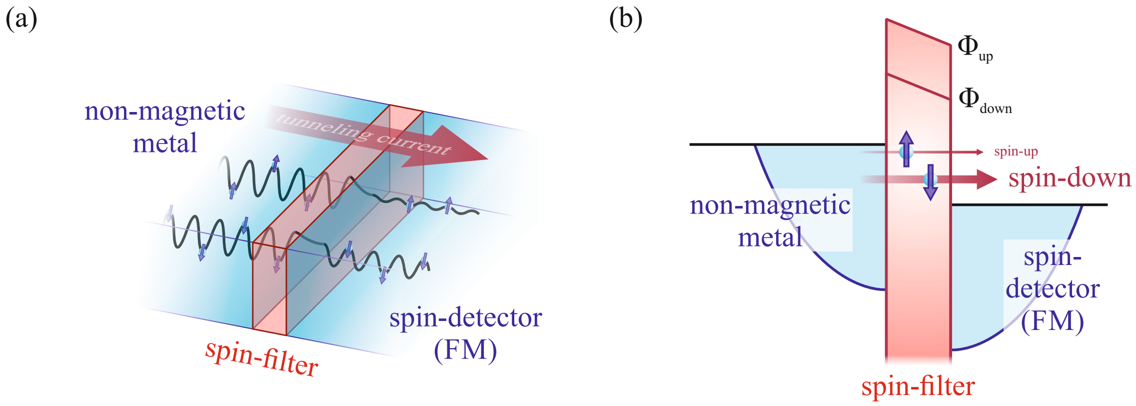

Fig. 1.1: (a) Schematics of a typical structure employing a ferro-/ferrimagnetic insulator as a spin-filter sandwiched between a non-magnetic metal and a ferromagnetic (FM) so-called spin-detector to generate highly polarized electron currents. (b) Origin of the spin-filtering effect. Due to the different tunneling barrier heights Φ_{up} and Φ_{down} for spin-up and spin-down electrons, respectively, the tunneling probability through such a spin filter is higher for electrons of one spin orientation than for the respective other. Adapted from Refs. [9, 19, 20].

An attractive alternative to classical MTJs is provided by structures consisting of spin-filters [9], in which strongly polarized electron currents are generated by ultrathin layers made of magnetic insulators such as $CoFe_2O_4$ (stoichiometric cobalt ferrite), acting as tunneling barriers (cf. Fig. 1.1) [21]. The spin-selective transport from magnetic insulators arises due to their exchange-split energy levels in the conduction band, leading to spin-dependent tunnel barrier heights for electrons. Consequently, tunneling through a magnetic insulator is favored for electrons only of a certain spin species due to a higher tunneling probability. Thus, a combination of a magnetic insulator and a non-magnetic electrode behaves like a kind of artificial half-metal [9]. Yet, the preparation of, for example, $CoFe_2O_4$ as a tunnel barrier presents a major challenge to overcome so far. On the one hand, the synthesis of oxides often leads to an abundance of structural imperfections, such as lattice defects in the crystal structure, which can affect the magnetic and electronic properties of the oxide. This, in turn, can have a significant impact on the spin-filter efficiency of $CoFe_2O_4$. On the other hand, it is possible that the controlled creation of oxygen vacancies in the $CoFe_2O_4$ crystal structure can tune and might even improve its spin-filter efficiency [14].

Driven by this motivation, this thesis addresses the epitaxial and crystalline growth of (ultra)thin magnetite and cobalt ferrite films and their structural, magnetic, and electronic analysis by a variety of (complementary) characterization methods. The necessary theoretical background, e.g., of the characterization methods used is discussed in Chap. 2. The description of the structural, electronic, and magnetic properties of the main materials investigated follows in Chap. 3. Thereafter, the experimental setups used for the different measurements are introduced in Chap. 4. The experimental results presented in Chap. 5–8 form the heart of the thesis.

The very first experimental results presented in Chap. 5 deal with ultrathin Fe_3O_4 films grown on $SrTiO_3(001)$ substrates by reactive molecular beam epitaxy (RMBE) and the often observed counter-intuitive strain behavior induced in these films by the substrate. For this purpose, the complementary measurement techniques high-resolution transmission electron microscopy (HRTEM) and (grazing incidence) X-ray diffraction (GI)XRD serve as key investigation techniques. In particular, valuable insights into the interface between Fe_3O_4 and $SrTiO_3(001)$ are retrieved from the HRTEM measurements.

In the next chapter Chap. 6, one step further will be taken and an additional CoO film is deposited on such $Fe_3O_4/SrTiO_3(001)$ structures to demonstrate an alternative pathway for the synthesis of cobalt ferrite films of high structural quality via the interdiffusion of both oxide films [22]. Here, the effects of post-deposition annealing (PDA) on the bilayer systems are studied *in situ* after each PDA step by soft and hard X-ray photoelectron spectroscopy (soft XPS and HAXPES) and (GI)XRD. With this, the evolution from the initial bilayer stacks to completely formed cobalt ferrite films in terms of electronic and structural variations is followed with maximum precision. Moreover, angular-resolved HAXPES (AR-HAXPES) as well as X-ray reflectivity (XRR) measurements are performed on the final films (after the last PDA step) to control complete intermixing of the CoO and Fe_3O_4 films.

Subsequently, the influence of cation distribution on the magnetic properties of the Co-rich cobalt ferrite thin films produced by this novel synthesis technique (cf. Chap. 6) are examined in Chap. 7. Within this scope, both surface and bulk specific techniques are employed, namely atomic force microscopy (AFM), X-ray absorption (XAS), X-ray magnetic circular dichroism (XMCD), AR-HAXPES, and superconducting quantum interference device (SQUID) magnetometry, to deliver a comprehensive and conclusive picture of the film properties under investigation [23].

Last but not least, in Chap. 8, the initial growth behavior of ultrathin cobalt ferrite films grown by RMBE on MgO(001), a substrate more suitable for cobalt ferrite than $SrTiO_3$ in terms of lattice mismatch (cf. Sec. 2.2.2), is examined depending on the Co content. The film growth and the evolving strain already starting from the very early growth stages are monitored extensively and time-resolved by synchrotron radiation-based specular XRD. Low energy electron diffraction (LEED) and XRR measurements are carried out to shed light especially on the final substrate-film interfaces and film surfaces. Furthermore, HAXPES and SQUID measurements provide fundamental information on the electronic, chemical, and magnetic properties of the different cobalt ferrite films produced.

Finally, this thesis concludes with a summary in Chap. 9 of all the results obtained. In addition, a small outlook of possible future research perspectives based on the results presented here is provided.

2 Theoretical background and experimental methods

In the following, the theoretical concepts relevant for this work are introduced, providing a theoretical basis for the results and publications presented in Chap. 5–8. The very first few sections focus on the characterization of crystalline structures in general and the growth of crystalline films, followed by a basic description of magnetism in the next section. The former considerations (cf. Sec. 2.1 and Sec. 2.2) are mainly based on information given in Refs. [24–29], whereas Refs. [26, 30–32] provided the information necessary for the latter (cf. Sec. 2.3). The focus is then turned toward the superconducting quantum interference device, which was used to study the integral magnetic properties of the samples produced, following Refs. [33–36]. Thereafter, the theory of the (core-level) spectroscopic and the experimental diffraction techniques used in this body of work are examined according to Refs. [30, 32, 37–40] and Refs. [24, 41–43], respectively. In addition, a brief overview of X-ray reflectivity is given next (cf. Refs. [44, 45]), which has been employed only as a supplementary characterization technique. Finally, the utilized spatial direct imaging tools are discussed, following Refs. [46–48].

2.1 Periodic structures - Single crystals

Ideal crystals are three-dimensional structures built from the periodically repeating juxtaposition of a smallest structural unit, also known as unit cell. Because of this periodic (long-range) order, crystals possess translation symmetry, unlike amorphous solids or liquids, for example, in which a long-range order is absent. The unit cell may contain only a single atom or even groups of atoms, forming the basis of the crystal. Three linearly independent crystallographic (lattice) vectors $\boldsymbol{a}$, $\boldsymbol{b}$, and $\boldsymbol{c}$ span the unit cell, whose non-overlapping translation

$$\boldsymbol{R}_n = n_a\,\boldsymbol{a} + n_b\,\boldsymbol{b} + n_c\,\boldsymbol{c} \quad \text{with} \quad n_a, n_b, n_c \in \mathbb{Z} \tag{2.1}$$

along its principal axes then defines the complete crystal lattice. Essentially, it is possible to define several different unit cells for the same crystal lattice, all satisfying the translation symmetry of the crystal lattice, yet only the smallest-volume unit cell is termed primitive, which is formed by its

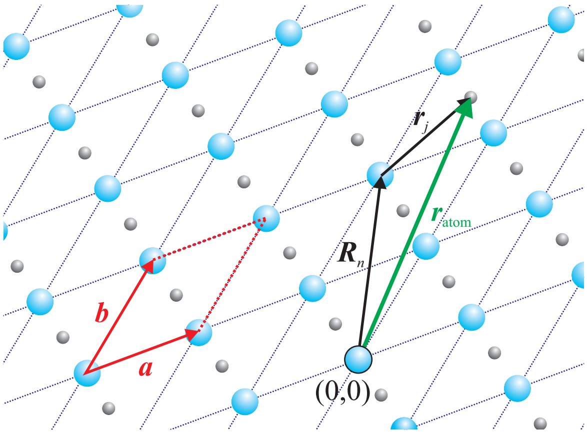

Fig. 2.1: Illustration of a two-dimensional crystal. The primitive lattice vectors $\boldsymbol{a}$ and $\boldsymbol{b}$ span the primitive unit cell (red), consisting of two atoms (blue and gray). The position of each unit cell in the crystal is given by the vector $\boldsymbol{R}_n$, whereas the vector $\boldsymbol{r}_j$ gives the position of each atom within the unit cells. The linear combination ($\boldsymbol{r}_{\text{atom}}$; depicted in green) of both position vectors ($\boldsymbol{R}_n$ and $\boldsymbol{r}_j$) covers the positions of all atoms in the crystal structure.

primitive lattice vectors $\boldsymbol{a}$, $\boldsymbol{b}$, and $\boldsymbol{c}$. However an all-encompassing description of a crystal structure requires information not only about the lattice but also about the positions of the individual atoms within a unit cell of the crystal, especially if the unit cell includes more than one atom. Hence, for a basis containing j atoms, also additional j vectors

$$\boldsymbol{r}_j = u_j\,\boldsymbol{a} + v_j\,\boldsymbol{b} + w_j\,\boldsymbol{c} \quad \text{with} \quad 0 \leq u_j, v_j, w_j \leq 1, \tag{2.2}$$

must be defined. Here, u_j, v_j, and w_j are the respective coordinates of the j atoms. Accordingly, any atom $\boldsymbol{r}_{\text{atom}}$ in the crystal can be reached by the linear combination

$$\boldsymbol{r}_{\text{atom}} = \boldsymbol{R}_n + \boldsymbol{r}_j \tag{2.3}$$

of the vector $\boldsymbol{R}_n$ (describing the position of unit cells) and the vector $\boldsymbol{r}_j$ (specifying the position of each atom within a unit cell). This is schematically illustrated in Fig. 2.1 for a two-dimensional crystal with a two atomic basis.

2.1.1 Classification of crystal lattices - The cubic crystal system

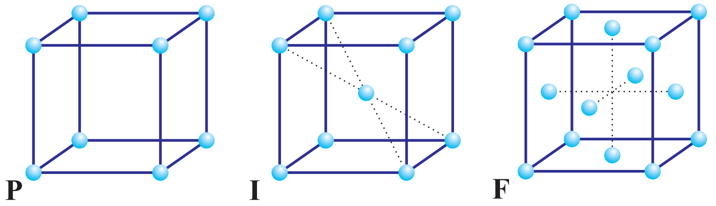

Fig. 2.2: The cubic crystal system. The different kinds of centering (primitive, body-centered, and face-centered) are denoted by the letters **P**, **I**, and **F**.

Apart from the characteristic translation symmetry as introduced before, many crystals possess additional symmetries such as rotation, mirror reflection, and inversion symmetry. With respect to the different symmetry operations, crystal lattices can basically be classified into seven different crystal systems, namely cubic, tetragonal, orthorhombic, hexagonal, trigonal, monoclinic, and triclinic. The different crystal systems are distinguishable according to the magnitudes of the respective lattice vectors $\boldsymbol{a}$, $\boldsymbol{b}$, and $\boldsymbol{c}$ (the magnitudes of $\boldsymbol{a}$, $\boldsymbol{b}$, and $\boldsymbol{c}$ correspond to the lattice constants a, b, and c of the crystal) and their angles α, β, and γ that they form with each other. Within this work, only materials were used that belong to the cubic crystal system with $a = b = c$ and $\alpha = \beta = \gamma = 90°$ (cf. Fig. 2.2). With respect to the different kinds of centering, the cubic crystal system can be further divided into three subtypes, exhibiting either a single lattice point or even more than one lattice point per unit cell. The different kinds are primitive, body-centered, and face-centered, which are commonly denoted by the letters **P**, **I**, and **F**, respectively [25].

2.1.2 Lattice planes, directions, and Miller indices

In order to quantitatively and unambiguously identify crystallographic planes in any crystal, they are indexed by three integer values h, k, and l, which are also known as Miller indices. First, the reciprocals of the interceptions points (in multiples of the lattice constants) between a certain lattice plane and the three crystallographic axes of the crystal are determined. Afterward, the values are multiplied by a factor, so that they become integer values without having a common divisor. The resulting integer values are the Miller indices of the respective crystallographic plane, which are generally written enclosed in round brackets/parentheses (hkl). For instance, the crystallographic plane with intersection points at 2, 3, and 6 (arbitrarily chosen), is indexed by the Miller indices (321). In the case that a crystallographic plane has no intersection with a crystallographic axis (the point of intersection is at infinity), the corresponding index is represented by zero [cf. Fig. 2.3 (a,b)].

For negative intersection points, the corresponding indices are written with a bar above them, by convention. The set of all lattice planes that are equivalent by symmetry is expressed using curly brackets/braces {}.

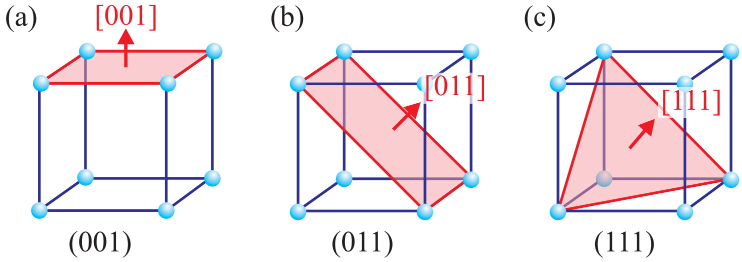

Fig. 2.3: Three representative lattice planes (marked in red) in a simple cubic crystal each displayed with its corresponding normal vector. (a) (001) plane, (b) (011) plane, and (c) (111) plane.

Directions in crystals are specified by indices as well (here denoted by the integer values u, v, and w), which are instead portrayed enclosed in square brackets $[uvw]$. Somewhat easier than for crystal planes, directions in a crystal are defined according to the vector components as integer values of the respective direction. In the special case of cubic crystals, the $[uvw]$ direction is conveniently always perpendicular to a lattice plane (hkl) of the same indices $u = h$, $v = k$, and $w = l$ [cf. Fig. 2.3 (a–c)]. All crystallographically equivalent directions in a crystal are identified using angular brackets $\langle\rangle$.

2.1.3 Reciprocal lattice

For each crystal lattice in real space, a reciprocal lattice in reciprocal space can be defined, which is analogously spanned by three reciprocal lattice vectors $\boldsymbol{a}^*$, $\boldsymbol{b}^*$, and $\boldsymbol{c}^*$. The reciprocal lattice vectors are directly linked to the crystallographic lattice vector $\boldsymbol{a}$, $\boldsymbol{b}$, and $\boldsymbol{c}$ (cf. Sec. 2.1) according to

$$\boldsymbol{a}^* = 2\pi\frac{\boldsymbol{b}\times\boldsymbol{c}}{\boldsymbol{a}\cdot(\boldsymbol{b}\times\boldsymbol{c})}\ ,\quad \boldsymbol{b}^* = 2\pi\frac{\boldsymbol{c}\times\boldsymbol{a}}{\boldsymbol{a}\cdot(\boldsymbol{b}\times\boldsymbol{c})}\ ,\ \text{and}\quad \boldsymbol{c}^* = 2\pi\frac{\boldsymbol{a}\times\boldsymbol{b}}{\boldsymbol{a}\cdot(\boldsymbol{b}\times\boldsymbol{c})}\ , \tag{2.4}$$

with $\boldsymbol{a}\cdot(\boldsymbol{b}\times\boldsymbol{c})$ being the volume of the crystall unit cell and $\boldsymbol{a}\cdot\boldsymbol{a}^* = \boldsymbol{b}\cdot\boldsymbol{b}^* = \boldsymbol{c}\cdot\boldsymbol{c}^* = 2\pi$. The set of all reciprocal lattice points can be expressed by the reciprocal lattice vector

$$\boldsymbol{G}_{hkl} = h\,\boldsymbol{a}^* + k\,\boldsymbol{b}^* + l\,\boldsymbol{c}^* \quad \text{with} \quad h,k,l \in \mathbb{Z}\ . \tag{2.5}$$

For cubic, tetragonal, and orthorhombic crystal lattices, their crystallographic lattice vectors $\boldsymbol{a}$, $\boldsymbol{b}$, and $\boldsymbol{c}$ are always perpendicular to each other ($\alpha = \beta = \gamma = 90°$). Thus, the corresponding reciprocal lattice vectors are perpendicular to each other as well and have lengths of

$$a^* = \frac{2\pi}{a}\ ,\quad b^* = \frac{2\pi}{b}\ ,\ \text{and}\quad c^* = \frac{2\pi}{c}\ . \tag{2.6}$$

Contrary to three-dimensional crystals, crystalline surfaces lack the periodicity in the vertical direction. As a result, the reciprocal lattice vector for a surface reduces to the form

$$\boldsymbol{G}_{hk} = h\,\boldsymbol{a}^* + k\,\boldsymbol{b}^* \quad \text{with} \quad h,k \in \mathbb{Z}\ , \tag{2.7}$$

where

$$\boldsymbol{a}^* = 2\pi\frac{\boldsymbol{b}\times\boldsymbol{n}}{\boldsymbol{a}\cdot(\boldsymbol{b}\times\boldsymbol{n})} \quad \text{and} \quad \boldsymbol{b}^* = 2\pi\frac{\boldsymbol{n}\times\boldsymbol{a}}{\boldsymbol{a}\cdot(\boldsymbol{b}\times\boldsymbol{n})} \tag{2.8}$$

are again the reciprocal lattice vectors with $\boldsymbol{n}$ being the unit vector perpendicular to the surface.

In principal, the concept of the reciprocal lattice is of particular interest with respect to the interpretation of diffraction processes and is therefore commonly used for the analysis of periodic structures by X-ray or electron diffraction (see Sec. 2.6 and Sec. 2.7).

2.2 Growth of epitaxial (ultra)thin films

(Ultra)thin films are often grown on substrates, which serve as a template for the films. Hereby, the growth of thin films is called epitactic when generally two conditions apply: first, the grown film must be crystalline, and second the film must have a well-defined orientation relative to the crystalline substrate underneath. Epitaxial (ultra)thin films can be prepared by different types of deposition techniques such as sputter deposition, pulsed laser deposition, or (reactive) molecular beam epitaxy. The latter technique was also utilized for the preparation of the different films for this work (cf. Sec. 4.1).

In molecular beam epitaxy, for instance, (transition) metals or rare earths are evaporated and directed as a molecular beam onto a substrate surface. The impinging particles can either adsorb as adatoms on the surface, where they are able to migrate over the surface by diffusion, or re-evaporate (desorb) if the temperature of the substrate during deposition is too high. Although it might now appear that excessively high temperatures are rather to be avoided for thin film growth, these temperatures are again occasionally desired in, e.g., (reactive) solid phase epitaxy, where the formation of crystalline films is mediated by post-deposition annealing of previously deposited films. However, this synthesis method for thin film preparation is heavily restricted by the material properties of the substrate since (even small) elevated temperatures can promote diffusion and segregation of substrate material into the growing film, as demonstrated, e.g., for Fe_3O_4 thin films grown on MgO substrates above a substrate temperature of 250 °C [49].

2.2.1 Growth modes in epitaxy

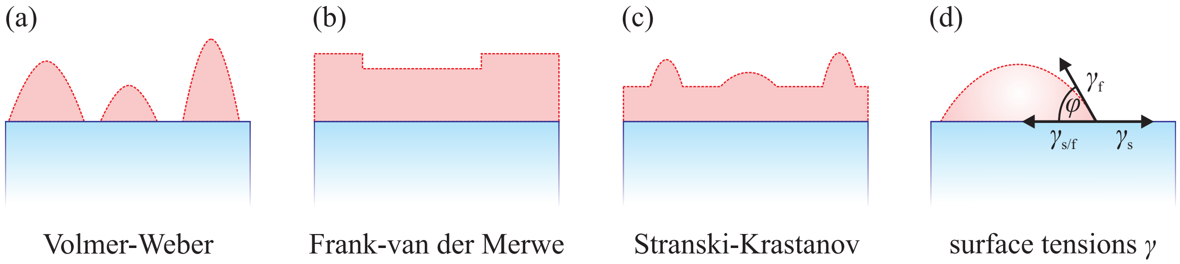

Fig. 2.4: Sketch of the different modes in which the growth of a thin film (red) on a substrate (blue) can proceed: (a) Volmer-Weber (3D island) growth, (b) Frank-van der Merwe (layer-by-layer) growth, and (c) Stranski-Krastanov (layer-plus-island) growth. The different growth modes can be derived considering the involved thermodynamic quantities (the three macroscopic surface tensions) γ_s,γ_f, and $\gamma_{s/f}$, as shown in (d). The wetting angle is denoted by φ as the angle between γ_f and $\gamma_{s/f}$.

In the case of adatoms, their mobility as well as interatomic interactions determine the growth mode of the film, which can be divided into three principal categories [cf. Fig. 2.4 (a–c)]: formation of three-dimensional islands (Volmer-Weber growth), layer-by-layer growth (Frank-van der Merwe growth), and a combination of both just mentioned growth types (2D layer and 3D island growth), called Stranski-Krastanov growth. The different growth modes are described in more detail below [29]:

- **Volmer-Weber (3D island) growth**
  Film growth proceeds in this growth mode if adatoms of the film tend to bond to one another rather than to the surface of the substrate. As a consequence, the adatoms directly nucleate on the surface and form three-dimensional islands.
- **Frank-van der Merwe (layer-by-layer) growth**
  If, in turn, the adatoms prefer to bond to the substrate surface and less to each other, two-dimensional growth occurs. In this process, each atomic layer is first completely closed before a new layer begins to form on top of it.
- **Stranski-Krastanov (layer-plus-island) growth**
  Here, the film initially starts to grow as a complete two-dimensional layer, but after a critical film thickness, three-dimensional islands form. Hence, this growth mode can be understood as an intermediate case between Volmer-Weber and Frank-van der Merwe growth.

For each growth type, individual conditions apply, under which the respective mode occurs. The specific conditions can be derived on the basis of a thermodynamic approach that addresses the different surface or interface tensions γ involved in the growth process – the surface tension of the substrate γ_s, the surface tension of the film γ_f, and the interface tension of the substrate-film interface $\gamma_\mathrm{s/f}$. Here, γ is equivalent to a characteristic free energy per unit area necessary to build a surface or interface. Alternatively, γ can be considered as a force per unit length, acting on a contact line and pulling in a particular direction [see Fig. 2.4 (d)]. The force equilibrium of all appearing forces is expressed by

$$\gamma_\mathrm{s} = \gamma_\mathrm{s/f} + \gamma_\mathrm{f} \cos(\varphi) \ , \tag{2.9}$$

with the wetting (or contact) angle φ between the surface tension of the film γ_f and the interface tension of the substrate-film interface $\gamma_\mathrm{s/f}$ [29]. For $\varphi = 0$, the surface tension of the substrate is larger than the sum of both the film surface tension and the interface tension, resulting in layer-by-layer growth for $\gamma_\mathrm{s} \geq \gamma_\mathrm{s/f} + \gamma_\mathrm{f}$. In contrast, island growth is favored for $\varphi > 0$ and, hence, $\gamma_\mathrm{s} < \gamma_\mathrm{s/f} + \gamma_\mathrm{f}$ applies. The layer-plus-island growth initially follows the layer-by-layer growth ($\varphi = 0$). However, the film growth changes both γ_s and $\gamma_\mathrm{s/f}$ in such a way that the layer-by-layer growth becomes unfavorable for the further growth process in this case. Thus, the film then complies with the criteria characteristic of island growth ($\varphi > 0$) and forms islands.

2.2.2 Substrate-induced strain effects

When a crystalline thin film is deposited on a crystalline substrate, their lattice constants usually differ from each other [cf. Fig. 2.5 (a)], unless film and substrate are made of the same material. In the following, a_f and a_s refer to the bulk lattice constants of the film and the substrate, respectively. The lattice mismatch

$$f = \frac{a_\mathrm{f} - a_\mathrm{s}}{a_\mathrm{s}} \tag{2.10}$$

is a quantitative measure of how much the film and substrate diverge from one another [29]. A non-zero lattice mismatch is usually accompanied by strain induced by the substrate into the deposited film due to the difference in lattice constants. The induced in-plane strain parallel to the substrate-film interface is defined by

$$\varepsilon_\parallel = \frac{a_\mathrm{f,str} - a_\mathrm{f}}{a_\mathrm{f}} = \frac{\Delta a_\mathrm{f}}{a_\mathrm{f}} \ , \tag{2.11}$$

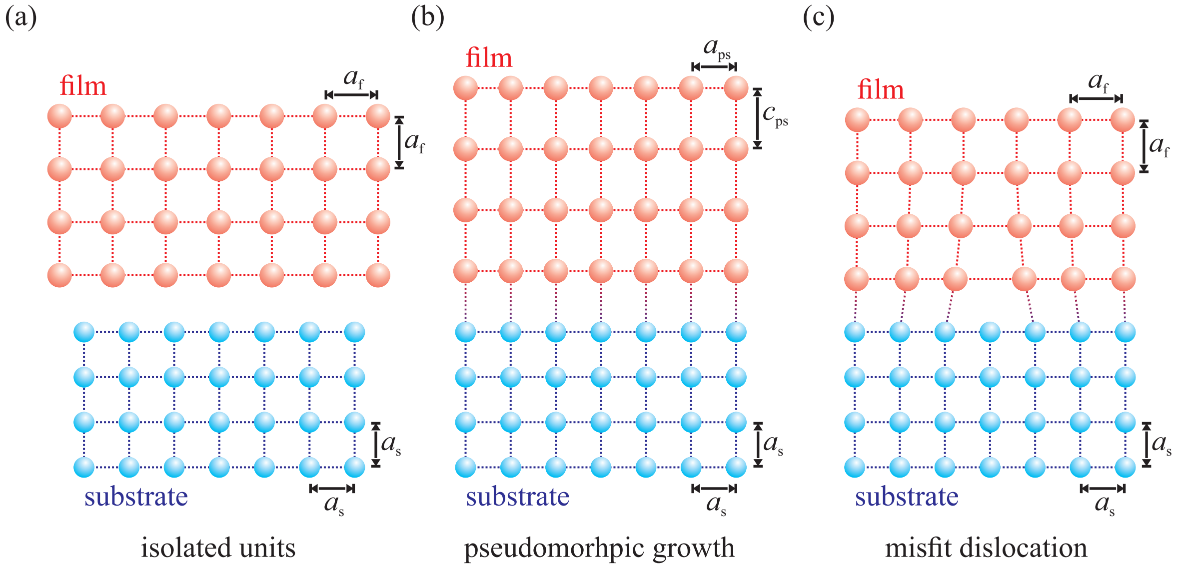

Fig. 2.5: Illustration of a film (red) with larger lattice constant a_f than the lattice constant a_s of the substrate (blue). (a) Both individual units in equilibrium without interaction at their interface. (b) Film and substrate joined as in the case of pseudomorphic growth with strong interaction at interface and lateral adaptation of the film lattice to the substrate lattice. $a_\mathrm{ps} = a_\mathrm{s}$ and c_ps are the strained lateral and vertical lattice constants of the film, respectively. (c) Film and substrate are connected through the formation of interfacial misfit dislocations, resulting in a relaxation of the film toward its bulk lattice constants with growing film thickness. Adapted from Ref. [50].

and the out-of-plane strain perpendicular to the substrate-film interface is analogously defined by

$$\varepsilon_\perp = \frac{c_\mathrm{f,str} - c_\mathrm{f}}{c_\mathrm{f}} = \frac{\Delta c_\mathrm{f}}{c_\mathrm{f}} \,, \tag{2.12}$$

in which $a_\mathrm{f,str}$ and $c_\mathrm{f,str}$ are the strained in-plane and out-of-plane film lattice constants, respectively [51]. Both the out-of-plane strain $\varepsilon_\perp$ and the in-plane strain $\varepsilon_\parallel$ are linked to each other by the Poisson ratio ν, which is unique for each material and describes the behavior of a certain material under mechanical stress [52–54]. A detailed derivation of the Poisson ratio ν by means of the material-specific elastic moduli or elastic constants [55] is presented in Refs. [25, 28]. In the case of an epitaxial film with cubic lattice symmetry subjected to equal biaxial stress within the (001) plane, the relationship between $\varepsilon_\perp$ and $\varepsilon_\parallel$ can be expressed by

$$\varepsilon_\perp = \frac{2\nu}{\nu - 1}\varepsilon_\parallel \,. \tag{2.13}$$

Consequently, despite the absence of stress in the normal film direction, the two-dimensional stress induced by the substrate will always cause additional strain in the out-of-plane direction and thus distortion of the film lattice in the lateral and vertical directions. If the lattice mismatch f is relatively small, the film usually attempts to laterally match the periodicity of the substrate, which, in most cases, is coupled with an opposing distortion in the vertical direction [cf. Fig. 2.5 (b)]. This growth behavior is referred to as pseudomorphic (or coherent [56]) growth. For instance, a lateral compression is accompanied by a vertical expansion, and vice versa. However, this type of behavior is reflected only in films exhibiting a positive Poisson ratio ν. For negative values of ν, the material instead behaves auxetically, i.e., the film in this case responds with both vertical and lateral compression or expansion depending on the induced stress. Therefore, the Poisson ratio dictates how the material will be elastically deformed in the vertical direction corresponding to a given lateral distortion due to the lattice mismatch. Based on Eq. (2.13), the vertical distortion Δc_f of a tetragonally strained film is thus

$$\Delta c_\mathrm{f} = \frac{2\nu}{\nu - 1} \Delta a_\mathrm{f} \ , \tag{2.14}$$

according to a given lateral distortion Δa_f and assuming an initial cubic structure of the film with $c_\mathrm{f} = a_\mathrm{f}$.

As the film proceeds to grow coherently, the strain energy involved in the growth process

$$E_\varepsilon = \varepsilon_{\|}^2 \, B \, d_\mathrm{f} \tag{2.15}$$

increases proportionally with the film thickness d_f until, at a certain critical film thickness d_c, the formation of so-called misfit dislocations becomes more favorable for the film [57] in order to minimize the total energy. Hereby, B represents a function of elastic constants, which depends on the crystal structure of the film as well as on the direction of film growth. The critical film thickness d_c for a given film system can be estimated by applying the most widely accepted model of Matthews and Blakeslee [58]

$$\frac{d_\mathrm{c}}{b} = \frac{\left(1 - \nu \cos^2 \alpha\right) \, \left(\ln\left(\frac{d_\mathrm{c}}{b}\right) + 1\right)}{2\pi \, f \, (1+\nu) \cos(\lambda)} \ , \tag{2.16}$$

with the magnitude of the Burgers vector b, the Poisson ratio ν of the film, the angle α between the Burgers vector and the dislocation line, the lattice mismatch f, and the angle λ between the Burgers vector and the direction perpendicular to the dislocation line and within the plane of the interface involved. As a result of the incorporation of misfit dislocations, the epitaxial film is able to relieve (partly) the induced lateral strain and relaxes toward its bulk lattice constant a_f. The distance between two dislocations formed depends on the amount of strain released during this process. Assuming a simple cubic structure for both film and substrate, the separation of neighboring dislocations in the film is given by

$$d_\mathrm{dis} = \frac{a_\mathrm{f}}{f - \varepsilon_{\|}} \simeq \frac{b}{f - \varepsilon_{\|}} \ , \tag{2.17}$$

where $\varepsilon_{\|}$ denotes the residual lateral strain of the film [51]. If the lateral strain is entirely compensated by misfit dislocations ($\varepsilon_{\|} \to 0$), which is the case when the film is totally relaxed, the distance of dislocations reduces to b/f.

For a relatively large lattice mismatch f between substrate and film, the strain imposed by the substrate is considerably higher and so is the strain energy involved, which depends quadratically upon the mismatch [59]. As a consequence, misfit dislocations can already form at the substrate-film interface to reduce the strain energy immediately at the onset of film growth [cf. Fig. 2.5 (c)].

2.3 Matter in external magnetic fields and collective magnetism

When matter is subjected to an external magnetic field $\boldsymbol{H}$, it responds with a corresponding magnetization

$$\boldsymbol{M} = \frac{\boldsymbol{m}_\mathrm{sum}}{V} = \frac{1}{V} \sum_j \boldsymbol{m}_j \ , \tag{2.18}$$

with $\boldsymbol{m}_{\mathrm{sum}}$ being the sum of all individual (atomic) magnetic moments $\boldsymbol{m}_j$ in a volume V. The atomic magnetic moment is composed of the orbital magnetic moment and the spin magnetic moment of the electrons within each atom. As the magnetic moments produced by the nuclei are far lower compared to electron magnetic moments, nuclear magnetism is usually neglected. Matter whose magnetization $\boldsymbol{M}$ is linearly related to the external magnetic field $\boldsymbol{H}$, i.e.,

$$\boldsymbol{M} = \chi \, \boldsymbol{H} \ , \tag{2.19}$$

is called a linear material with the dimensionless proportionality constant χ, being the magnetic susceptibility of the material. Strictly speaking, the magnetic susceptibility is a scalar quantity only in very few crystals since the magnetic response $\boldsymbol{M}$ often depends on the orientation of the sample with respect to the external magnetic field $\boldsymbol{H}$. Consequently, the magnetic susceptibility is in fact a symmetric second-rank tensor $\overline{\overline{\chi}}$. Both the external magnetic field $\boldsymbol{H}$ and the magnetization $\boldsymbol{M}$ generate a magnetic induction (also named magnetic flux density), which add up to

$$\boldsymbol{B} = \mu_0 \, (\boldsymbol{H} + \boldsymbol{M}) = \mu_0 \underbrace{(1+\chi)}_{\mu_{\mathrm{r}}} \boldsymbol{H} = \mu_0 \, \mu_{\mathrm{r}} \, \boldsymbol{H} \ , \tag{2.20}$$

neglecting any demagnetizing and stray fields. μ_0 is the permeability of free space (or vacuum permeability) and $\mu_{\mathrm{r}} = (1 + \chi)$ is the relative permeability of the material.

With regard to the magnetic susceptibility χ, matter without a collective magnetic order can basically be divided into two principle types: diamagnets and paramagnets. Diamagnets have a magnetic susceptibility $\chi < 0$ and do not possess any permanent atomic magnetic moment for vanishing external magnetic field. However, upon influence of an external magnetic field, circular charge currents are induced in a diamagnet according to Lenz's law, producing a magnetic field that counteracts the external magnetic field. In contrast, paramagnets are characterized by a magnetic susceptibility $\chi > 0$ and possess permanent magnetic moments even in the absence of an external magnetic field. The permanent magnetic moments are not coupled to each other and, therefore, they orient randomly in a vanishing external magnetic field, resulting in zero magnetization. When exposed to an external magnetic field, the permanent magnetic moments align in the direction of the magnetic field and generate a non-zero magnetization. It is to be noted that depending on whether the particular type of magnetism is caused solely by localized or primarily by delocalized (conduction band) electrons further subtypes can be differentiated, such as Langevin diamagnetism and Langevin paramagnetism, both evoked by localized electrons, or Landau diamagnetism and Pauli paramagnetism in metals with delocalized electrons.

Matter exhibiting permanent magnetic moments but unlike paramagnets with additional long-range collective magnetic order fall into a different category with respect to magnetism (collective magnetism). Materials of this type retain their magnetic collective order even in the absence of an external magnetic field, resulting in a spontaneous magnetization within the material up to a critical material-specific temperature. Above the critical temperature, they undergo a magnetic phase transition, lose their collective magnetic order, and become paramagnetic instead.

Figure 2.6 presents three characteristic examples of magnetic materials belonging to this variety, namely ferromagnets, antiferromagnets, and ferrimagnets. Ferromagnets have atomic magnetic moments all pointing in one and the same direction, yielding maximum magnetization [cf. Fig. 2.6 (a)]. In antiferromagnets, adjacent atomic magnetic moments align antiparallel to one another, such that no net magnetization occurs on a macroscopic scale [cf. Fig. 2.6 (b)]. Accordingly, antiferromagnets can be seen as two interpenetrating sublattices, in which the magnetic moments pointing into the same direction are arranged on one sublattice while the opposing magnetic moments are arranged on the respective other sublattice. Ferrimagnets can be understood in the same way with the dif-

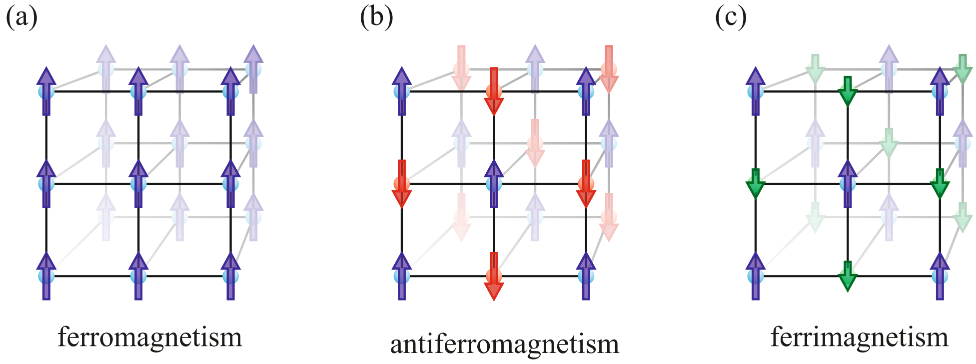

Fig. 2.6: Collective magnetic materials exhibit three main magnetic orders: (a) ferromagnetism, (b) antiferromagnetism, and (c) ferrimagnetism. Both antiferromagnetism and ferrimagnetism can be described by two interacting antiparallel sublattices. In antiferromagnetism, both sublattices are equivalent, so that the magnetization of both sublattices cancel each other out. This is not the case for ferrimagnetism, for which the two sublattices are not equivalent and, therefore, a non-vanishing overall magnetization occurs.

ference that both sublattices are not equivalent [cf. Fig. 2.6 (c)]. As a result, the magnetizations of the two sublattices do not cancel each other out entirely. For both ferromagnets and ferrimagnets, the critical temperature above which their collective magnetic order vanishes and turns into paramagnetism is called Curie temperature T_C, whereas for antiferromagnets, it is referred to as Néel temperature T_N.

In the following, the phenomenon of collective magnetic ordering of localized electrons will be described in more detail since the ferrite films (cf. Chap 3) that have been magnetically characterized in this work belong to this group of magnetic materials. For a complete description of collective magnetism, including the collective magnetic ordering of itinerant magnetic moments in metals by means of the Stoner model, see Refs. [31,32].

2.3.1 Collective magnetic ordering

The influence of the magnetic dipolar interaction is far too weak ($\sim 0.1\,\mathrm{meV}$ [30]) to account for the magnetic long-range ordering in magnetic materials except at very low temperatures. Instead, the origin of the magnetic order can be traced back to the so-called exchange interaction. The exchange interaction is a quantum-mechanical effect and can basically be understood as electrostatic interaction between two close electrons, usually of neighboring atoms, in conjunction with the Pauli exclusion principle, precluding the two electrons to be simultaneously at the same location due to possible overlapping wave functions if both have the same spin. In a magnetic material with collective magnetic order, the exchange interaction is by far the strongest magnetic interaction.

The overall wave function Ψ for the joint state of (two) electrons comprises a spatial part ψ and a spin part[1] χ. Since electrons are fermions, the overall wave function is postulated to be antisymmetric under the exchange of any electron pair. Thus, either the spatial part of the overall wave function must be symmetric ψ_sym in combination with an antisymmetric spin singlet state χ_S (antiparallel spin alignment with total spin quantum number $S = 0$) or vice versa with antisymmetric spatial part ψ_as and a symmetric spin triplet state χ_T ($S = 1$). The overall wave function

---

[1] It is common to express spin states also like the magnetic susceptibility by χ. In order to avoid confusion, it should be noted that in the following χ refers exclusively to spin states.

is therefore given by

$$\Psi_{\mathrm{S}} = \psi_{\mathrm{sym}}\left(\boldsymbol{r}\right)\,\chi_{\mathrm{S}}\left(\boldsymbol{s}\right) \text{ or by } \Psi_{\mathrm{T}} = \psi_{\mathrm{as}}\left(\boldsymbol{r}\right)\,\chi_{\mathrm{T}}\left(\boldsymbol{s}\right)\ , \tag{2.21}$$

where $\boldsymbol{r} = (\boldsymbol{r}_1, \boldsymbol{r}_2)$ and $\boldsymbol{s} = (\boldsymbol{s}_1, \boldsymbol{s}_2)$ are the spatial and spin coordinates of the two electrons, respectively. The energies associated with the two possible states are given by E_{S} and E_{T}, considering electron-electron interaction. The difference of the two energies defines the so-called exchange constant (or exchange integral)

$$J = \frac{E_{\mathrm{S}} - E_{\mathrm{T}}}{2}\ . \tag{2.22}$$

For $E_{\mathrm{S}} > E_{\mathrm{T}}$, J is positive ($J > 0$) and consequently the triplet state Ψ_{T} is preferred by the system as it is the state with the lower energy. In this case, the interaction between the two electrons is ferromagnetic, resulting in complete parallel alignment of all spins in a single direction and a ferromagnetic spin structure. In contrast, the singlet state Ψ_{T} is favored for $J < 0$ due to $E_{\mathrm{S}} < E_{\mathrm{T}}$, indicating antiferromagnetic interaction. This leads to antiparallel orientation of adjacent spins and an antiferromagnetic spin structure.

Heisenberg model and Hubbard model

In modern physics, it is often convenient to investigate the magnetic properties of materials with the help of model Hamiltonians, which reproduce correct results even without establishing a first-principles theory [32]. The Heisenberg model [60] as well as the Hubbard model[2] [63] are among the most widely used and popular Hamiltonian models. In the Heisenberg model, the exchange interaction is described in terms of two interacting spins $\hat{\boldsymbol{S}}_1$ and $\hat{\boldsymbol{S}}_2$ within an effective Hamiltonian

$$\hat{\mathcal{H}} = -2J\,\hat{\boldsymbol{S}}_1 \cdot \hat{\boldsymbol{S}}_2\ , \tag{2.23}$$

which acts solely on the spin wave function χ and produces the same energy splitting for antiparallel and parallel alignment. Since it was recognized that Eq. (2.23) probably also applies, e.g., between neighboring atoms of a lattice [30], the two-spin Hamiltonian can be extended and generalized for a many-body system to

$$\hat{\mathcal{H}} = -2\sum_{i>j} J_{ij}\,\hat{\boldsymbol{S}}_i \cdot \hat{\boldsymbol{S}}_j \tag{2.24}$$

as a sum over all atoms i and all interacting neighbors j with the restriction $i > j$ to avoid 'double-counting'. This coupling of atomic moments (sums of spins) of different atoms in a lattice is commonly called inter-atomic exchange, whereas the coupling of individual spins located on the same atom is called intra-atomic exchange [32]. In addition, usually only the nearest-neighbor spin interactions are considered in the many-electron Heisenberg Hamiltonian and all other spin interactions are regarded as negligible.

Unlike the Heisenberg model, the spin operator is not an explicit element in the effective Hamiltonian of the Hubbard model, although the spin is considered in further calculations. The Hubbard model describes in terms of two interacting electrons the possibility of virtual electron hopping between lattice sites (from one atom to the next and back again) based on the competing interplay

---

[2] Although the Hubbard model was named after Hubbard alone, Gutzwiller [61] and Kanamori [62] independently developed the same approaches in the same year as Hubbard to describe electrons in $3d$ transition metals under the influence of strong Coulomb repulsions.

of electrostatic Coulomb energy and kinetic (or hopping) energy of the electrons. Thereby, the hopping processes are subject to the Pauli principle as every lattice site in the picture of one orbital, containing already one electron per lattice atom, can be doubly occupied with one spin-down and one spin-up electron. The phenomenon of (virtual) electron hopping plays a central role especially in the indirect exchange interaction types, i.e., when the exchange interaction between electrons of neighboring magnetic moments proceeds by means of an intermediary. Both the direct and especially the indirect exchange will be described in more detail later. The electrostatic Coulomb energy addresses the Coulomb repulsion of electrons and describes the energy required to place two electrons on the same lattice site (double occupation on the same atom). The strength of the Coulomb repulsion is parameterized by U. As the distance between the electrons increases, the Coulomb energy decreases, causing the electrons to be more likely to be localized to their atoms. The kinetic energy is associated with the motion of electrons between different atoms. By conserving kinetic energy, the electrons tend to be less confined to their respective atoms and are thus delocalized, allowing electrons to hop from one atom to another. The relationship between kinetic energy and delocalization is a direct consequence of the Heisenberg uncertainty principle. The probability for a hopping process is characterized by the hopping matrix element t, where hopping itself can be understood as a process in which an electron is annihilated on one lattice site and then created on a neighboring lattice site, or vice versa. The corresponding Hubbard model Hamiltonian can be expressed by

$$\hat{\mathcal{H}} = -t \sum_{\langle i,j \rangle,\sigma} \left(c^{\dagger}_{i,\sigma}\, c_{j,\sigma} + c^{\dagger}_{j,\sigma}\, c_{i,\sigma} \right) + U \sum_{i=1}^{N} n_{i,\uparrow}\, n_{i,\downarrow} = \hat{\mathcal{H}}_t + \hat{\mathcal{H}}_U \ , \tag{2.25}$$

with the first term representing the kinetic energy involving the annihilation ($c_{i,\sigma}$) of the electron of spin σ on lattice site i and its creation ($c^{\dagger}_{j,\sigma}$) on an adjacent lattice site j, or vice versa. In the process, the spin of the electron is preserved. The second term represents the electrostatic Coulomb energy, which contributes only in the case of double occupation of electrons on lattice site i, indicated by the counting operator $n_{i,\sigma} = c^{\dagger}_{i,\sigma}\, c_{i,\sigma}$.

In the limiting case of $U \gg t$ and $U \geq 0$, the double occupation of lattice sites becomes energetically unfavorable and electrons are localized at their atoms (contribution of $\hat{\mathcal{H}}_U$ dominates). In this limit, the Hubbard model, similar to the Heisenberg model for $J < 0$, gives rise to an antiferromagnetic alignment of the localized electron spins, resulting in an antiferromagnetic isolator (Mott insulator). Metallic behavior, on the other hand, is realized for $t \gg U$ due to delocalized electrons. The metal-insulator transition occurs when $U \sim t$.

Direct exchange and indirect exchange

Depending on whether an intermediary is involved in the exchange interaction, a distinction can be made between direct exchange and indirect exchange. In direct exchange, the electrons on neighboring magnetic atoms interact with each other due to directly overlapping electron wave functions. Although this exchange mechanism seems to be the most obvious one, the direct spatial overlap between neighboring magnetic orbitals is often, however, insufficient in most materials, so that direct exchange occurs generally rather rarely.

Indirect exchange is much more common, e.g., in (transition) metal oxides, in which the exchange interaction is mediated across a diamagnetic oxygen ligand, possessing a fully occupied $2p$ shell. Sandwiched between two cations of the same element, the overlap of the $2p$ oxygen anion orbital and the neighboring orbitals of the cations renders the indirect exchange possible. In (transition) metal oxides such as Fe_3O_4 and $CoFe_2O_4$, the governing indirect exchange interactions are the superexchange [64, 65] and the double exchange [66]. The manifestation of a magnetic coupling in both cases can be understood in terms of electron hopping processes, although in superexchange, the electron hopping proceeds only virtually without actually modifying the occupancies of the shells of the two cations.

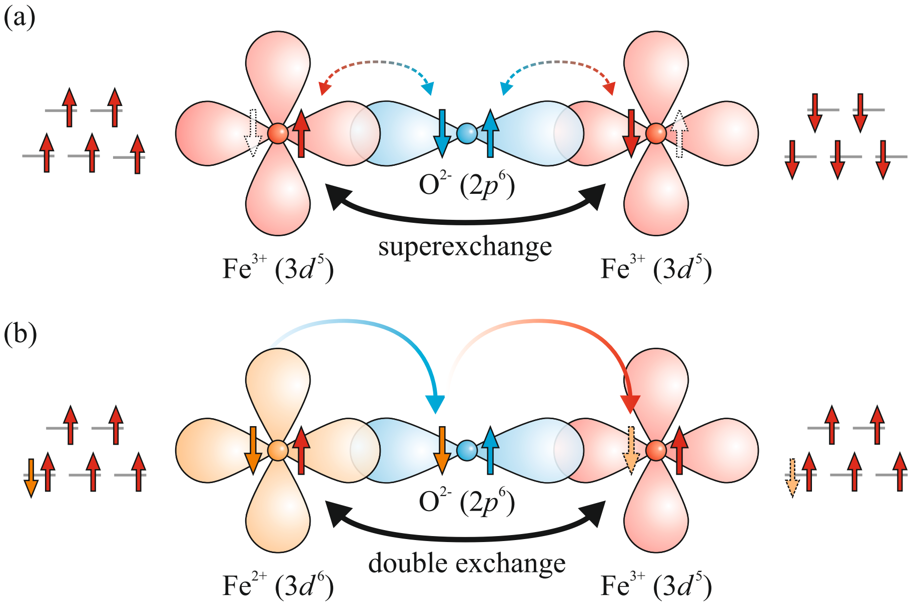

Fig. 2.7: Illustration of (a) superexchange and (b) double exchange. In superexchange, two electrons are simultaneously virtually hopping (dashed arrows) between the $2p$ orbital of the non-magnetic oxygen anion and the overlapping non-fully occupied $3d$ orbital of the Fe^{3+} cations, resulting in an indirect antiferromagnetic coupling between both Fe^{3+} cations. Here, empty states are indicated by white arrows. Since no real charge transport is involved, the occupations of the $3d$ orbital of the two cations remain unchanged. In double exchange, both cations couple ferromagnetically by transferring an extra electron of the Fe^{2+} cation to the Fe^{3+} cation via the hybridized oxygen anion (solid blue and red arrow). Due to the electron transfer, the occupation of the $3d$ orbitals of the cations is altered. In both exchange interactions, the hopping electrons must obey the Pauli principle. Based on Ref. [67].

Figure 2.7 (a) illustrates the mechanism of superexchange for two Fe^{3+} cations separated by an oxygen anion in a typical 180° TM–O–TM bond geometry. Each $3d$ shell is half-filled by itself with five electrons ($3d^5$ configuration) of the same spin (Hund's rule). An electron can (virtually) hop from the $2p$ orbital of the oxygen anion into an overlapping and not fully occupied $3d$ orbital of a neighboring Fe^{3+} cation only when it meets the constraints imposed by the Pauli principle, i.e., two electrons having identical spins are prohibited to occupy the same single state in the $3d$ orbital. Therefore, if the $3d$ orbital of the Fe^{3+} cation exhibits exclusively spin-up electrons, only spin-down electrons are allowed to transfer, resulting in a virtual $3d^{n+1}$ state in the Fe^{3+} cation at an energy cost U due to the on-site $3d$ Coulomb interaction [cf. Eq. (2.25)] [68]. The hole created in the $2p$ orbital of the oxygen anion can then simultaneously be filled by an electron transfer from the other adjacent Fe^{3+} cation. Alternatively, the remaining $2p$ electron could also transfer into the aforementioned adjacent Fe^{3+} cation. In both cases, the hopping electron must again obey the Pauli principle. At last, the system is restored to its original initial state by the corresponding hopping processes in the reverse order. As (virtual) electron hopping with both Fe^{3+} cations involved is thus only possible for antiparallel alignment of the Fe^{3+} cations, the superexchange between the two cations in this bond geometry is antiferromagnetic with coupling constant

$$J = -\frac{2t^2}{U} \, , \tag{2.26}$$

with t describing the hopping probability between the $2p$ orbital of the oxygen anion and the $3d$ orbitals of adjacent Fe^{3+} cations. However, the exchange does not necessarily have to be antiferromagnetic. For instance, if the oxygen anion forms a bridge with TM–O–TM bond angle of about 90° with respect to the transition metal cations, the interaction will instead be ferromagnetic with positive but weak coupling constant J. Apart from the TM-O-TM bond angle, the magnetic coupling is also vastly sensitive to the interatomic separation as well as to the occupation and orbital degeneracy of the $3d$ states. This is where the rules proposed by Goodenough, Kanamori, and Anderson, known as the Goodenough-Kanamori rules [69–71], come into play, allowing the type of resulting magnetic coupling to be predicted in most transition metal oxides. As just mentioned, the exchange is antiferromagnetic if the superexchange interaction occurs between singly occupied $3d$ orbitals of magnetic cations pointing to each other (TM–O–TM bond angle is 120° to 180°), while it is ferromagnetic at 90° TM–O–TM bond angle. The exchange is also ferromagnetic if the two magnetic cations with singly occupied $3d$ orbitals interact across a full or empty $3d$ orbital of the same type. Most importantly, these Goodenough-Kanamori rules also hold for transition metal ferrites such as $CoFe_2O_4$, which has been vastly studied in this work.

Double exchange is essentially similar to ferromagnetic superexchange but with real electron transfer due to mixed-valence configuration of the two magnetic cations involved, like in the case of the common double-exchange pair Fe^{3+} and Fe^{2+}, as sketched in Fig. 2.7 (b). Fe^{2+} has $3d^6$ configuration and thus possesses one electron more compared to Fe^{3+} with $3d^5$ configuration. This additional electron occupies, e.g., the first spin-down state in a $3d$ orbital containing already five electrons fully occupying the spin-up states. Due to the hybridization with the non-magnetic oxygen anion, the spin-down electron can 'directly' transfer from one $3d$ orbital to the next [68] through transfer of the electron from the Fe^{2+} cation to the central oxygen anion with simultaneous transfer of an electron from the oxygen anion to the Fe^{3+} cation. However, electron transfer is only possible if in the $3d$ orbital of the Fe^{3+} cation there is an empty state available dictated by the Pauli principle. This is provided when the states of both $3d$ orbitals are filled with electrons of matching spin orientation (parallel alignment) as spin-flips of the hopping electrons are not allowed during the hopping processes. Therefore, the double exchange interaction is always ferromagnetic because in the opposite case (antiparallel orientation) the hopping process would be forbidden.

2.3.2 Domain formation and magnetization curves

Based on the previous descriptions, it would be intuitive to assume that, e.g., in a perfect ferromagnetic solid all magnetic moments are aligned parallel to each other imparted by the exchange interaction, resulting in a maximum overall magnetization. Ordinarily, however, a much lower magnetization is observed, drastically undercutting the magnetization for completely parallel aligned magnetic moments. The deviations from the expected magnetization can be ascribed to the formation of magnetic domains in the ferromagnetic material, known as Weiss domains, which are separated by domain walls from each other. Within each magnetic domain, all magnetic moments are aligned in the same direction with the direction differing between different magnetic domains. Consequently, the overall magnetization is an average of the magnetizations of all magnetic domains, which can thus be smaller than the respective individual magnetizations due to different orientations. Hereby, the transition from one magnetization direction to the other of two adjacent magnetic domains does not occur within a discontinuous jump but rather extends gradually over several atomic planes, in which the individual magnetic moments rotate smoothly from one direction to the other [24].

The formation of magnetic domains in a magnetic material is a direct response of minimizing the total free energy of the system, including, e.g., the self-energy associated with dipolar fields [30,31].

A material that has been (homogeneously) magnetized will produce demagnetization/stray fields[3] $\boldsymbol{H}_\mathrm{d}$, depending on the physical shape of the material [32]. The energy related to $\boldsymbol{H}_\mathrm{d}$ is called the (demagnetization/magnetostatic/dipolar) self-energy and is given by

$$E_\mathrm{s} = -\frac{\mu_0}{2} \int \boldsymbol{M} \cdot \boldsymbol{H}_\mathrm{d} \, dV \ , \tag{2.27}$$

in which the integral is taken over the volume V of the magnetic body. By forming magnetic domains, this type of energy can be saved, however, at an energy cost due to creation of domain walls between adjacent magnetic domains characterized by the domain wall energy E_dw. Thus, the cost associated with building a domain wall and the cost of demagnetizing and stray fields compete with each other with respect to the creation of magnetic domains, which is illustrated in Fig. 2.8.

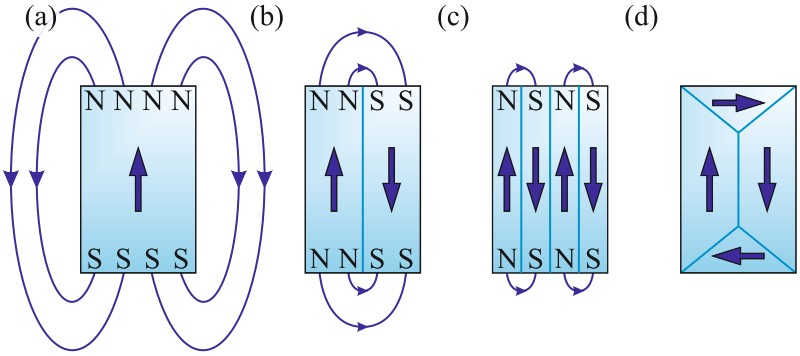

Fig. 2.8: Four different types of domain structures with their respective stray fields. To reduce the self-energy E_s, the (a) monodomain state splits into (b-d) several magnetic domains, leading to continuously smaller stray fields the larger the number of domains inside the material. Adapted from Ref. [24].

A single domain structure as a monodomain state without any domain walls leads to large stray fields and, therefore, to a large self-energy E_s [cf. Fig. 2.8 (a)]. The self-energy E_s causes an enhancement of the total free energy. Breaking the magnetic ordering into several magnetic domains with antiparallel orientations of the magnetizations reduces the self-energy E_s, however, at a cost of an increased domain wall energy E_dw required to create domain walls [cf. Fig. 2.8 (b,c)]. Thereby, each magnetic domain generates its own demagnetization and stray field and is, in turn, prone to the stray fields produced by the other magnetic domains [31]. Comparatively to a monodomain state, this domain structure is then referred to as a multidomain state. In the sense of minimizing E_s to the maximum extent possible, it is energetically favored for the material to confine magnetic domains of antiparallel orientation by closure domains, leading to a complete stray-field-free configuration due to the absence of any magnetic poles [cf. Fig. 2.8 (d)]. In addition, the accurate domain structure as well as its shape is determined not only by the self-energy and domain wall energy but also by additional energy contributions relevant to the total free energy such as the Zeeman energy, strain energy, and several anisotropy energies. In principle, these additional energy contributions must also be taken into account when minimizing the total free energy. Since this, however, is a rather subordinate element for this work, please refer to Refs. [26, 31, 72] for an in-depth description of the numerous different energy terms and the formation of magnetic domains at greater length.

If the magnetic body, exhibiting initially multiple magnetic domains, is now subjected to an external magnetic field, its magnetization will change either by motion of domain walls or by rotation of the magnetization in the individual domains in direction of the applied field. As a result, the various magnetic domains can change in size and shape according to the applied magnetic field. This behavior of magnetic domains is reflected in so-called magnetization curves or M vs H curves, which is schematically depicted in Fig. 2.9 representative for a ferro-/ferrimagnet.

In the early stages, when the ferro-/ferrimagnet is exposed to the influence of an external mag-

---

[3] The fields generated inside the material are referred to as demagnetizing fields and the fields generated outside the material are referred to as stray fields.

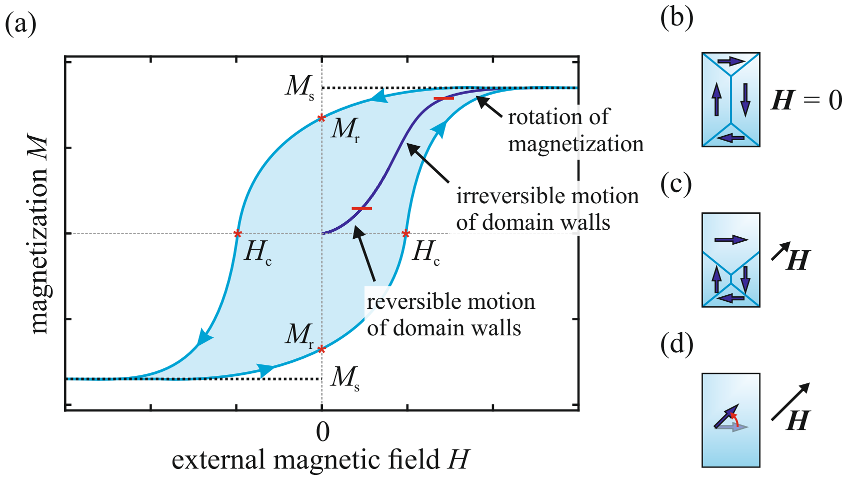

Fig. 2.9: (a) Characteristic magnetization (M vs H) curve of a ferro-/ferrimagnet with the dark blue curve representing the initial magnetization process and the blue curve denoting the subsequent hysteresis curve. The three characteristic quantities M_s, M_r, and H_c are annotated accordingly. (b–d) Impact of external magnetic fields $\boldsymbol{H}$ of different strengths on the domain structure. Adapted from Ref. [26].

netic field for the first time (magnetization process), the domain walls initially move reversibly at relatively low fields [cf. dark blue line in Fig. 2.9 (a)]. By increasing the magnetic field beyond this point, the motion of domain walls becomes irreversibly with additional coherent rotation of domain magnetizations toward the magnetic field direction for even higher magnetic fields. During this process, the volume of magnetic domains that are favorably oriented in terms of the applied magnetic field increases at the expense of magnetic domains with correspondingly unfavorable orientation. This continues until, at a certain magnetic field, only a single magnetic domain remains (monodomain state), whose magnetization is completely parallel to the magnetic field direction [cf. Fig. 2.9 (b–d)] [24]. The corresponding magnetization then represents the saturation magnetization M_s of the ferro-/ferrimagnet, which cannot be further amplified with increasing magnetic field and is thus saturated. Removal of the external magnetic field causes individual magnetic domains to form again but with partially retained orientation, resulting in an overall non-vanishing remanent magnetization at zero external magnetic field characterized by M_r. Still, in order to demagnetize the ferro-/ferrimagnet, a corresponding magnetic field H_c must be applied in the opposite direction, known as coercive field. If the magnetic field is increased in this direction even further, the ferro-/ferrimagnet reaches again a monodomain state with a corresponding saturation magnetization M_s for the reversed direction (magnetization reversal process). The complete magnetization curve is obtained by reversing the magnetization reversal process and returning to the initial saturation magnetization.

Several magnetic properties of the ferro-/ferrimagnet can be derived from the resulting hysteresis behavior. For instance, it epitomizes the characteristic non-linear response of the ferro-/ferrimagnet in terms of its magnetization with respect to an applied external magnetic field. Additionally, it allows the ferro-/ferrimagnet to be classified as either magnetically soft or magnetically hard, based on whether the magnetic material is easy or difficult to magnetize, respectively [30].

2.4 Superconducting quantum interference device - SQUID

In order to probe the integral magnetic properties of magnetic matter, several measurement techniques can be employed. Among the variety of techniques, the superconducting quantum interference device (SQUID) is compelling due to its high sensitivity even for samples that exhibit quite small magnetic signals. Hereby, the SQUID combines two physical phenomena [26,34], namely flux quantization [73] and the Josephson effect [74], which are both simultaneously utilized in a certain SQUID sensor type.

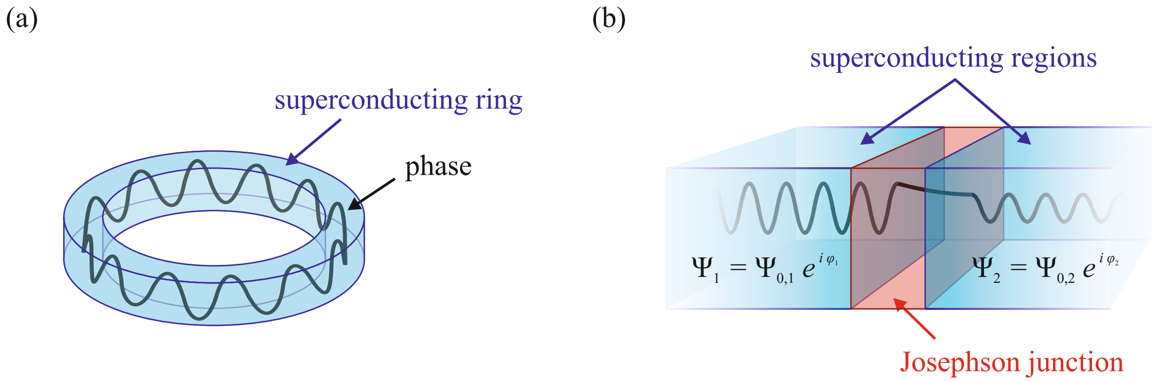

Fig. 2.10: The two main phenomena exploited in a SQUID: flux quantization and Josephson effect. (a) Flux quantization arises from the fact that, in the case of a superconducting closed ring, the macroscopic quantum-mechanical wave function describing the superconducting state must reproduce itself exactly within the ring when traced in a complete loop around the ring. Thus, since the phase of the wave function can only change by multiples of 2π, only discrete steady states are allowed within the ring. (b) The Josephson effect describes the possible tunneling process of Cooper pairs through a thin insulating barrier (Josephson junction) from one superconducting region to another. Based on Ref. [50].

2.4.1 Flux quantization

In the superconducting state, two electrons of opposite spin and momentum condense into a weakly bound so-called Cooper pair [75,76], which can be interpreted in terms of one electron being chased by a second electron. When an electron propagates through the lattice of a solid, positively charged ion cores are attracted by it and pulled in toward the passing electron, resulting in a distortion of the lattice. This creates an area of enhanced positive charge, which attracts another electron nearby before the lattice returns to its initial state and accordingly follows the preceding electron on its way through the material. In contrast to the non-superconducting state, where individual electrons carry the current and are subject to scattering at, e.g., lattice vibrations, endowing the material with resistance, Cooper pairs can travel through the superconducting material without resistance, making it a perfect conductor.

The superconducting state or rather the entire ensemble of Cooper pairs can be represented by a single quantum-mechanical wave function $\Psi = \Psi_0\, e^{i\varphi}$ with amplitude Ψ_0 and phase φ. In the case of a closed superconducting ring, the phase φ of this wave function must be coherent around the contour, i.e., the wave function must reproduce itself exactly at a certain initial point as it goes around the ring [cf. Fig. 2.10 (a)]. This leaves only discrete stationary states within the closed superconducting ring. The passing of a magnetic flux Φ through the superconducting ring induces a phase change of the wave function, related to the Aharanov-Bohm effect [77]. Since the phase of the wave function must still be continuous around the closed loop, only certain portions of the flux are allowed to be contained in the interior of the ring, which are integer multiples of the flux quantum $\Phi_0 = h/2e$ and is thus known as flux quantization [73, 78, 79]. Note that solely the magnetic flux threading superconducting ring is quantized. The magnetic flux itself is continuous.

2.4.2 Josephson effect

Interrupting the superconducting ring by a thin resistive (insulating) barrier, there is a possibility that Cooper pairs can tunnel through the barrier from one superconducting region to another [80]. This physical phenomena was already predicted by Brian David Josephson as early as 1962 [74] and is therefore referred to as the Josephson effect or Josephson tunneling [cf. Fig. 2.10 (b)]. An electrical current I flowing through such a (Josephson) junction is equal to

$$I = I_\mathrm{c} \sin(\delta) \ , \tag{2.28}$$

with $\delta = \varphi_1 - \varphi_2$ being the phase difference of the macroscopic quantum-mechanical wave functions of the two superconducting regions separated by the junction. I_c denotes the critical maximum supercurrent the junction can sustain. For $I < I_\mathrm{c}$, the Cooper pairs tunnel through the resistive barrier, constituting a supercurrent with initially zero voltage across the junction. However, when the current I exceeds I_c, this causes a temporal change of the phase difference

$$\frac{d\,\delta}{d\,t} = \frac{2e}{\hbar} V = 2\pi \frac{V}{\Phi_0} \tag{2.29}$$

and the voltage V across the junction switches abruptly to a non-zero value [34].

2.4.3 SQUID sensor

Both flux quantization and Josephson effect are internalized in the SQUID sensor – typically a superconducting closed ring, which incorporates at least one Josephson junction depending on the SQUID type. If the sensor comprises a single Josephson junction, the SQUID is a rf SQUID (rf: radio frequency) [81] and dc SQUID (dc: direct current) [82] in the case of two identical Josephson junctions connected in parallel in the superconducting loop [36]. For the SQUID measurements conducted in this work, solely the dc SQUID was used [cf. Fig 2.11 (a)].

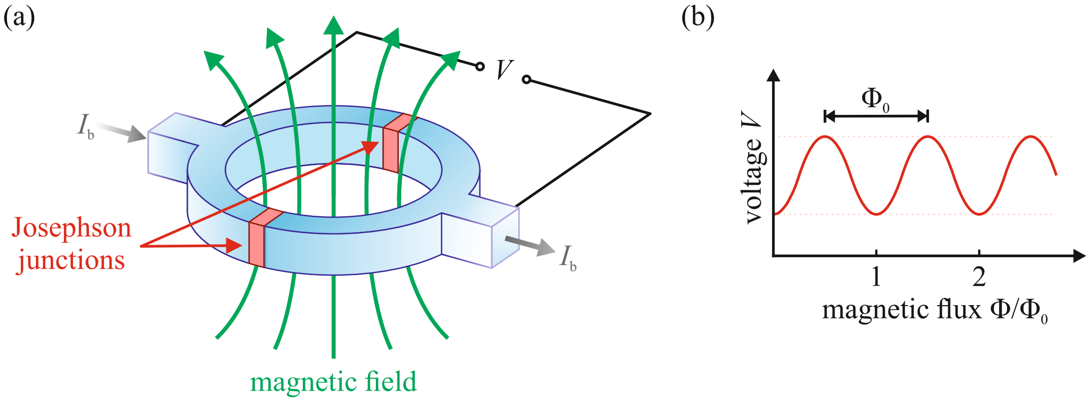

Fig. 2.11: (a) Illustration of a typical dc SQUID sensor consisting of two similar Josephson junctions (red) integrated in parallel in a superconducting ring (blue). The SQUID is biased with a constant current I_b, which divides equally between both junctions, half in each branch of the loop. Due to the presence of an applied magnetic field (green), the flow in each branch of the loop is altered, causing a voltage change V across the SQUID. (b) The increase (or decrease) of the external magnetic field and thus the increase (or decrease) of the magnetic flux threading through the SQUID leads to an oscillating voltage. The period of the oscillation corresponds to the magnetic flux quantum Φ_0. Adapted from Ref. [33].

The dc SQUID is operated by biasing the SQUID with a constant dc current I_b slightly higher than approximately twice the critical maximum supercurrent I_c of the junctions ($I_\mathrm{b} > 2I_\mathrm{c}$). With no magnetic flux being applied, the bias current I_b divides in equal parts between both Josephson junctions. Hence, the SQUID is driven in the resistive or voltage mode with small voltage drops across the Josephson junctions, developing an average dc voltage V across the SQUID. Yet, if a magnetic flux is inductively coupled into the SQUID loop, the flux enclosed inside the loop is quantized and corresponding screening currents I_s are generated circulating in the superconducting ring.

These screening currents I_s produce an opposing magnetic field compared to the applied magnetic field, counteracting the flux in the superconducting ring in order to maintain flux quantization. The screening currents I_s add to the bias current I_b flowing through one junction ($I_\mathrm{b}/2 + I_\mathrm{s}$), but substract from I_b flowing through the respective other junction ($I_\mathrm{b}/2 - I_\mathrm{s}$), leading to a modified dc voltage V across the SQUID dependent on the external magnetic flux. Thereby, the dc voltage V across the SQUID changes in a periodic manner as the applied flux is incremented (or decremented), with the period equal to the magnetic flux quantum Φ_0 [35]. Integer multiples of Φ_0 correspond to voltage minima, while voltage maxima are characterized by half integer multiples of Φ_0 [cf. Fig 2.11 (b)]. By monitoring the voltage change, it is possible to determine the magnetic flux coupled into the superconducting ring of the SQUID [35], which provides access to the magnetic properties of the magnetic samples under examination. Thus, in essence, the SQUID can effectively be considered a flux-to-voltage transducer.

2.5 Core-level spectroscopy - XPS, XAS, and XMCD

The core-level spectroscopy is a powerful tool, mainly utilized to probe the electronic states of solids. Hereby, the information about the electronic structure is obtained through the excitation of deeply-bound core-level electrons by X-ray photons, resulting in the simultaneous creation of core-holes in the respective core-levels. For an excitation of a core-electron, it is compellingly necessary that the incident X-ray photons energies are comparable to binding energies of core-levels, which can reach up to several thousand of eV. The core-electrons are excited either into unoccupied states below the ionization threshold or into high-energy continuum states above the ionization threshold, where they can be regarded as free electrons, exhibiting residual kinetic energy. This is basically the photoelectric effect, first discovered by Heinrich Hertz in 1887 [83] and later on explained by Albert Einstein in 1905 [84] by invoking the quantum nature of electromagnetic radiation. The photoelectric effect lays the foundation for some of the most important representatives of core-level spectroscopy, namely X-ray photoelectron emission spectroscopy (XPS), X-ray absorption spectroscopy (XAS), and X-ray magnetic circular dichroism (XMCD). All three techniques have in common that they are first-order optical absorption processes, in which solely one photon is involved in the whole excitation process of one core-electron. In contrast, X-ray emission spectroscopy (XES) utilizing X-ray photons as excitation source, for example, can be classified as a second-order optical process, where an X-ray photon first collides with a deeply-bound core-electron, excites it, and subsequently, the excited state decays radiatively by emitting a photon.

The quantum-mechanical essence of the photoelectric effect is basically laid down in Fermi's golden rule

$$W_{i\to f} = \frac{2\pi}{\hbar} \left| \left\langle \Psi_\mathrm{f} \middle| \hat{\mathcal{T}} \middle| \Psi_\mathrm{i} \right\rangle \right|^2 \delta\left(E_\mathrm{f} - E_\mathrm{i} - h\nu\right) \ , \tag{2.30}$$

which describes the probability W for a (direct) transition of an electron from an initial ground state Ψ_i at energy E_i into an allowed excited final state Ψ_f at energy E_f by the absorption of an incident photon of energy $h\nu$ [85]. It is assumed that the electromagnetic field of the incident X-ray photon imposes a weak perturbation to an initial unperturbed system for a short period of time. The delta function ensures energy conservation, so that a transition between two states is only possible if their energy difference is equivalent to the energy of the incoming photon. The squared matrix element determines the transition rate with the transition operator $\hat{\mathcal{T}}$, which in first-order describes transitions including only one photon as they typically appear in XPS, XAS and XMCD. At X-ray photon energies below 10 keV, X-ray absorption is essentially dominated by electric dipole transitions and electric quadrupole transitions can be neglected (electric dipole approximation).

Hence, in this energy range, the transition operator $\hat{\mathcal{T}}$ reduces to a dipole transition operator when determining transition probabilities. For such transitions, the quantum numbers of initial and final states may differ only as prescribed by the so-called dipole selection rules ($\Delta j = 0, \pm 1$, $\Delta m_j = 0, \pm 1$, $\Delta s = 0$), allowing only for very specific transitions with respect to a given initial ground state.

2.5.1 X-ray photoelectron spectroscopy - XPS

The method of XPS is used to probe the occupied core-levels of a material. In terms of the one-electron picture, a colliding X-ray photon with energy $h\nu$ excites an electron originating from a filled core-level of binding energy E_b (relative to the Fermi level E_F at $E_\mathrm{b} = 0\,\mathrm{eV}$) to a high-energy continuum state, where it can be detected as a photoelectron with kinetic energy

$$E_\mathrm{kin} = h\nu - E_\mathrm{b} - \Phi \; . \tag{2.31}$$

$\Phi = E_\mathrm{vac} - E_\mathrm{F}$ is the work function of the material, which is the energy required to completely liberate an electron at the Fermi level from the solid. The corresponding spectroscopic process is schematically illustrated in Fig. 2.12. In the case of conductive samples, both the sample and the spectrometer have identical Fermi levels as they are grounded to the same electrical potential and, therefore, only the spectrometer work function Φ_spec is decisive in the measurement of the kinetic energy of the photoelectrons. Thus, by knowing Φ_spec (and $h\nu$ of course), it is possible to infer E_b of the emitted photoelectrons from the measurement of their kinetic energies, independently of the work function of any sample under examination. The binding energy E_b is element-specific and characteristic for the core-level of the emitted photoelectron, making XPS an element-sensitive technique also capable of analyzing the chemical composition of solids. In the resulting photoelectron spectrum, in which the intensity is plotted as a function of the binding energy, each photoelectron peak can be assigned to a specific core-level of a specific element. The core-levels are denoted according to nl such as $1s$, $2s$, and $3d$, for which n and l are the characterizing quantum numbers of the core-level (principal quantum number n and orbital angular quantum number l).

Although this approach seems quite intuitive, it is somewhat too simplistic as the photoelectron is removed from a solid, which consists of a large number of interacting electrons. Consequently, the many-body interaction of the remaining electrons is neglected in this approach. For a ground state with initial N electrons, the removal of an electron from this state leaves a hole, producing a final state with thus $(N-1)$ electrons. Hence, more aptly and rigorously, the binding energy E_b of the photoelectron obtained by an XPS experiment represents rather the difference in total energies between the initial state (E_i) before photoemission and the final state (E_f) after photoemission

$$E_\mathrm{b} = E_\mathrm{f}\,(N-1) - E_\mathrm{i}\,(N) \tag{2.32}$$

based on energy conservation and in the scope of the so-called sudden approximation, i.e., the photoelectron is considered decoupled from the $(N-1)$ electron state due to a rapid photoemission process [86, 87]. Assuming that the spatial distribution of the remaining orbitals does not change due to photoemission (frozen-orbital approximation), the binding energy only then corresponds to the negative orbital energy of the orbital from which the emitting photoelectron originates (Koopmans' theorem [88]). However, this assumption does not include relaxation effects, electron correlation effects, and relativistic effects. Leaving aside electron correlation and relativistic effects, which are usually rather small, solely relaxation effects need to be taken into account in order to better relate the binding energies to the binding energies that are actually measured [38]. In a solid, these relaxation effects involve energy contributions arising from two basic mechanisms by which the overall system adapts to the core-hole left by the photoelectric effect in a certain core-

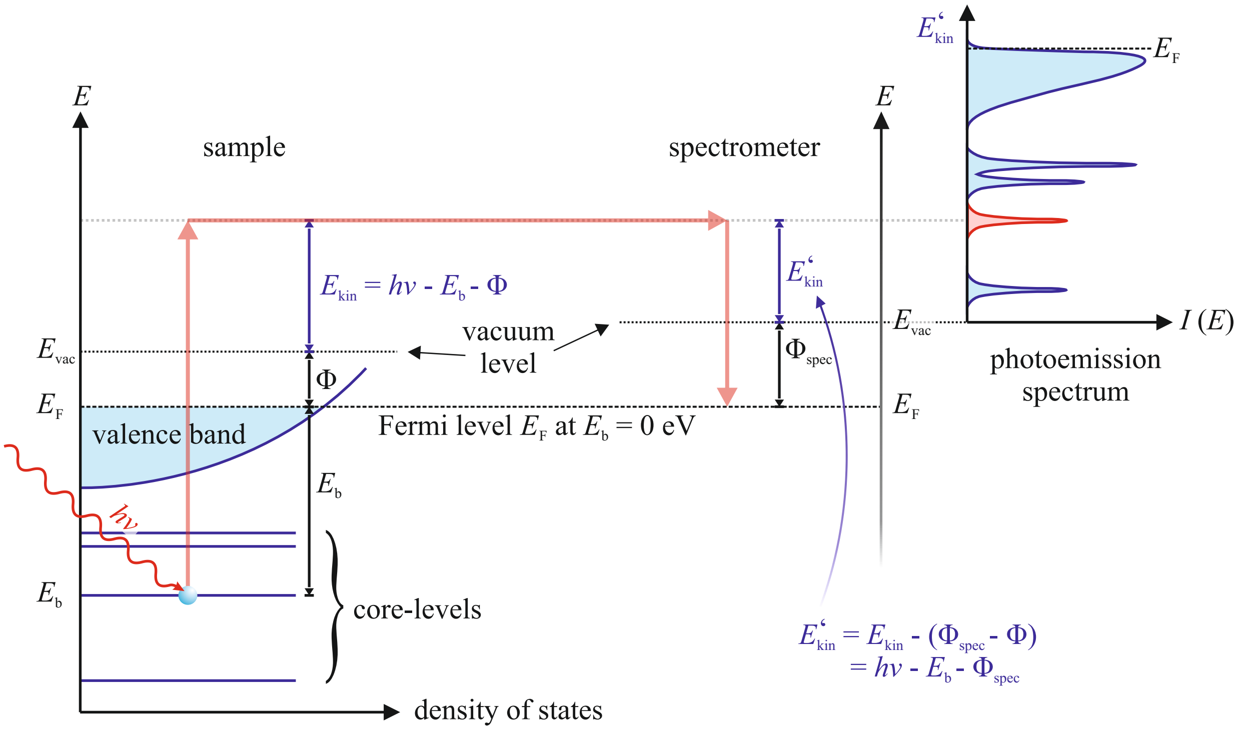

Fig. 2.12: Principle of the photoelectron emission process, represented in an energy level diagram with final detection of the emitted photoelectron by a spectrometer. A corresponding photoelectron spectrum is shown to the right. The absorption of a photon of energy $h\nu$ excites a core-level electron into the quasi-continuum, whose residual kinetic energy is determined by the binding energy E_{b} of the involved core-level and the work function Φ of the sample. Afterward, the photoelectron is analyzed according to its kinetic energy $E'_{\mathrm{kin}} = h\nu - E_{\mathrm{b}} - \Phi_{\mathrm{spec}}$ by a spectrometer with work function Φ_{spec}. Adapted from Refs. [19, 38].

level, namely the intra-atomic relaxation of the orbitals associated with the same atom and the extra-atomic relaxation, resulting from surrounding atoms (cf. chemical shift).

Nevertheless, only photoelectrons that have not suffered any energy loss due to inelastic collisions during their path toward the surface and out of the solid contain direct information on the electronic structure of the solid. In contrast, photoelectrons that have been subject to inelastic scattering events but still have sufficient residual kinetic energy to leave the solid and get detected, contribute to the XP spectrum as continuous background intensity instead of photoelectron peaks. The distance electrons can travel in a solid without losing a significant amount of their kinetic energy is defined as the inelastic mean free path (IMFP) λ. The IMFP is a key limiting factor for the information depth

$$\mathrm{ID}\,(95\,\%) = -\lambda \cos(\varphi) \ln\left(1 - \frac{95}{100}\right) \approx 3\lambda \cos(\varphi) \tag{2.33}$$

achievable in XPS, assuming that 95 % of all photoelectrons come from this sampling depth. Here, φ denotes the off-normal photoelectron emission angle. [89]. λ depends strongly on the physical properties of the material the photoelectrons propagate in as well as their kinetic energies. It can be predicted for a given kinetic energy by means of the TPP-2M algorithm established by Tanuma, Powell and Penn [90]. For soft X-rays with excitation energies of $h\nu \lesssim 2\,\mathrm{keV}$, the IMFP of photoelectrons is on the order of a few nanometers ($< 3\,\mathrm{nm}$) [91], yielding high surface sensitivity due to a low ID ($< 9\,\mathrm{nm}$ for $\varphi = 0°$). Using instead hard X-rays with higher excitation energies, a more bulk-like sensitivity (large ID) is obtained due to drastically enhanced kinetic energies and IMFPs of photoelectrons. Therefore, XPS is commonly divided into two regimes based on the energy of the photons they operate with. These are soft XPS, which uses soft X-rays, and HAXPES, which employs hard X-rays. Both techniques are complementary to each other and provide comprehensive information about the electronic structure and chemical composition either from the surface or from deeper layers.

Besides the continuous background due to the inelastically scattered photoelectrons, considerably more different effects are able to significantly change XP spectra, e.g., with respect to the shape and position of photoelectron peaks as well as the appearance of additional intensity maxima in the spectrum. The most relevant effects for the XP spectra recorded in this work are briefly highlighted below. Thereafter, this section is concluded with a basic description of the quantitative analysis of XP spectra.

Chemical shift

It is quite common for photoelectron peaks of compounds consisting of dissimilar chemical elements to exhibit a strong perceptible shift of their binding energies in the XP spectrum, so that the measured binding energies sometimes deviate significantly from the expected binding energies of free atoms. This shift is referred to as chemical shift, caused by the bonding of different chemical species, as in the case of Fe_3O_4 compared to elemental (or metal) Fe. The bonding in such ionic crystals arises from the transfer of valence electrons from the cations to the adjacent anions. This, in turn, has an effect on the electrostatic interaction between the nucleus and the electron shells due to a modified screening of the core by the shell. For cations exhibiting a deprivation of some electrons, the remaining electrons of the cation are more strongly bound to the nucleus, resulting in a higher binding energy. As more valence electrons participate in the bonding, the higher the binding energy of the remaining electrons. Consequently, the chemical shift can serve as an indication for the valence state of a particular cation species.

Core-hole spin-orbit splitting

The excitation of an electron from a core-level leaves a core-hole in the respective core-level, which becomes noticeable in the final state created. Since XPS actually measures the energy difference between the final and initial states, the emergent core-hole can thus have a significant effect on XP spectra. The core-hole created has a spin angular momentum $s = 1/2$ and an orbital angular momentum l. The latter is represented by the familiar terms, e.g., s, p, d, and f, corresponding to orbital angular momenta ranging from 0 to 3. Both the spin angular momentum and the orbital angular momentum couple via spin-orbit interaction to a total angular momentum j, given by $l + s$ or $l - s$, and produce an energetic splitting into doublet peak structures of the so far degenerate states. In the case of zero orbital angular momentum, the spin-orbit interaction is absent and no (spin-orbit) splitting of states occurs (singlet peak structures). If, on the other hand, the orbital angular momentum equals 1, for example, the total angular momentum can be either 1/2 or 3/2 and two peaks will appear in the XP spectrum separated from each other. The relative intensity of the split peaks follows a straightforward rule provided by the degeneracy of the states $2j + 1$:

$$\frac{I_{l-1/2}}{I_{l+1/2}} = \frac{2j_{l-1/2} + 1}{2j_{l+1/2} + 1} = \frac{l}{l+1} \ . \tag{2.34}$$

Hence, the intensity ratio for p shells is $1 : 2$, for d shells $2 : 3$, etc.

Multiplet splitting

A related phenomenon is multiplet splitting, which also causes splitting of photoelectron peaks. This type of splitting is common in systems with unpaired electrons in the valence band and can even affect s-type orbitals. The interaction between the spins of the unpaired electrons in the valence band with the spins of the remaining unpaired electrons in the ionized core-levels, resulting from photoemission, gives rise to several possible final state configurations with an equal number of different but similar energies. In the XP spectrum, this effect appears as a multipeak envelope containing several components and is much more pronounced and complex for core-levels that are not s-type (orbital angular momentum $l > 0$) due to the additionally occurring spin-orbit interaction.

Auger electron peaks

In the event of photoelectron emission, two other possible processes can occur, accompanying the photoelectron emission process simultaneously. Both additional processes rely upon a recombination process of the emerging hole with a second electron originating from an outer core-level. The energy released in this recombination process is either emitted as an X-ray photon (fluorescence) or, alternatively, can be transmitted to a third (core-)electron. In the latter case, if the energy transfer is sufficiently large and exceeds the binding energy of the electron plus the work function of the material, this electron can leave the solid with residual kinetic energy and be detected as an Auger electron. The kinetic energy of this Auger electron is determined by the energy difference between the involved core-levels and is therefore independent of the primary excitation energy $h\nu$.

Satellites

The ejection of photoelectrons from a core-level of a many-electron system leads in the simplest case to the formation of ions in the ground state. The resulting XP spectrum then consists primarily of the main photoelectron lines. However, there is also a finite probability that the ions will be left in excited states after the photoelectric process due to the internal excitations of other electrons by the departing photoelectrons. These excited states then show up in the XP spectrum as additional lines, the so-called satellites, a few eV higher in binding energy than the main lines since the necessary energy for the transitions is supplied by the kinetic energy of the primary photoelectrons. If another electron is excited simultaneously with the emission of a core-electron into an unoccupied higher-energy bound state, these distinct lines are called shake-up satellites. If the second electron is instead promoted into a continuum state above the vacuum level and is thus able to leave the atom, the corresponding photoemission loss signals are called shake-off satellites. The latter appears as a broad feature in the XP spectrum due to a wide range of possible final states.

Another type of satellites, commonly observed in transition metal oxides and ferrites, are charge-transfer satellites. They arise when upon photoexcitation one electron is transferred from an oxygen ligand L into the d shell of the transition metal, leading to a modified configuration of the d shell. The energy Δ required for such an electron transfer and supplied by the photoelectron is given by

$$\Delta = E\left(3d^{N+1}L^{-1}\right) - E\left(3d^{N}L\right) \ . \tag{2.35}$$

Here, the transfer is considered exemplarily from a $2p$ shell of the ligand L into a $3d$ shell, initially consisting of N electrons before and $(N+1)$ electrons after the charge-transfer process, respectively. L^{-1} denotes the ligand hole created in the $2p$ shell.

Particularly in metallic samples, quantized excitations of electrons in the conduction band, so called plasmons, may occur in consequence of the photoemission process. These excitations result also in a well-defined energy loss of the photoelectron denoted as plasmon satellites.

Quantitative analysis: determination of stoichiometries and depth profiling

Apart from the identification of elements and their valence states, XPS also offers the possibility to quantitatively determine the chemical composition in a sample containing different atomic species. Furthermore, for samples exhibiting different valencies of an ionic species, it is also possible to determine their relative proportions if the respective chemically shifted peaks are resolved separately in the XP spectrum.

For the quantitative analysis of XP spectra, the photoelectron intensities, i.e., the areas under the respective photoelectron peaks, which are directly related to the amount of the corresponding element (or ion species) in the analyzed specimen, are essential. In order to determine the exact areas, the background created by inelastically scattered photoelectrons must be subtracted from the XP spectrum in advance, for which the well-known method developed by Shirley [92] has been used exclusively in this work. In addition, certain factors must be taken into account such as the instrumental properties of the X-ray source and spectrometer, the IMFP of the photoelectrons, and the element- and orbital-specific photoelectron cross-sections. All these different factors can be conjoined into a single (sensitivity) factor

$$S_i^{nl} = \Phi\left(h\nu\right)\, D\left(E_{\mathrm{kin}}\right)\, n_i\, A\, \sigma_i^{nl}\left(h\nu\right) \ , \tag{2.36}$$

in which $\Phi\left(h\nu\right)$ and $D\left(E_{\mathrm{kin}}\right)$ are the flux of the incident X-rays of energy $h\nu$ and the spectrometer efficiency, respectively, n_i is the number of atoms of element i per unit volume, A is the effective area of the analyzed sample, and $\sigma_i^{nl}\left(h\nu\right)$ is the energy-dependent atomic subshell photoelectric cross-section for photoelectrons from inner shell orbital nl of element i. When evaluating intensity ratios of different photoelectron peaks but of comparable kinetic energies, some parameters in the sensitivity factor can usually be omitted like the photon flux $\Phi\left(h\nu\right)$ of the X-ray source, the spectrometer efficiency $D\left(E_{\mathrm{kin}}\right)$, and the effective area A. Both the photon flux and the effective area are typically held constant during the measurement, whereas the spectrometer efficiency can be considered constant due to similar kinetic energies of the compared photoelectron peaks.

The atomic subshell photoelectric cross-section σ_i^{nl} is the integration of the differential photoelectric cross-section $d\sigma_i^{nl}/d\Omega$ over the differential solid angle $d\Omega$, into which the emission of electrons occurs:

$$\sigma_i^{nl}\left(h\nu\right) = \int \frac{d\sigma_i^{nl}\left(h\nu\right)}{d\Omega} d\Omega \ . \tag{2.37}$$

Hence, the differential photoelectric cross-section $d\sigma_i^{nl}/d\Omega$ can be associated with a possible angular anisotropic distribution of the photoelectrons. In most cases, $d\sigma_i^{nl}/d\Omega$ is sufficiently described within the electric dipole approximation and can be expressed by

$$\frac{d\sigma_i^{nl}\left(h\nu\right)}{d\Omega} = \frac{\bar{\sigma}_i^{nl}\left(h\nu\right)}{4\pi}\left[1 - \frac{\beta_i^{nl}\left(h\nu\right)}{2}\, P_2\left(\cos\left(\underline{\vartheta}\right)\right)\right] \tag{2.38}$$

in terms of circularly polarized and unpolarized X-rays [93], and by

$$\frac{d\sigma_i^{nl}\left(h\nu\right)}{d\Omega} = \frac{\bar{\sigma}_i^{nl}\left(h\nu\right)}{4\pi}\left[1 + \beta_i^{nl}\left(h\nu\right)\, P_2\left(\cos\left(\vartheta\right)\right)\right] \tag{2.39}$$

in terms of linearly polarized X-rays [94]. Hereby, $\bar{\sigma}_i^{nl}(h\nu)$ is the total subshell photoelectric cross-section, $\beta_i^{nl}(h\nu)$ is the dipolar angular distribution parameter, which is zero for an isotropic distribution, and $P_2(\cos\underline{\vartheta})$ and $P_2(\cos\vartheta)$ are second-order Legendre polynomials, with $\underline{\vartheta}$ and ϑ denoting the angle of the incident X-ray beam and its polarization with respect to the propagation direction of the emitted photoelectrons, respectively. A more general and accurate expression for the differential photoelectric cross-section includes not only the electric dipole terms but also higher multipole contributions such as those due to electric quadrupole and magnetic dipole transitions, which become increasingly more relevant at larger ionizing photon energies when the electric dipole approximation reaches its limits [95, 96]. Within these first-order corrections, the non-dipolar angular distribution parameters γ and δ usually quantify the non-dipolar effects [95].

The integrated photoemission intensity originating from an inner shell orbital nl of element i in an atomically flat thin film f of thickness d_f is given by

$$I_\mathrm{f} = S_i^{nl} \int_0^{d_\mathrm{f}} e^{-z/\lambda_i'} dz = S_i^{nl}\,\lambda_i' \left(1 - e^{-d_\mathrm{f}/\lambda_i'}\right) , \tag{2.40}$$

assuming that the photoelectrons follow straight-line paths from their generation in a certain depth z with respect to the film surface to their emission from the sample, i.e., the photoelectrons do not undergo elastic scattering on their way out of the film [97, 98]. $\lambda_i' = \lambda_i \cos(\varphi)$ is the effective IMFP, in which λ_i is the IMFP of the respective photoelectrons at a given kinetic energy, and φ denotes the photoemission angle between surface normal and detector under which photoelectrons are detected. Analogously, integration with the upper limit $d_\mathrm{f} \to \infty$ would give the integrated photoemission intensity in the case of a bulk-like material.

In terms of a multilayer system, comprising several single homogeneous layers above a given buried film or bulk material, each additional overlying layer attenuates the intensity of that film or bulk material according to Lambert-Beer's law. Consequently, the XPS intensity of a buried bulk material b covered by N layers is

$$I_\mathrm{b}^\mathrm{m} = I_\mathrm{b} \prod_{i=1}^{N} e^{-d_i/\lambda_i'} , \tag{2.41}$$

where the superscript m donates the multilayer system and $I_\mathrm{b} = S_i^{nl}\,\lambda_i'$ is the non-attenuated intensity of photoelectrons from the uncovered bulk material. With respect to a buried film f with $(N - f)$ layers above, the resulting photoemission intensity is thus

$$I_\mathrm{f}^\mathrm{m} = I_\mathrm{f} \prod_{i=f+1}^{N} e^{-d_i/\lambda_i'} . \tag{2.42}$$

Depth-profile measurements, as performed in angle-resolved HAXPES (AR-HAXPES), exploit the angular dependence of the effektive IMFP λ_i'. Depending on the detection angle φ between the surface normal and the detector, photoelectrons from different escape depths of the analyzed sample can be detected. At larger detection angles, e.g., due to tilting of the sample with respect to the analyzer, the effective IMFP of photoelectrons is reduced. This results in a larger contribution of photoelectrons from the surface and near-surface regions to the total photoemission intensity. Consequently, the surface sensitivity is significantly increased at higher detection angles compared to photoelectron detection normal to the surface ($\varphi = 0°$), which in turn would yield maximum bulk sensitivity. Thus, by continuously varying the detection angle between single measurements, information about the electronic structure and the chemical composition of, e.g., films with a certain depth resolution can be extracted from the recorded spectra. Furthermore, such depth-dependent measurements also provide access to information about the thicknesses of individual layers in a multilayer system.

2.5.2 X-ray absorption spectroscopy - XAS

In contrast to XPS, XAS provides information about the unoccupied density of states. Therefore, primarily the excitation of electrons by absorption of incident X-rays below the ionization threshold, i.e., transitions into the valence shell [cf. Fig. 2.13 (a)], is of relevance. For $3d$ transition metal and $3d$ transition metal ferrites, electron excitations involve mainly (dipole) transitions from the occupied $2p$ shell into empty states of the $3d$ shell.

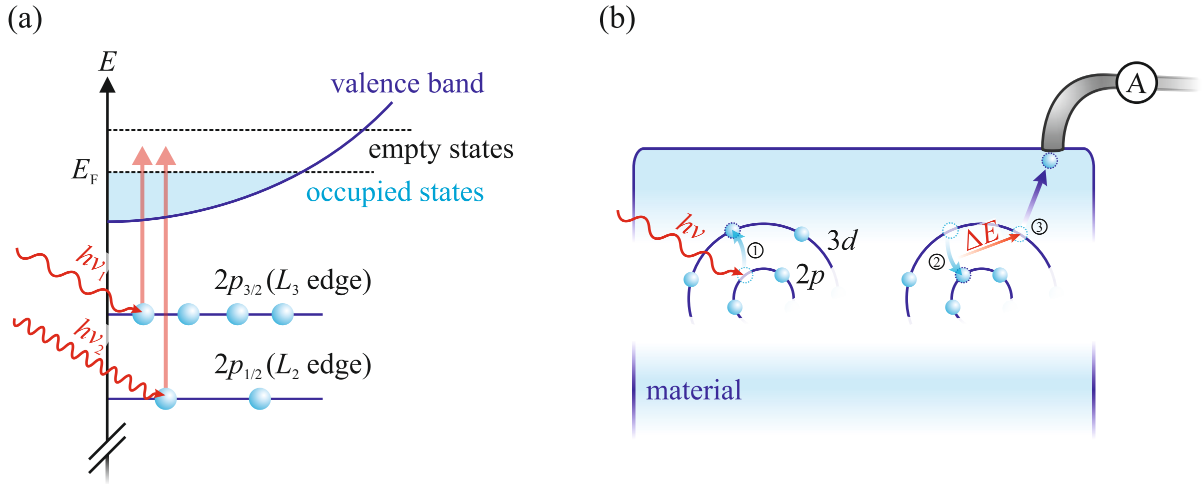

Fig. 2.13: (a) Illustration of electron excitation in XAS from filled spin-orbit split $2p$ orbitals into empty states of the valence band above the Fermi level E_F. Depending on the excitation energy of the X-ray photons ($h\nu_1$ and $h\nu_2$), the excitation originates either from the $2p_{3/2}$ orbital or from the $2p_{1/2}$ orbital. (b) Schematic drawing of total electron yield detection illustrated as a three-step process. After electron excitation (1), the system relaxes and the excited electron recombines with the core-hole in the $2p$ orbital that was created during excitation by emitting a photon (2). The energy of the photon can be used by a second electron to leave the atom as an Auger electron and later be detected as a charge current (3). Adapted from Refs. [50, 67].

Quantitatively, absorption is characterized by the material- and energy-dependent linear absorption coefficient μ [45], which describes the attenuation of intensity of electromagnetic radiation due to absorption when passing through a certain material. Assuming a homogeneous material of thickness z, this attenuation can be described by means of the Lambert-Beer's law

$$I_z\,(h\nu) = I_0\,(h\nu)\ e^{\,-\mu\,(h\nu)\ z}\ , \tag{2.43}$$

in which I_z and I_0 are the transmitted and initial intensity of the radiation, respectively. Thus, by measuring the intensity both before and after passing through the material (transmission experiment), the absorption coefficient can be determined directly from Eq. (2.43). If, in addition, the photon energy $h\nu$ of the incident radiation is also varied, the energy dependence of μ is obtained, which overall decreases with increasing photon energy. Only at specific photon energies the absorption coefficient increases abruptly, which are the element-specific absorption edges of the material. At these absorption edges, the photon energy is just large enough to excite electrons into unoccupied states, e.g., of the $3d$ shell. Contrary to the XPS convention, absorption edges are historically denoted by, e.g., L_3 and L_2 when referring to absorption from the spin-orbit split $2p_{3/2}$ and $2p_{1/2}$ core-levels, respectively.

Since simple transmission experiments are only applicable to very thin homogeneous and single samples due to excessive intensity attenuation for thicker samples below the detection threshold and non-separable signals in heterostructures, photon absorption can alternatively be measured via the radiative or electronic decay of excited core-electrons in the sample. Similarly to XPS, both photons and Auger electrons can be emitted upon relaxation of the excited states to their ground states as a result of recombination of the core-holes with the excited electrons. Each of these decay products can be detected, either as total fluorescence yield (TFY) or as total electron yield (TEY). In total fluorescence yield detection, the mean free path of the photons resulting from fluorescence decay is of the same order of magnitude as the incident radiation. Hence, this method is well suited to analyze bulk-like specimens as well as thinner samples. Nevertheless, the recorded absorption spectra often suffer from strong saturation effects if the sample is not diluted, and the subsequent precise analysis must be performed with special care. More common, therefore, is total electron yield detection [cf. Fig. 2.13 (b)], although this detection type is largely confined to electrically conductive materials. As Auger decay is the dominating process for all core-levels for excitation energies below 1 keV, total electron yield detection is typically carried out in the soft X-ray energy regime. The Auger electrons created during Auger decay excite even more electrons on their way out of the sample, forming an avalanche of electrons that leaves the sample. The number of all lost electrons can then be measured as a drain current, which is proportional to the (X-ray) absorption. However, the detection of (Auger) electrons comes at the downside of a relatively small mean free path compared to the detection of photons, which severely limits the information depth of this mode to the top few nm (near-surface region) of the samples under investigation.

2.5.3 X-ray magnetic circular dichroism - XMCD

A particularly powerful application of XAS is to exploit the circular polarization effect on the absorption of magnetic samples. The switching from positive σ_+ to negative σ_- (or right to left) helicity of the circularly polarized incident X-rays produces a modified XAS intensity in the case of ferro-/ferrimagnetic materials. The difference of both XA spectra μ_+ and μ_- with opposite helicities σ_+ and σ_-, respectively, is referred to as the X-ray magnetic circular dichroism (XMCD)

$$\Delta\mu = \mu_+ - \mu_- \ , \tag{2.44}$$

which is sensitive to the magnetic properties of the different valence electrons within the magnetic material. By analogy, the 'unpolarized' XA spectrum, including both helicities, can be defined according to

$$\mu = \mu_+ + \mu_- \ . \tag{2.45}$$

The XMCD effect was first theorized by Erskine and Stern in 1975 [99] and later confirmed experimentally by Schütz *et al.* in 1987 [100]. The origin of the XMCD effect resides in the spin-dependent absorption process as schematically depicted in Fig. 2.14 (a) and can be understood with the help of the atomic one-electron picture and the so-called two-step model [101].

The first step involves the creation of photoelectrons with a spin and/or orbital momentum from localized atomic core-levels by the absorption of incident circularly polarized X-rays. Here, the angular momentum of the photon is transferred to the excited core-level electron due to conservation of angular momentum in optical excitation. In the case of, e.g., *s*-type core-levels, which do not exhibit spin-orbit coupling, the angular momentum is fully transferred to the orbital momentum of the electron [101]. However, upon excitation from spin-orbit split core-levels like $2p_{3/2}$ (L_3 absorption edge), the angular momentum of the photon is partially transferred to the spin through the

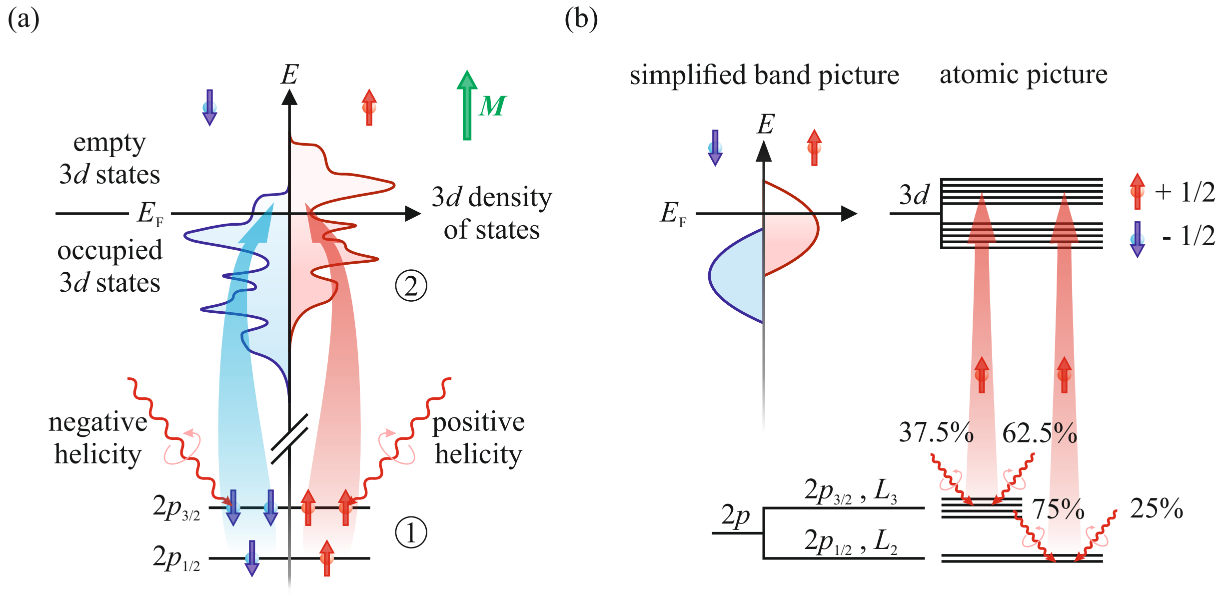

Fig. 2.14: (a) Illustration of the XMCD effect at the $L_{2,3}$ absorption edges in a magnetized $3d$ transition metal (ferrite) according to the two-step model, involving only transitions from the occupied spin-orbit split $2p$ core-level to empty states of the valence shell. The absorption of circularly polarized X-rays (1) produces the excitation of spin-polarized electrons of either spin-up or spin-down, depending on the helicity, which is subsequently 'analyzed' by the spin-split valence shell (2), exhibiting unequal spin-up and spin-down populations. For simplicity, only the preferred absorption processes for a given helicity are shown. (b) The XMCD effect is maximized when the transition of only one spin orientation is allowed, e.g., in the case of a completely occupied spin-down $3d$ shell and a (partially) unoccupied spin-up $3d$ shell. In this particular case, exclusively spin-up electrons are excited into the valence shell, with transition probabilities governed by the absorption edge and the helicity of the circularly polarized X-rays. Adapted from Refs. [50, 101].

spin-orbit coupling, leading to an enhanced excitation of electrons of a certain type of spin and thus to spin-polarized excited photoelectrons (Fano effect [102, 103]). The spin-polarization produced depends on the spin orientation of the X-ray photons and is opposite for opposite helicities. It arises from different dipole selection rules that apply to right ($\Delta m_j = +1$) and left ($\Delta m_j = -1$) circularly polarized light, leading to a different absorption depending on the helicity [101]. Furthermore, due to the opposite spin-orbit coupling of the core-levels $2p_{3/2}$ (L_3) and $2p_{1/2}$ (L_2) according to $l + s$ and $l - s$, respectively, there is also an opposite spin-polarization for the two absorption edges.

In the second step, the valence shell behaves like a spin-sensitive detector for the spin or orbital momentum of the excited electron. In magnetized materials, the valence shell is spin-split into majority and minority states as a result of the exchange interaction, i.e., there are unequal spin-up and spin-down populations and, thus, there is also an unequal number of unoccupied states available for the excited electron of either spin-up or spin-down. Consequently, the valence shell preferentially accepts electrons of a particular kind of spin orientation, and the corresponding XMCD signal thereby reflects the imbalance of the majority and minority states.

It follows directly that the spin-dependent density of empty states in the valence shell has substantial impact on the resulting XMCD signal. For instance, in the absence of an imbalance between the number of spin-up and spin-down states available, no magnetic dichroism effect would arise due to identical total (spin-up plus spin-down) transition intensities for positive and negative circular polarization [101], which is the case for non-magnetic materials. Once an imbalance exists, the absorption is different for both helicities of circular polarization, giving rise to a magnetic dichroism effect. In this case, the magnetic dichroism effect becomes maximal when, e.g., the spin-down (majority) states are entirely filled and there are exclusively unfilled spin-up (minority) states [cf. Fig. 2.14 (b)]. In this special situation, the 'detector' is sensitive only to spin-up electrons and solely electrons with spin-up orientation can be excited since spin-flips are not allowed during optical excitation. The total transition probabilities are then at the L_3 absorption edge 62.5 % (37.5 %) for positive (negative) X-ray helicity and 25 % (75 %) for positive (negative) X-ray helicity at the L_2 absorption edge.

2.5.4 Sum rules

Since the relative size of the XMCD signal is proportional to the difference between spin-up and spin-down holes, it is therefore directly related to the magnetic spin moment m_s [101]. Yet, the XMCD signal contains also information about the orbital moment m_o of the $3d$ shell. Both spin- and orbital-related contributions superimpose and form the XMCD signal. Thole *et al.* and Carra *et al.* have proposed so-called sum rules, with which, to a good approximation and in a relatively simple way, the spin and orbital moments (in units of μ_B/atom) for transition metals can be derived separately from each other using energy-integrated intensities of $L_{2,3}$ XAS and XMCD spectra without resort to any simulation or fitting techniques [104, 105]. Here, the orbital moment m_o is associated with the XMCD signal integrated over the two absorption edges L_3 and L_2 via

$$\begin{aligned} m_\mathrm{o} &= -\frac{4\int_{L_3+L_2}(\mu_+ - \mu_-)\,dE}{3\int_{L_3+L_2}(\mu_+ + \mu_-)\,dE}\,(10-n_{3d}) && (2.46)\\ &= -\frac{4q}{3r}\,(10-n_{3d})\ , && (2.47)\end{aligned}$$

where q corresponds to the integral over the XMCD signal from both absorption edges normalized to the entire integrated 'unpolarized' XA spectrum r, and n_{3d} denotes the number of empty $3d$ states of the respective transition metal (cation). Within the same framework, the spin moment m_s is obtained from

$$\begin{aligned} m_\mathrm{s} &= -\frac{6\int_{L_3}(\mu_+ - \mu_-)\,dE - 4\int_{L_3+L_2}(\mu_+ - \mu_-)\,dE}{\int_{L_3+L_2}(\mu_+ + \mu_-)\,dE}\,(10-n_{3d})\left(1+\frac{7\,\langle T_z\rangle}{2\,\langle S_z\rangle}\right)^{-1} && (2.48)\\ &= -\frac{6p-4q}{r}\,(10-n_{3d})\left(1+\frac{7\,\langle T_z\rangle}{2\,\langle S_z\rangle}\right)^{-1}\ , && (2.49)\end{aligned}$$

in which p refers to the XMCD signal integrated over the spin-orbit-split absorption edge L_3. $\langle T_z\rangle$ and $\langle S_z\rangle$ are the ground state expectation values of the magnetic dipole operator and spin operator, respectively. In the case of cubic crystals, the magnetic dipole contribution is often so small that $\langle T_z\rangle$ is negligible with respect to $\langle S_z\rangle$ [105] and, hence, the $\langle T_z\rangle\,/\,\langle S_z\rangle$ term is usually omitted in the spin sum rule.

Still, the sum rules apply only to $2p \rightarrow 3d$ transitions, i.e., all other transitions must be separated out from the XA spectrum. This is achieved by subtracting an edge-like step function from the XA spectrum prior to sum rules analysis, which describes all other transitions under the assumption that they are continuum transitions [37]. The validity of the sum rules for the determination of spin and orbital moments was first experimentally verified and confirmed by Chen *et al.* [106]. A similar sum rule analysis is shown schematically in Fig. 2.15 at the Fe $L_{2,3}$ absorption edges of a thin Fe_3O_4 film.

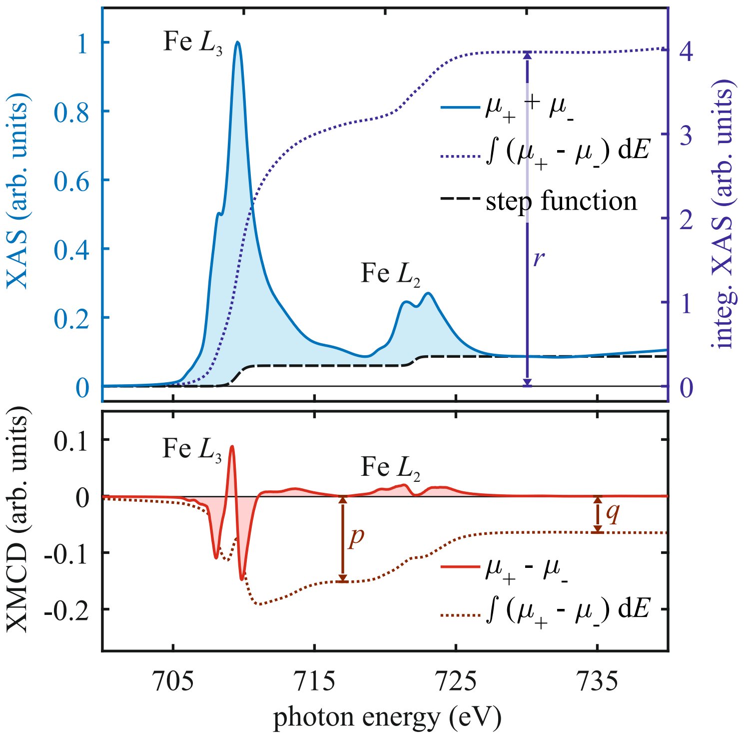

Fig. 2.15: Sketch of the application of the sum rules, including the designation of the parameters p, q, and r, to the Fe $L_{2,3}$ absorption edges of a thin Fe_3O_4 film to determine the spin and orbital moments of the Fe cations from both XA and XMCD spectra. $r = \int_{L_3+L_2} (\mu_+ + \mu_-)\, dE$ corresponds to the integration over the entire XA spectrum corrected by subtracting a step-like function, whereas $p = \int_{L_3} (\mu_+ - \mu_-)\, dE$ and $q = \int_{L_3+L_2} (\mu_+ - \mu_-)\, dE$ are the integrated XMCD intensities over the sole L_3 absorption edge and the complete $L_{2,3}$ absorption edges, respectively.

2.5.5 Charge-transfer multiplet theory

In the case of rare earths, X-ray absorption spectra such as those from the $M_{4,5}$ absorption edges can be sufficiently described by atomic multiplet theory alone, i.e., sole atomic $3d \rightarrow 4f$ transitions are considered along with atomic multiplet effects (cf. Sec. 2.5.1). However, in the theoretical description of absorption spectra from $3d$ transition metal cations, the atomic multiplet theory is no longer reasonable due to the influence of surrounding ions (also called ligands) like oxygen anions in transition metal ferrites. As a result, necessarily more effects must be included in the calculations to accurately describe the spectra. For instance, the neighboring (oxygen) ligands produce an electric so-called crystal field or ligand field, which, depending on its strength and the local symmetry of the ligands around the respective central cation, causes a different splitting of so far degenerate energetic states in the cation. In addition, effects of charge-transfer processes (cf. Sec. 2.5.1), resulting from charge fluctuations between the bonding cations with the oxygen anions, must be considered as well. The extension of the atomic multiplet theory in terms of ligand field splitting and charge-transfer is referred to as charge-transfer multiplet theory. Although charge-transfer multiplet theory is applicable to the description of both photoelectron and absorption spectra, it is more frequently used for the analysis of XA and XMCD spectra. Compared to XAS and XMCD, XPS is more sensitive to charge-transfer effects, so that XP spectra of, e.g., transition metal oxides can contain very pronounced charge-transfer satellites [107]. As a result, an accurate description of XP spectra is often quite challenging if not insufficient.

Ligand field splitting

Ligand field splitting arises when a transition metal ion is placed in a crystal, where it is surrounded by, for example, six oxygen anions equidistant from each other, forming an octahedron. A free transition metal ion exhibits five energetically degenerate $3d$ orbitals. If this ion now bonds with surrounding (oxygen) ions via its $3d$ orbitals, the negatively charged electrons of the oxygen orbitals act on the $3d$ electrons of the ion through electrostatic repulsion. In the case of a transition metal ion in a local spherically symmetric environment of oxygen anions, its $3d$ orbitals still remain degenerate, but due to the presence of the electric charge, the energy of the whole system is raised [30]. If, on the other hand, the electric charge around the central cation concentrates at discrete points, the $3d$ orbitals are no longer degenerate and split in energy, characterized by the crystal field parameter $10Dq$ for a simple twofold energy splitting (cf. Fig. 2.16). In octahedral environment, for example, i.e., six (oxygen) ligands surround the transition metal cation, each located at the vertex of an octahedron, the crystal field produced by the charge distribution causes the $3d$ orbitals to split into three levels (t_{2g}) of lower energy and two levels (e_g) of higher energy ($10Dq > 0$). The crystal field can even have an opposite effect in non-octahedral symmetric environments. In a tetrahedral environment, where the ligands lie at four of the corners of a tetrahedron, the crystal field again splits the $3d$ orbitals into threefold levels and twofold levels with the threefold levels, however, now energetically above the twofold levels ($10Dq < 0$). In contrast to the octahedral environment, the threefold and twofold levels are denoted by t and e, respectively.

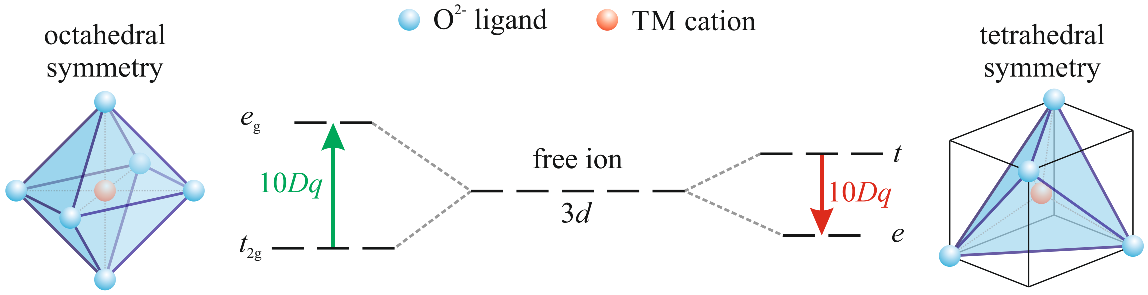

Fig. 2.16: Influence of surrounding oxygen anions on a central transition metal (TM) cation, leading to ligand field splitting $10Dq$ of the degenerate $3d$ states in dependence on the symmetry of the oxygen environment. If the environment exhibits octahedral symmetry, the $3d$ states split into threefold t_{2g} levels of lower energy and twofold e_g levels of higher energy ($10Dq > 0$), while for tetrahedral symmetry the splitting leads to three energetically higher t states and two energetically lower e states ($10Dq < 0$).

In addition, the (relative) strength of the crystal field determines the electron occupation within the entire $3d$ orbital. It results from the competition between the energy associated with the crystal field and the Coulomb energy cost of having two electrons occupy the same orbital [30]. If the crystal field energy is small compared to the Coulomb energy cost, each $3d$ orbital is first singly occupied by electrons before being doubly occupied, which is referred to as the high-spin (ground) state. In contrast, if the crystal field energy is much larger than the Coulomb energy cost, all lower-energy orbitals are first fully occupied before the electrons occupy the higher-energy orbitals, which is called the low-spin (ground) state. The way the $3d$ orbitals in a transition metal cation are arranged hereby sets the resulting magnetic moment of the cation. For example, in the case of a Fe^{3+} cation in an octahedral oxygen environment and in the high-spin state, all $3d$ orbitals of both e_g and t_{2g} are singly occupied each by one of the total five (valence) electrons, resulting in a magnetic moment of $5\,\mu_B$/atom of the Fe^{3+} cation. In the low-spin state, instead, one of the t_{2g} orbitals is only singly occupied, while the others are doubly occupied and all e_g orbitals are completely unoccupied, leading to a net magnetic moment of $1\,\mu_B$/atom of the Fe^{3+} cation.

Charge-transfer

Charge-transfer effects can be considered as charge fluctuations due to an electron transfer from a filled $2p$ orbital of an oxygen ligand to an empty state of a $3d$ orbital of a transition metal cation. Thus, the electronic configuration of the ground state of a $3d$ transition metal with initial

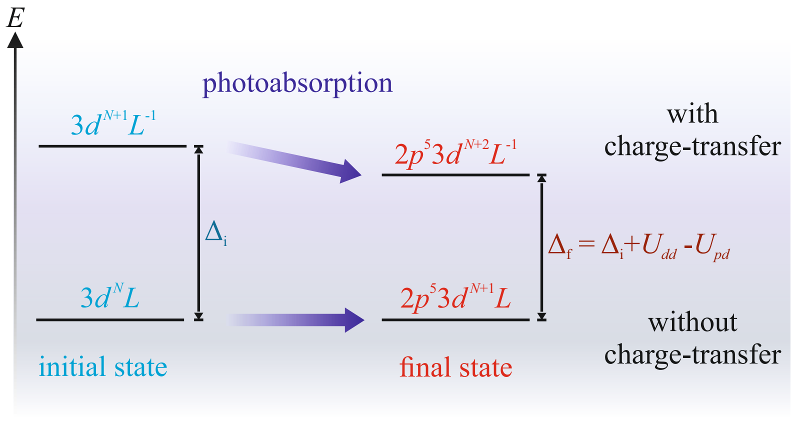

Fig. 2.17: Initial and final state configurations in photoabsorption from a $2p$ into a $3d$ state, neglecting or including charge-transfer effects. Δ_i and $\Delta_\mathrm{f} = \Delta_\mathrm{i} + U_{dd} - U_{pd}$ are the charge-transfer energies of the initial and final states, respectively, U_{dd} is the potential due to Coulomb interactions between the $3d$ electrons, and U_{pd} denotes the Coulomb interactions between $3d$ electrons and the $2p$ core-hole. Based on Refs. [50, 107].

N electrons can no longer be represented by the single configuration $3d^N L$ but as a mixture (linear combination) between the configurations $3d^N L$ and $3d^{N+1}L^{-1}$, where L and L^{-1} indicate the absence and existence of a ligand hole due to an electron transfer from the ligand-like bond orbital, respectively. Here, $3d^{N+1}L^{-1}$ represents the charge-transfer state, which is separated from the $3d^N L$ ground state by the charge-transfer energy Δ_i [cf. Eq. (2.35)], as indicated in Fig. 2.17, and is associated with the cost for the electron transfer.

In core-level excitation, the emergent core-hole in the $2p$ orbital during the X-ray absorption process creates an additional attractive potential U_{pd} that affects all electrons of other orbitals above it, i.e., the $3d$ valence electrons of the transition metal cation, pulling them down [107]. This, in turn, has a direct effect on the final state energies. The final $3d$ state, similar to the ground state, is given as a mixture between the $2p^5 3d^{N+1}L$ (final state without charge-transfer) and $2p^5 3d^{N+2}L^{-1}$ (charge-transfer final state) configurations. Both states in their original, unmixed configuration are separated by the energy

$$\Delta_\mathrm{f} = \Delta_\mathrm{i} + U_{dd} - U_{pd} \ , \tag{2.50}$$

where the on-site Coulomb repulsion U_{dd} of the excited electron by the other $3d$ electrons is addressed as well. In general, the U_{dd} potential is about 1 eV to 2 eV smaller than the U_{pd} potential resulting from the created core-hole [37]. Thus, it is $\Delta_\mathrm{f} < \Delta_\mathrm{i}$ (cf. Fig. 2.17). For charge-transfer multiplet calculations to describe absorption spectra of transition metal cations, all four parameters Δ_i, Δ_f, U_{dd}, and U_{pd} must be taken into account.

2.6 X-ray diffraction - XRD

To elucidate structural properties of (poly-)crystalline materials at atomic resolution, the technique of X-ray diffraction (XRD) has proven to be very useful [42], which exploits the phenomena of diffraction of X-rays, i.e., the elastic scattering of X-rays at the electron distribution inside periodically long-ranged ordered structures. The scattered X-rays can interfere with each other constructively or destructively, which manifests in Bragg reflections of very high intensity. One of the major advantages of XRD is the generally rather weak interaction of X-rays with matter, which makes it possible to probe the bulk of crystalline samples as X-rays can deeply penetrate into solids [29, 108]. Moreover, because of the weak interaction with matter, a single scattering (kinematical) approximation is sufficient for analysis [42, 109], in which, e.g., multiple scattering events or refraction effects can be neglected. However, this does not necessarily mean that X-rays are limited only to acquiring information from the bulk of multilayer-thick samples. For example, in film-substrate heterostructures, the contribution of the (ultra)thin film to the total scattering signal can be significantly enhanced if the incident X-rays hit the sample at grazing incidence angles[4] close to the critical angle of the material under investigation ($< 0.5°$) since the X-ray penetration depth is greatly reduced at these angles [108].

2.6.1 Bragg condition and Laue condition

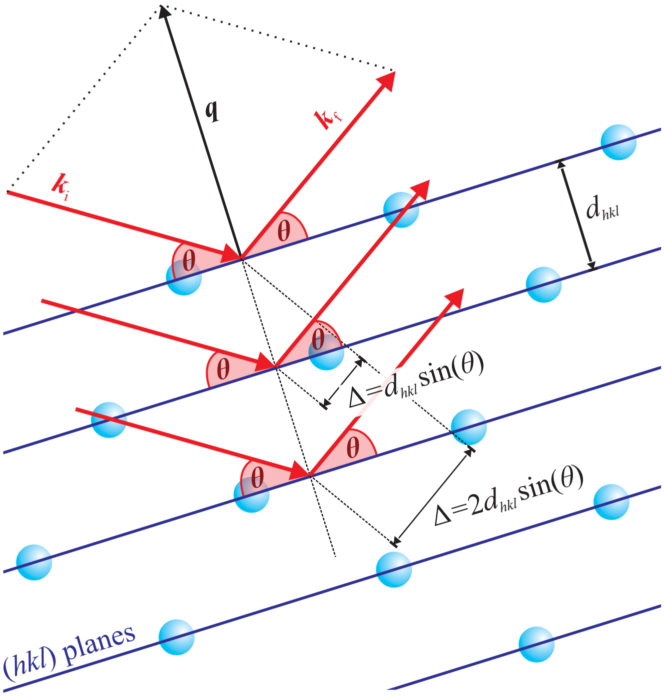

Fig. 2.18: Sketch of the Bragg condition for the constructive interference of waves reflected at lattice planes with layer distance d_{hkl} of a crystal. Incident X-rays (red) with wavelength λ and wave vector $\boldsymbol{k}_\mathrm{i}$ hit a set of parallel lattice planes (dark blue) under an angle θ and get reflected at each lattice plane under the same angle θ. $\boldsymbol{k}_\mathrm{f}$ denotes the wave vector of the outgoing X-rays, which have different phases due to path differences (2Δ). The resulting scattering vector $\boldsymbol{q}$ (black) for this scattering event is normal to the lattice planes. If the path differences are integer multitudes of the X-ray wavelength ($2\Delta = n\,\lambda$), the outgoing X-rays interfere constructively, leading to the occurrence of a Bragg reflection.

In 1913, William Lawrence Bragg and William Henry Bragg provided a relatively simple but descriptive explanation for the occurrence of the aforementioned Bragg reflections by considering the reflections of X-rays from crystal lattice planes (hkl) acting as semi-transparent mirrors [25, 110]. When incident X-rays with wave vector $\boldsymbol{k}_\mathrm{i}$ and wavelength λ hit a crystal at an angle θ, they are reflected at each set of parallel lattice planes at the same angle θ as the incidence angle with wave vector $\boldsymbol{k}_\mathrm{f}$. The scattering vector $\boldsymbol{q} = \boldsymbol{k}_\mathrm{f} - \boldsymbol{k}_\mathrm{i}$ denotes the difference between the wave vectors of the scattered (final) wave $\boldsymbol{k}_\mathrm{f}$ and the incoming (initial) wave $\boldsymbol{k}_\mathrm{i}$. In a set of parallel lattice planes, each discrete plane is separated by a constant parameter d_{hkl}. Consequently, starting from the first plane of the family of parallel planes, the X-rays must travel a multiple longer path in the crystal for each subsequent one, i.e., the path difference of the X-rays reflected at the second plane is $2d_{hkl}\sin(\theta)$ with respect to the first plane, $4d_{hkl}\sin(\theta)$ according to the third plane, etc. This leads to different phases for the corresponding reflected X-rays due to the respective path differences. For path differences that are integer multitudes of the X-ray wavelength λ, the reflected X-rays are in phase and interfere constructively, causing the appearance of the Bragg reflections. This condition is known as the Bragg condition

$$n\,\lambda = 2d_{hkl}\sin(\theta) \quad \text{with} \quad n \in \mathbb{N}\,, \tag{2.51}$$

in which the integer n denotes the order of the resulting Bragg reflection. From Eq. (2.51) it directly follows that the wavelength of the X-rays must be comparable to atomic distances (in the

---

[4] In the X-ray literature, it has become widely accepted to define angles with respect to surfaces. In optics, however, angles are defined according to the surface normal [44].

Ångström range) for Bragg reflections to occur ($\lambda \leq 2d_{hkl}$).

An alternative but more general derivation of the diffraction condition was presented a little earlier by Max von Laue in 1912 [111], who established the three Laue equations

$$\boldsymbol{q} \cdot \boldsymbol{a} = 2\pi\, h \;, \quad \boldsymbol{q} \cdot \boldsymbol{b} = 2\pi\, k \;, \;\text{ and }\; \boldsymbol{q} \cdot \boldsymbol{c} = 2\pi\, l \;\text{ with }\; h, k, l \in \mathbb{Z} \;, \tag{2.52}$$

with the scattering vector $\boldsymbol{q}$ and the basis vectors $\boldsymbol{a}$, $\boldsymbol{b}$, and $\boldsymbol{c}$ of the crystal lattice. h, k,and l are integer numbers and correspond to the Miller indices introduced in Sec. 2.1.2. For each $\boldsymbol{q}$ that satisfies the Laue equations, constructive interference can be observed. Using instead the reciprocal lattice vectors (cf. Sec. 2.1.3) as basis vectors, the scattering vector $\boldsymbol{q}$ can be expressed as

$$\boldsymbol{q} = h\, \boldsymbol{a}^* + k\, \boldsymbol{b}^* + l\, \boldsymbol{c}^* = \boldsymbol{G}_{hkl} \;. \tag{2.53}$$

Thus, constructive interference occurs whenever the scattering vector $\boldsymbol{q}$ coincides with a reciprocal lattice point, which is known as the Laue condition. The reciprocal lattice can therefore be conceived as a set of positions of potential Bragg peaks denoted by the integer numbers h, k, and l as (hkl).

2.6.2 Kinematic diffraction theory

The previous considerations provided information only about the periodicity (or translational symmetry) of the structure and not about the actual location of atoms within a unit cell, i.e., the arrangement of atoms within the crystal lattice [108, 112]. In order to extract this information, it is necessary to analyze the intensities of the diffracted beams. This is done by looking at the scattering processes involving the smallest constituents of the crystal first, and then building the whole crystal around it. Therefore, the necessary theoretical foundations are derived in the following according to Refs. [41–43].

Free electron scattering

When X-rays impinge on an atom, it is mainly the electrons around the atomic nuclei that act as scattering centers due to the higher scattering cross-section compared to the atomic nuclei [28]. Assuming the dipole approximation and taking into account the Thomson formula [113–115], the amplitude A_e of a wave with wave vector $\boldsymbol{k}_\mathrm{f}$ that was scattered at a single (free) electron at position $\boldsymbol{r}_\mathrm{e}$ is related via

$$A_\mathrm{e}\, e^{-i\, \boldsymbol{k}_\mathrm{f} \cdot \boldsymbol{r}_\mathrm{e}} = A_0\, \underbrace{\frac{e^2\, P^{1/2}}{m_\mathrm{e}\, c^2\, R_0}}_{\equiv C}\, e^{-i\, \boldsymbol{k}_\mathrm{i} \cdot \boldsymbol{r}_\mathrm{e}} \tag{2.54}$$

to the amplitude A_0 of the incoming wave with wave vector $\boldsymbol{k}_\mathrm{i}$ prior to the scattering process. e is the elementary charge o the electron, m_e is the mass of the electron, P is the polarization factor of the incoming wave, and R_0 is distance to the detector. If the incident waves are 100 % linearly polarized perpendicular to the scattering plane, the polarization factor is $P = 1$, whereas $P = \cos^2(\vartheta)$ applies for waves that are 100 % linearly polarized in the scattering plane (ϑ denotes the scattering angle). With respect to the scattering vector (or momentum transfer) $\boldsymbol{q} = \boldsymbol{k}_\mathrm{f} - \boldsymbol{k}_\mathrm{i}$, Eq. (2.54) can be rearranged to

$$A_\mathrm{e}(\boldsymbol{q}) = A_0\, C\, e^{i\, \boldsymbol{q} \cdot \boldsymbol{r}_\mathrm{e}} \;, \tag{2.55}$$

which gives the amplitude of the scattered wave.

Scattering from a free atom

The scattering amplitude A_{atom} for a wave scattered at a free atom at position $\boldsymbol{r}_{\mathrm{atom}}$ is obtained by summing the independent scattering contributions A_{e} from all individual electrons surrounding the nucleus of the corresponding atom. By expressing all electrons as an electron density distribution $\rho(\boldsymbol{r})$ of the atom with nucleus-electron distance $|\boldsymbol{r}|$, the summation then becomes an integration and A_{atom} is given by

$$\begin{aligned} A_{\mathrm{atom}}(\boldsymbol{q}) &= \int d^3r\,\rho(\boldsymbol{r})\,A_{\mathrm{e}}(\boldsymbol{q}) && (2.56)\\ &= A_0\,C\int d^3r\,\rho(\boldsymbol{r})\;e^{\,i\,\boldsymbol{q}\,\cdot\,(\boldsymbol{r}\,+\,\boldsymbol{r}_{\mathrm{atom}})} && (2.57)\\ &= A_0\,C\,f^0(\boldsymbol{q})\;e^{\,i\,\boldsymbol{q}\,\cdot\,\boldsymbol{r}_{\mathrm{atom}}}\;, && (2.58) \end{aligned}$$

where

$$f^0(\boldsymbol{q}) = \int d^3r\,\rho(\boldsymbol{r})\;e^{\,i\,\boldsymbol{q}\,\cdot\,\boldsymbol{r}} \qquad (2.59)$$

is referred to as the atomic form factor, which is specific for each atom. In the case of spherically symmetric atoms, which is an adequate approximation in most cases, the atomic form factor depends only on the magnitude of the scattering vector [43], i.e., $f^0(\boldsymbol{q}) = f^0(q)$, and tabulated values of $f^0(q)$ can be looked up in, e.g., Ref. [116]. Though, for photon energies of the incident wave close to an absorption edge of the atom, the atomic form factor can no longer be sufficiently described by $f^0(q)$ alone. In this case, two additional (correction) terms $f'(h\nu)$ and $f''(h\nu)$ are generally required [42, 114].

Scattering from a single unit cell

Adding the individual contributions of all atoms j within a unit cell, the scattering amplitude A_{uc} for the scattering at a single unit cell can intuitively and analogously be derived. Accordingly, the amplitude A_{uc} of a wave scattered at a unit cell is given by

$$\begin{aligned} A_{\mathrm{uc}}(\boldsymbol{q}) &= A_0\,C\sum_j f_j(q)\;e^{\,i\,\boldsymbol{q}\,\cdot\,(\boldsymbol{R}_n\,+\,\boldsymbol{r}_j)} && (2.60)\\ &= A_0\,C\,F(\boldsymbol{q})\;e^{\,i\,\boldsymbol{q}\,\cdot\,\boldsymbol{R}_n}\;, && (2.61) \end{aligned}$$

where $\boldsymbol{R}_n$ denotes the position of the unit cell that is involved in the scattering process, and $\boldsymbol{r}_j$ denotes the atom position of the j-th atom within this unit cell. Furthermore,

$$F(\boldsymbol{q}) = \sum_j f_j(q)\;e^{\,i\,\boldsymbol{q}\,\cdot\,\boldsymbol{r}_j} \qquad (2.62)$$

is the so-called structure factor, defined as the summation of atomic form factors $f_j(q)$ from all j atoms inside the respective unit cell. The structure factor takes into account that the unit cell may be composed of chemically distinct atoms, each with its own unique atomic form factor.

The structure factor $F(\boldsymbol{q})$ causes a strong modulation of the scattered intensity. This can even lead to the point that, due to destructive interference, certain Bragg reflections, although they fulfill the Laue condition $\boldsymbol{q} = \boldsymbol{G}_{hkl}$ (cf. Sec. 2.6.1), nevertheless do not show any intensity. For instance, considering all reciprocal lattice points at which the Laue condition is satisfied, the structure factor can be expressed as

$$F\left(\boldsymbol{q}=\boldsymbol{G}_{hkl}\right)=\sum_{j} f_{j}\left(q\right)\, e^{\,i\,2\pi\,\left(hu_{j}+kv_{j}+lw_{j}\right)} \quad . \tag{2.63}$$

In the case of a body-centered cubic unit cell exhibiting exclusively identical atoms $[f_1\left(q\right)=f_2\left(q\right)]$ at $\boldsymbol{r}_1=(0,0,0)$ and $\boldsymbol{r}_2=(1/2,1/2,1/2)$, the resulting structure factor is then given by

$$F_{\mathrm{bcc}}\left(\boldsymbol{q}=\boldsymbol{G}_{hkl}\right)=f\left(q\right)+f\left(q\right)\, e^{\,i\,\pi\,\left(h+k+l\right)}=\begin{cases}2\,f\left(q\right), & \text{for } h+k+l=\text{even integer}\\ 0, & \text{for } h+k+l=\text{odd integer}\end{cases} \quad . \tag{2.64}$$

Consequently, not all values of h, k, and l result in a Bragg peak. The corresponding Bragg reflection that would result due to constructive interference with respect to the crystal lattice is thus structurally forbidden, so to speak, for this particular structure of the unit cell due to destructive interference of waves scattered at different atoms in the unit cell. In contrast, for a primitive cubic unit cell, no Bragg reflections are structurally forbidden.

Debye-Waller factor

Naturally, the atoms at their corresponding lattice sites are not at rest but are individually thermally vibrating around an average position [42], leading to a scattered intensity into an incoherent background. As a result, the intensity of Bragg reflections is weaker the higher the temperature and thus the stronger the vibration of the atoms. The temperature-dependent vibration of the atoms can be addressed by including an additional parameter, the Debye-Waller factor [114, 115], in the structure factor, such that $F\left(\boldsymbol{q}\right)$ can be written as

$$F\left(\boldsymbol{q}\right)=\sum_{j} f_{j}\left(q\right)\, e^{\,-B_{j}\left(q/4\pi\right)^{2}}\, e^{\,i\,\boldsymbol{q}\cdot\boldsymbol{r}_{j}} \quad , \tag{2.65}$$

where B_j denotes the Debye-Waller factor[5] for the respective j-th atom [117]. Due to the fact that the magnitude of the scattering vector enters quadratically in the exponential term with the Debye-Waller factor, Bragg reflections of higher scattering vector are affected stronger by this effect. For isotropic vibrations, the Debye-Waller factor can simply be described by

$$B_{j}=\frac{8\pi^{2}}{3}\left\langle u_{j}^{2}\right\rangle \quad , \tag{2.66}$$

with the three-dimensional mean-squared displacement $\langle u_j^2\rangle$ of the respective atom [42, 45], which generally is a function of temperature. At room temperature, the average vibrational amplitude can be estimated to be about 0.05 Å [117], which represents rather small perturbations of atomic positions in the unit cell compared to the relatively large size of a unit cell (in the range of several Ångström). Nonetheless, these temperature-induced atomic vibrations are clearly perceptible, and their effects on the intensity of the Bragg reflections are thus not negligible.

In the case of anisotropic thermal vibrations with, e.g., a larger vibrational amplitude perpendicular to the respective atomic bonds, the Debye-Waller factor must instead be modified and expressed using a second-order tensor (vibrational/thermal ellipsoid) [45, 115, 117].

---

[5] Note that in the literature sometimes the entire additional exponential term in Eq. (2.65) is called the Debye-Waller factor [45, 115] with the commonly used substitution $M=B\left(q/4\pi\right)^{2}$ [115, 117]. Thus, the Debye-Waller factor is then given by e^{-M} [45].

Scattering from single crystalline extended structures

Because a crystal can be considered a periodically repetition of unit cells in each spatial direction, the summation over all scattering amplitudes A_{uc} of all N_a, N_b, and N_c identical unit cells along the three crystallographic axes $\boldsymbol{a}$, $\boldsymbol{b}$, and $\boldsymbol{c}$ gives the scattering amplitude

$$\begin{aligned} A_{\text{cryst}}(\boldsymbol{q}) &= A_0\, C\, F(\boldsymbol{q}) \sum_{n_a=0}^{N_a-1} \sum_{n_b=0}^{N_b-1} \sum_{n_c=0}^{N_c-1} e^{\,i\,\boldsymbol{q}\cdot(n_a\boldsymbol{a}+n_b\boldsymbol{b}+n_c\boldsymbol{c})} && (2.67)\\ &= A_0\, C\, F(\boldsymbol{q}) \sum_{n_a=0}^{N_a-1} e^{\,i\,n_a\,\boldsymbol{q}\cdot\boldsymbol{a}} \sum_{n_b=0}^{N_b-1} e^{\,i\,n_b\,\boldsymbol{q}\cdot\boldsymbol{b}} \sum_{n_c=0}^{N_c-1} e^{\,i\,n_c\,\boldsymbol{q}\cdot\boldsymbol{c}} && (2.68)\end{aligned}$$

for scattering at a three-dimensional perfect crystal, assuming a uniform structure factor for all unit cells. Each of the summations in Eq. (2.67) is identical to a geometric series

$$S_N(x) = \sum_{n=0}^{N-1} e^{\,i\,n\,x} = \frac{1-e^{\,i\,N\,x}}{1-e^{\,i\,x}}\ , \tag{2.69}$$

with which $A_{\text{cryst}}(\boldsymbol{q})$ can be rearranged as a product of geometric series to

$$A_{\text{cryst}}(\boldsymbol{q}) = A_0\, C\, F(\boldsymbol{q})\ S_{N_a}(\boldsymbol{q}\cdot\boldsymbol{a})\ S_{N_b}(\boldsymbol{q}\cdot\boldsymbol{b})\ S_{N_c}(\boldsymbol{q}\cdot\boldsymbol{c})\ . \tag{2.70}$$

The modulus squared of $S_N(x)$ is also known as the N-slit interference function

$$|S_N(x)|^2 = \frac{\sin^2(N\,x/2)}{\sin^2(x/2)}\ , \tag{2.71}$$

which is commonly used in optics and describes the intensity distribution of a wave that is scattered at a grating of N slits.

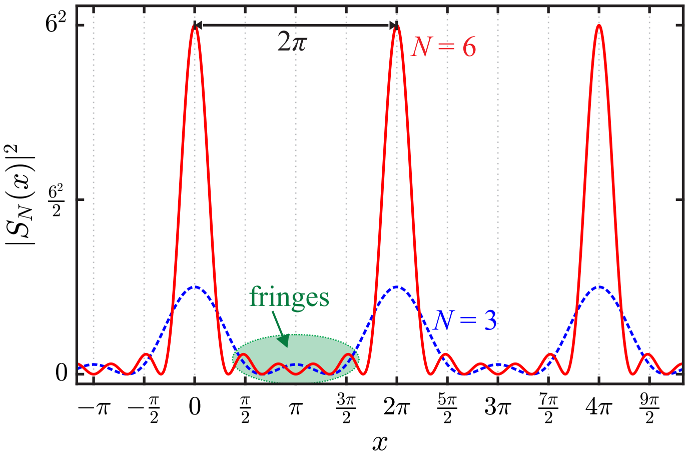

Fig. 2.19: Representation of the modulus squared of the N-slit interference function $|S_N(x)|^2$ for $N = 6$ (red). For comparison, the squared modulus for $N = 3$ is depicted as well (blue). The main maxima have amplitudes of N^2 and are separated by a distance of 2π, while the $(N-2)$ subsidiary maxima (fringes) between the main maxima have distances of $2\pi/N$.

Figure 2.19 shows a typical N-slit interference function $|S_N(x)|^2$ for both $N = 6$ and $N = 3$, which is analogous to a crystal with six and three unit cells, respectively. Both functions exhibit strong main maxima with amplitudes of N^2 centered at multiples of 2π. Hence the distance between two main maxima equals 2π as well. In addition, $(N-2)$ subsidiary maxima are visible, which are separated by a constant distance of $2\pi/N$. The intensity oscillations are called fringes. As the number N of slits/unit cells increases, the number of subsidiary maxima also increases and the main maxima become drastically more intense and sharper. Thus, the full width at half-maximum

(FWHM) of the main maxima is inverse proportional to the number N of slits/unit cells and can be determined according to the Scherrer formula [118]

$$\mathrm{FWHM} = K_{\mathrm{S}} \frac{2\pi}{N} \ , \tag{2.72}$$

with the Scherrer or (shape) factor $K_{\mathrm{S}} = 0.89$ for an ideal block-shaped crystal. Depending on the shape of unit cells and, accordingly, on the symmetry of the crystal [119], the value of K_{S} may differ slightly from the ideal value.

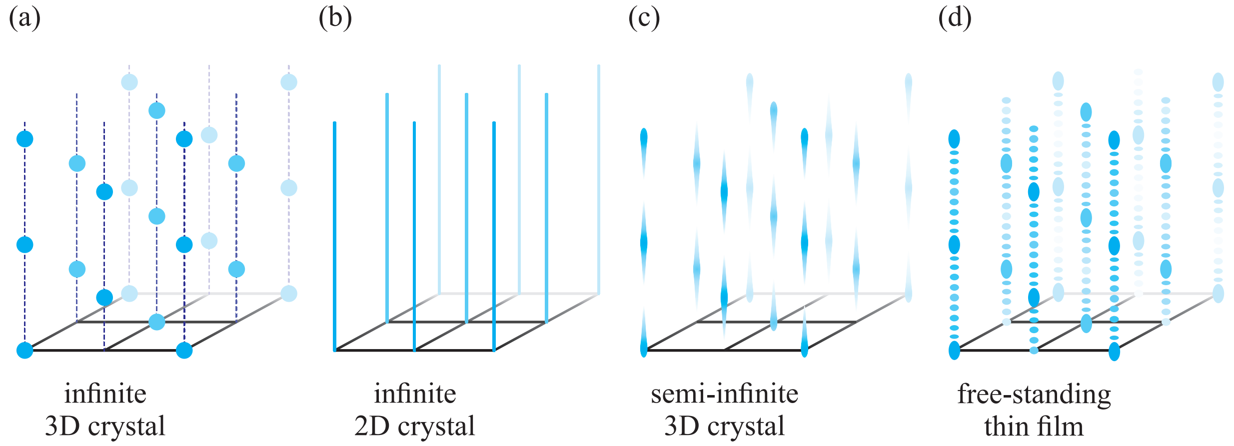

Fig. 2.20: Illustration of the diffracted intensity distribution for selected crystalline structures in reciprocal space. (a) Diffraction at a 3D bulk crystal with an infinite number of unit cells in the three spatial directions causes sharp point-like diffraction spots at designated positions, called Bragg peaks. The dashed lines serve only as guides to the eye. (b) Diffraction at a 2D crystal in 3D space results in diffraction rods. (c) The consideration of a semi-infinite (real) 3D crystal results in smeared-out Bragg peaks in vertical direction with intensity even between two intensity maxima. (d) The diffraction at a free-standing thin crystalline film produces diffraction spots accompanied by intensity oscillations (fringes) in vertical direction. For a better overview, all diffraction spots and diffraction rods with higher indexing are displayed with lower brightness. Adapted from Refs. [43, 120].

In the limit of an infinite number of unit cells, as in the case of an infinitely extended three-dimensional crystal, the N-slit interference function transforms into a periodic distribution of δ-like peaks [42] according to

$$\lim_{N\to\infty} S_N\left(x\right) \propto \sum_{n=0}^{\infty} \delta\left(x - 2\pi n\right) \ . \tag{2.73}$$

The scattering amplitude [cf. Eq. (2.70)] can then be rewritten as

$$A_{\mathrm{cryst}}\left(\boldsymbol{q}\right) \propto F\left(\boldsymbol{q}\right) \sum_{h} \sum_{k} \sum_{l} \delta\left(\boldsymbol{q}\cdot\boldsymbol{a} - 2\pi\, h\right) \delta\left(\boldsymbol{q}\cdot\boldsymbol{b} - 2\pi\, k\right) \delta\left(\boldsymbol{q}\cdot\boldsymbol{c} - 2\pi\, l\right) \ . \tag{2.74}$$

Therefore, in the case of an infinitely extended three-dimensional crystal, $A_{\mathrm{cryst}}\left(\boldsymbol{q}\right)$ leads to non-zero scattering intensity and sharp peaks only if the Laue equations [cf. Eq. (2.52)] are satisfied, and thus to discrete Bragg peaks in the reciprocal space [cf. Fig. 2.20 (a)].

From this point, if the number of unit cells is completely reduced only in the vertical direction, leaving merely a single crystal layer (complete crystal truncation), the diffraction from an infinitely extended two-dimensional crystal is obtained. Since the scattering from a 2D crystal is independent of $\boldsymbol{q}\cdot\boldsymbol{c}$ and solely the lateral Laue equations need to be satisfied, a two-dimensional lattice of diffraction rods forms in the reciprocal space with constant intensity along the vertical direction [cf. Fig. 2.20 (b)].

As a first approximation, the scattered intensity distribution from a semi-infinite 3D crystal – an infinitely extended 3D crystal with a surface – might be described by the trivial superimposition of the scattered intensity from the infinite 2D crystal and from the infinite 3D crystal. Following this approximation, the reciprocal space would consist of a lattice of diffraction rods of constant intensity passing through the Bragg peaks along the vertical direction [43]. However, this picture for the scattered intensity from a semi-infinite 3D crystal is not very accurate because the intensity profile along the vertical direction between two Bragg peaks is by no means constant. More genuinely, diffraction at a semi-infinite 3D crystal leads to smeared-out Bragg peaks in the out-of-plane direction of the surface [cf. Fig. 2.20 (c)], producing what are called crystal truncation rods (CTRs) [41]. The CTRs have intensity maxima at the nominal Bragg peak positions. Between two peaks the intensity declines drastically with intensity minima exactly in the center.

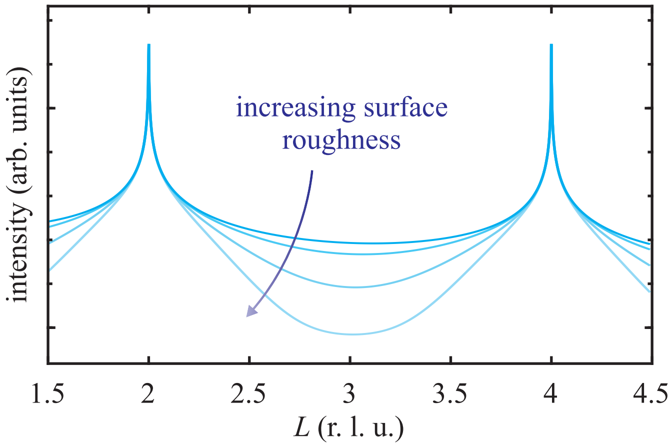

Fig. 2.21: Impact of surface roughness on the intensity distribution along a CTR (in L direction). From blue to light blue: increase of the surface roughness, resulting in a stronger reduction of the intensity between Bragg reflections.

The intensity variation along CTRs can be grasped by considering the diffraction of a semi-infinite 3D crystal in combination with a finite penetration depth of X-rays (∼ µm) due to absorption processes in the crystal. At each layer in the crystal, a portion of the X-rays is absorbed, which causes a continuous decrease in the intensity, i.e., only a finite number of layers can effectively contribute to diffraction. As a result, layers near the surface have a higher contribution than deeper layers in the crystal. Furthermore, in reality, crystal surfaces have certain roughnesses that can significantly alter the intensity distribution along CTRs as well [121–124], as demonstrated in Fig. 2.21. Therefore, for a complete description regarding the diffraction of X-rays at semi-infinite (real) crystals, the finite surface roughness of the crystal has to be included also in addition to the absorption of each layer represented by ϵ. The amplitude A_{cryst} resulting from scattering from a semi-infinite 3D crystal can thus be expressed by

$$A_{\text{cryst}}\left(\boldsymbol{q}\right) = A_0\, C\, F\left(\boldsymbol{q}\right) \sum_{n_a=0}^{N_a-1} e^{\,i\, n_a\, \boldsymbol{q}\cdot\boldsymbol{a}} \sum_{n_b=0}^{N_b-1} e^{\,i\, n_b\, \boldsymbol{q}\cdot\boldsymbol{b}} \sum_{n_c=-\infty}^{N_c(n_a,n_b)} e^{\,i\, n_c\, \boldsymbol{q}\cdot\boldsymbol{c}}\; e^{\,n_c\,\epsilon}\;, \tag{2.75}$$

with $N_c\left(n_a, n_b\right)$ as the height distribution in the direction parallel to the surface, which can be interpreted as the roughness of the surface. Here, the average height is set at zero level, i.e., the summation over n_c in Eq. (2.75) must start from $n_c = -\infty$ because of the consideration of a semi-infinite crystal. Please note that this approach assumes a perfect crystal structure and, thus, any structural imperfections have been neglected.

In the following, only the intensity distribution along a CTR is of interest. In this context, the lateral Laue equations $\boldsymbol{q} \cdot \boldsymbol{a} = 2\pi\, h$ and $\boldsymbol{q} \cdot \boldsymbol{b} = 2\pi\, k$ are fulfilled and $A_{\text{cryst}}\left(\boldsymbol{q}\right)$ can be simplified to

$$\begin{aligned}
A_{\text{cryst}}\left(\boldsymbol{q}\right) &= A_0\, C\, F\left(\boldsymbol{q}\right) \sum_{n_a=0}^{N_a-1} 1 \sum_{n_b=0}^{N_b-1} 1 \sum_{n_c=-\infty}^{N_c(n_a,n_b)} e^{\,i\, n_c\, \boldsymbol{q} \cdot \boldsymbol{c} + n_c\, \epsilon} && (2.76)\\
&= A_0\, C\, F\left(\boldsymbol{q}\right) \sum_{n_a=0}^{N_a-1} \sum_{n_b=0}^{N_b-1} \frac{e^{\left(i\, \boldsymbol{q} \cdot \boldsymbol{c} + \epsilon\right)\, N_c\left(n_a, n_b\right)}}{1 - e^{-\left(i\, \boldsymbol{q} \cdot \boldsymbol{c} + \epsilon\right)}} && (2.77)\\
&= A_0\, C\, F\left(\boldsymbol{q}\right)\, N_a\, N_b\, \frac{\left\langle e^{\left(i\, \boldsymbol{q} \cdot \boldsymbol{c} + \epsilon\right)\, N_c\left(n_a, n_b\right)} \right\rangle}{1 - e^{-\left(i\, \boldsymbol{q} \cdot \boldsymbol{c} + \epsilon\right)}}\,, && (2.78)
\end{aligned}$$

where the sums over n_a and n_b were treated as an averaging over $N_c\left(n_a, n_b\right)$. Approximating the height distribution by a Gaussian finally gives

$$A_{\text{cryst}}\left(\boldsymbol{q}\right) = A_0\, C\, F\left(\boldsymbol{q}\right)\, N_a\, N_b\, \frac{e^{-\sigma^2\left(1 - \cos\left(\boldsymbol{q} \cdot \boldsymbol{c}\right)\right)}}{1 - e^{-\left(i\, \boldsymbol{q} \cdot \boldsymbol{c} + \epsilon\right)}}\,, \qquad (2.79)$$

with σ being the root mean square roughness of the surface [120, 125]. In terms of this work, the modulus squared of Eq. (2.79) corresponds to the intensity distribution resulting from crystalline substrates [cf. Fig. 2.20 (c) and Fig. 2.21].

Scattering from a free-standing crystalline thin film

As previously shown, the scattering from a crystalline substrate can be explained by assuming a semi-infinite crystal with the inclusion of the finite X-ray penetration depth and finite surface roughness. For crystalline thin films, this description is no longer sufficient since two interfaces/surfaces have to be treated due to their small finite size. Hence, they can not be regarded as semi-infinite. Moreover, since the finite X-ray penetration depth usually outstrips the size of (ultra)thin films such as those prepared in this work ($< 50\,\text{nm}$), the influence of absorption can, to a good approximation, be neglected when treating the scattering at these crystalline structures.

Considering a thin crystalline film with a height distribution of $N_c^-\left(n_a, n_b\right)$ at the bottom side of the film (w.l.o.g. the average height is set at zero level) and a height distribution of $N_c^+\left(n_a, n_b\right)$ at the top side of the film with the mean height of $\overline{N_c}$, the resulting scattering amplitude A_{cf} is analogous to Eq. (2.76–2.78) given by

$$\begin{aligned}
A_{\text{f}}\left(\boldsymbol{q}\right) &= A_0\, C\, F\left(\boldsymbol{q}\right) \sum_{n_a=0}^{N_a-1} 1 \sum_{n_b=0}^{N_b-1} 1 \sum_{n_c=N_c^-(n_a,n_b)}^{N_c^+(n_a,n_b)} e^{\,i\, n_c\, \boldsymbol{q} \cdot \boldsymbol{c}} && (2.80)\\
&= A_0\, C\, F\left(\boldsymbol{q}\right) \sum_{n_a=0}^{N_a-1} \sum_{n_b=0}^{N_b-1} \frac{e^{\,i\, \boldsymbol{q} \cdot \boldsymbol{c}\, N_c^-\left(n_a, n_b\right)} - e^{\,i\, \boldsymbol{q} \cdot \boldsymbol{c}\, N_c^+\left(n_a, n_b\right) + 1}}{1 - e^{\,i\, \boldsymbol{q} \cdot \boldsymbol{c}}} && (2.81)\\
&= A_0\, C\, F\left(\boldsymbol{q}\right)\, N_a\, N_b\, \frac{\left\langle e^{\,i\, \boldsymbol{q} \cdot \boldsymbol{c}\, u_c^-} \right\rangle - e^{\,i\, \boldsymbol{q} \cdot \boldsymbol{c}\, \overline{N_c}} \left\langle e^{\,i\, \boldsymbol{q} \cdot \boldsymbol{c}\, u_c^+} \right\rangle}{1 - e^{\,i\, \boldsymbol{q} \cdot \boldsymbol{c}}}\,, && (2.82)
\end{aligned}$$

with u_c^+ and u_c^- corresponding to the respective height variations of $\overline{N_c}$ at the top and bottom side of the film, respectively. In a similar manner to Eq. (2.79), both height variations can be approximated by a Gaussian each, resulting in

$$A_{\mathrm{f}}\left(\boldsymbol{q}\right) = A_0\, C\, F\left(\boldsymbol{q}\right)\, N_a\, N_b\, \frac{e^{-\sigma_-^2\,\left(1-\cos \boldsymbol{q}\cdot\boldsymbol{c}\right)} - e^{i\,\boldsymbol{q}\cdot\boldsymbol{c}\,\overline{N_c}}\, e^{-\sigma_+^2\,\left(1-\cos \boldsymbol{q}\cdot\boldsymbol{c}\right)}}{1 - e^{i\,\boldsymbol{q}\cdot\boldsymbol{c}}} \tag{2.83}$$

for the amplitude of a wave scattered at a thin crystalline film. Its modulus squared features distinct intensity maxima with fringes in between, as schematically represented in Fig. 2.20 (d).

Scattering from crystalline film-substrate (multilayer) structures

In the previous considerations, only crystalline single structures were treated. However, when one or even more crystalline films are grown on a crystalline substrate, each individual film contributes with the substrate to an overall scattering signal. The scattering amplitude for the whole (multilayer) structure, consisting of one or more films on a substrate, is then given by the superposition of the contributions of all i films plus the contribution of the substrate according to

$$A_{\mathrm{total}}\left(\boldsymbol{q}\right) = A_{\mathrm{cryst}}\left(\boldsymbol{q}\right) + \sum_i \Theta_i\, e^{\,i\,\boldsymbol{q}\,\cdot\,\boldsymbol{p}_i}\, A_{\mathrm{f},i}\left(\boldsymbol{q}\right)\ , \tag{2.84}$$

with Θ_i as the occupation factor of the i-th film, which takes into account structural defects such as impurities or dislocations in the film, reducing the diffracted intensity. Furthermore, $\boldsymbol{p}_i$ is the phase vector

$$\boldsymbol{p}_i = \sum_{j=0}^{i-1} \boldsymbol{g}_j + \overline{N_{cj}}\, \boldsymbol{c}_j\ , \tag{2.85}$$

describing the shift of the respective film at the interface, with $\boldsymbol{g}_j$ as the interface vector between j-th and $(j+1)$-th film, and $\overline{N_{cj}}\,\boldsymbol{c}_j$ as the phase shift caused by the underlying films due to their film thicknesses.

2.7 Low-energy electron diffraction - LEED

Just like XRD (cf. Sec. 2.6), low-energy electron diffraction (LEED) is a diffraction technique utilized for structure determination of crystalline samples. In a typical LEED experiment, electrons with a (kinetic) energy of 20 eV to 500 eV are incident perpendicularly to the surface of a sample [126]. The incoming electrons that are scattered elastically at the crystal surface contribute directly to a diffraction pattern. However, due to a higher interaction (larger cross-section) of electrons with matter compared to X-rays, most electrons suffer severe energy losses already after a IMFP (cf. Sec. 2.5.1) of $< 1\,\mathrm{nm}$ [91], resulting from inelastic scattering processes as, e.g., electron-electron interactions or phononic and plasmonic excitations [126]. Therefore, with LEED, primarily the structure and morphology of crystalline surfaces is probed.

According to de-Broglie, the electrons used for LEED have wavelengths that are of the same order of atomic distances in crystals. Consequently, the elastically scattered electron waves can interfere coherently with each other, leading to the appearance of a diffraction pattern that directly reflects the symmetry of the crystal surface structure. Since essentially only the crystal surface is involved in the diffraction process, diffraction rods form in reciprocal space analogous to X-ray diffraction at a single free-standing crystalline surface [cf. Fig. 2.20 (b)] due to the lack of periodicity in the direction perpendicular to the sample surface in real space.

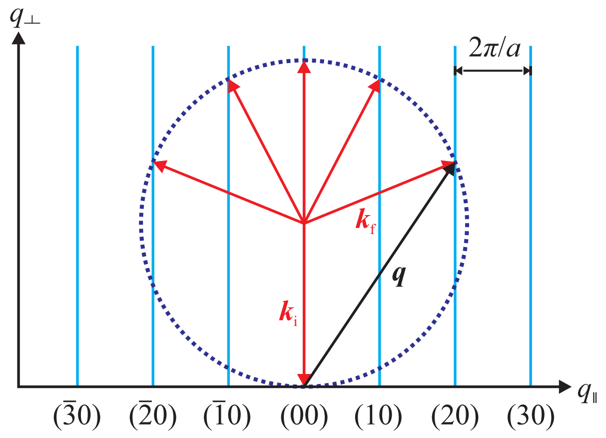

Fig. 2.22: Visualization for the appearance of diffraction spots by means of the Ewald construction for electron diffraction at a crystalline surface. The electrons are incident normal to a surface with wave vector $\boldsymbol{k}_\mathrm{i}$. The length of $|\boldsymbol{k}_\mathrm{i}|$ is equal to the radius of the Ewald sphere (dashed line). For each interception point of the Ewald sphere with a diffraction rod (solid blue lines), the two-dimensional Laue condition is fulfilled and diffraction occurs. Only the backscattered wave vectors $\boldsymbol{k}_\mathrm{f}$ are displayed, which result in diffraction spots. Adapted from Ref. [50].

The occurrence of diffraction is commonly visualized in terms of the Ewald (sphere) construction, which is shown in Fig. 2.22 in terms of electron diffraction at a crystalline surface. Electrons with wave vector $\boldsymbol{k}_\mathrm{i}$ are incident normal to the sample surface [$\boldsymbol{k}_\mathrm{i}$ is along the (00) rod and points to the origin of the reciprocal space] and are constructively (and elastically) scattered for wave vectors $\boldsymbol{k}_\mathrm{f}$ that terminate on an intersection point of a diffraction rod with the Ewald sphere of radius $|\boldsymbol{k}_\mathrm{i}| = |\boldsymbol{k}_\mathrm{f}|$. For these points, the two-dimensional Laue condition $\boldsymbol{q}_{||} = \boldsymbol{G}_{hk}$ [cf. Eq. (2.53) and Eq. (2.7)] is satisfied and diffraction can be observed. By changing the kinetic energy of the electrons, the radius of the Ewald sphere can be modified to produce either more or fewer intersections, which in turn grants access to a larger or smaller portion of the reciprocal space, respectively.

Due to the high surface sensitivity of this method, deviations from the ideal surface can cause a direct visible change in the diffraction pattern. Here, the effects of inhomogeneities and randomly distributed structural defects like local point defects are rather small and cause only a diffuse background intensity in the pattern. Far greater influence is exerted by extended defects such as atomic steps, domain and grain boundaries, etc., which lead to an altered intensity distribution [126] due to finite size effects from atomic terraces, superstructure domains and grains or mosaics. In addition, dangling bonds or adatoms on the surface can lead to a reconstruction of the surface, resulting in a superstructure and, therefore, in additional peaks in the LEED pattern due to a modified periodicity.

2.8 X-ray reflectivity - XRR

X-ray reflectivity (XRR) is a quite useful and efficient technique, most commonly employed for thickness determination and to probe the quality of interfaces of thin film heterostructures in terms of roughness [127]. The basic principal of XRR is the measurement of the reflected beam intensity of X-rays from surfaces and interfaces of a single or multilayer structure depending on the relatively small glancing incidence angle $\theta_\mathrm{i} \lesssim 5°$.

When X-rays ($\boldsymbol{k}_\mathrm{i}$) encounter an interface under an incidence angle θ_i between two optical media with different refractive indices n_1 and n_2, part of the X-rays are reflected ($\boldsymbol{k}_\mathrm{f}$) under the same angle $\theta_\mathrm{f} = \theta_\mathrm{i}$ as the incidence angle [cf. Fig. 2.23 (a)]. As both the incidence angle θ_i and the reflected angle θ_f are identical, the resulting momentum transfer vector or scattering vector $\boldsymbol{q} = \boldsymbol{k}_\mathrm{f} - \boldsymbol{k}_\mathrm{i}$ is always perpendicular to the interface the X-rays are incident to. Hence, $\boldsymbol{q}$ has only a vertical component q_z (with the z axis along the interface normal) and the magnitude of the scattering

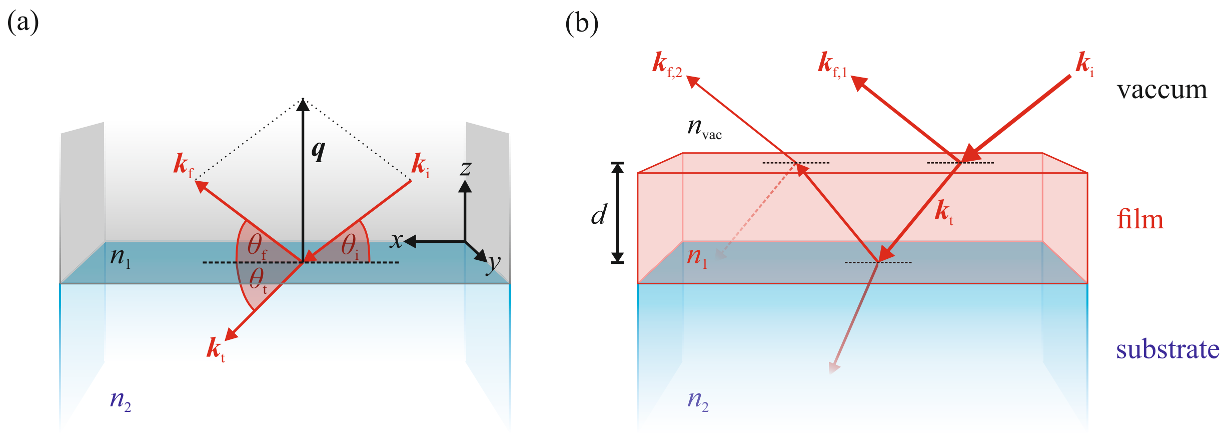

Fig. 2.23: (a) Reflection of an incidence beam ($\boldsymbol{k}_\mathrm{i}$) at an interface between two optical media, having refractive indices n_1 and n_2, with $n_1 < n_2$, for an incidence angle θ_i above the critical angle θ_c. The beam is partly reflected ($\boldsymbol{k}_\mathrm{f}$) under a reflection angle $\theta_\mathrm{f} = \theta_\mathrm{i}$ and partly transmitted ($\boldsymbol{k}_\mathrm{t}$) under a transmission angle θ_t. $\boldsymbol{q}$ denotes the scattering vector with $\boldsymbol{q} = \boldsymbol{k}_\mathrm{f} - \boldsymbol{k}_\mathrm{i}$ normal to the interface. (b) Reflectivity of a basic multilayer system consisting of single film of thickness d on top of a substrate with refractive indices n_1 and n_2, respectively, and $n_1 < n_2$. n_vac is the refractive index of vacuum/air with $n_\mathrm{vac} = 1$. Here, reflection and transmission of the incoming beam occurs at each interface.

vector $q = q_z$ is given by

$$q = q_z = 2k \sin(\theta_\mathrm{i}) = \frac{4\pi}{\lambda} \sin(\theta_\mathrm{i}) \ . \tag{2.86}$$

The residual part of the X-rays is refracted ($\boldsymbol{k}_\mathrm{t}$) under a transmission angle θ_t and propagates in the medium with refractive index n_2. However, this is only the case if the incidence angle exceeds a specific critical angle θ_c (see discussion below). In the case of X-rays, the real part of the refractive index

$$n = 1 - \delta + i\,\beta \tag{2.87}$$

of any matter is marginal smaller than unity [44], where $\delta = \lambda^2\, r_\mathrm{e}\, \rho / 2\pi$ is the dispersion and $\beta = \lambda\, \mu / 4\pi$ is the absorption, considering a homogeneous medium irradiated by X-rays with an energy far from the absorption edges of the material. Moreover, λ is the wavelength of the X-rays, r_e is the classical electron radius and ρ and μ are the the electron density and the absorption coefficient, respectively. Consequently, for the reflection of X-rays at a single interface between either air or vacuum ($n_1 = 1$) and matter, total external reflection can occur for nearly flat incidence angles and all incoming X-rays are reflected. The critical angle θ_c below which no X-rays are transmitted is approximately given by $\theta_\mathrm{c} \approx \sqrt{2\delta}$. As the angle of incidence is increased beyond the critical angle ($\theta_\mathrm{i} > \theta_\mathrm{c}$), more of the initial X-rays are continuously transmitted and enter the medium n_2, resulting in a reduced fraction of X-rays that contributes to reflection.

The (Fresnel) reflectivity R and the (Fresnel) transmission T for an interface illuminated by X-rays are linked to the complex reflection coefficient $r_\mathrm{s/p}$ with $R = |r_\mathrm{s/p}|^2$ and the complex transmission coefficient $t_\mathrm{s/p}$ with $T = |t_\mathrm{s/p}|^2$, respectively, which both generally depend on the polarization state of the X-rays (s- or p-polarization). Since the refractive index n is usually close to one for X-rays, both optical coefficients $r_\mathrm{s/p}$ and $t_\mathrm{s/p}$ are similar for s- and p-polarization ($r = r_\mathrm{s/p}$ and $t = t_\mathrm{s/p}$) and, thus, the Fresnel coefficients are simply given by

$$r = \frac{k_{\mathrm{i},z} - k_{\mathrm{t},z}}{k_{\mathrm{i},z} + k_{\mathrm{t},z}} \quad \text{and} \quad t = \frac{2\, k_{\mathrm{i},z}}{k_{\mathrm{i},z} + k_{\mathrm{t},z}} \ , \tag{2.88}$$

in which $k_{\mathrm{i},z} = n_1\, k \sin(\theta_\mathrm{i})$ and $k_{\mathrm{t},z} = n_2\, k \sin(\theta_\mathrm{t}) = k\sqrt{n_2^2 - \cos^2(\theta_\mathrm{i})}$ are the vertical components (along z direction) of the wave vectors $\boldsymbol{k}_\mathrm{i}$ and $\boldsymbol{k}_\mathrm{t}$, respectively.

In the case of a multilayer system, comprising one or even more films and a substrate underneath, the scattering at all interfaces must be taken into account. Here, the reflection and transmission of the impinging X-rays occurs at each single interface, starting with the uppermost interface between vacuum/air and the first film [cf. fig. 2.23 (b)]. For simplicity, the substrate is usually treated to be infinitely thick. As a result, the scattering of X-rays at the backside of the substrate can be neglected due to the finite penetration depth. The reflectivity R for a multilayer system is given by the superimposition of the individual reflectivity of each interface and can be calculated by applying the recursive approach presented by Parratt in 1954 [128]. Thereby, the reflectivity $R_{j,j+1}$, stemming from the partial reflection of an interface between the j-th and the $(j+1)$-th layer in the multilayer system, is given by

$$R_{j,j+1} = \frac{r_{j,j+1} + R_{j+1,j+2}\, e^{\,i\, d_{j+1}\, q_{j+1}}}{1 + r_{j,j+1}\, R_{j+1,j+2}\, e^{\,i\, d_{j+1}\, q_{j+1}}}\ , \tag{2.89}$$

where

$$r_{j,j+1} = \frac{q_j - q_{j+1}}{q_j + q_{j+1}} \tag{2.90}$$

is the Fresnel coefficient associated with the respective interface, with $q_j = q_{z,j}$ and d_j being the vertical component of scattering vector and the thickness of the corresponding layer, respectively.

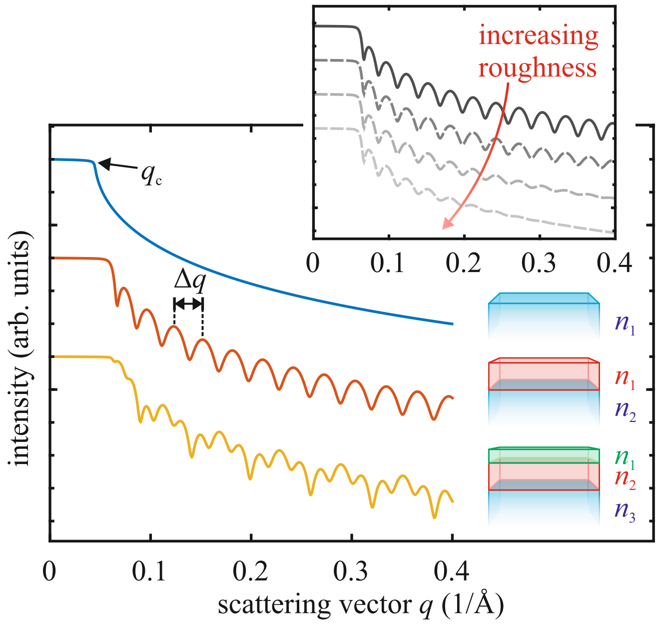

Fig. 2.24: Representative XRR curves for the models of a pure substrat (blue curve), a single 20 nm-thick film on top of a substrate (red curve) and two films on top of a substrate with film thicknesses of 10 nm and 20 nm (yellow curve). All media are optically different with the uppermost interface in the respective models adjacent to vacuum/air. The inset shows XRR curves of a single film of constant thickness on top of a substrate with increasing substrate-film interface roughness, resulting in a stronger damping of the Kiessig fringes the higher the roughness of the interface. All XRR curves are shifted in vertical direction for clarity.

Figure 2.24 shows typical theoretical X-ray reflectivity curves as a function of the (vertical) scattering vector $q = q_z$ for three different models to which the Parratt formalism has been applied: a pure substrate (n_1), a single film (n_1) on top of a substrate (n_2), and two films (n_1 and n_2) on top of a substrate (n_3). For each curve, total external reflection is observed until the critical angle θ_c or, in terms of q, until the corresponding critical scattering vector q_c is reached. For larger scattering vectors, the reflected intensities drop following overall a characteristic q^{-4} dependence. In contrast to the reflectivity curve of the pure substrate, the decrease of the reflectivity in the other reflectivity curves is accompanied by oscillations, which are called Kiessig fringes and are caused by constructive and destructive interference of X-rays reflected from smooth interfaces. The number of different periodicities of the oscillations scales with the number of additional films on the substrate. As a result, oscillations of different periodicities superpose in a reflectivity curve of a multilayer system. For a single layer system with oscillations of only one periodicity, the film thickness d can be estimated from the distance of the oscillations Δq via $d \approx 2\pi/\Delta q$. Since the reflectivity in a multilayer system is much more complex due to the larger number of interference possibilities, the individual film thicknesses can inevitably only be estimated by accurately modeling the reflectivity of the film system.

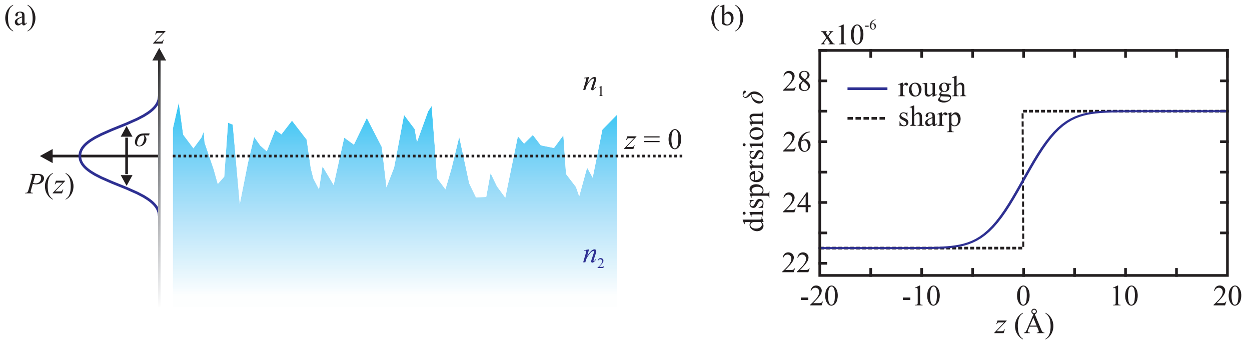

Fig. 2.25: (a) Illustration of a rough interface between two optical media n_1 and n_2 with a mean height of the height fluctuations at $z = 0$. The height variations are described by a probability density function $P(z)$ with standard deviation σ. (b) Dispersion profile (from $\delta = 22.5 \times 10^{-6}$ to $\delta = 27 \times 10^{-6}$) for one sharp and one rough (RMS roughness = 3 Å) interface represented by an error function. Adapted from [44, 129].

The example reflectivity curves in Fig. 2.24 discussed so far are all presented without the influence of any interfacial roughness σ. Realistic interfaces, however, are rarely sharp or flat due to structural defects, resulting in a continuous change of the refractive index at the interface, i.e., of the electron density profile [44], as illustrated in Fig. 2.25. Here, for comparable small roughnesses ($\sigma \ll d$), the Névot-Croce method [130] has proven to be quite effective by approximating the electron density profile by an error function, leading to a slightly modified Fresnel coefficient

$$r_{j,j+1}^{\text{rough}} = r_{j,j+1}\, e^{-2k_{z,j}\, k_{z,j+1}\, \sigma_j^2} \, , \tag{2.91}$$

which substitutes for the Fresnel coefficient $r_{j,j+1}$ in Eq. (2.89). The exponential damping (or Névot-Croce) factor reduces the reflected intensity depending on the quantity of the root mean square (RMS) roughness σ of the respective interface j. The effect of interface roughness on the reflectivity curves is demonstrated in the inset of Fig. 2.24 for a single film on a substrate with continuously increasing substrate-film interface roughness. With increasing interface roughness, a much stronger attenuation of the intensity modulations is evident for larger scattering vectors q. In contrast, if the interface roughness is significant higher, the electron density profile must instead be segmented into a series of very thin and flat layers [127].

2.9 Direct imaging of structures

Both XRD (cf. Sec. 2.6) and LEED (cf. Sec. 2.7) are methods that provide information about the reciprocal space of samples. In order to obtain information about real space as well, other complementary investigation methods are necessary, allowing direct imaging of interfaces and structural elements in general with spatial resolution. There are a variety of methods that can be used to directly visualize structural properties of materials on the nanometer or even atomic scale, such as atomic force microscopy[6] (AFM), transmission electron microscopy (TEM), and scanning tunneling microscopy (STM). Within the scope of this work, only the first two methods were employed to examine the structure and interface of the thin (ferrite) films produced.

2.9.1 Atomic force microscopy - AFM

In AFM, the imaging is based on the measurement of the force acting between a surface of a sample and an atomic sharp tip as it is scanned across the surface [cf. Fig. 2.26 (a)]. The advantage of AFM is that it can be used for samples independent on their conducting character and even insulating materials can be probed. Depending on the distance between tip and surface (0.1 nm to 100 nm [131]), three different regimes can be identified with respect to the forces acting on the tip: initially, at very large distances, the force which the tip is experiencing is negligible. As the distance decreases and the tip approaches the surface, the influence of attractive forces such as, e.g., van der Waals interactions, electrostatic force, and chemical force gradually increase. If the tip is only a few Ångström away from the surface, short-range repulsive forces like sphere repulsion, Pauli-exclusion interaction, and electron-electron Coulomb interaction dominate [131].

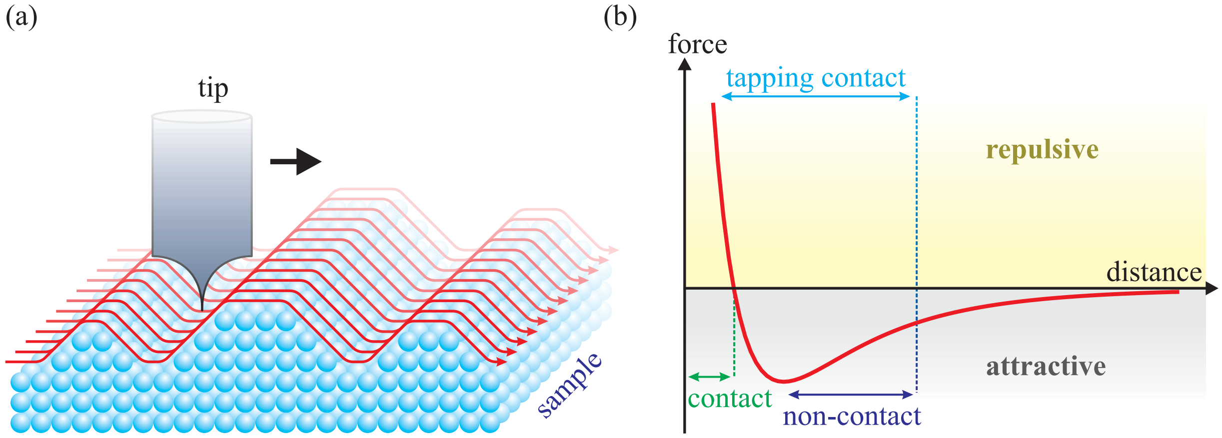

Fig. 2.26: (a) Sketch of the operation of an AFM. The sharp tip maps the surface by scanning across it line by line. Adapted from Refs. [132, 133]. (b) Typical shape of the interacting force (red curve) between a tip and a surface as a function of their distance from each other. The three main operating modes (contact mode, non-contact mode, and tapping mode) are marked according to their operating ranges.

The force exerted by the sample on the tip is typically measured by the deflection of the cantilever to which the tip is attached. Here, the cantilever behaves as a spring and bends in response to the forces acting on the tip, obeying Hooke's Law. Thus, the bending of the cantilever can be used to directly infer the acting force if the stiffness (spring constant) of the cantilever is known. The deflection of the cantilever, in turn, can be measured, for instance, by a laser beam reflected from its backside into a split photodiode (cf. Sec. 4.4). Other methods that have been developed for cantilever deflection detection include optical fiber interferometry, tunneling current measurement, capacitance measurement, and piezoelectric (or piezoresistive) detection [131, 134–138], which, however, have been demonstrated to be less reliable and sensitive compared to the optical deflection technique [131].

In principle, the AFM can be operated in two major modes: static mode and dynamic mode. In static (or contact) mode, the tip is brought into close proximity to the sample surface, where

---

[6] Atomic force microscopy is sometimes alternatively referred to as scanning force microscopy (SFM) in the literature.

small repulsive forces act on the tip and bend it accordingly. The surface contour of the sample can be mapped, for instance, by changing the position of the tip vertically to the surface during the scanning process, so that the force on the tip and hence its distance to the surface is kept constant, as indicated by constant bending of the cantilever. In contrast, in the dynamic (or non-contact) mode, the cantilever does not remain static but is vibrated by an actuator close to its free resonance frequency with a constant vibration amplitude [139]. For this purpose, the tip is often positioned some distance away from the sample surface into the area of action of attractive forces. The tip-surface interaction causes a modification of the resonance frequency of the cantilever and thus a changing vibration amplitude. The surface contour is imaged in this operating mode, for example, by regulating the distance according to a constant vibration amplitude, i.e., a constant force gradient. The tapping mode is a small modification of the AFM within the dynamic mode with a relatively stiff cantilever and a larger vibration amplitude, resulting in the tip being partially affected by the repulsive forces as well [140]. The advantage of the tapping mode is the more straightforward interpretation of the data analysis compared to the conventional non-contact mode. Nonetheless, just as in contact mode, images recorded in tapping mode may suffer more greatly from thermal drift of the mechanical setup, caused, e.g., by the substrate temperature. The respective operating ranges of the different operating modes of the AFM with respect to the tip-to-surface distance are shown in Fig. 2.26 (b).

2.9.2 (High-resolution) transmission electron microscopy - (HR)TEM

The TEM is based on the principle of an optical microscope (cf. Fig. 2.27), which, in contrast to a conventional light microscope, uses electrons and exploits their wavelength [141–143]. For this purpose, highly collimated electrons are accelerated up to 300 keV, leading to a theoretical (point) resolution[7]

$$r_{\mathrm{th}} \approx \frac{1.22\lambda}{\beta} \approx \frac{3\,\mathrm{pm}}{\beta} \tag{2.92}$$

even below the atomic level. Hereby, λ is the wavelength of the electrons and β is a numerical factor in radians, characterizing the maximum collection angle of the aperture [48]. So far, however, it has not been possible to even come close to this resolution in a TEM experiment. The reason for the poorer resolution resides in lens aberrations, which severely limit the effective resolution of the TEM to about 1 Å [144].

The electrons are directed as an electron beam onto a sample using a condenser lens system, where they interact with the sample and are partially scattered as well as diffracted. The objective lens behind the sample conjoins the propagating electrons and produces an (intermediate) image in the image plane. The diffracted electron beams that left the sample under the same emergent angle are additionally also combined in the back focal plane of the objective, resulting in a diffraction pattern (Fourier transform). Placing an objective aperture at this position, a diffraction contrast can be created by selecting only certain electron beams for image generation. A distinction can be made between dark-field and bright-field imaging. Dark-field imaging solely uses diffracted electron beams, whereas bright-field imaging utilizes only the undiffracted primary beam. The ability to use different imaging techniques allows certain features in the final image to be visualized more clearly in the respective imaging technique that are less high in contrast in the corresponding other imaging technique. The objective lens can be considered the most important imaging lens in a TEM setup. Any imperfections or aberrations of this lens are further amplified by subsequent lenses in

---

[7] For visible light microscopy, a slightly changed expression for the the maximum resolving limit is customarily used. In terms of the the classical Rayleigh criterion, the maximum resolution obtainable is given by $r_{\mathrm{th}} = 0.61\lambda/\mathrm{NA}$, in which NA denotes the numerical aperture.

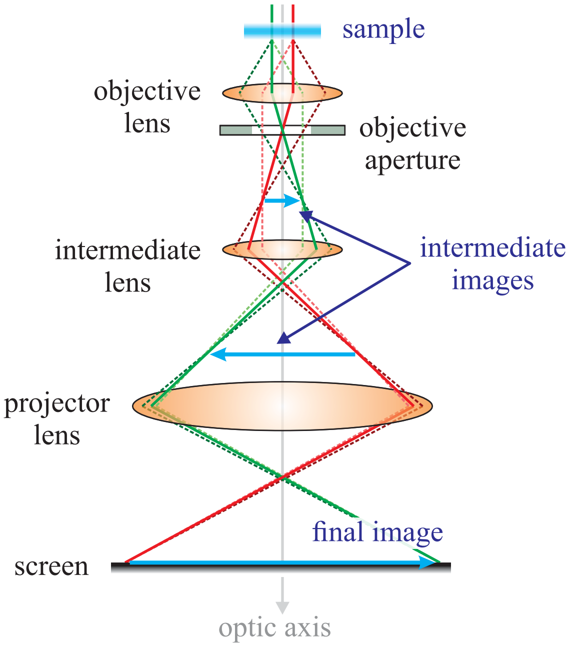

Fig. 2.27: Highly simplified illustration of the beam paths beginning from a sample down the optical column of the TEM to the complete final image when using the image mode. The dashed lines indicate the beam paths of scattered/diffracted electron beams. In general, TEMs are equipped with a significantly larger number of imaging lenses, which offer greater flexibility in terms of magnification and focus range for images [48]. The objective aperture located in the back focal plane of the objective lens enables switching between dark field mode and bright field mode by allowing only certain beams to pass. The intermediate lens is set in a way that its object plane corresponds to the image plane of the objective lens, which in combination with the appropriately set projector lens results in a magnification onto a viewing screen. Based on Ref. [48].

the optical path. A combination of intermediate lenses and projector lenses post-magnifies the intermediate image enormously, which is then finally projected onto a viewing screen as the final image.

HRTEM represents a subtype of TEM that provides high-resolution imaging of structures at atomic level using both the scattered/diffracted beams as well as the undiffracted beam to form an interference image [145, 146]. Here, the phase shifts or phase differences of the electrons are exploited that arise when the electrons interact with different columns of atoms while traversing the sample in the direction of irradiation. These phase shifts become noticeable in the final (interference) image as phase contrast. Aberrations of the objective lens, including, e.g., spherical and chromatic aberration as well as defocusing of the objective lens, are able to further modify the phase shifts on top. This can either enhance the phase contrast or, in the worst and more common case, lead to a smearing/blurring of the resulting HRTEM image, which makes a correct interpretation initially impossible. To circumvent this, lens aberrations have to be corrected to the best possible extent, e.g., *a priori* by additional hardware like multipole lenses [147–149].

Nevertheless, in principle, the phase information is undesirably lost in the (HR)TEM images upon imaging on the viewing screen since only the squared modulus of the wave function of the electrons, i.e., the intensity of the electron beam, is measured. Since the information of the object regarding the structure is largely encoded in the phase of the electron wave function, this is a predicament and attempts must be made to reconstruct the electron wave function *a posteriori*. For this purpose, the method of focal series reconstruction can be applied [150–152], which involves recording a series of HRTEM images from the same area at different objective lens defocuses [153–155]. Each image contains a fraction of the information of the electrons immediately as they emerged from the sample, allowing the electron wave function to be reassembled [152,156]. Being free from any effects of aberrations, this electron wave function grants direct access to object information. Alternatively, in-line or off-axis electron holography can also be employed to retrieve the electron wave function [157, 158], in which the beam containing the object information is coherently overlapped with an unaffected reference beam to form a hologram. On the basis of an hypothesized structural model, a corresponding HRTEM image can be simulated or calculated [159]. The subsequent comparison of the theoretical HRTEM image with the recorded experimental HRTEM image supplies the ultimate confirmation of the structural model at hand.

3 Investigated materials

This work focuses on the growth and characterization of (ultra)thin ferrite films such as Fe_3O_4 and $Co_xFe_{3-x}O_4$ prepared on single crystalline MgO(001) and $SrTiO_3(001)$ substrates by reactive molecular beam epitaxy. In addition, this work presents an essential noval synthesis technique for the preparation of cobalt ferrite films via thermally induced interdiffusion of CoO/Fe_3O_4 bilayers on $SrTiO_3(001)$. Thus, in this part of the work, the most relevant physical properties of the materials used and fabricated are introduced, starting with the substrates (MgO and $SrTiO_3$) and completing with the films (CoO, Fe_3O_4, and $CoFe_2O_4$), including a comprehensive description of the electronic structure and magnetism of the analyzed ferrites as well as a basic description of antiphase boundaries.

3.1 Materials used as substrates

3.1.1 Magnesium oxide - MgO

Magnesium oxide (MgO) is diamagnetic, electrically insulating with a band gap of $\sim 7.8\,\mathrm{eV}$ [160], and falls into the type of crystals that crystallize in the rock-salt structure with a bulk lattice constant of $a_{\mathrm{MgO}} = 4.212\,\text{Å}$ (at room temperature) [161]. Within this structure, the two ion species, Mg^{2+} and O^{2-}, each form a separate face-centered cubic (fcc) sublattice, with both sublattices shifted along a cubic lattice vector by half a lattice constant. Consequently, the Mg^{2+} ions occupy the octahedral lattice sites of the fcc sublattice built by the O^{2-} ion species and vice versa. The unit cell of MgO is illustrated in Fig. 3.1 (a).

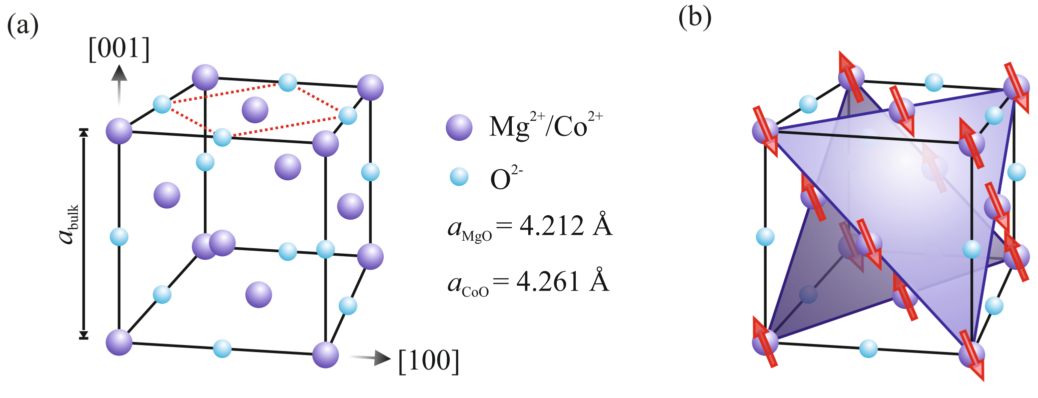

rock-salt structure

antiferromagnetic CoO

Fig. 3.1: (a) Typical unit cell of a rock-salt-type crystal such as MgO and CoO made up of two face-centered cubic sublattices populated by either O^{2-} anions (blue) or by $Mg^{2+}(Co^{2+})$ cations (purple) in the case of MgO(CoO). Compared to the bulk unit cell, the surface unit cell of rock-salt structures (red and dashed) has lateral lattice vectors in [110] and [$\bar{1}$10] bulk directions and is thus rotated by 45°. (b) Antiferromagnetic spin structure of the Co^{2+} cations in CoO. Within each individual (111) plane, all spins align in parallel, while they are oriented antiparallelly with respect to the spins within the adjacent (111) planes.

For the (001) plane of MgO, which was used in this work solely as the surface on which films were grown, a primitive quadratic unit cell can be defined with lateral lattice vectors in [110] and [$\bar{1}$10] bulk directions. Hence, this primitive quadratic surface unit cell is rotated by 45° with respect to the bulk MgO unit cell and has a surface lattice constant of $a^{s}_{\mathrm{MgO}} = a_{\mathrm{MgO}}/\sqrt{2}$.

3.1.2 Strontium titanate - $SrTiO_3$

Strontium titanate ($SrTiO_3$, STO), similar to MgO, is a diamagnetic insulator with a band gap of around 3.2 eV [162] but crystallizes in the cubic perovskite structure with a bulk lattice constant of $a_{\mathrm{STO}} = 3.905$ Å at room temperature [163]. The ideal unit cell of STO is shown in Fig. 3.2. It comprises Ti^{4+} cations coordinated sixfold by O^{2-} anions and Sr^{2+} cations, with four TiO_6 octahedra each surrounding one Sr^{2+} cation. Thus, each single Sr^{2+} cation has twelve O^{2-} anions as nearest-neighbors.

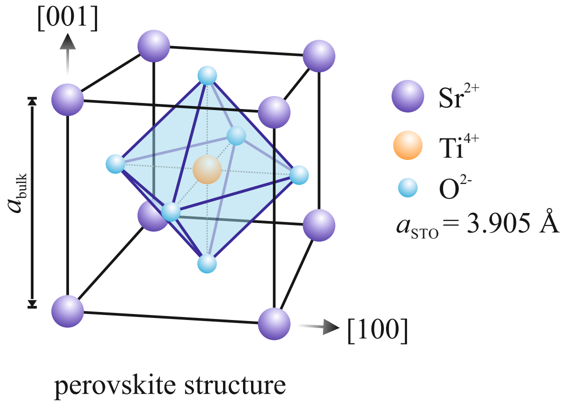

Fig. 3.2: Illustration of the cubic perovskite unit cell of $SrTiO_3$. Six O^{2-} anions (blue) form an octahedron with a Ti^{4+} cation (orange) in the center. Each O^{2-} anion is located on the face-centered sites of a cube formed by Sr^{2+} cations (purple). Since $SrTiO_3$ is composed of alternating SrO and TiO_2 atomic planes in the [001] direction, the $SrTiO_3$(001) surface can be terminated with either atomic plane.

For thin film deposition, exclusively the (001) plane of STO served as the substrate surface in this work. In the [001] direction, STO has two different types of atomic alternating planes, namely SrO and TiO_2, both half a lattice constant apart. Consequently, the $SrTiO_3$(001) surface can be terminated either with SrO or TiO_2. However, this does not affect the size and orientation of the resulting surface unit cell with lateral lattice vectors always along [100] and [010] bulk directions, consistent with the cubic bulk structure of STO.

Doping STO with even small quantities of Nb (~ 0.05 wt%), for example, has the effect of significantly modifying the electronic properties of STO depending on the relative concentration of Nb dopants, such that STO becomes conductive (n-type conductivity) [164]. This has the advantage that conductive STO is particularly suitable as film support material for a variety of measurement techniques such as the spectroscopic measurement techniques that have been utilized in this work because charging effects are averted.

3.2 Film materials

3.2.1 Cobalt(II) oxide - CoO

The transition metal oxide cobalt(II) oxide (CoO) can be regarded as the archetype of all antiferromagnetic oxides, exhibiting a bulk Néel temperature of $T_{\mathrm{N}} = 293$ K [165,166]. Just like MgO, CoO is insulating (band gap of ~ 2.7 eV [167]) and crystallizes in the rock-salt structure [cf. Fig. 3.1 (a)]. Analogously, the Co^{2+} cations occupy the octahedral sites of the fcc sublattice constituted by the O^{2-} ions and vice versa. The bulk lattice constant of CoO at room temperature corresponds to

$a_{\mathrm{CoO}} = 4.261\,\text{Å}$ [168] and the surface lattice constant of the quadratic surface unit cell is given by $a^{\mathrm{s}}_{\mathrm{CoO}} = a_{\mathrm{CoO}}/\sqrt{2}$, which is rotated by 45° with respect to the CoO bulk unit cell.

In the antiferromagnetic phase of CoO, all atomic magnetic moments of the Co^{2+} cations are aligned in parallel within one (111) plane but couple antiparallelly with the magnetic moments of the Co^{2+} cations in neighboring (111) planes, leading to an overall antiferromagnetic structure [cf. Fig. 3.1 (b)].

3.2.2 Magnetite - Fe_3O_4

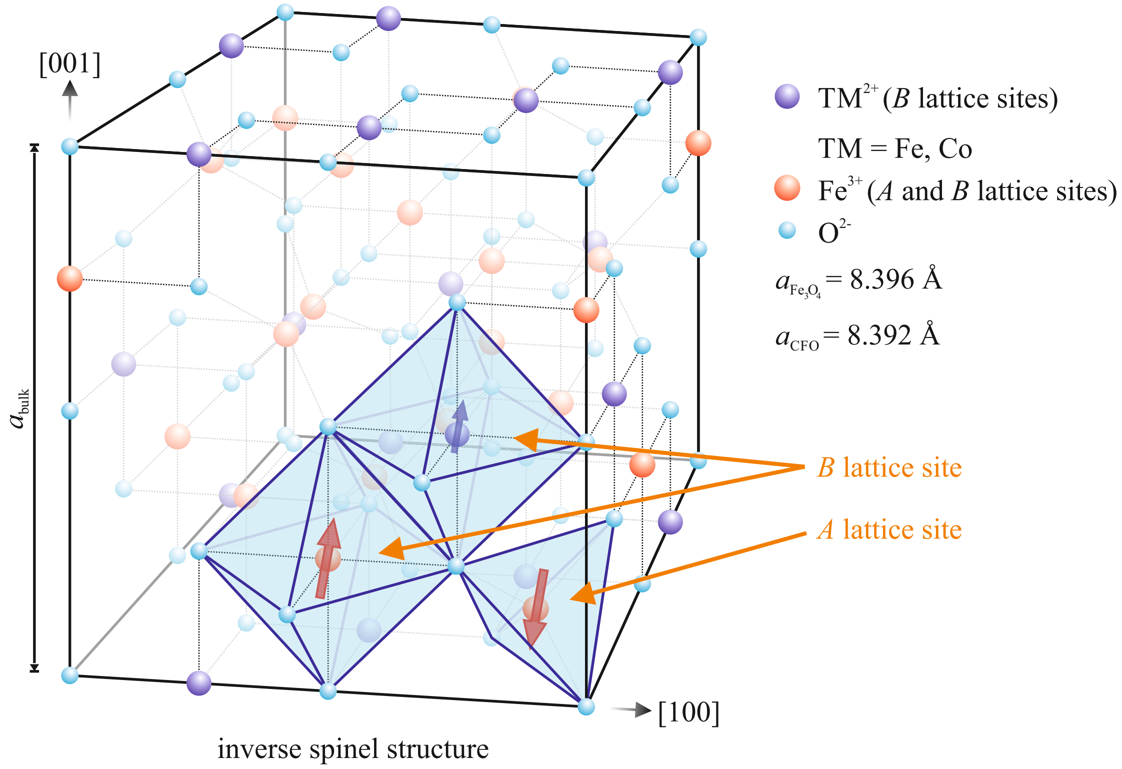

Fig. 3.3: Illustration of the bulk unit cell of a transition metal (TM) ferrite such as Fe_3O_4 or $CoFe_2O_4$, exhibiting inverse spinel structure. Within the fcc sublattice formed by O^{2-} anions, divalent transition metal cations (Fe^{2+} for Fe_3O_4 and Co^{2+} for $CoFe_2O_4$; indicated in purple) occupy solely octahedral *B* lattice sites, whereas trivalent transition metal cations (Fe^{3+}; indicated in red) are distributed equally on octahedral *B* as well as tetrahedral *A* lattice sites. The trivalent transition metal cations residing on the *B* and *A* sites couple antiferromagnetically with each other. As a result, the net macroscopic magnetization of ferrites with ideal inverse spinel structure stems exclusively from the octahedral divalent transition metal cations. For clarity, ions inside the oxygen sublattice are displayed with less intensity. Adapted from Refs. [19, 50].

Magnetite (Fe_3O_4) is a half-metallic and ferrimagnetic ferrite with a band gap of around 0.1 eV and a high bulk Curie temperature of about $T_{\mathrm{C}} = 850\,\mathrm{K}$ [169]. Fe_3O_4 crystallizes in the cubic inverse spinel structure at room temperature, as illustrated in Fig. 3.3. The bulk unit cell includes 32 O^{2-} anions and 24 Fe cations, eight of which are Fe^{2+} and 16 of which are Fe^{3+} cations, and has a lattice constant of $a_{\mathrm{Fe_3O_4}} = 8.396\,\text{Å}$ [169]. The basic framework of the (inverse) spinel structure is provided by the O^{2-} anions, which form a fcc oxygen sublattice with Fe cations distributed across octahedral and tetrahedral interstitial sites[1]. Hereby, two adjacent octahedra are sharing a

---

[1] It is often also common to denote the tetrahedral and octahedral lattice sites of the (inverse) spinel structure as *A* and *B* lattice sites, respectively.

common edge. Additionally, each octahedron has a common vertex with a corresponding closest tetrahedron.

In the ideal inverse spinel structure, 1/2 of the octahedral sites are populated in equal proportion by Fe^{2+} and Fe^{3+} cations, while 1/8 of the tetrahedral sites are occupied by Fe^{3+} cations as well. In contrast, if Fe_3O_4 would crystallize as a normal spinel, all Fe^{2+} cations would reside on tetrahedral lattice sites instead of the octahedral lattice sites, leaving the octahedral lattice sites filled exclusively with Fe^{3+} cations and the tetrahedral lattice sites occupied solely by Fe^{2+} cations. Although a perfect inverse spinel structure is expected for Fe_3O_4 (and also for $CoFe_2O_4$), small deviations from the ideal structure are sometimes observed, with cation distributions corresponding to a weighted mixture of normal and inverse spinel structures. The cationic order of these intermediate states

$$\left[\mathrm{TM}^{2+}_{1-\gamma}\mathrm{Fe}^{3+}_{\gamma}\right]_A \left[\mathrm{TM}^{2+}_{\gamma}\mathrm{Fe}^{3+}_{2-\gamma}\right]_B \mathrm{O}^{2-}_4 \tag{3.1}$$

can be quantitatively described for any transition metal (TM = Fe, Co, etc.) ferrite by the inversion parameter γ, with γ ranging from 0 (normal spinel) to 1 (completely inverse spinel). Here, the first brackets denote the occupancy of the tetrahedral A sites and the second brackets specify the occupancy of the octahedral B sites. Such structural modifications away from the ideal inverse spinel structure can have a major impact on the electronic and magnetic properties of spinel ferrites, as will be briefly described later in Sec. 3.2.4 and Sec. 3.2.5.

The surface unit cell of the $Fe_3O_4(001)$ surface has lateral lattice vectors along [110] and $[\bar{1}10]$ bulk directions and a lattice constant of $a^{\mathrm{s}}_{\mathrm{Fe_3O_4}} = a_{\mathrm{Fe_3O_4}}/\sqrt{2}$. Consequently, it is rotated by 45° with respect to the bulk Fe_3O_4 unit cell. In addition, a $(\sqrt{2}\times\sqrt{2})R45°$ reconstruction is typically observed for well-ordered $Fe_3O_4(001)$ surfaces [170]. After years of intensive research, it has been demonstrated that this reconstruction can be attributed to a ordered structure of subsurface cation vacancies (SCV), such that a completely different iron oxide phase ($Fe_{11}O_{16}$) with only Fe^{3+} cations forms at the surface [18].

3.2.3 Cobalt ferrite - $CoFe_2O_4$

Despite its insulating character, cobalt ferrite ($CoFe_2O_4$, CFO) strongly resembles magnetite both structurally and magnetically. CFO has a (theoretically predicted) band gap of $\sim 0.8\,\mathrm{eV}$ [171] and is ferrimagnetic with a high bulk Curie temperature of about $T_{\mathrm{C}} = 793\,\mathrm{K}$ [9]. Identical to Fe_3O_4, CFO crystallizes as an inverse spinel (cf. Fig. 3.3) but with a slightly smaller room temperature bulk lattice constant of $a_{\mathrm{Fe_3O_4}} = 8.392\,\text{Å}$ [172]. Thereby, in the case of ideal and stoichiometric CFO, Co^{2+} cations have replaced in equal parts the Fe^{2+} cations on the octahedral sites, which are present in Fe_3O_4, while the distribution of Fe^{3+} cations on octahedral and tetrahedral lattice sites remains the same. Thus, the octahedral lattice sites of the fcc oxygen sublattice formed by the 32 O^{2-} anions host both eight Co^{2+} and eight Fe^{3+} cations, whereas eight Fe^{3+} cations reside on the tetrahedral sites of the fcc oxygen sublattice.

Compared to the bulk unit cell, the surface unit cell of the $CoFe_2O_4(001)$ surface is analogous to Fe_3O_4 rotated by 45° with lateral lattice vectors in [110] and $[\bar{1}10]$ bulk directions and a lattice constant of $a^{\mathrm{s}}_{\mathrm{CoFe_2O_4}} = a_{\mathrm{CoFe_2O_4}}/\sqrt{2}$. Yet, a $(\sqrt{2}\times\sqrt{2})R45°$ surface reconstruction commonly visible for Fe_3O_4 is absent in the case of $CoFe_2O_4$.

3.2.4 Electronic structure of ferrites

Many approximations such as local spin density (LSD) approximation or generalized gradient approximation (GGA) have been applied in first-principle density functional theory (DFT) calculations in order to derive the accurate electronic band structure of spinel transition metal ferrites. However, due to the strong electron correlation of the 3*d* transition electrons, the electronic structure of most spinel ferrites was often placed too high in energy near the Fermi energy [171], making them half-metallic when they were supposed to be insulating. Greater success has been achieved with the self-interaction corrected (SIC-)LSD approximation, yielding a much more adequate description for ferrites. The electronic band structure in the vicinity of the Fermi level of the Fe_3O_4 and $CoFe_2O_4$ ferrites studied in this work, which was theoretically predicted using DFT calculations and SIC-LSD [171], is shown in Fig. 3.4.

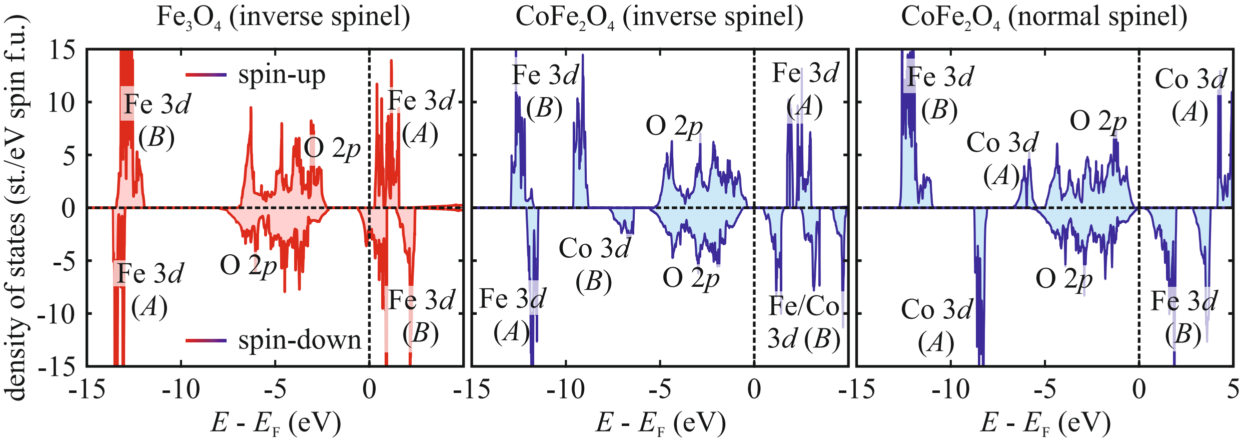

Fig. 3.4: Density functional theory calculations of the electronic band structure for Fe_3O_4 as an inverse spinel and $CoFe_2O_4$ as an inverse as well as a normal spinel. The respective total density of states (DOS) is decomposed according to the spin, with the minority DOS (spin-down) shown in the bottom panel (negative values) and the majority contributions (spin-up) in the top panel (positive values). Dashed vertical lines denote the Fermi level. The main contributions of the different ion species to the respective bands are labeled, where *A* and *B* represent the tetrahedral and octahedral lattice sites. Adapted from Ref. [171].

For both Fe_3O_4 and $CoFe_2O_4$, the inverse spinel arrangement of the transition metal cations is preferred as the ground state configuration based on total energy considerations [171]. In the case of Fe_3O_4, a half-metallic-like electronic band structure is obtained by assuming only localized Fe^{3+} cations, while the Fe^{2+} cations are partially delocalized and together randomly populate the octahedral lattice sites along with the Fe^{3+} cations. These partially delocalized cations in combination with other ten unoccupied minority states corresponding to octahedral lattice sites constitute a peak at the Fermi level, which thus gives rise to the half-metallic character of Fe_3O_4.

$CoFe_2O_4$, on the other hand, exhibits an electronic band structure resembling an insulator with a theoretical band gap between the valence and conduction bands of 0.8 eV. The valence band, just as in Fe_3O_4, is largely due to oxygen with a small admixture of transition metals. For $CoFe_2O_4$, the highest occupied states are thus given predominantly by O 2*p* states. The lowest unoccupied states are in turn given by Fe 3*d* electrons residing on tetrahedral and octahedral lattice sites for the majority and minority spin channel, respectively. In addition, the conduction band exhibits an exchange splitting, i.e., the energy difference between the two spin channels, of 1.28 eV. As a result, considering the capability of $CoFe_2O_4$ as a spin-filter, this implies that the tunnel barrier height for spin-down electrons is lower than for spin-up electrons and, therefore, spin-filtering should be negatively polarized. Consequently, based on this prediction, $CoFe_2O_4$ sufficiently meets the requirements for spin-filter applications.

Furthermore, as mentioned above, the cationic site inversion within the spinel structure exerts a strong influence on the electronic band structure of ferrites. During the crossover from the inverse spinel structure of $CoFe_2O_4$ to its normal spinel structure, the exchange splitting of the conduction band increases immensely to 4.07 eV, which at first glance is more advantageous for the spin-filter application due to a theoretically enhanced spin-filtering efficiency. However, simultaneously, the band gap decreases to 0.21 eV, turning $CoFe_2O_4$ with normal spinel structure nearly into a half-metal, which counteracts the improved spin-filter efficiency. Taking into account that the crystal structure of $CoFe_2O_4$ in reality often deviates slightly from that of an ideal inverse spinel compound [173, 174], it can be assumed that the actual value of the exchange splitting of the conduction band and the band gap lies somewhere between the theoretical ones of both extreme scenarios ($CoFe_2O_4$ either as a perfect inverse spinel or as a normal spinel).

3.2.5 Magnetism of ferrites

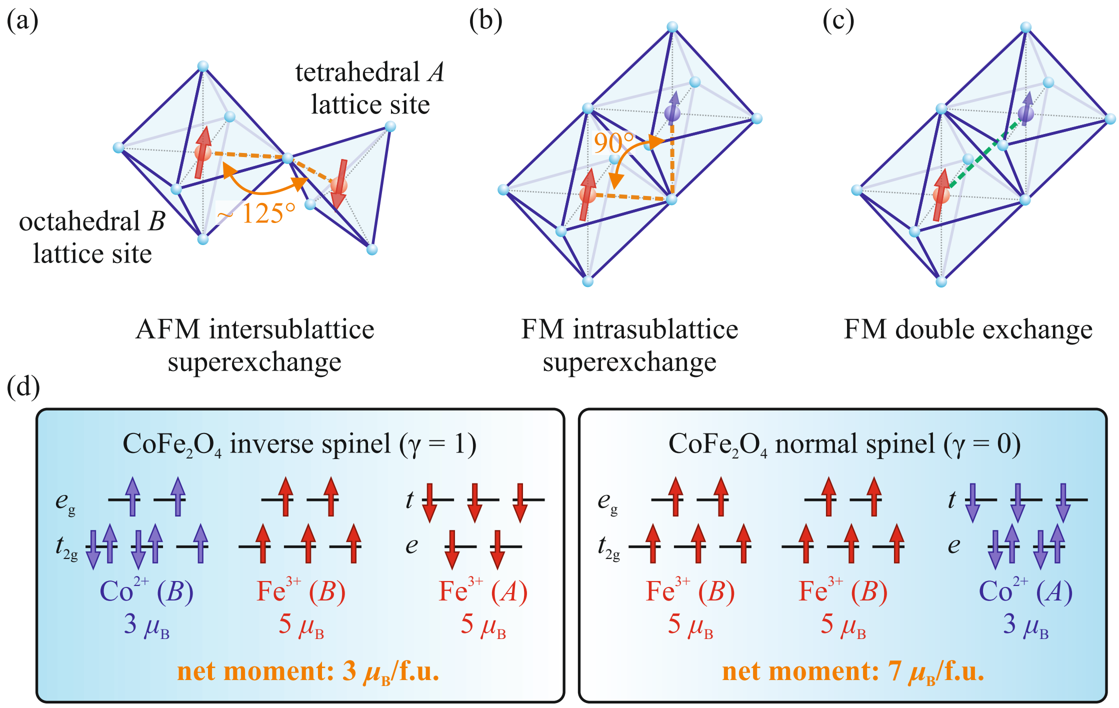

Fig. 3.5: Illustration of the most important different magnetic exchange interactions and their effect on the net moment of spinel transition metal ferrites. (a) Intersublattice superexchange interaction between cations on octahedral *B* and tetrahedral *A* lattice sites, causing an antiferromagnetic (AFM) coupling between the cations. (b) Intrasublattice superexchange interaction involving cations on octahedral *B* lattice sites, which couples both cations ferromagnetically (FM) with each other. (c) Double exchange interaction between cations located on octahedral *B* lattice sites, which also induces ferromagnetic (FM) coupling of both cations. (d) Electronic configurations of the individual cations in $CoFe_2O_4$ with ideal inverse spinel structure and normal spinel structure, including the resulting net moments. Adapted from Ref. [19].

The occurring ferrimagnetic properties of most (inverse) spinel transition metal ferrites such as Fe_3O_4 and $CoFe_2O_4$ stems from the competing interplay of multiple magnetic exchange couplings between the different transition metal cations within the (inverse) spinel crystal structure [9, 31]. The first magnetic exchange interaction to be mentioned here, which is also the strongest, is the intersublattice $A - B$ superexchange interaction, where trivalent transition metal cations (Fe^{3+}) on the different lattice sites (octahedral and tetrahedral) interact via an intervening diamagnetic oxygen anion. Since the overlapping Fe $3d$ and O $2p$ orbitals form a bonding angle of about 125° [cf. Fig. 3.5 (a)], the Fe–O–Fe exchange interaction is strongly antiferromagnetic according to the Goodenough-Kanamori rules (cf. Sec. 2.3.1) with a strength of $J_{AB} \approx -23\,k_\mathrm{B}$ [175] for Fe_3O_4 and $J_{AB} \approx -24\,k_\mathrm{B}$ [176] in the case of $CoFe_2O_4$. In addition, there is a further antiferromagnetic coupling of the trivalent transition metal cations (Fe^{3+}) on the tetrahedral lattice sites. This intrasublattice $A - A$ superexchange interaction has a strength of $J_{AA} \approx -15\,k_\mathrm{B}$ [175] and $J_{AA} \approx -18\,k_\mathrm{B}$ [176] for Fe_3O_4 and $CoFe_2O_4$, respectively. In contrast, the intrasublattice $B - B$ superexchange interaction, involving divalent and trivalent transition metal cations (Co^{2+} or Fe^{2+} and Fe^{3+}) in exclusively octahedral symmetry, is weakly ferromagnetic with a strength of $J_{BB} \approx 1\,k_\mathrm{B}$ [175] for Fe_3O_4 and $J_{BB} \approx 4\,k_\mathrm{B}$ [176] for $CoFe_2O_4$ due to the 90° bonding angle with the intermediate diamagnetic oxygen anion [cf. Fig. 3.5 (b)]. Finally, there is another ferromagnetic interaction resulting from the double exchange interaction between the divalent and trivalent transition metal cations on octahedral lattice sites due to mixed valencies [cf. Fig. 3.5 (c)], in which an electron is transferred from the divalent cation to an unoccupied $3d$ state of the trivalent cation. As this ferromagnetic double exchange interaction is also quite weak, it is often masked by the superexchange interaction associated with the same transition metal cations [9].

The interplay of all these magnetic exchange interactions in (inverse) spinel transition metal ferrites leads to the formation of a ferrimagnetic order with a corresponding net magnetic moment resulting from the addition of the different magnetic couplings between the individual transition metal cations [9]. For instance, Fe^{3+} has $3d^5$ configuration and therefore five unpaired (valence) electrons. Assuming a high-spin state of Fe^{3+} (cf. Sec. 2.5.5), the magnetic moments of all five electrons add up to an atomic magnetic moment of $5\,\mu_\mathrm{B}$/atom independent of the symmetry of the surrounding oxygen ligands. Here, the angular moments of the electrons have been neglected because their contribution to the total magnetic moment is often rather small compared to the contribution stemming from the electron spin. As a result of the strong prevailing antiferromagnetic superexchange interaction between Fe^{3+} cations on octahedral and tetrahedral lattice sites, their magnetic moments effectively cancel each other out. Consequently, the macroscopic bulk magnetization of, e.g., Fe_3O_4 and $CoFe_2O_4$ is mainly due to their uncompensated octahedrally coordinated divalent transition metal cations and their ferromagnetic coupling. Fe^{2+} ($3d^6$) and Co^{2+} ($3d^7$) possess one and two fewer unpaired (valence) electrons, respectively, in their $3d$ shells than Fe^{3+}. Therefore, the atomic magnetic moments of Fe^{2+} and Co^{2+} in the high-spin state are $4\,\mu_\mathrm{B}$/atom and $3\,\mu_\mathrm{B}$/atom, respectively, again regardless of their coordination and without consideration of any angular moments. Hence, the macroscopic bulk magnetization of ideal Fe_3O_4 amounts to $4\,\mu_\mathrm{B}$/f.u. and to $3\,\mu_\mathrm{B}$/f.u. for ideal $CoFe_2O_4$ [cf. Fig. 3.5 (d)].

In contrast, if, for example, in $CoFe_2O_4$ the Co^{2+} and Fe^{3+} cations are located only on tetrahedral and octahedral sites, respectively, as in the normal spinel structure of $CoFe_2O_4$, there is still an $A - B$ superexchange interaction between the cations on the different lattice sites, with the only difference being that their magnetic moments now no longer fully compensate due to the smaller magnetic moment of Co^{2+}. This leads to a significantly enhanced macroscopic bulk magnetization of $7\,\mu_\mathrm{B}$/f.u. [171] for $CoFe_2O_4$ with normal spinel structure [cf. Fig. 3.5 (d)] .

3.2.6 Antiphase boundaries - APB

The growth of a film on a substrate with a lattice constant approximately half the lattice constant of the film, which is the case, for example, for Fe_3O_4 or $CoFe_2O_4$ on MgO(001), can lead to the emergence of so-called antiphase domains (APDs) in the film due to the symmetry breaking between film and substrate [177]. Hereby, two neighboring APDs are separated by an antiphase boundary (APB). These two-dimensional structural defects occur when, e.g., the film orders concurrently at several different nucleation sites during film growth. As these differently arranged islands grow in size, they eventually collide and coalesce. In this event, if adjacent islands do not merge perfectly into one another with respect to their respective lattices, i.e., they are shifted against each other

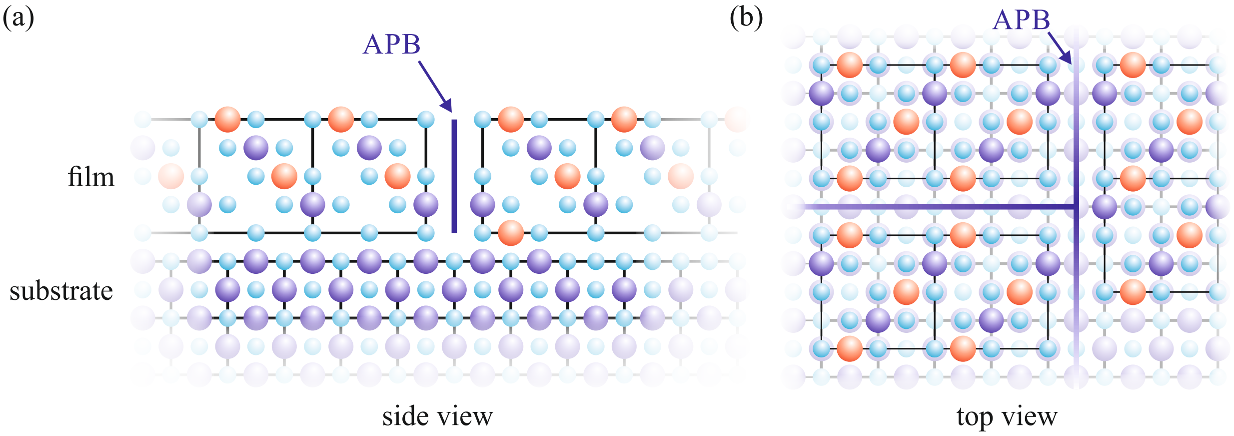

Fig. 3.6: Antiphase boundary (APB) in an ultrathin (inverse spinel-like) film formed during its growth on a (rock-salt-like) substrate, which has a lattice constant half that of the film. (a) Side view. (b) Top view. The colliding antiphase domains are displaced from each other by a translation (vector) of 1/2 [100].

by a non-integer translation (vector) and, thus, the periodicity of the film lattice is not preserved, the islands remain independently as APDs separated by an APB.

For films showing a high density of APBs, these APBs can have a crucial influence on their magnetic [178–182], electric [183–185], and magnetoresistive properties [186, 187], which in particular can lead to a variety of anomalous physical properties of the films. For instance, in inverse spinel ferrimagnetic transition metal ferrites, two neighboring APDs can couple either antiferromagnetically or ferromagnetically across their common APB depending on the direction from which the two APDs impinge on each other and the distance between them [188]. This coupling, in turn, then strongly affects the magnetic behavior of the films and can, among other things, cause the corresponding films to be much more difficult to saturate magnetically [179] and to exhibit lower saturation magnetization [178, 182, 189] compared to ideal bulk samples. Furthermore, APBs are also suspected to play an essential part in the strain relaxation behavior of ultrathin ferrite films as APBs may alter the elastic material properties and lead to an anisotropic stress accommodation [190, 191].

In order to reduce a possibly unwanted effect of APBs on the film properties, it is necessary to minimize the density of APBs in the film, which can be achieved, for example, by the proper choice of growth parameters such as temperature or oxygen flux prior to film deposition [192]. In addition, post-deposition annealing of the produced films even at moderate temperatures and a larger film thickness also ensure a lower APB density [192, 193].

4 Experimental setups

The experimental setups for the various experimental techniques used are presented in this chapter, including a brief description of sample preparation and synchrotron radiation generation. Among the experimental methods, the setups of the *in situ* surface characterization techniques (LEED and XPS) are introduced first, followed by the setups of the synchrotron radiation-based characterization techniques, such as (GI)XRD and XRR, (AR-)HAXPES, XAS and XMCD, the practical aspects of the spatial direct imaging techniques (AFM and HRTEM), and finally the setup used for magnetic sample characterization (SQUID).

4.1 Sample preparation

The majority of the films that have been analyzed in the course of this work have been prepared in an interconnected multi-component UHV system at the Osnabrück University (Germany). The UHV system consists in total of four individual UHV chambers separated by manual gate valves. Each chamber is accessible by manipulator transfer arms to transfer samples between the different chambers without breaking the UHV conditions. The samples are inserted via a load lock into the UHV system from, where they can be then transferred to the preparation chamber for substrate cleaning. Similarly, the load lock can also be used for sample removal from the UHV system. The preparation chamber with a base pressure of around 1×10^{-8}mbar is equipped with a rotary sample stage and an O_2 leak valve. A thermocouple and a heating element are attached to the sample stage, which can be used to anneal the samples up to 450 °C by passing a current through a filament placed directly behind the sample holder. The thermocouple is used to control the temperature during heating. For substrate annealing at even higher temperatures ($T \gtrapprox 600\,^{\circ}\mathrm{C}$), additionally, a high voltage can be applied between the filament and the sample. The preparation chamber is connected to a deposition chamber and an analysis chamber with base pressures of about 1×10^{-9}mbar and 1×10^{-10}mbar, respectively. The deposition chamber is equipped with a rotary manipulator, a heating element, a thermocouple, as well as an O_2 leak valve, and several thermal evaporation sources that enable the deposition of thin films in a diluted O_2 atmosphere. The analysis chamber contains an XPS system and a LEED system for immediate *in situ* surface characterization of previously prepared substrates and films. A more detailed description of both systems is given in Sec. 4.2.1 and Sec. 4.2.2.

As mentioned above (cf. Sec. 2.2), all oxide films used and investigated within this work have been fabricated by reactive molecular beam epitaxy (RMBE) via the thermal evaporation of transition metals (Co and/or Fe) from pure metal rods in a diluted molecular oxygen atmosphere[1]. For this purpose, electrons emitted from a filament are accelerated toward the metal rod using a high voltage applied between the filament and the metal rod, leading to the emission of atoms or molecules from the metal rod as soon as the sublimation temperature is reached (cf. Fig. 4.1). Together, the emitted particles depart from the evaporator shaped as a molecular beam toward the sample, on whose surface they eventually condense, react with oxygen, and form an oxide film. Hereby, a

---

[1] If the evaporation process is carried out without the supply of extra oxygen, this film deposition method is called just molecular beam epitaxy (MBE), otherwise reactive molecular beam epitaxy (RMBE) if the evaporation process takes place in a diluted oxygen atmosphere.

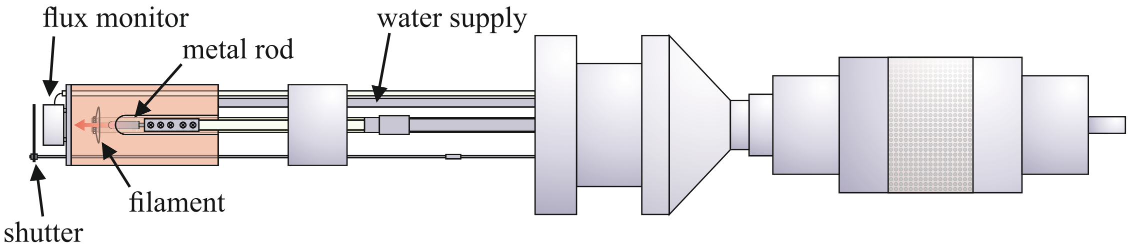

Fig. 4.1: Illustration of the used evaporator for film deposition. The different electrical connections on the evaporator exterior and the water connection have been omitted due to reasons of clarity. Electrons emitted from a filament are accelerated onto a metal rod, which begins to sublimate when its sublimation temperature is reached. The shutter at the evaporator opening determines the start and end of film growth while the flux meter controls the evaporation rate of the evaporating material.

shutter located at the evaporator aperture determines the timing of the onset and end of film growth. The material deposition rate is controlled by a flux monitor, which has been individually calibrated beforehand for each composition based on an *ex situ* film thickness XRR measurement of a previously produced film containing the same transition metal element that is being evaporated. In order to avoid overheating of the evaporator during operation as well as to minimize its degassing, the evaporator is continuously water-cooled. Furthermore, when preparing ferrite films that consist of more than one transition metal element, such as in CFO, the respective transition metals (Co and Fe in the case of CFO) are simultaneously evaporated and directed onto the sample surface. The desired stoichiometry of the ferrite film is achieved by adjusting the deposition rates of the respective evaporators with respect to each other.

All MgO(001) and 0.05 wt% Nb-doped $SrTiO_3$(001) substrates used as film support materials were supplied either by CrysTec GmbH or SurfaceNet GmbH with a surface orientation tolerance of $< 0.1°$ guaranteed by the manufacturers. After insertion into the UHV system and prior to film deposition, the substrates were first annealed in the preparation chamber for 1 h at 400 °C in a diluted O_2 atmosphere of 1×10^{-4}mbar to remove unwanted adsorbates such as carbon from the surfaces as well as to obtain well-defined substrate surfaces. The chemical purity and high crystallinity of the crystal surface structures were confirmed for each substrate by subsequent *in situ* XPS and LEED measurements in the analysis chamber, revealing no elemental quantities other than those expected, as well as LEED patterns with sharp diffraction spots and an overall low background intensity. Afterward, the substrates were transferred to the deposition chamber for film deposition. In the case of the Fe_3O_4 and cobalt ferrite films, a substrate deposition temperature of 250 °C and a molecular oxygen pressure of 5×10^{-6}mbar has been used, which has been demonstrated to ensure well-ordering and high film crystallinity for epitaxially grown Fe_3O_4 films on MgO(001) by RMBE [194]. The CoO films were deposited also at a substrate temperature of 250 °C but in a molecular oxygen pressure of 1×10^{-5}mbar instead, which ensures epitaxial growth of high crystalline quality in the case of CoO [195]. The resulting film stoichiometry and film surface structure of each film produced were examined immediately after film growth by *in situ* XPS and LEED measurements.

4.2 Surface characterization

4.2.1 XPS - Experimental setup

The XPS system (cf. Fig. 4.2) used for the sample preparation comprises basically an X-ray source, which generates either Al K_α ($h\nu = 1486.6\,\mathrm{eV}$) or Mg K_α ($h\nu = 1253.6\,\mathrm{eV}$) radiation, electron optics, a hemispherical analyzer (Phoibos HSA 150, SPECS, Germany, Berlin), and an energy-dispersive electron detector. The angle between X-ray source and entrance of the electron optics is fixed at 54.7° in this experimental setup. Hence, only photoelectrons that escaped the sample in direction of the electron optics are collected and can potentially be further analyzed. Inside the electron optics, the photoelectrons are collimated and focused onto the entrance of the hemispherical analyzer by a combination of different electron lenses and apertures. In addition, these lenses and apertures reduce the kinetic energy of the photoelectrons on their way to the analyzer. An electrostatic field in the interior of the hemispherical analyzer forces the photoelectrons onto curved trajectories, which are determined by the kinetic energy of the entering photoelectrons as well as by the applied electrostatic field of the analyzer. Therefore, only those photoelectrons are able to pass through the analyzer and subsequently arrive at the detector whose kinetic energy matches the specific pass energy E_{pass} of the hemispherical analyzer. An XP spectrum is recorded by, e.g., keeping the electrostatic field in the analyzer constant throughout the entire XPS operation (constantly fixed pass energy E_{pass}) while the electron optics progressively varies the (kinetic) energy of the photoelectrons by appropriately altering the retarding potential within. As a result, all photoelectrons with initially different kinetic energies are gradually decelerated to the kinetic energy that lies within the energy window accepted by the analyzer (around E_{pass}). This operation mode is called fixed analyzer transmission (FAT) and was utilized in all XPS measurements performed in this work. The FAT mode offers the advantage that, due to the fixed pass energy of the analyzer, the energy resolution is also constant for the entire XP spectrum regardless of the kinetic energy of the photoelectrons. An increase of the pass energy also increases the absolute XPS intensity, resulting in a significantly improved signal-to-noise ratio. However, a higher pass energy comes with the downside of a reduced energy resolution. Both aspects must be taken into account for each scan and individually weighed against each other when setting the pass energy.

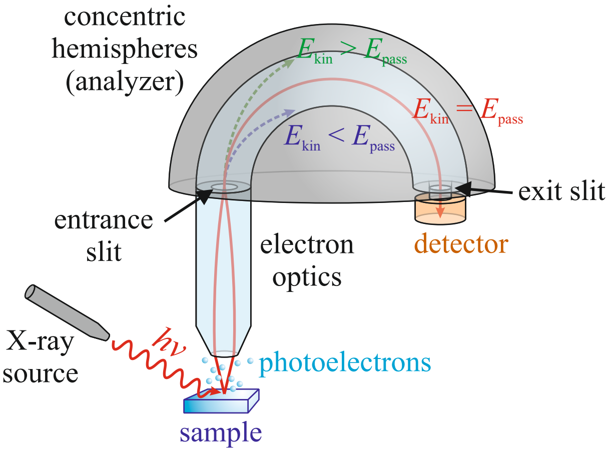

Fig. 4.2: Illustration of the XPS setup used including the main parts such as an X-ray source, electron optics, a hemispherical analyzer, and a detector. The photoelectrons that left the sample in consequence of photoemission first pass the electron optics, where they are retarded as well as focused onto the entrance of the hemispherical analyzer. Due to an electrostatic field inside the hemispherical analyzer, the photoelectrons entering the analyzer are forced on curved paths. Only those photoelectrons whose kinetic energies E_{kin} match the pass energy E_{pass} of the hemispherical analyzer can reach the detector located at the end of the analyzer.

4.2.2 LEED - Experimental setup

The experimentally used LEED setup is a 4-grid LEED optics (ErLEED 150, SPECS, Germany, Berlin). It is composed of an electron gun and a hemispherical fluorescent screen with a series of grids in front of it, which are arranged concentrically with the fluorescent screen around a common center, where the sample surface is placed (cf. Fig. 4.3). The electron gun, which consists of a cathode (filament), a Wehnelt cylinder, an anode, and an electrostatic lens system, generates a focused electron beam with adjustable energy and accelerates it onto a sample surface. The electrons backscattered from the sample surface are then detected by the fluorescent screen, whereby they first have to pass through the multigrid system. The first grid of the multigrid system is used to prevent possible deflections of the electrons from their ideal trajectories, which would result in a distorted diffraction pattern. This is accomplished by grounding the first grid and the sample to a common potential (ground potential), creating a field-free space between them. The second and third grids serve to sort out inelastically scattered electrons by applying a negative voltage to both grids that is slightly smaller than the voltage used to accelerate the electrons onto the sample surface. With this, only elastically scattered electrons (as well as electrons with only marginal energy losses) have sufficient kinetic energy to reach the fluorescent screen and contribute to a diffraction pattern, reducing the diffuse background. The last and fourth grid is grounded to earth potential as well and screens the other grids in front of it from the field caused by applying a (positive) high voltage of typically 6 kV to the fluorescent screen in order to trigger fluorescence. The LEED pattern, appearing on the fluorescent screen, is then recorded using a camera at the rear side of the LEED setup (behind screen system and electron gun).

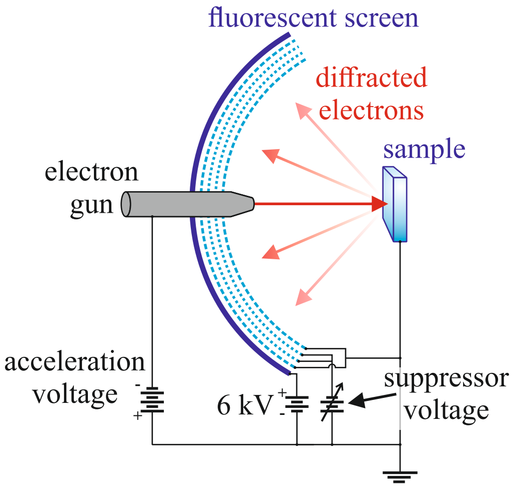

Fig. 4.3: Schematic of a 4-grid LEED optics, including an electron gun, a hemispherical fluorescent screen and a series of grids in front of the fluorescent screen. The electron gun generates a focused electron beam and accelerates it onto the sample surface located at the center of the hemispherical fluorescent screen, giving rise to elastically and inelastically scattered electrons. While the latter are repelled from the grid array, only elastically scattered electrons can pass through the array and are subsequently further accelerated onto the fluorescent screen, where they produce the diffraction pattern of the crystalline sample surface. Adapted from Ref. [29].

4.3 Experimental setups at synchrotron radiation facilities

The use of synchrotron radiation generated by large-scale synchrotron radiation facilities opens up new possibilities for the characterization of (ultra)thin films compared to conventional laboratory-based X-ray sources due to its unique beam characteristics such as extremely high beam intensity, low divergence, small beam size, as well as the capability to (almost) continuously tune the photon energy of the X-rays within experimental limits. The qualities of these superior X-ray sources not only provide the necessary sensitivity for non-bulk structures, permitting even the weak signals of (ultra)thin films to be detected, but also the opportunity to investigate, e.g., the elemental absorption edges of a material with highest precision or to supply the excitation energy required in the case of HAXPES experiments. As a result, a large number of film characterization techniques applied in this work were performed at several different synchrotron radiation facilities. Here, the methods of (GI)XRD and XRR were carried out at the European Synchrotron Radiation Facility (ESRF) in Grenoble (France) and at the Diamond Light Source (DLS) at the Harwell Science and Innovation Campus near Didcot (UK) using the beamline BM25-SpLine and I07, respectively. The (AR-)HAXPES experiments were also conducted at beamline BM25-SpLine of ESRF, as well as at beamlines P09 and P22 at the Deutsches Elektronensynchrotron (DESY) in Hamburg (Germany), and at 7-ID of the National Synchrotron Light Source II (NSLS-II) at Brookhaven National Laboratory in Brookhaven (USA). The XAS, and XMCD measurements were performed at the Advanced Light Source (ALS) at Lawrence Berkeley National Laboratory in Berkeley (USA) using beamline 4.0.2.

Furthermore, many beamlines offer the possibility to also use standard laboratory-based experimental techniques such as (soft) XPS and LEED in addition to the main research methods for a more comprehensive sample characterization. However, since their experimental setups and instrumentation do not differ significantly from the ones already presented in Sec. 4.2.1 and Sec. 4.2.2, they are not addressed separately here.

4.3.1 Generation of synchrotron radiation

In synchrotron radiation facilities, charged particles (mainly electrons) are accelerated to nearly the speed of light and then fed into a so-called storage ring, where they continue to circulate at a constant speed. Although the storage ring is referred to as a ring and therefore associates a perfect circular structure, its geometric structure is more like a polygon with alternating curved and straight segments. At these curved segments, bending magnets are used to bend the trajectory of the particles, keeping them in the closed orbit of the storage ring. However, due to the forced circular trajectory of the charged particles on the curved segments, the particles experience a constant acceleration toward the center of the circular arc caused by the Lorentz force. Thus, as long as the charged particles follow a curved path, they continuously emit electromagnetic radiation (synchrotron radiation) tangential to their direction of motion, which is collimated into a narrow cone of radiation [cf. Fig. 4.4 (a)].

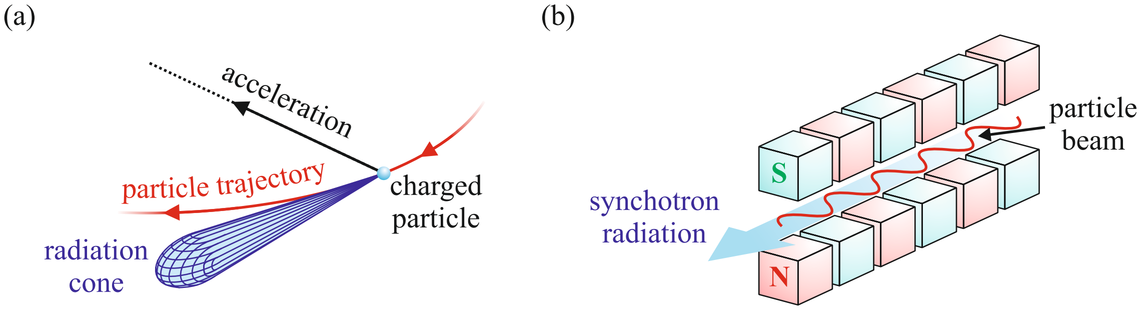

Fig. 4.4: (a) Schematic representation of (synchrotron) radiation produced by the circular motion of a charged particle, traveling near the speed of light. (b) Illustration of a typical insertion device. Due to the alternating magnetic field directions between adjacent magnets, charged particles are forced onto oscillating paths as they pass through the insertion device, leading to the emission of (synchrotron) radiation. Adapted from Ref. [120].

In the straight sections of the storage ring (between two adjacent bending magnets), synchrotron radiation is instead generated by means of insertion devices like undulators or wigglers [cf. Fig. 4.4 (b)]. An insertion device usually consists of several magnets connected in series, where each magnet generates a magnetic field that is equal in size but opposite in direction to the magnetic field of the neighboring magnets. The alternation of magnetic fields forces the charged particles onto oscillating trajectories instead of a straight line [45]. As in the case of bending magnets, these deflections in the movement of the particles cause them to radiate electromagnetic waves. Here, the electromagnetic waves radiated in similar directions in the orbit plane of the particles superimpose. For undulators, this superposition of the individual electromagnetic waves is coherent, which causes constructive interference and thus synchrotron radiation with significantly enhanced intensity. With wigglers, on the other hand, the individual electromagnetic waves only add up independently of each other (incoherent superposition) due to a larger angular deviation of the particles. This leads to synchrotron radiation that has a significantly lower brilliance compared to the synchrotron radiation of undulators but is still very high compared to the synchrotron radiation of bending magnets.

At each section of the storage ring, where synchrotron radiation has been generated either by bending magnets or insertion devices, there is a beamline aligned along the propagation direction of the radiation. In these, the required beam characteristics of the generated synchrotron radiation are first adjusted and optimized by various beamline optics before the radiation is then later used for the upcoming experiments carried out in the corresponding endstations of the respective beamline.

4.3.2 (GI)XRD and XRR - Experimental setup

For the X-ray diffraction and X-ray reflectivity measurements, the respective EH2 (EH: experimental hutch) endstation of beamlines BM25-SpLine (ESRF) and I07 (DLS) was used. Both EH2 endstations house a UHV chamber for *in situ* experiments under UHV conditions and a large (2S+3D) diffractometer in vertical geometry for sample and detector positioning to obtain a certain scattering/diffraction condition. For this type of diffractometer [cf. Fig. 4.5 (a)], the angles α and ω define the sample incidence angle and sample azimuth, respectively[2]. The detector, whose rotations are decoupled from the sample rotations, can be moved about the angles γ and δ, where the angle γ enables the horizontal detector rotation and the angle δ enables the vertical detector rotation. In front of the detector, along the detector-sample axis, there are a set of slits mounted on another rotation stage, providing the last rotational degree of freedom of the diffractometer, specified by the angle ν. Additionally, the EH2 endstation at the BM25-SpLine beamline includes also an electron analyzer for the simultaneous combination of X-ray diffraction and HAXPES experiments (cf. Sec. 4.3.4), allowing the atomic structure of a sample under investigation to be correlated with its chemical and electronic properties under equivalent experimental conditions and for the same sample region.

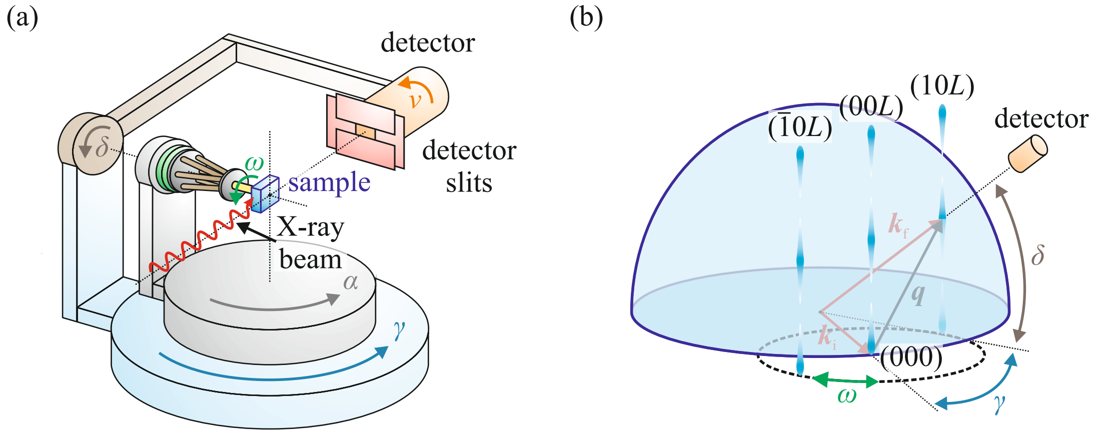

Fig. 4.5: (a) Illustration of a typical (2S+3D) diffractometer in vertical geometry, which was employed at beamlines BM25-SpLine (ESRF) and I07 (DLS) for (GI)XRD and XRR experiments. (b) Schematics of the relationship between the Ewald sphere, the reciprocal lattice and the motors of the diffractometer for performing GIXRD measurements. Due to the variation of the angles ω, γ, and δ, diffraction rods (blue) other than the (00L) CTR can be measured. Diffraction conditions are fulfilled when the Ewald sphere intersects with a CTR. Adapted from Ref. [196].

X-ray scattering experiments can be performed in many different measurement geometries. For the results obtained in this work, only the specular geometry and the grazing incidence geometry were used. In specular measurement geometry, which is utilized for both specular X-ray diffraction and XRR measurements, the angles ω, δ, and ν are kept fixed at 0° and the incident angle $\alpha = \theta$ is gradually increased. Concurrently, the detector is rotated by twice that angle ($\gamma = 2\theta$) with

---

[2] Please note that the angle designation for the individual rotations of a diffractometer may differ from beamline to beamline.

respect to the incident X-ray beam to fullfill the diffraction condition. Since only the incidence angle and the detector position are changed by the corresponding angles during the measurement, this measurement geometry is also known as $\theta - 2\theta$ geometry. Thus, in this specular setup, the incident and scattered wave vectors as well as the resulting scattering vectors exclusively lie in out-of-plane direction of the sample and lack any lateral components ($H = K = 0$). As a result, only the intensity distribution along the specular ($00L$) CTR is obtained by means of the specular geometry.

In contrast, the grazing incidence geometry is used when performing so-called grazing incidence X-ray diffraction (GIXRD) measurements, in which the incidence angle is fixed during the measurement to a relatively small angle slightly above the sample's critical angle (typical $< 0.5°$). Since the penetration depth of the X-rays is severely limited at these grazing angles, this measurement geometry provides enhanced surface sensitivity, such that a film grown on a substrate has a higher contribution to the overall scattered signal. The diffraction condition is satisfied in this measurement geometry by rotating the sample by the angle ω about its surface normal and adjusting the detector accordingly using the angles γ and δ [cf. Fig. 4.5 (b)]. Consequently, with this measuring geometry, non-specular diffraction rods can be probed as well as lateral measurements, so-called 'in-plane' scans, along the H or K directions of the reciprocal space, are possible as the scattering vector is no longer limited to vertical components only.

4.3.3 Processing and analysis of (GI)XRD and XRR data

All X-ray scattering experiments were performed using a two-dimensional area detector, where each detector image of a single scan corresponds to a small segment of the reciprocal space. The intensity distribution along that scan, e.g., along the L direction of a CTR, can be obtained by numerically integrating the pixel intensities within a predefined (rectangular) region of interest (ROI) for each detector image. As an example, in the case of (GI)XRD scans, the size and position of the ROI are set to encapsulate the entire intersection of the detector with the CTR (or with the Bragg reflection) for each detector image of the scan. Furthermore, a background is subtracted from the extracted intensity distribution in order to obtain the actual intensity distribution of the CTR. The background is determined in the same manner as the intensity distribution of a CTR but in a region of the detector images that is free of any scattered signal.

For the further analysis of (GI)XRD data, a version of the specially developed fitting program 'RodsNPlots' was employed. This program, first developed by A. Greuling [197] and later on extended by the works of S. Hahne [198] and F. Bertram [199], is able to calculate a theoretical intensity curve along a given CTR (specular or non-specular) using kinematic diffraction theory [cf. Eq. (2.84)] and on the basis of a preimplemented structural model. Furthermore it is capable of fitting this calculated intensity curve by varying the structural parameters within the model in such a way that it reproduces the experimentally obtained intensity curve as accurately as possible. The structural model consists of a variable number of crystalline layers stacked on top of a given substrate. The substrate as well as each layer has a set of structural parameters that define them. These include among others the type of material (sets the structure factor and the vertical layer distance), the number of unit cells in the vertical direction, the scaling factor of the vertical lattice vector as well as the interface vector (vertical component only), the top and bottom RMS roughnesses and the Debye-Waller factor. The single structure parameters can each be fixed to specific values or left variable during the fitting procedure of the program to find a final structural model that best describes the experimental data. For a more detailed description of the program 'RodsNPlots' and available structural parameters, see Ref. [120].

The deeper analysis of XRR data is instead performed using the fitting program 'iXRR' in-house developed by F. Bertram [129]. This software allows the reflected intensity for an expected layer system to be calculated theoretically based on the Parratt formalism and the Névot-Croce roughness model (cf. Sec. 2.8), which is then fitted to the experimentally measured XRR data. As in the 'RodsNPlots' fitting program, each layer of the layer system, including the substrate, is characterized by its own parameters such as refractive index (dispersion and absorption), layer thickness, and interface roughness, all of which can be either fixed or used as free fitting parameters for the fitting procedure. More detailed information of the applied fitting program 'iXRR' can be found in Ref. [129].

4.3.4 (AR-)HAXPES - Experimental setup

The results of the (AR-)HAXPES experiments presented in this thesis were recorded at several beamlines and synchrotron radiation facilities. Still, the principle experimental (AR-)HAXPES setups at the different beamlines differ only slightly from each other. A UHV chamber, a multi-axis manipulator to align the samples to the incident X-ray beam, and an electrostatic analyzer with an attached high-resolution photoelectron detector are the most essential elements of the experimental setup, which is used in similar ways at all beamlines. At beamlines P09 (DESY), P22 (DESY), and 7-ID (NSLS-II), a concentric hemispherical analyzer (CHA) is employed, whereas at BM25-SpLine (ESRF) the electrostatic analyzer is a cylinder sector analyzer (CSA) due to its compact geometry, allowing a simultaneous combination of photoemission and diffraction experiments without the instruments interfering with each other.

In principle, HAXPES experiments are performed in order to retrieve information from deeper sample regions or from buried structures. The more bulk-like sensitivity of HAXPES compared to conventional XPS measurements with soft X-rays is achieved by using higher X-ray photon energies, which drastically increase the probing depth due to a higher IMFP of photoelectrons. Hence, at the beamlines P09 (DESY), P22 (DESY), and 7-ID (NSLS-II), X-ray photon energies of $\sim 6\,\mathrm{keV}$ have been used, providing IMFPs of 5 nm–8 nm and thus information depths of 15 nm–24 nm (at normal detection). At the BM25-SpLine beamline (ESRF) an even higher excitation energy of $\sim 16\,\mathrm{keV}$ was used due to the simultaneous realization of HAXPES and GIXRD experiments (IMFPs of 11 nm–19 nm and IDs of 33 nm–57 nm). In addition, the information depth is also decisively determined by the photoelectron emission angle φ relative to the surface normal of the sample [cf. Eq. (2.33)]. Photoelectron detection is essentially restricted to those photoelectrons that propagate in the direction of the analyzer. Therefore, an emission angle at which photoelectrons are detected of $\varphi \rightarrow 0°$ provides the highest possible information depth and thus the maximum bulk-like sensitivity in the spectrum. As the detector is fixed in the measurement geometry and thus offers no rotational possibilities around the sample position, the detection angle can only be changed by tilting the sample. Given the experimental circumstances, a sample angle must therefore be chosen for which the detection angle becomes minimal to achieve the highest ID/bulk sensitivity (it is not always possible to realize a detection angle $\varphi = 0$).

The AR-HAXPES experiments were carried out exclusively at the beamlines P09 and P22 (DESY) with the same excitation energy as for the HAXPES experiments. In contrast to HAXPES, the photoelectron detection angle is varied by tilting the sample away from the analyzer for each single measurement (cf. Fig. 4.6) to attain the depth sensitivity of photoemission spectra. As the detection angle increases, the bulk sensitivity steadily decreases due to the decreasing information depth. Photoelectrons released in deeper sample regions, which would provide more information about the electronic structure of the sample under normal photoelectron emission, must travel a considerably longer distance within the sample to the analyzer. Therefore, these photoelectrons cannot reach the analyzer and be detected because their propagation distance exceeds the finite ID. Thus, progressively fewer photoelectrons from deeper sample regions contribute to the total photoemission spectra for increasing detection angles, achieving a steadily higher surface-like sensitivity.

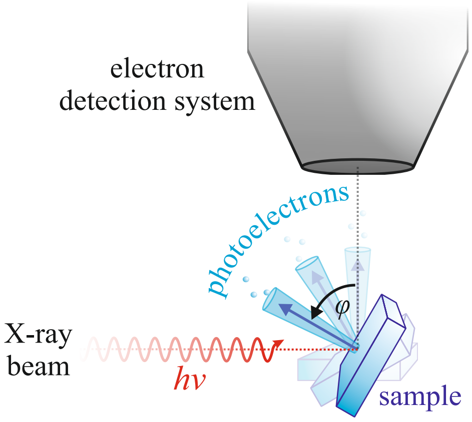

Fig. 4.6: Principle sketch of an AR-HAXPES experiment. Between single measurements, the sample is rotated away from the analyzer to steadily enhance the surface sensitivity and, therefore, to obtain a depth profile of the sample. The sample rotation leads to an increased angle φ between the surface normal of the sample and the analyzer (black arrow). Due to the increased distance to the surface in direction of the analyzer for photoelectrons released in deeper layers as well as the limiting IMFP, only photoelectrons from regions near the sample surface are able to be detected at larger angles φ. Blue cones indicate the photoelectrons originating from the maximum probing depth, which can be detected only at a normal detection angle.

4.3.5 XAS and XMCD - Experimental setup and data analysis

The experimental setup for the XAS/XMCD experiments performed at beamline 4.0.2 (ALS) is illustrated in Fig. 4.7 and comprises in total three main parts: a UHV chamber, a rotatable sample stage, and an external superconducting vector magnet to magnetize the sample (in-plane) with a magnetic field of up to 4 T. The samples are mounted on the sample stage and contacted with a conducting wire at an edge of the sample surface using silver paste for measurements in surface-sensitive TEY mode (cf. Sec. 2.5.2). The XAS/XMCD measurements were performed for all samples with a glancing incidence angle of the circularly polarized X-rays of 30° relative to the sample surfaces to avoid possible blocking of the X-ray beam by other instruments. In addition, for each measurement, two XA spectra were recorded, with the magnetic field direction changed between each XA spectrum ($\boldsymbol{M} \rightarrow -\boldsymbol{M}$). The latter has the same effect on the X-ray absorption signal as changing the helicities of the X-ray beam with the result that the same dichroic spectrum can be obtained from the difference of two XA spectra recorded with reversed magnetic field directions.

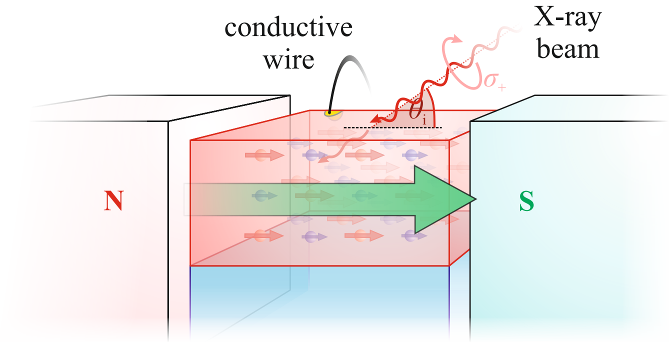

Fig. 4.7: Schematics of the experimental setup for XAS/XMCD experiments. The sample is placed in the center of a magnetic field (green arrow) and illuminated by an X-ray beam with a certain helicity (σ_+) at an angle θ_i relative to the sample surface. The resulting XAS signal is measured by a conductive wire contacted to the sample surface. Adapted from Ref. [67].

The quantitative analysis of XA and XMCD spectra is commonly performed applying both sum rules and charge-transfer multiplet calculations (cf. Sec. 2.5.4 and Sec. 2.5.5). Thus, for the quantitative evaluation of the recorded XA and XMCD spectra of the Co ferrite films prepared within this work, the graphical user interface 'Ferridor Magnetowitsch Dostöchjewskij (FMD)' developed by T. Pohlmann [67] was used, which has both analysis methods implemented. The graphical user interface 'FMD' is based on the software 'CTM4XAS' developed by F. de Groot [200, 201] and utilizes the Cowan code by T. Thole [202] to calculate (atomic) multiplet spectra for the divalent and trivalent transition metal cation species of Fe, Co, and Ni, taking into account crystal field and charge-transfer effects. The advantage of using 'FMD' over 'CTM4XAS' is that it provides a better comparison of charge-transfer multiplet calculations with experimental data, as well as a 'on-the-fly' and convenient application of the sum rules. The charge-transfer multiplet calculations for each cation species are carried out using a set of different multiplet parameters characteristic for the respective cation type, such as charge-transfer energies of the ground and final states, crystal field splitting ($10Dq$), and exchange splitting. The respective cationic contributions at a given absorption edge are then added in a weighted manner to obtain overall XAS and XMCD simulations, which are simultaneously compared to the corresponding experimental XAS and XMCD data. A more detailed description of 'FMD', including additional parameters like broadening parameters and more extensive details on each multiplet parameter, can be found in Ref. [67].

4.4 AFM - Experimental setup

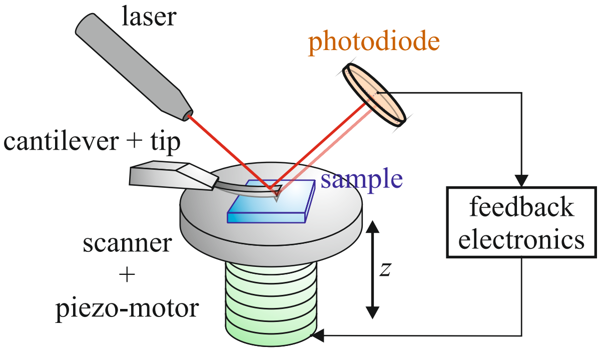

Fig. 4.8: Typical basic setup for the operation of an AFM, including the main components. The surface of a sample is imaged by a tip attached to a cantilever. For this purpose, the deflection of the cantilever caused by the various forces acting on the tip is continuously monitored using a laser and a split photodiode while the sample is moved laterally. The signal from the photodiode is further coupled to feedback electronics that set and control the height of the sample for measurements in constant force mode according to a given deflection of the cantilever by means of a piezo-motor.

The determination of the surface topography of the films, including their surface roughness, was achieved by AFM (NT-MDT NTEGRA) measurements employing the constant force measurement method in contact mode (cf. Sec. 2.9.1). The AFM setup includes a scanner, a measuring head with a cantilever and a tip attached, and an optical cantilever deflection detection system. The scanner holds the sample to be measured and can be moved both vertically (using moving screws and a piezo-motor for more precise movements) and laterally (using moving screws) to set the distance between the tip and the sample surface as well as to specify the measured area. The deflection of the cantilever due to the various types of forces acting on the tip and exerted by the surface is monitored by the optical cantilever deflection detection system (cf. Fig. 4.8). The optical detection system comprises a laser diode with its laser beam focused on the end of the cantilever backside, and a split photodiode, which subsequently detects the reflected beam. Prior to an initial AFM measurement, the center of the photodiode is aligned with the reflected beam. Smallest local changes in the strength of the probing interactions during an AFM measurement lead to changes in the deflection of the cantilever and thus directly affect the position of the reflected beam on the photodiode. Consequently, in order to maintain a constant (total) force during operation, i.e., a constant deflection of the cantilever, as in the conducted constant-force mode measurements, the system must counteract such changes in the probing interactions that lead to a change of the reflected beam on the photodiode as soon as they occur. This is realized by coupling the signal from the photodiode to a feedback control system that reacts immediately when the reflected beam position begins to change and adjusts the tip-to-surface distance accordingly to ensure that the reflected beam maintains the central position on the photodiode.

4.5 HRTEM - Sample preparation

The basic experimental setup of the conducted HRTEM experiments is already presented and discussed in Sec. 2.9.2. Hence, this part has its focus rather on the non-trivial sample preparation necessary for cross-sectional HRTEM examination of (ultra)thin films. Due to the strong interaction of electrons with matter, samples to be analyzed must be thinned to electron transparency. A variety of techniques can be used for (HR)TEM sample preparation [48], some of which are more suitable than others for certain types of structures and materials (bulk or thin film, ductile or brittle, soft or hard, etc). Also important is which part (top view or cross-section) of the sample is being examined, so a distinction can be made here as well. Within this work, a conventional so-called cross-section preparation [48, 203], as illustrated in Fig. 4.9, was used for the subsequent cross-sectional HRTEM experiments. By means of these experiments, structural information about interfaces, structural defects and composition gradients of the analyzed sample can be extracted, which make them extremely useful for studying the growth of (ultra)thin films on a given substrate.

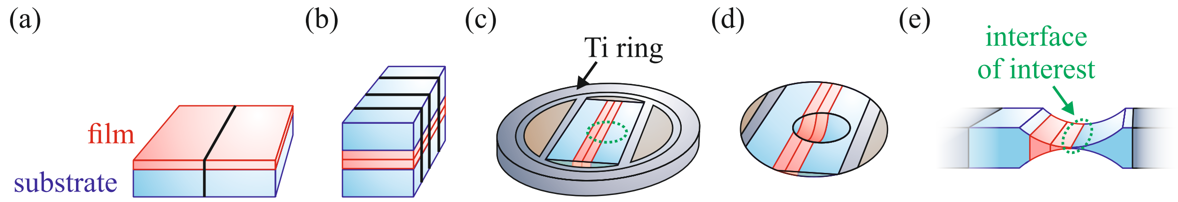

Fig. 4.9: Illustration of the different steps of the cross-section preparation necessary for cross-sectional HRTEM experiments. (a) The sample is cut into slices and then glued with their faces on top of each other. (b) The resulting 'sandwich' is cut into multiple sample pieces and (c) embedded in a Ti ring in such a way that the interface of interest of each sample piece is in line with the others. (d) The top and bottom of the specimen are each thinned by means of dimple-grinding and ion-milling until electron transparency is achieved. (e) Final cross-sectional view of the interface between a substrate and a film after the thinning process. Adapted from Ref. [133].

The first steps of this preparation techniques involve cutting the whole sample into thin sample slices and gluing the bulk slices with their faces together (film on film). Thereafter, the 'sandwich' is cut once again into several pieces and embedded with adhesive into a ring of Ti, with the interface of interest (e.g., between film and substrate) uniformly along a line. Both sample sides are then thinned and dimple-grinded until the sample thickness at the region of interest is only a few µm thick. Finally, to achieve electron transparency at these respective regions, the sample is further thinned to perforation by ion-milling. For some regions near the hole edges, the necessary electron transparency for the HRTEM measurements is obtained.

4.6 SQUID magnetometer - Experimental setup and data processing

The integral magnetic properties of the samples prepared within this work were analyzed by a SQUID magnetometer (MPMS3, Quantum Design, Darmstadt, Germany), exhibiting a sensitivity of $\leq 10^{-8}$emu (emu: electromagnetic units). The major elements of the used magnetometer are a cryogen dewar filled with liquid-helium and a cryogenic insert (probe) with a superconducting niobium-titanium (NbTi) solenoid on the outside. The latter provides the external magnetic field of up to 7 T for the experiments. Inside the probe are a sample chamber at the level of the solenoid, a heater, and a SQUID detection circuit, consisting of a dc SQUID and a set of superconducting detection coils (or pick-up coils) inductively coupled to the SQUID via one or a series of matching superconducting input coils, referred to as a flux transformer (cf. Fig. 4.10). The detection coils surrounding the sample chamber are used to detect and transmit any magnetic flux changes within, resulting, for example, from the motion of a magnetic sample. They are designed as a second-order gradiometer with counterclockwise-wound outer loops and a clockwise-wound inner loop pair to reliably suppress signals of any external disturbances. In addition, the dc SQUID is magnetically shielded to prevent the generation of noise originating from magnetic sources such as the environment or the magnetic flux of the solenoid. In order to provide the necessary cooling for the several superconducting parts inside and outside the cryogenic insert, as well as for cooling of samples for low-temperature measurements down to 1.8 K, the insert is immersed into the liquid-helium bath of the large dewar.

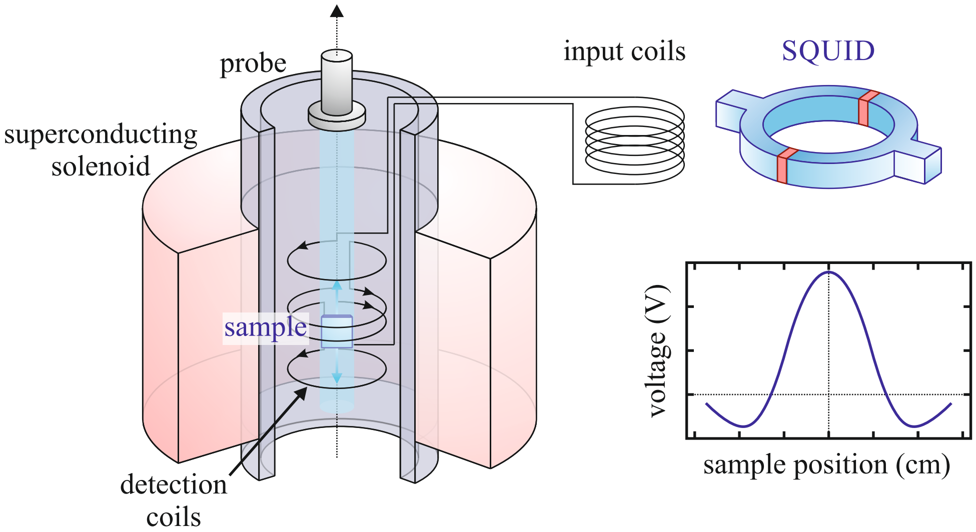

Fig. 4.10: Illustration of a cryogenic insert (probe) with externally attached superconducting solenoid in a typical SQUID magnetometer. For clarity, the sample chamber is omitted and the input coils as well as the dc SQUID are shown outside the insert. The magnetic sample is placed in the center of the magnetic field gernerated by the superconducting magnet. Detection coils surrounding the sample register any local changes in the magnetic flux in its interior caused by the movement of the magnetic sample along the vertical axis. These changes are then transmitted via input coils to a dc SQUID, which converts the signal to an output voltage proportional to the magnetic flux change in dependence of the sample position. Please note that in reality both the input coils and the SQUID are also contained in the insert. Adapted from Ref. [19].

The samples to be measured are first mounted on a quartz sample holder and then placed in the sample chamber of the probe. After the installation of each new sample, the sample is centered within the detection coils to maximize the accuracy of the subsequent magnetic measurements. A SQUID measurement is performed by mechanically moving the sample up and down at a constant speed in the vertical direction through the detection coils and analyzing the SQUID output signal. In this process, the motion of the magnetic sample or rather the magnetic moment of the sample causes a local disturbance of the applied magnetic flux in the detection coils [204], which induces a current proportional to the magnetic flux change in response. This current is further coupled into the input coils, where they generate a magnetic flux that in turn is then coupled into the superconducting loop of the SQUID, producing an output voltage (cf. Sec. 2.4.3) as a function of the sample position. Hence, the magnetic sample under investigation is only indirectly probed by the SQUID in this setup. From the recorded voltage profile, the magnetic moment of the sample can be derived by fitting the measured profile to a response function assuming an ideal point dipole source with constant sign and value as it moves through a second-order gradiometer [205]. By normalizing the inferred magnetic moment to the sample volume, the magnetization of the sample can be determined. However, since a complete voltage profile must be recorded for each magnetic field and/or temperature step, SQUID measurements over a wide measurement range usually take quite a long time.

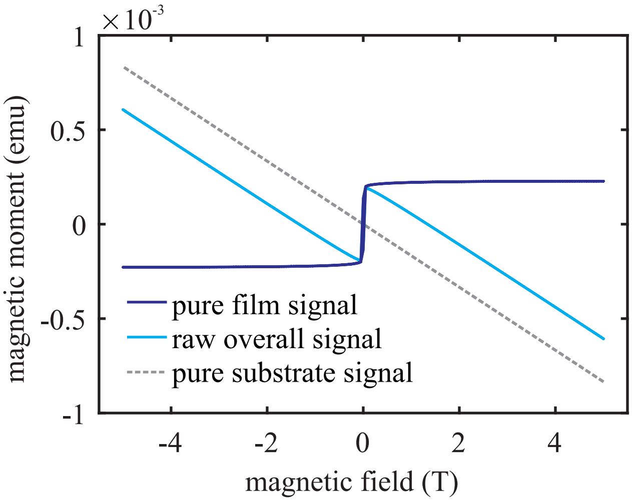

Fig. 4.11: Schematic representation of the individual contributions to a recorded overall SQUID signal, originating from a ferro-/ferrimagnetic film deposited on a diamagnetic substrate. The raw overall SQUID signal, the film contribution, and the substrate contribution are reflected by blue, dark blue, and gray curves, respectively. The pure ferro-/ferrimagnetic film signal is extracted by subtracting a linear slope due to the diamagnetic response of the substrate from the raw overall SQUID signal. The linear slope, in turn, is obtained by fitting the high-field regimes ($> 3\,\mathrm{T}$) of the raw overall SQUID signal.

Special care must be taken when magnetically characterizing one or more (ultra)thin films deposited on a substrate using this measurement technique since it is always the magnetic response of the entire sample that is detected. Consequently, all non-relevant magnetic contributions to the overall signal must be removed in order to extract the magnetic signal of the film of interest. For a single ferro-/ferrimagnetic film grown on a diamagnetic substrate such as MgO or $SrTiO_3$, this is relatively easy to accomplish. Diamagnetic (and paramagnetic) materials show a linear response when exposed to an external magnetic field and hence give a linear background in the overall signal measured by the SQUID magnetometer. By fitting the high-field regime of the raw measurement signal (where the ferro-/ferrimagnetic film indicates magnetic saturation), the linear slope of the diamagnetic contribution of the substrate can be determined and used to subtract a line with this slope from the overall signal to obtain the pure ferro-/ferrimagnetic signal of the film (cf. Fig. 4.11). Please note that this approach is only applicable to heterostructures for extracting the magnetic signal of a specific film where solely the film of interest provides a non-linear contribution to the overall SQUID signal and all other materials of this heterostructures give a linear contribution as indicated above.

Anomalously Strained Fe_3O_4 Thin Films on $SrTiO_3(001)$ Resolved by HRTEM and X-ray Diffraction

J. Thien[1], T. Niermann[2], M. Lehmann[2], J. Bahlmann[1], J. Rodewald[1], and J. Wollschläger[1]

[1]*Department of Physics, Osnabrück University, 49076 Osnabrück, Germany*
[2]*Institute of Optics and Atomic Physics, Technische Universität Berlin, Berlin, Germany*

Abstract

In this work, Fe_3O_4 thin films of different film thicknesses have been prepared by reactive molecular beam epitaxy on $SrTiO_3(001)$ substrates. The stoichiometry of the films is verified by X-ray photoelectron spectroscopy, while the surface structure is probed by low energy electron diffraction. The Fe_3O_4 films produced are counter-intuitively compressively strained in the vertical direction and exhibit marginal tensile strain in the lateral direction as deduced from the X-ray diffraction and surface-sensitive grazing incidence X-ray diffraction measurements, which is in accordance with the high-resolution transmission electron microscopy measurement of the thinnest Fe_3O_4 film. Moreover, the high-resolution transmission electron microscopy measurement reveals a well-defined interface and the formation of stress-releasing misfit dislocations located at the interface between Fe_3O_4 film and $SrTiO_3$ substrate.

5.1 Introduction

Fe_3O_4 (lattice constant 8.396 Å) is one of the most studied and thus most well-known (inverse) spinel-type materials, which has attracted much attention in the fields of spintronics [206] during the last decades and also in the relative novel research field of spin caloritronics [207]. Nevertheless, the last couple of years of intensive research have proven that Fe_3O_4 – even though it is fairly well understood nowadays – is still good for surprises and there is still a lot to discover. For instance, only just recently the origin of the long-known surface reconstruction typical for Fe_3O_4 has been adequately clarified by introducing the so-called subsurface cation vacancy (SCV) structure of Fe_3O_4 [18].

Some of the last few unresolved remaining and challenging issues include the specific cationic ordering at the Verwey transition of Fe_3O_4 [208] and the controversial strain observed in Fe_3O_4 thin films, especially if grown on $SrTiO_3(001)$ substrates (lattice constant 3.905 Å) [209]. In the latter case, the Fe_3O_4 films showed most surprisingly compressive strain out-of-plane, which is contrary to classical relaxation theory considering, e.g., a pseudomorphic strained Fe_3O_4 film grown on $SrTiO_3(001)$ with complete lateral adaptation of the Fe_3O_4 lattice to the underlying substrate lattice. Here, it expected that the film is laterally compressively strained due to the smaller lattice constant of the substrate, which is accompanied by vertical tensile strain. Moreover, this atypical compressive vertical strain was also observed in similar ferrites such as cobalt ferrite [22, 53, 210] and nickel ferrite [211, 212] grown on $SrTiO_3(001)$ substrates as well. For both ferrite films, an auxetic behavior has often been discussed in the literature [53, 211, 213, 214] due to an assumed or observed negative Poisson ratio [53, 213, 214]. Yet, a positive Poisson ratio was also observed for these ferrite films by other authors [22,54,209,212]. Furthermore, it has been reported that Fe_3O_4 films instead relax normally with lateral compressive and vertical tensile strain when they are not in direct contact with the $SrTiO_3(001)$ substrate due to a NiO interlayer at the interface [215]. Accordingly, the origin of the anomalous relaxation process of Fe_3O_4 ultrathin films remains yet to be comprehended.

5.2 Experimental details

Therefore, two Fe_3O_4 thin films with film thicknesses of about 15 nm and 37 nm prepared by reactive molecular beam epitaxy on $SrTiO_3(001)$ substrates are studied in this work. The $SrTiO_3(001)$ substrates were cleaned for 1 h at 400 °C in an oxygen atmosphere of 1×10^{-4}mbar prior to film deposition. Low-energy electron diffraction (LEED) and X-ray photoelectron spectroscopy (XPS) measurements were carried out to check the results of the cleaning process. Afterward, the Fe_3O_4 films were grown each at a substrate temperature of 250 °C and in 5×10^{-6}mbar O_2 by evaporating Fe from a pure metal rod. Subsequent XPS measurements were performed to confirm the stoichiometry of both films. LEED has been used to verify that the surfaces of the films are ordered well.

The structural characterization of the films by means of synchrotron-based X-ray diffraction (XRD) and surface-sensitive grazing incidence X-ray diffraction (GIXRD) were performed at beamline I07 of the Diamond Light Source (DLS). For both, 20.5 keV X-ray photons, a $2+3$ circle diffractometer with a hexapod sample stage, and a two-dimensional Pilatus 100K detector were used. The XRD measurements were carried out in specular geometry along the $(00L)$ crystal truncation rod close to the (002) $SrTiO_3(001)$ Bragg reflection and the GIXRD measurements in grazing incident geometry along the $[H00]$ direction close to the (200) Bragg reflection of $SrTiO_3(001)$. The film thicknesses of the Fe_3O_4 films were confirmed by X-ray reflectivity (XRR) measurements carried out in specular geometry at beamline I07 of DLS as well using the same energy of the X-ray photons.

A conclusive high-resolution transmission electron microscopy (HRTEM) measurement of the Fe_3O_4 film with a film thickness of 15 nm was employed in order to gain more detailed information regarding the internal atomic structure of the film. For the HRTEM measurement, the sample was prepared by means of conventional cross-section preparation.

5.3 Results and discussion

5.3.1 Surface characterization by means of XPS and LEED

In order to verify the electronic structure and the surface structure of the Fe_3O_4 films, *in situ* surface-sensitive XPS and LEED measurements were carried out directly after film deposition. For XPS measurements, the radiation of a Al Kα source was used with a photon energy of $h\nu$ =1486.6 eV. The results of the XPS and LEED measurements are depicted in Fig. 5.1.

Fe $2p$ core-level spectra obtained from both samples and depicted in Fig. 5.1 (a) have completely identical shape. The main photoemission lines are at binding energies of about 723.9 eV and 710.6 eV, coinciding with well-known binding energies of Fe $2p_{1/2}$ and Fe $2p_{3/2}$ photoelectrons emitted from Fe_3O_4 [216]. In addition, no distinct Fe^{3+} or Fe^{2+} charge-transfer satellite is visible between the $2p$ peaks, as also expected for stoichiometric Fe_3O_4 [216,217]. Because Fe_3O_4 has both Fe^{3+} and Fe^{2+} cations on different lattice sites of its inverse spinel structure, their corresponding charge-transfer satellites superpose to equal parts in the spectrum, leveling the region between

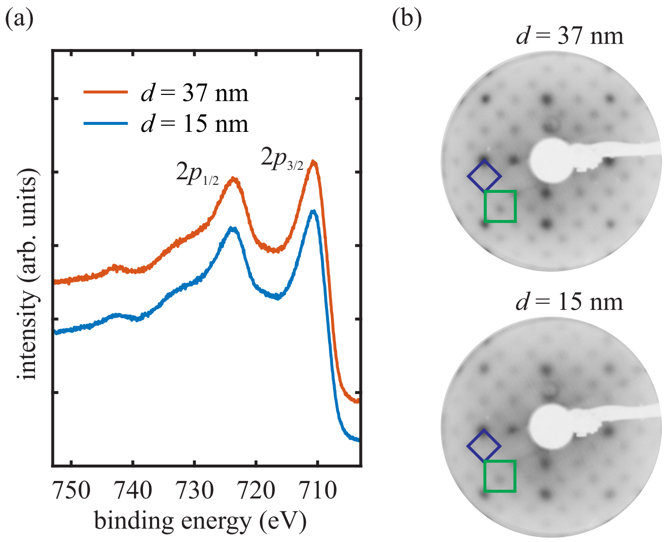

Fig. 5.1: (a) Fe 2*p* core-level XP spectra of both Fe_3O_4 films from the XPS measurements. (b) LEED images of both Fe_3O_4 films recorded at an electron energy of 101 eV. The green and blue squares indicate the (1×1) surface structure and the $(\sqrt{2} \times \sqrt{2})R45°$ superstructure, respectively.

the 2*p* peaks. Consequently, no satellite structures are observable in stoichiometric Fe_3O_4 with balanced cation species.

The LEED images in Fig. 5.1 (b) show for both iron oxide films a clear square (1×1) fundamental surface structure as well as a well-pronounced $(\sqrt{2} \times \sqrt{2})R45°$ superstructure. The latter is typical for well-ordered Fe_3O_4 surfaces [18, 170, 218–220].

Concluding the XPS and LEED results, both iron oxide films exhibit the near-surface stoichiometry and surface structure characteristic for stoichiometric $Fe_3O_4(001)$, confirming the growth of stoichiometric epitaxial Fe_3O_4 thin films on $SrTiO_3(001)$ substrates in this study.

5.3.2 XRD and GIXRD

CTR scans of each Fe_3O_4 film performed by XRD and GIXRD along the $[00L]$ and $[H00]$ direction, respectively, are depicted in Fig. 5.2 (a,b). The data were scaled to the reciprocal lattice units (r. l. u.) of $SrTiO_3(001)$ for both directions.

The XRD and GIXRD measurements reveal sharp and intense Bragg reflections at $L = 2$ (XRD) and $H = 2$ (GIXRD) corresponding to the (002) and (200) Bragg reflections of $SrTiO_3(001)$, respectively. Because the layer distance of Fe_3O_4 (bulk 2.099 Å) is larger than the layer distance of $SrTiO_3$ (bulk 1.953 Å), the (004) and (400) Bragg reflections of the Fe_3O_4 films are located at lower L and H values compared to the (002) and (002) Bragg reflections of the $SrTiO_3$ substrates. For the Fe_3O_4 film with lower film thickness, the Bragg peaks are wider and less intense. This can be attributed to a lower amount of coherent crystallites contributing to the (GI)XRD signals. In addition, no Laue oscillations are overall evident, indicating an inhomogeneous crystalline structure with broad distribution of crystallite sizes for both films as a result of the high lattice mismatch between Fe_3O_4 and $SrTiO_3(001)$.

The vertical layer distance c and lateral layer distance a of both Fe_3O_4 films have been determined from the positions of their corresponding (004) and (400) Bragg reflections in the XRD and GIXRD scans, respectively. The XRD scans have been analyzed according to complete calculations based on kinematic diffraction theory due to partly overlapping (004) and (002) Bragg peaks of Fe_3O_4 and $SrTiO_3(001)$, respectively. For the calculations, atomic form factors of all contributing ions have been taken into account. In contrast, a simple Gaussian diffraction peak profile sufficiently described the entire $(400)Fe_3O_4$ Bragg peaks in the GIXRD scans and was used to obtain the

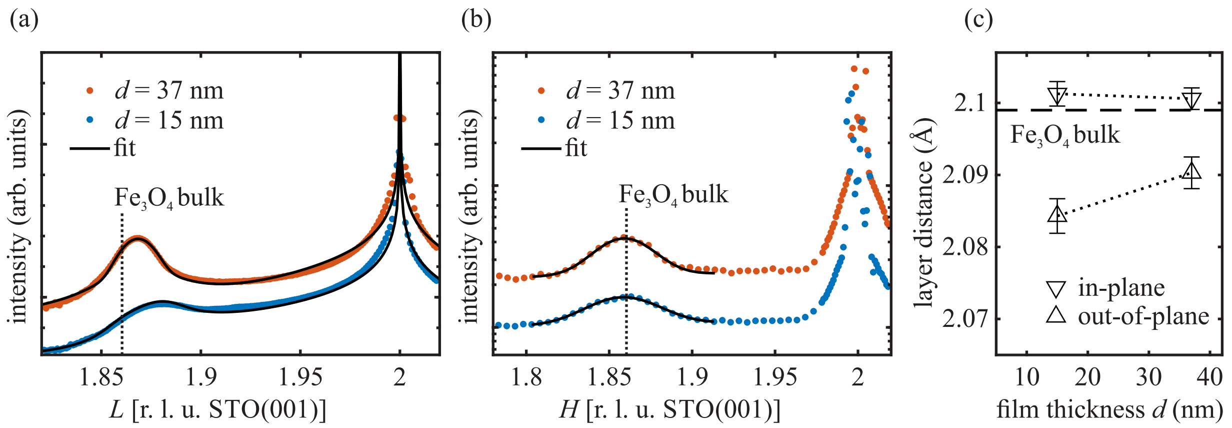

Fig. 5.2: (a) XRD and (b) GIXRD scans for each Fe_3O_4 film. The dashed black lines in (a) and (b) indicate the position in the $[00L]$ and $[H00]$ direction expected for bulk Fe_3O_4. (c) Vertical and lateral layer distances determined from the XRD and GIXRD scans, respectively. The dashed black line indicates the layer distance of bulk Fe_3O_4.

positions of the $(400)Fe_3O_4$ Bragg peak. The resulting out-of-plane and in-plane layer distances of both Fe_3O_4 films are depicted in Fig. 5.2 (c).

Both Fe_3O_4 films show very small lateral expansion and larger vertical compression of their lattices. The resulting tensile strain in-plane of $\Delta a_\mathrm{f}/a_\mathrm{f} = (0.1 \pm 0.1)\,\%$ remains constant independent on the Fe_3O_4 film thickness, whereas the compressive strain out-of-plane declines from $\Delta c_\mathrm{f}/c_\mathrm{f} = (-0.7 \pm 0.1)\,\%$ to $(-0.4 \pm 0.1)\,\%$ for the Fe_3O_4 film with higher film thickness compared to the Fe_3O_4 film with lower film thickness. Hence, both film lattices are vertically compressed, although they are laterally almost completely relaxed.

In principle, the incorporation of interfacial misfit dislocations in films plays a crucial role in releasing lateral stress that resulted from a large lattice mismatch between a film and a substrate [about 7.5 % between Fe_3O_4 and $SrTiO_3(001)$]. Based on the model of Matthews and Blakeslee [58] to describe the critical thickness d_c for nucleation of misfit dislocations via

$$\frac{d_\mathrm{c}}{b} = \frac{\left(1-\nu\cos^2\alpha\right)\left(\ln\left(\frac{d_\mathrm{c}}{b}\right)+1\right)}{2\pi f\,(1+\nu)\cos\lambda}\,, \tag{5.1}$$

the formation of misfit dislocations become energetically more favorable in the case of a thin Fe_3O_4 film grown on $SrTiO_3(001)$ if the film thickness exceeds the critical film thickness d_c of about 2 nm. Hereby, b is the magnitude of the Burgers vector $\boldsymbol{b} = a_\mathrm{f}/4\,\langle 110\rangle$ [221], $\nu = 0.356$ is the Poisson ratio of Fe_3O_4 [55], $\alpha = 90°$ is the angle between the Burgers vector and the dislocation line, f is the lattice mismatch, and $\lambda = 45°$ is the angle between the Burgers vector and the direction being perpendicular to the dislocation line and being within the plane of the interface. Consequently, both Fe_3O_4 films prepared in this study are expected to release their substrate-induced lateral strain through forming misfit dislocations as both film thicknesses exceed d_c.

As cited above, the anomalous relaxation process of ferrite films on $SrTiO_3(001)$ with tensile and compressive stress for lateral and vertical directions has also been reported in detail for $NiFe_2O_4$ thin films [212]. The $NiFe_2O_4$ films relax laterally almost completely for film thickness above 20 nm. The lateral relaxation is accompanied simultaneously by a vertical relaxation of the ferrite films. Thus, these films show bulk structure. The Fe_3O_4 films produced in this study, however, are completely relaxed only in the lateral direction, while they are still compressively strained vertically.

5.3.3 HRTEM

Figure 5.3 (a) shows a typical cross-sectional HRTEM image of the interface between the Fe_3O_4 film (with lower film thickness) and the $SrTiO_3$ substrate in the [010] zone axis. The interface between $SrTiO_3$ substrate (bottom part) and Fe_3O_4 film (central part) is atomically sharp and well-defined. According to the HRTEM image, the Fe_3O_4 film has a total film thickness of $\sim 16\,\mathrm{nm}$, which agrees well with the Fe_3O_4 film thickness of 15 nm obtained from the XRR measurements. Amorphous adhesive from the sample preparation for the HRTEM measurement is seen above the Fe_3O_4 film at the top part of Fig. 5.3 (a).

Furthermore, an interlayer with (cubic/tetragonal-like) crystallographic structure might be assumed at the interface, extending in average approximately over the first 1 nm of the total Fe_3O_4 film [cf. yellow square in the magnification inset of Fig. 5.3 (a)]. A second cubic crystal structure in Fe_3O_4 thin films besides the one of Fe_3O_4 was also found by Zhu *et al.* [222] and attributed to an ultrathin FeO interface layer ($\sim 5\,\mathrm{nm}$), formed between the Fe_3O_4 film and the $SrTiO_3(001)$ substrate. Their findings correlate with the conclusions drawn a little earlier by Bertram *et al.* [194, 223] based on their conducted XRD measurements on Fe_3O_4 thin films grown on MgO(001) substrates. However, with a vertical and lateral spacing of $(2.093 \pm 0.015)\,\mathrm{Å}$, the second crystal structure in our case resembles bulk Fe_3O_4 (2.099 Å) more than bulk FeO (2.166 Å) or even pseudomorphic strained FeO ($a = 1.953\,\mathrm{Å}$ and $c = 2.394\,\mathrm{Å}$). High substrate temperatures during film deposition and post-deposition annealing also at higher temperatures were further reported to favor the growth of (111)-oriented Fe_3O_4 on $SrTiO_3(001)$ substrates [224, 225]. The crossover from $Fe_3O_4(001)$ to $Fe_3O_4(111)$ was obtained above a temperature of 600 °C, which is significantly higher than the deposition temperature used in this work. Furthermore, because Fe_3O_4 with (111)-orientation manifests with hexagonal symmetry and far larger vertical layer distance ($c = 2.424\,\mathrm{Å}$), the presence of an ultrathin $Fe_3O_4(111)$ layer at the interface can most likely be ruled out.

From a selected area of the HRTEM image [cf. white dashed square in Fig. 5.3 (a)], covering both the Fe_3O_4 film and the $SrTiO_3$ substrate, a diffractogram has been determined by applying a fast Fourier transform (FFT). As a result, the diffractogram exhibits peaks related to both Fe_3O_4 and $SrTiO_3$, as presented in the upper inset of Fig. 5.3 (a). Compared to the $SrTiO_3$ related peaks, the peaks related to Fe_3O_4 are closer to the origin of the diffractogram. Analogous to the explanation above for XRD and GIXRD, this finding is caused by the fact that the lateral and vertical layer distances of Fe_3O_4 are larger than the layer distance of $SrTiO_3$. The vertical and lateral layer distances of the $SrTiO_3$ substrate are $c_\mathrm{s} = (1.955 \pm 0.010)\,\mathrm{Å}$ and $a_\mathrm{s} = (1.960 \pm 0.010)\,\mathrm{Å}$, respectively, according to the positions of the corresponding (002) and (200) peaks related to $SrTiO_3$ in the diffractogram. Thus, the obtained layer distances of the $SrTiO_3$ substrate match perfectly the literature value for bulk $SrTiO_3$ with $a_\mathrm{s} = c_\mathrm{s} = 1.953\,\mathrm{Å}$.

Analogously, we obtain for the Fe_3O_4 film vertical layer distances of $c_\mathrm{f} = (2.075 \pm 0.015)\,\mathrm{Å}$ and a lateral layer distances of $a_\mathrm{f} = (2.090 \pm 0.015)\,\mathrm{Å}$ from the positions of the corresponding (004) and (400) Fe_3O_4 related peaks. Thus, in agreement with the lattice distortion observed in the XRD and GIXRD measurements, the Fe_3O_4 film is laterally (almost) completely relaxed but shows large compressive strain $[\Delta c_\mathrm{f}/c_\mathrm{f} = (-1.1 \pm 0.7)\,\%]$ in the vertical direction. The values of the vertical and lateral strain obtained for this Fe_3O_4 film coincides well with the respective values obtained from the (GI)XRD experiments considering experimental errors. Still, we like to note that due to the averaging character of the XRD and GIXRD measurements, values derived from these measurements have a higher accuracy compared to the values obtained from the FFT diffractogram that was calculated from the HRTEM measurement.

As already presumed from the XRD and GIXRD measurements, misfit dislocations are expected to release the substrate-induced strain in the lateral direction. This is in fact confirmed by the Fourier filtered image presented in Fig. 5.3 (b), revealing misfit dislocations that are located exclusively at

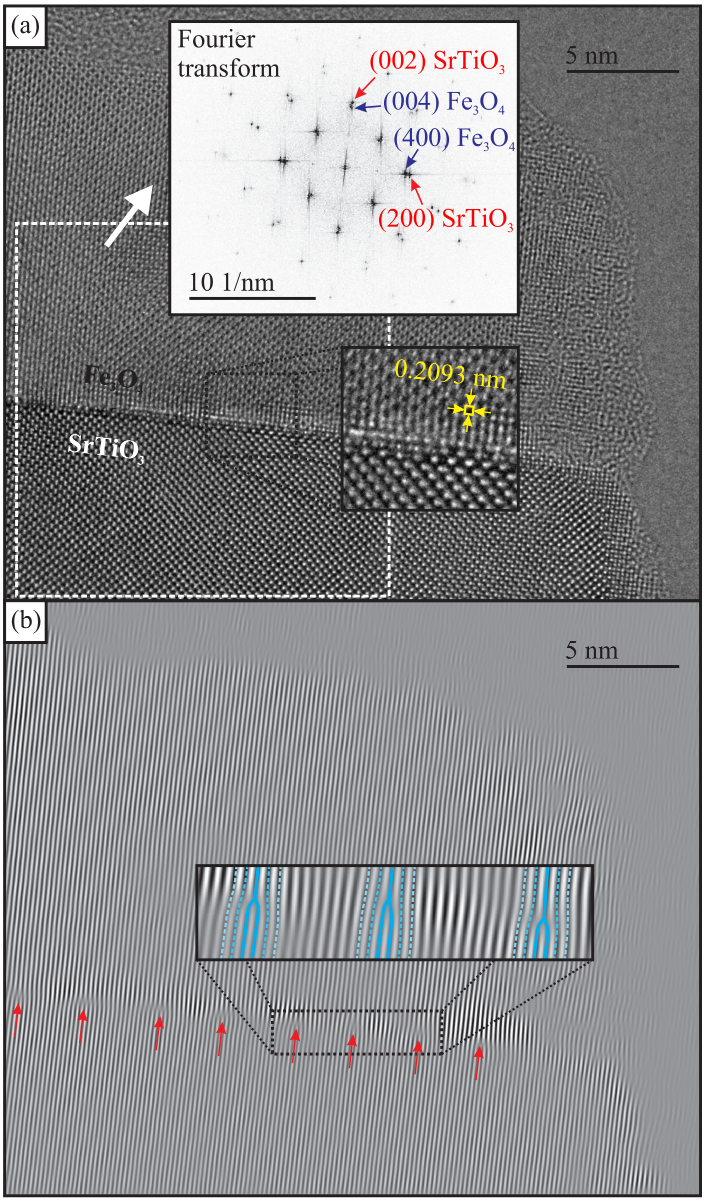

Fig. 5.3: (a) Cross-sectional HRTEM image ([010] zone axis) of the Fe_3O_4 film with a film thickness of about 15 nm. A magnification of the film-substrate interface marked by the black dashed square is displayed in the smaller inset. Here, the yellow square marks an additional crystallographic cubic structure at the interface. The larger inset in (a) is a diffractogram obtained from the fast Fourier transform of the area marked by the white dashed square. (b) Fourier filtered image of (a). The red arrows indicate the dislocations present at the interface. The inset presents a magnification of the misfit dislocations (turquoise solid lines) in the area marked by the black dashed square.

the interface (cf. red arrows). The misfit dislocations are distributed almost periodically with an average distance of (2.86 ± 0.20) nm from each other. For a complete lattice misfit compensation by dislocation formation, a distance (with respect to layer distances) of about $a_s a_f / |a_f - a_s| = 2.80$ nm between the misfit dislocations is required. Nevertheless, this very small deviation may be used to determine the residual lateral strain. In this context, a lateral layer distance of $a = (2.096 \pm 0.030)$ Å is obtained, which is to be compared with the bulk value of $a_f = 2.099$ Å. Therefore, it can be stated that the lattice misfit in the Fe_3O_4 film has been almost completely compensated by the occurring interfacial misfit dislocations. The compressive strain observed in the vertical direction, however, cannot be ascribed to the presence of dislocations. In this regard, the results presented in this study do not yet allow definite and conclusive explanations for this anomalous strain accumulation. Still, we would like to point out that antiphase boundaries could point in the right direction since these structural defects are able to contribute significantly to strain accumulation, as so often shown [190,191].

5.4 Summary and conclusions

In summary, Fe_3O_4 thin films of different film thicknesses have been grown on $SrTiO_3(001)$ substrates and were extensively structurally characterized by means of (GI)XRD and HRTEM. XPS and LEED measurements confirmed the near-surface stoichiometry and surface structure of the epitaxially grown Fe_3O_4 films. Both films are almost completely relaxed in the lateral direction parallel to the interfaces. Despite of this, we observe residual vertical compressive strain. The lateral relaxation can probably be related to the incorporation of strain-releasing interfacial misfit dislocations as directly revealed by the Fourier filtered HRTEM image.

5.5 Acknowledgements

We acknowledge Diamond Light Source for time on I07 under proposal SI20857 and financial support from the Deutsche Forschungsgemeinschaft (DFG, grant nos. KU2321/6-1 and WO533/20-1).

Original publication: The Journal of Physical Chemistry C **124**, 23895-23904 (2020)
available at http://dx.doi.org/10.1021/acs.jpcc.0c05503

Effects of Post-deposition Annealing on Epitaxial CoO/Fe_3O_4 Bilayers on $SrTiO_3(001)$ and Formation of Thin High-Quality Cobalt Ferrite-like Films

J. Thien[1], J. Bahlmann[1], A. Alexander[1], M. Hoppe[1,2], T. Pohlmann[1,2], K. Ruwisch[1], C. Meyer[1], F. Bertram[1], K. Küpper[1], and J. Wollschläger[1]

[1] *Department of Physics, Osnabrück University, 49076 Osnabrück, Germany*
[2] *Deutsches Elektronen-Synchrotron (DESY), Photon Science, 22607 Hamburg, Germany*

Abstract

In order to explore an alternative pathway to prepare ultrathin $CoFe_2O_4$ films, epitaxial CoO/Fe_3O_4 bilayers with varying film thickness of the CoO film were grown on Nb-doped $SrTiO_3(001)$ substrates via reactive molecular beam epitaxy. Thereafter, cobalt ferrite films with varying stoichiometry were prepared by post-deposition annealing at different temperatures. The thermally mediated interdiffusion resulted in the formation of vertical compressive and lateral tensile strained $Co_xFe_{3-x}O_4$ films ($x = 0.6 - 1.4$) with homogeneous distribution of Fe and Co cations for each film. The chemical and electronic variations after each annealing step were studied by means of soft and hard X-ray photoelectron spectroscopy. The homogeneity of the cation distributions in the films were additionally verified after the last annealing step by angle-resolved hard X-ray photoelectron spectroscopy. For the cobalt ferrite film with $x = 1.4$, an additional crystallographic phase of $Co_{1-y}Fe_yO$ was observed by (grazing incidence) X-ray diffraction measurements after annealing at 600 °C. X-ray reflectivity measurements were performed to determine the film thickness of the formed $Co_xFe_{3-x}O_4$ films.

Original publication: Materials **15**, 46 (2022)
available at http://dx.doi.org/10.3390/ma15010046

Cationic Ordering and Its Influence on the Magnetic Properties of Co-Rich Cobalt Ferrite Thin Films Prepared by Reactive Solid Phase Epitaxy on Nb-Doped $SrTiO_3(001)$

J. Thien[1], J. Bahlmann[1], A. Alexander[1], K. Ruwisch[1], J. Rodewald[1], T. Pohlmann[1,2], M. Hoppe[1,2], F. Alarslan[3], M. Steinhart[3], B. Altuncevahir[4], P. Shafer[5], C. Meyer[1], F. Bertram[2], J. Wollschläger[1], and K. Küpper[1]

[1]*Department of Physics, Osnabrück University, 49076 Osnabrück, Germany*
[2]*Deutsches Elektronen-Synchrotron (DESY), Photon Science, 22607 Hamburg, Germany*
[3]*Institute for Chemistry of New Materials and Center for Cellular Nanoanalytics (CellNanOs), Osnabrück University, 49076 Osnabrück, Germany*
[4]*Physics Engineering Department, Faculty of Science and Letters, Istanbul Technical University, Maslak, Istanbul TR-34469, Turkey*
[5]*Advanced Light Source, Lawrence Berkeley National Laboratory, Berkeley, CA 94720, USA*

Abstract

Here, we present the (element-specific) magnetic properties and cation ordering for ultrathin Co-rich cobalt ferrite films. Two Co-rich $Co_xFe_{3-x}O_4$ films with different stoichiometry ($x = 1.1$ and $x = 1.4$) have been formed by reactive solid phase epitaxy due to post-deposition annealing from epitaxial CoO/Fe_3O_4 bilayers deposited before on Nb-doped $SrTiO_3(001)$. The electronic structure, stoichiometry and homogeneity of the cation distribution of the resulting cobalt ferrite films were verified by angle-resolved hard X-ray photoelectron spectroscopy. From X-ray magnetic circular dichroism measurements, the occupancies of the different sublattices were determined using charge-transfer multiplet calculations. For both ferrite films, a partially inverse spinel structure is found with increased amount of Co^{3+} cations in the low-spin state on octahedral sites for the $Co_{1.4}Fe_{1.6}O_4$ film. These findings concur with the results obtained by superconducting quantum interference device measurements. Further, the latter measurements revealed the presence of an additional soft magnetic phase probably due to cobalt ferrite islands emerging from the surface, as suggested by atomic force microscope measurements.

7.1 Introduction

Ferrites such as $CoFe_2O_4$ (CFO) have intriguing electronic and magnetic properties that are increasingly attracting attention, particularly for advancing the fields of spintronics and spin caloritronics. For instance, in these fields magnetic insulators (MI) can be used as spin-filters for the generation of highly spin-polarized electron currents due to their spin-dependent band gaps [9, 226–230], thereby creating the possibility of faster and less energy consuming spintronic devices. As the spin-filter effect decreases drastically with the thickness of the spin-filter film, ultrathin MI films are essential to realize high-efficiency spin-filters. Additionally, thin CFO films are useful as supports for Pt films to create thermally generated spin currents [231,232] via the spin Seebeck effect (SSE) [233]. Owing to the absence of a magnetic proximity effect in $Pt/CoFe_2O_4$ bilayers [234], no parasitic effects, such as the anomalous Nernst effect [235], are induced, simplifying the evaluation of the SSE signal and thus making CFO films also quite interesting for spin caloritronic applications. Furthermore, CFO has significant potential in the fields of iron-based supercapacitors [236] and electrocatalysts [237].

Whereas stoichiometric $CoFe_2O_4$ ($x = 1$) and the Co-deficient phase $Co_xFe_{3-x}O_4$ ($x < 1$) have been investigated intensely during the last two decades, the Co-rich phase $Co_xFe_{3-x}O_4$ ($x > 1$) has gained only little attention up to now. Nevertheless, Co_2FeO_4 thin films have been reported in one of these few works to have highly interesting magnetic properties with the potential for novel spintronic applications [238].

Stoichiometric CFO crystallizes as a cubic inverse spinel with a lattice constant of 8.392 Å. For a perfect inversion of the spinel structure, the octahedral B lattice sites in the face-centered cubic oxygen sublattice of CFO are occupied by divalent Co^{2+} cations, while trivalent Fe^{3+} cations occupy both the octahedral B lattice sites and the tetrahedral A lattice sites with a $1:1$ distribution. Due to the antiferromagnetic super-exchange interaction between the Fe^{3+} cations at the A and B lattice sites, their magnetic moments effectively compensate for each other. Hence, the resulting magnetization originates mostly from the ferromagnetic interaction between the Co^{2+} and Fe^{3+} cations at the B lattice sites, resulting in a net magnetization of 3 μ_B/f.u. [9] due to the spin moment of Co^{2+} and neglecting orbital moments.

However, it has been reported that cobalt ferrite quite often exhibits only partially inverse spinel structure [9,239] with Co^{2+} on both tetrahedral A and octahedral B lattice sites. As a consequence, the distribution of cations can have a strong impact on the magnetic properties and thus also on the resulting net magnetization based on the magnitude of the cation disorder. In principle, the cation disorder of stoichiometric $CoFe_2O_4$ can be described by the inversion parameter γ with $0 \leq \gamma \leq 1$ according to the structural formula

$$\left[Co^{2+}_{1-\gamma}Fe^{3+}_{\gamma}\right]_A \left[Co^{2+}_{\gamma}Fe^{3+}_{2-\gamma}\right]_B O^{2-}_4 . \tag{7.1}$$

The indices A and B represent the respective lattice sites. For $\gamma = 0$, all Co^{2+} cations occupy tetrahedral A lattice sites and all Fe^{3+} cations occupy octahedral B lattice sites, corresponding to the case for a normal spinel structure. In contrast, $\gamma = 1$ indicates a complete inverse spinel. Values between $\gamma = 0$ and $\gamma = 1$ characterize intermediate states with a partially inverse cation distribution.

As for the Co-rich phase, there have been contradicting results for the coordination of the excessive Co ions. Whereas Mössbauer spectroscopy studies suggest Co^{3+} cations in octahedral coordination, which are in the low-spin state [240], more recent work found Co^{3+} cations in tetrahedral coordination and in high-spin state [241]. We wanted to go a step further and performed a comprehensive analysis of the electronic and magnetic properties of ultrathin Co ferrite films, which we produced very recently by intermixing epitaxial CoO/Fe_3O_4 bilayers using a post-deposition annealing (PDA) approach [22].

Generally, cobalt ferrite thin films are often prepared by deposition methods such as molecular beam epitaxy [242], sputter deposition [229] and pulsed laser deposition [243]. Quite recently, we demonstrated that thin cobalt ferrite films can be prepared by reactive solid phase epitaxy (RSPE) due to the intermixing of epitaxial Fe_3O_4/CoO and CoO/Fe_3O_4 bilayers [22,244]. For both bilayer systems, the intermixing of the oxide layers was caused by PDA on Nb-doped $SrTiO_3(001)$ substrates (lattice constant 3.905 Å). However, the large lattice mismatch of 7.45% between the formed Co ferrite film and the $SrTiO_3$ (comparing the lattice constant of $SrTiO_3$ with the halved lattice constant of CFO) induces strain in the Co ferrite films. This strain, on the other hand, may also be used to steer the physical properties of these Co ferrite films [245,246], especially their electronic and magnetic properties, as demonstrated, for example, in Fe_3O_4 thin films prepared on $SrTiO_3(001)$ [247,248].

Since the cation distribution of cobalt ferrite can easily be changed by thermal treatment [249,250], we report here on a case study concerning mainly the cation distribution and the resulting magnetic behavior of two cobalt ferrite films prepared by RSPE. To gain insight into the occupation of the octahedral and tetrahedral sites in the inverse spinel structure and to probe the element-specific magnetic properties of the cobalt ferrite films, X-ray absorption spectroscopy (XAS) and X-ray magnetic circular dichroism (XMCD) measurements were utilized. The integral magnetic properties were examined by superconducting quantum interference device (SQUID) measurements. Furthermore, the electronic and chemical properties throughout the whole films and the surface morphologies of the films were studied by angle-resolved hard X-ray photoelectron spectroscopy (AR-HAXPES) and atomic force microscope (AFM) measurements, respectively. Detailed knowledge of the cationic distribution is a key point in understanding the complex magnetic properties of these cobalt ferrites, which is in turn necessary for potential future applications mentioned above.

7.2 Materials and methods

Two $Co_xFe_{3-x}O_4$ films with stoichiometries of $x = 1.1$ and $x = 1.4$ and total film thicknesses of (16.5 ± 0.5) nm and (18.1 ± 0.5) nm, respectively, were prepared by RSPE from epitaxial CoO/Fe_3O_4 bilayers grown on Nb-doped $SrTiO_3(001)$ substrates (cf. Fig. 7.1) at the beamline BM25-SpLine of the European Synchrotron Radiation Facility (ESRF) [22]. The sample preparation was extensively monitored by several chemical and structural characterization techniques such as soft and hard X-ray photoelectron spectroscopy and synchrotron radiation based X-ray diffraction including surface sensitive grazing incidence X-ray diffraction to follow the evolution from the CoO/Fe_3O_4 bilayer stacks to completely reacted Co ferrite films. A detailed description of the sample preparation can be found in reference [22].

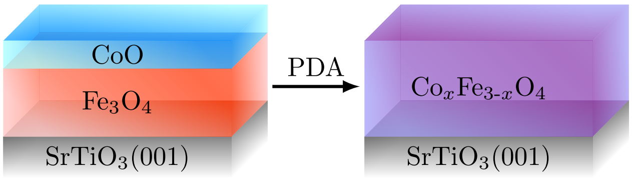

Fig. 7.1: Principal sketch of the conducted film preparation. The thermally induced interdiffusion results in the formation of homogeneous $Co_xFe_{3-x}O_4$ films from initial epitaxial CoO/Fe_3O_4 bilayers grown on Nb-doped $SrTiO_3(001)$.

To probe the homogeneity of the cation distribution as well as the electronic and chemical properties after the whole PDA treatment, AR-HAXPES measurements at beamline P22 of PETRA III at Deutsches Elektronen-Synchrotron (DESY) were conducted using an excitation energy of $h\nu = 5945$ eV. The photoelectrons were detected by a Phoibos 225 HV hemispherical analyzer (SPECS, Berlin, Germany) with a delay-line electron detector. As a result of the finite acceptance angle of the detector, increasing the glancing incidence angle of the X-ray beam with respect to the sample surface leads to a higher surface sensitivity since less photoelectrons from the bulk are detected due to the fixed angle between source and detector. Consequently, lower glancing incidence angles allow probing of deeper layers of samples and vice versa. In order to probe both the bulk and the surface-near region of the formed $Co_xFe_{3-x}O_4$ films, incidence angles of 5°, 45°, and 60° were used.

The surface morphologies of the resulting $Co_xFe_{3-x}O_4$ films were examined by AFM measurements using a NT-MDT NTEGRA device. The measurements were performed in contact mode. For the measurements, a field of view area of 1500 nm × 1000 nm was chosen.

XAS and XMCD measurements at the Co $L_{2,3}$ (770 eV–818 eV) and Fe $L_{2,3}$ (700 eV–750 eV) edges were conducted at beamline 4.0.2 of the Advanced Light Source (ALS) using an external magnetic field of 4 T parallel to the X-ray beam and a degree of circular polarization of 90 %. For each $L_{2,3}$ edge, two absorption spectra were recorded for two opposite directions of the external magnetic field, which is analogous to changing the helicity of the circular polarization. Each absorption spectrum was recorded utilizing the total electron yield (TEY). From the sum and the difference of the two absorption spectra, the corresponding XAS and XMCD signals were obtained, respectively. All XAS and XMCD measurements were carried out at a temperature of 300 K and at a glancing incidence angle of 30° between the surface of the samples and the X-ray beam.

The XA and XMCD spectra were analyzed according to full multiplet calculations based on crystal-field theory and charge-transfer [200] using CTM4XAS [201]. In addition, we used a spin-orbit coupling of 100 % and the Slater integrals $F(dd)$, $F(pd)$, and $G(pd)$ to consider d-d and p-d Coulomb and exchange interactions [251]. To take into account interatomic screening, the Slater integrals were reduced to 80 % of their atomic values. Furthermore, all transition lines at the $L_3(L_2)$ edges were broadened by a Lorentzian width of 0.25 eV (0.45 eV) due to core-hole lifetime broadening and by a Gaussian width of 0.2 eV due to instrumental broadening.

SQUID measurements were performed at the Diamond Light Source (DLS) to get better insight on the integral magnetic properties of the samples. Magnetization curves from −5 T to 5 T were recorded at 300 K and 5 K using a MPMS system (MPMS3, Quantum Design, Darmstadt, Germany). The magnetization curves were corrected with respect to all non-ferrimagnetic contributions, such as the diamagnetic background caused by the $SrTiO_3$ substrates and the sample holder.

7.3 Results and discussion

7.3.1 AR-HAXPES

In Fig. 7.2, the Co $2p$ and Fe $2p$ HAXPES spectra (angular integrated) of each sample are displayed. All recorded spectra were calibrated according to the O $1s$ core level at 530 eV binding energy.

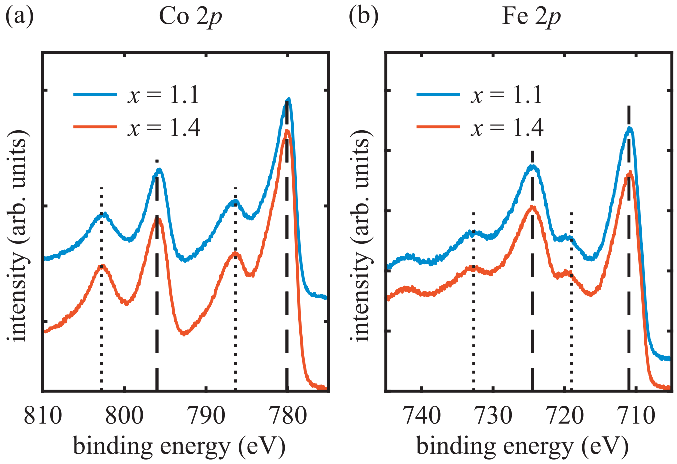

Fig. 7.2: Angular integrated (a) Co $2p$ and (b) Fe $2p$ HAXPES spectra for both samples. In both spectra, the dashed lines indicate positions of the particular $2p_{1/2}$ and $2p_{3/2}$ peaks. The dotted lines correspond to positions of the shake-up satellites in (**a**) and the charge-transfer satellites in (**b**).

The Co $2p$ spectra show the characteristic shape for cobalt ferrite [242,252]. The main peaks ($2p_{1/2}$ and $2p_{3/2}$) are located at binding energies of (795.8 ± 0.3) eV and (780.1 ± 0.3) eV, respectively. The peaks are accompanied by one shake-up satellite each, lying about 6 eV at higher binding energies.

For the Fe $2p$ spectra, the Fe $2p_{1/2}$ and Fe $2p_{3/2}$ peaks have binding energies of (724.5 ± 0.3) eV and (711.0 ± 0.3) eV, respectively. In addition, the Fe $2p$ spectrum of each sample exhibits distinct charge-transfer satellites at (719.0 ± 0.4) eV and (732.7 ± 0.4) eV. Both the appearance of the charge-transfer satellites and the positions of the Fe $2p$ peaks indicate a majority of Fe^{3+} cations [216, 217, 253], as expected for cobalt ferrite [242].

In order to gain information on the chemical composition and the homogeneity of the Co and Fe cation distribution of the cobalt ferrite films, a quantitative analysis was performed for each incidence angle mentioned in the experimental details section [22]. We found for each cobalt ferrite film a homogeneous depth distribution of the Co and Fe cations throughout the whole film. Thus, both oxide films are fully intermixed, confirming the formation of single $Co_xFe_{3-x}O_4$ films with stoichiometries of $x = 1.1$ and $x = 1.4$. Nevertheless, an additional rock-salt phase was observed for the $Co_{1.4}Fe_{1.6}O_4$ film. This additional phase coexists homogeneously distributed with the ferrite spinel phase, with both phases together forming a single film rather than a bilayer structure. For more details, see reference [22].

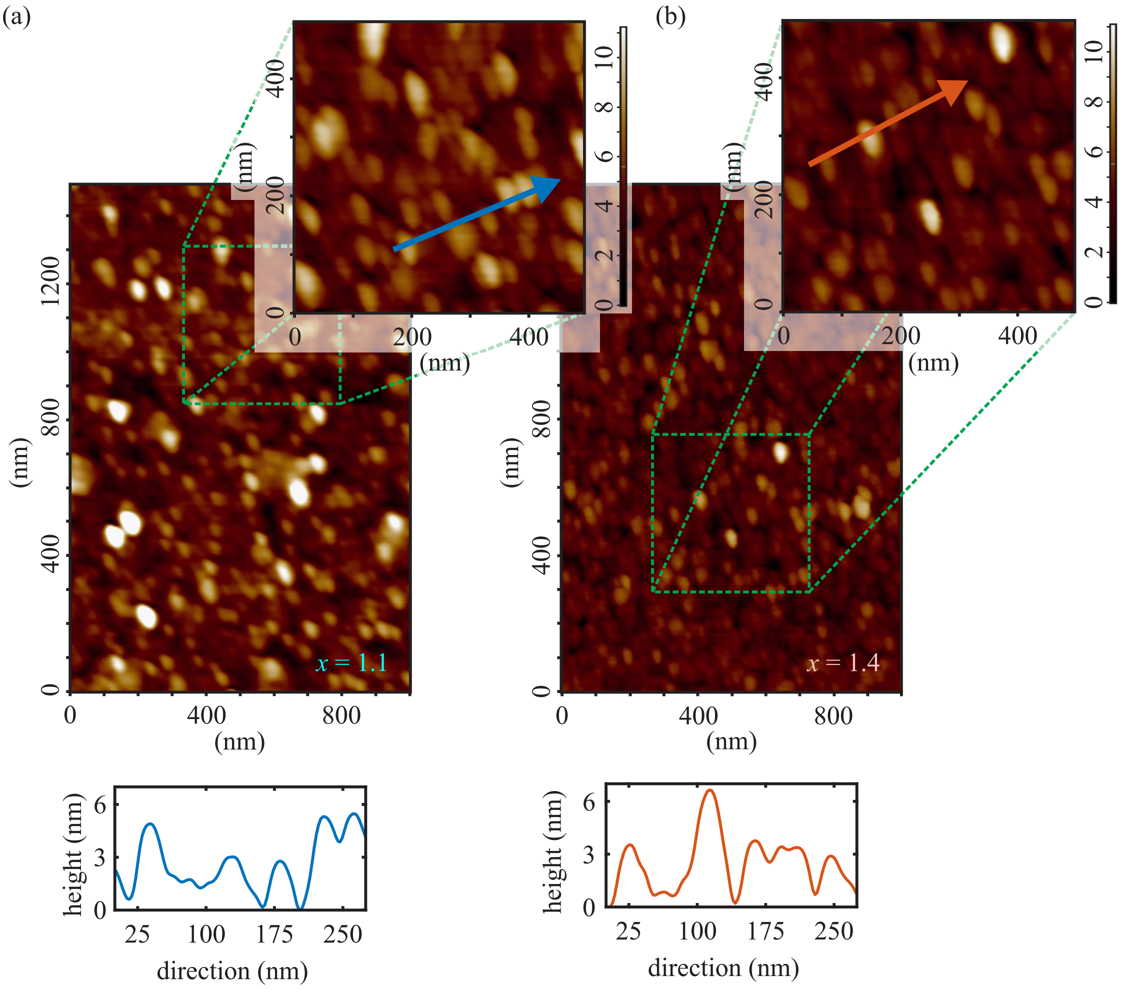

Fig. 7.3: Representative AFM images and height profiles of the $Co_xFe_{3-x}O_4$ films with (a) $x = 1.1$ and (b) $x = 1.4$. The blue and red arrows represent the directions of the respective height profiles presented underneath.

7.3.2 AFM

The morphologies of the cobalt ferrite film surfaces of both samples were obtained by AFM and are depicted in Fig. 7.3. An area of 1500 nm × 1000 nm was used for the AFM micrographs in both cases. Respective height profiles were made to estimate the average island heights and sizes.

For both samples, the cobalt ferrite film surface is covered by islands with an average island size of (55 ± 5) nm in diameter. Similar results of $CoFe_2O_4$ thin films prepared by radiofrequency magnetron sputtering on $SrTiO_3(001)$ were obtained by Rigato *et al.* [254]. The average island heights of both films are comparable (cf. respective height profiles), although the $Co_xFe_{3-x}O_4$ film with $x = 1.1$ has occasionally even significantly higher islands. A root mean square roughness (RMS) analysis revealed vertical RMS roughnesses of (1.7 ± 0.2) nm and (1.3 ± 0.2) nm for the $Co_{1.1}Fe_{1.9}O_4$ film and the $Co_{1.4}Fe_{1.6}O_4$ film, respectively. Thus, the $Co_{1.4}Fe_{1.6}O_4$ film has a lower vertical roughness than the $Co_{1.1}Fe_{1.9}O_4$ film. It should be noted that the sporadically occurring higher islands on the $Co_{1.1}Fe_{1.9}O_4$ film's surface were not included in the RMS analysis. Hence, the volume fraction of the islands relative to the total film volume is about 15 % (at least) for the $Co_{1.1}Fe_{1.9}O_4$ film and about 10 % for the $Co_{1.4}Fe_{1.6}O_4$ film.

7.3.3 XAS/XMCD

To probe the cationic distribution of the resulting cobalt ferrite films after the heat treatment, and to gain element-specific information about the resulting magnetic properties, we performed XAS/XMCD measurements at the Co $L_{2,3}$ and Fe $L_{2,3}$ edges. The absorption spectra with their resulting XMCD spectra at 300 K of both samples are depicted in Fig. 7.4.

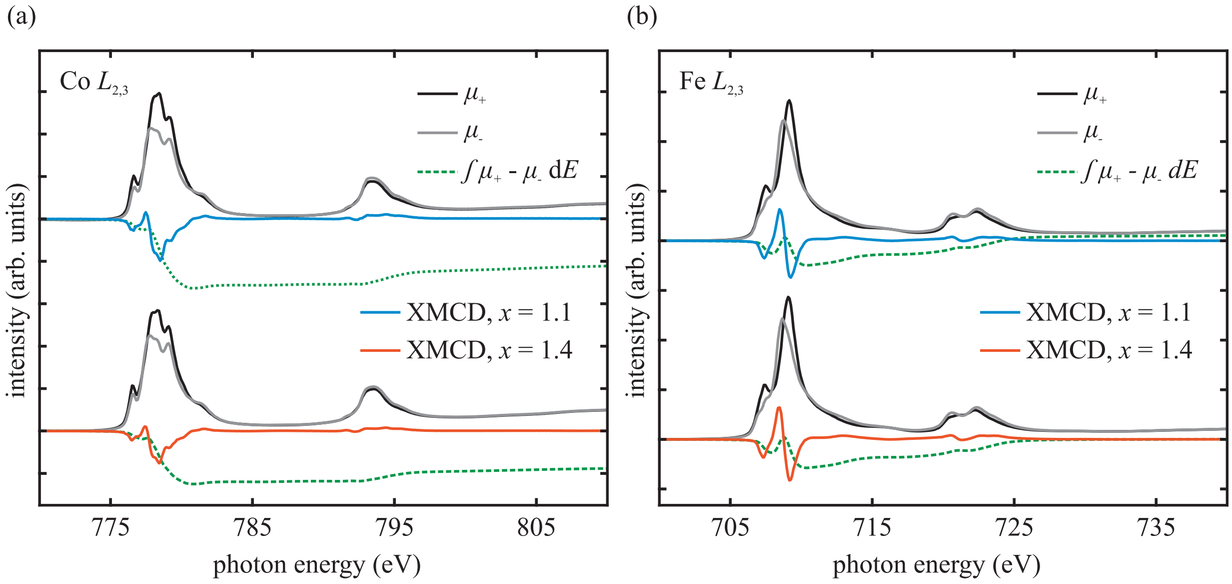

Fig. 7.4: XMCD spectra (blue and red) and integrated XMCD spectra (dashed green) recorded at 300 K across the (a) Co $L_{2,3}$ and (b) Fe $L_{2,3}$ edges of both samples. The spectra in gray (μ_+) and black (μ_-) are the absorption spectra recorded with two opposite directions of the external magnetic field.

The absorption spectra at the Co $L_{2,3}$ edges of both samples exhibit the characteristic shape of predominant divalent Co [244, 255, 256]. For the Fe $L_{2,3}$ edges, the shape of the absorption spectra of both samples resembles the shape of the Fe $L_{2,3}$ spectra of $CoFe_2O_4$ and Fe_2O_3 with predominant trivalent Fe [244, 257–259].

Further, both samples show strong magnetic dichroic signals of Co and Fe. Compared to the

Tab. 7.1: Orbital moment m_o, spin moment m_s, and total moment for the Co and Fe ions for the $\mathrm{Co}_x\mathrm{Fe}_{3-x}\mathrm{O}_4$ films with Co contents of $x = 1.1$ and $x = 1.4$ determined from the Co XMCD and Fe XMCD spectra using the sum rules [104–106, 260] and the sum rules' correction factors as derived by Teramura *et al.* [261]. For comparison, the respective magnetic moments normalized to the number of holes ($n_\mathrm{h} = 3$ for the Co ions and $n_\mathrm{h} = 5$ for the Fe ions) are displayed underneath.

Co Content	Co Moment (μ_B/Co ion)			Fe Moment (μ_B/Fe ion)		
x	m_o	m_s	total	m_o	m_s	total
1.1	0.26 ± 0.03	1.13 ± 0.06	1.39 ± 0.09	-0.04 ± 0.01	0.80 ± 0.04	0.76 ± 0.05
1.4	0.16 ± 0.02	0.72 ± 0.04	0.88 ± 0.06	0.01 ± 0.01	0.76 ± 0.04	0.77 ± 0.05
x	$m_\mathrm{o}/n_\mathrm{h}$	$m_\mathrm{s}/n_\mathrm{h}$	total	$m_\mathrm{o}/n_\mathrm{h}$	$m_\mathrm{s}/n_\mathrm{h}$	total
1.1	0.09 ± 0.01	0.38 ± 0.02	0.47 ± 0.03	-0.01 ± 0.01	0.16 ± 0.01	0.15 ± 0.02
1.4	0.05 ± 0.01	0.24 ± 0.01	0.29 ± 0.02	0.00 ± 0.01	0.15 ± 0.01	0.15 ± 0.02

$\mathrm{Co}_x\mathrm{Fe}_{3-x}\mathrm{O}_4$ film with $x = 1.4$, the $\mathrm{Co}_x\mathrm{Fe}_{3-x}\mathrm{O}_4$ film with $x = 1.1$ exhibits an increased Co XMCD signal, indicating a higher magnetic moment of Co. The Fe XMCD signals are almost commensurate.

From the Co XMCD and Fe XMCD spectra, the orbital moment m_o and the spin moment m_s of the Co and Fe ions were determined, by applying the sum rules [104–106, 260] and the sum rules' correction factors as derived by Teramura *et al.* [261]. The correction factors take into account the mixing of the L_2 and L_3 excitations due to core-hole interactions [261]. The values of the orbital moment m_o, the spin moment m_s, and the resulting total moments of the respective Co and Fe cations are listed in Table 7.1 for both Co ferrite films. The results reveal for the $\mathrm{Co}_{1.1}\mathrm{Fe}_{1.9}\mathrm{O}_4$ film a significantly higher total Co moment per ion compared to the $\mathrm{Co}_{1.4}\mathrm{Fe}_{1.6}\mathrm{O}_4$ film. The total Fe moments per ion of both Co ferrite films are commensurate considering experimental uncertainties, as noted before.

For the Co-rich phase of $\mathrm{Co}_x\mathrm{Fe}_{3-x}\mathrm{O}_4$, it has been reported in the literature that increasing the Co content ($x > 1$) results in an increased amount of Co^{3+} cations [240, 262–265], replacing Fe^{3+} cations in the crystal structure due to charge neutrality. In oxides with (inverse) spinel structures, Co^{3+} cations prefer strongly octahedral sites [239, 263, 266–268]. Depending on the crystal field (cf. Fig. 7.5), these Co^{3+} cations in octahedral coordination can either be found in high-spin state ($\mathrm{S} = 2$) or in diamagnetic low-spin state ($\mathrm{S} = 0$) [266]. For the $\mathrm{Co}_{1.4}\mathrm{Fe}_{1.6}\mathrm{O}_4$ film in this present study, only an increased amount of Co^{3+} cations at octahedral B sites being in the low-spin state can explain the lower total Co moment per Co ion compared to the $\mathrm{Co}_{1.1}\mathrm{Fe}_{1.9}\mathrm{O}_4$ film. In contrast, Co^{3+} in high-spin state would increase the spin moment per Co ion (cf. Fig. 7.5) and thus the total magnetic moment per Co ion.

Assuming instead that no Co^{3+} ions are present in the ferrite film, excess Co^{2+} cations have to occupy tetrahedral A sites, reducing the degree of inversion. Thus, a decreased total Co moment per ion could essentially be also related to the antiferromagnetic coupling between Co^{2+} cations, occupying tetrahedral A and octahedral B sites.

A lower degree of inversion would affect the Fe ions likewise, under the assumption that the total number of cations in the oxygen sublattices remains constant. As a consequence, more Fe ions would be at octahedral B sites, resulting in a higher total magnetic moment per Fe ion. This behavior, however, is not observed, since the total Fe moments per ion are fairly equal for both stoichiometries, indicating similar degrees of inversion for the films. Thus, this effect can be excluded as the origin for the reduced total magnetic moment of the $\mathrm{Co}_{1.4}\mathrm{Fe}_{1.6}\mathrm{O}_4$ film.

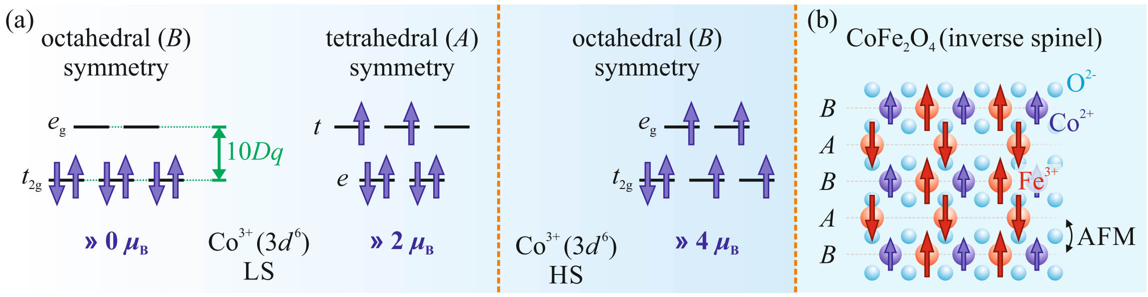

Fig. 7.5: (a) The occupation of the $3d$ states of Co^{3+} in the low-spin (LS) state at either octahedral B or tetrahedral A lattice sites, including the resulting net spin moments. The occupation of octahedrally coordinated Co^{3+} in the high-spin (HS) state is shown for comparison. (b) Antiferromagnetic (AFM) coupling between cations at octahedral B and tetrahedral A lattice sites for stoichiometric $CoFe_2O_4$ as an inverse spinel.

Our previous growth study [22] suggested for the $Co_{1.4}Fe_{1.6}O_4$ film in particular the existence of a second crystallographic phase, which was attributed to Co–Fe oxide precipitates in the film. These precipitates are not present in the $Co_{1.1}Fe_{1.9}O_4$ film. Both CoO and FeO are antiferromagnetic with bulk Néel temperatures of 293 K [165, 166] and 198 K [166], respectively. Including finite-size effects, which reduce the critical temperature, it can be assumed that a solid dispersion of CoO and FeO also has a Néel temperature fairly below 300 K, where the XAS/XMCD measurements were carried out. Hence, the Co–Fe oxide precipitates should be paramagnetic and consequently contribute only slightly, if at all, to the XMCD signal. The magnetic moments of soley the Co ferrite phase is thus slightly underestimated when applying the sum rules.

Assuming as worst case scenario that a second Co–Fe oxide phase forms for a Co content of $x > 1.1$ (cf. $Co_{1.1}Fe_{1.9}O_4$ film) and considering that both samples initially had equal Fe_3O_4 film thicknesses, the averaged magnetic moment per Co cation would only be reduced by at most $(17 \pm 4)\,\%$ for the $Co_{1.4}Fe_{1.6}O_4$ film compared with the $Co_{1.1}Fe_{1.9}O_4$ film. Thus, the resulting XAS signal from this phase would be too small to produce such a reduction of the magnetic moments. Moreover, it has been reported that doping of, e.g., paramagnetic ZnO or CuO with even small quantities of transition metal elements such as Co, Fe, and Ni, results in an unexpected low ferromagnetic behavior [269–272]. Furthermore, it has been demonstrated that CoO, FeO, CuO, and ZnO often exhibit defects such as (oxygen) vacancies, which can also lead to a non-negligible ferromagnetic behavior even above their Néel temperatures [273–276]. Thus, the averaged magnetic moment per Co cation would even be less reduced, comparing the stoichiometry $x = 1.4$ with $x = 1.1$ due to these effects.

In summary, considering all these possibilities, it is more plausible that the significantly lower total Co moment per ion of the $Co_{1.4}Fe_{1.6}O_4$ film is primarily caused by rather an increased amount of trivalent low-spin Co cations at octahedral B sites.

Additionally, the XA and XMCD spectra were analyzed simultaneously according to charge-transfer multiplet (CTM) calculations. In these calculations, the transitions from the occupied $2p$ state into the unoccupied $3d$ state in each transition metal cation located in an oxygen ligand field are calculated, taking into account multiplet effects and charge-transfer interactions. For $Co_xFe_{3-x}O_4$, the different transition metal cations can either be octahedrally or tetrahedrally coordinated by the surrounding oxygen anions due to its (inverse) spinel structure and can also be in high-spin state or low-spin state dependent on the crystal field. The respective XA and XMCD spectra were fitted by a weighted linear superposition, consisting of CTM contributions from the corresponding cationic states.

For the Co $L_{2,3}$ edges, both Co^{2+} and Co^{3+} cations were used to reproduce the data based on a reduced total Co moment per ion originating from low-spin Co^{3+} cations, as suggested before. The Co^{2+} cations were considered at both tetrahedral and octahedral sites with crystal fields of -0.6 eV and 0.8 eV (high-spin state), respectively. Thus, we conclude that the inversion of the spinel structure was not complete. The crystal fields are comparable with values used in previous studies of CoFe$_2$O$_4$ thin films [244]. Since it is reported that Co^{3+} cations preferably occupy octahedral lattice sites [239, 263, 266–268], only Co^{3+} cations in octahedral coordination were assumed for the analysis. Best fits were obtained for Co^{3+} cations in low-spin state with a crystal field of $10Dq = 2.1$ eV (cf. Fig. 7.6).

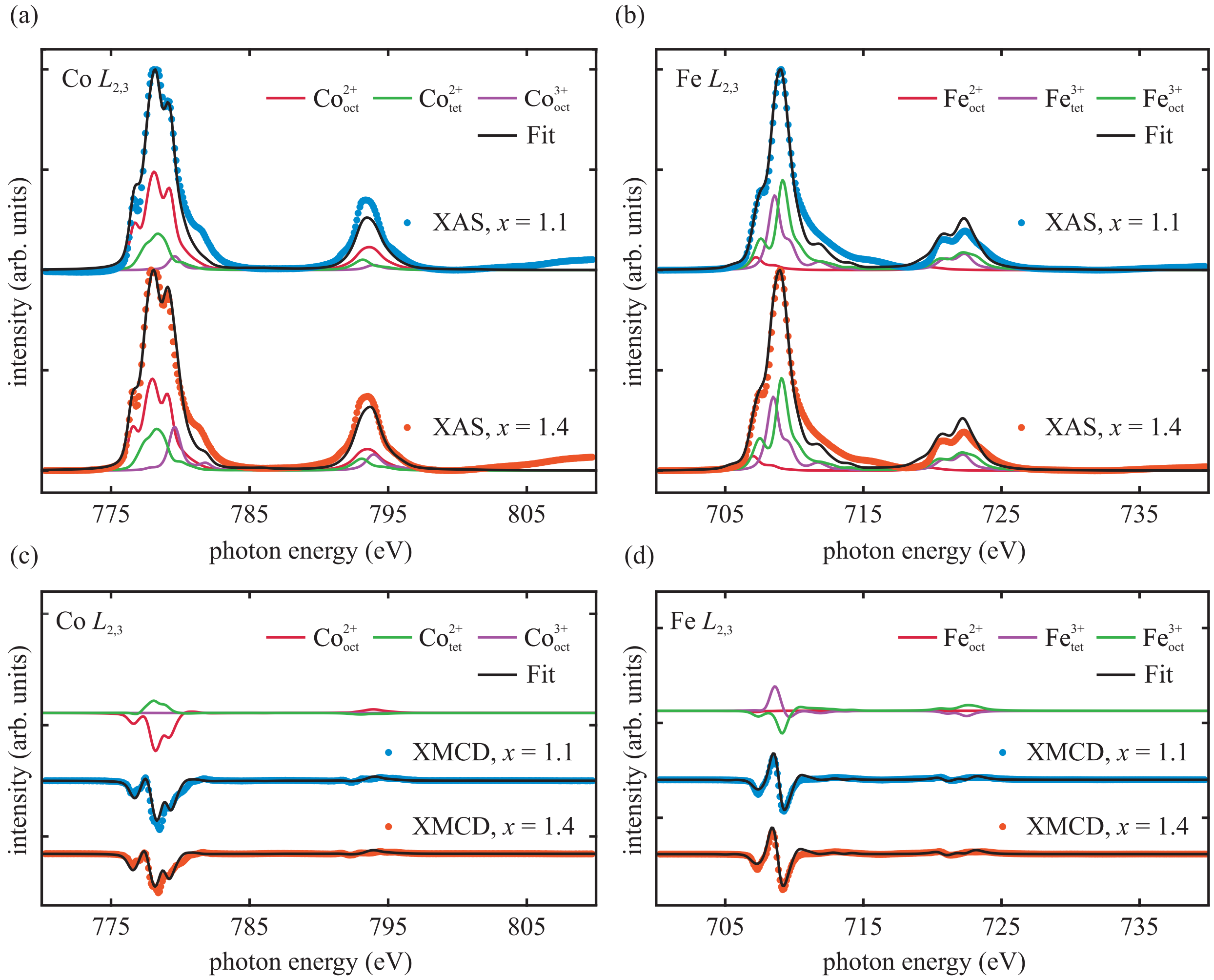

Fig. 7.6: XA and XMCD spectra of the Co $L_{2,3}$ and Fe $L_{2,3}$ edges with their corresponding CTM calculations (black lines) for each sample. The XA and XMCD spectra at the Co $L_{2,3}$ edge in (a,c), respectively, were fitted with superpositions of octahedral coordinated Co^{2+} and Co^{3+} cations and tetrahedral coordinated Co^{2+} cations. For the XA and XMCD spectra at the Fe $L_{2,3}$ edge in (b,d), respectively, superpositions of octahedral coordinated Fe^{2+} and Fe^{3+} cations and tetrahedral coordinated Fe^{3+} cations were used. The individual cationic contributions to the total CTM spectra are shown for each XA spectrum and each sample. For the XMCD spectra, only the individual cationic contributions of the Co$_{1.1}$Fe$_{1.9}$O$_4$ film are depicted for clarity, serving as a representative for the Co$_{1.4}$Fe$_{1.6}$O$_4$ film.

Regarding the Fe $L_{2,3}$ edges, Co ferrite should in principal solely contain Fe cations as Fe^{3+}. However, oxygen vacancies or the presence of Co^{3+} cations in the film can lead to the presence of small amounts of Fe^{2+} cations due to preserving charge neutrality of the films [244, 277]. In order to account for these effects, Fe^{2+} cations at octahedral sites and Fe^{3+} cations at both tetrahedral and octahedral sites were assumed based on our previous XAS and XMCD results of $CoFe_2O_4$ [244] and $NiFe_2O_4$ [278] thin films. The crystal fields were set to 1.15 eV for Fe^{2+}_{oct}, −0.5 eV for Fe^{3+}_{tet}, and 1.2 eV for Fe^{3+}_{oct} (high-spin state), which are in good accordance with values used in the literature for both Fe_3O_4 [279, 280] and $CoFe_2O_4$ [244]. The XA and XMCD spectra of our study with their corresponding best fits are depicted in Fig. 7.6.

The analysis revealed for the $Co_{1.1}Fe_{1.9}O_4$ film a cation distribution of

$$\left[Co^{2+}_{0.25}Fe^{3+}_{0.73}\right]_A \left[Co^{2+}_{0.80}Fe^{2+}_{0.18}Co^{3+}_{0.05}Fe^{3+}_{0.99}\right]_B O^{2-}_{4-\delta}$$

and for the $Co_{1.4}Fe_{1.6}O_4$ film a cation distribution of

$$\left[Co^{2+}_{0.34}Fe^{3+}_{0.59}\right]_A \left[Co^{2+}_{0.85}Fe^{2+}_{0.16}Co^{3+}_{0.21}Fe^{3+}_{0.85}\right]_B O^{2-}_{4-\delta}$$

with $\delta = 0.15 \pm 0.25$, which is in accordance with the value of δ calculated from relative intensity ratios of the Co $2p$, Fe $2p$, and O $1s$ core-level spectra of the AR-HAXPES measurements [22]. We like to point out that the values of the cation distribution have uncertainties of about 10 %. For both cation distributions, the stoichiometry determined from AR-HAXPES was taken into account. We further point out that the cation distribution of the $Co_{1.4}Fe_{1.6}O_4$ film includes both the $Co_xFe_{3-x}O_4$ phase and the Co–Fe oxide phase, which were reported in reference [22]. As discussed earlier, we expect that the effect due to the Co–Fe oxide phase is rather weak as the fraction of the ferrite phase in the film is considerably preponderant. Additionally, because the XA and XMCD spectra were fitted simultaneously and the crystallographic rock-salt phase should only contribute to the XAS signal, it should be contained within the limits of this fitting approach. Therefore, the determined cation distribution still mainly reflects the $Co_xFe_{3-x}O_4$ phase. Consistently with our previous assumptions, both $Co_xFe_{3-x}O_4$ films exhibit small amounts of Fe^{2+} and Co^{3+} cations, though the $Co_{1.4}Fe_{1.6}O_4$ film has a considerably larger amount. Since Fe^{3+} and Co^{2+} cations in both films still clearly predominate in terms of numbers, Fe^{2+} and Co^{3+} characteristic features do not contribute significantly in the (AR-)HAXPES and XA spectra.

In addition, the exact number of holes [$n_h(Co^{2+}_{oct}) = 2.89$, $n_h(Co^{2+}_{tet}) = 2.95$, $n_h(Co^{3+}_{oct}) = 3.83$, $n_h(Fe^{2+}_{oct}) = 3.82$, $n_h(Fe^{3+}_{oct}) = 4.89$, and $n_h(Fe^{3+}_{tet}) = 4.88$] of each film was extracted from the CTM calculations. As a consequence, we correct the total Co and Fe moments of the $Co_{1.1}Fe_{1.9}O_4$ film to (1.37 ± 0.09) μ_B/Co ion and (0.72 ± 0.05) μ_B/Fe ion, respectively. For the $Co_{1.4}Fe_{1.6}O_4$ film, we obtain a corrected total Co moment of (0.90 ± 0.06) μ_B/Co ion and a corrected total Fe moment of (0.74 ± 0.04) μ_B/Fe ion. Considering the stoichiometry determined by AR-HAXPES, we derive an overall magnetic moment of (2.88 ± 0.28) μ_B/f.u. for the $Co_{1.1}Fe_{1.9}O_4$ film and (2.44 ± 0.23) μ_B/f.u. for the $Co_{1.4}Fe_{1.6}O_4$ film at 300 K.

Based solely on the cation distribution determined from the CTM calculations and the theoretical spin moment of each individual cation, we obtain overall magnetic moments of (3.67 ± 0.25) μ_B/f.u. and (3.47 ± 0.25) μ_B/f.u. for the $Co_{1.1}Fe_{1.9}O_4$ film and $Co_{1.4}Fe_{1.6}O_4$ film, respectively. Since these estimates do not take into account thermal effects such as thermal agitation, they are not quite comparable with the experimentally derived values, and rather indicate the overall magnetic moments of both films at absolute zero, considering pure spin magnetic moments.

7.3.4 SQUID

In order to study the integral magnetic properties of the formed cobalt ferrite films, complementary SQUID measurements at 5 K and 300 K were carried out. The measured magnetization was converted into the unit μ_B/f.u. for each magnetization curve. The external magnetic field was varied from −5 T to 5 T. Figure 7.7 shows the respective magnetization curves for both samples.

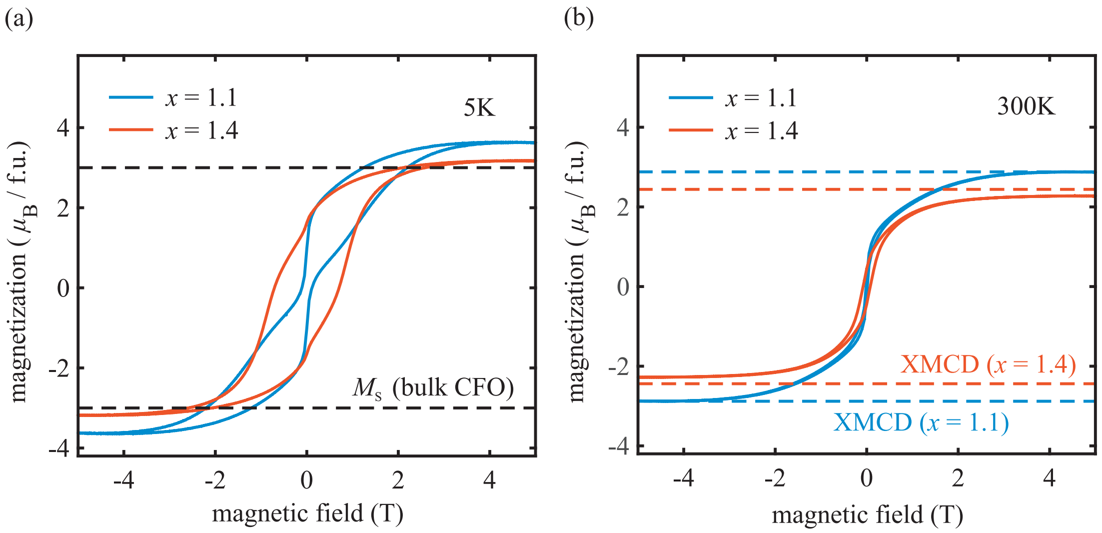

Fig. 7.7: SQUID measurements for the $Co_xFe_{3-x}O_4$ film with $x = 1.1$ and $x = 1.4$ at (a) 5 K and (b) 300 K. Dashed lines in (a) correspond to the values of the saturation magnetization M_s for bulk $CoFe_2O_4$ [9] with complete inverse spinel structure, whereas dashed lines in (b) correspond to the overall magnetic moments of both films as derived from the XMCD analysis.

The magnetization curves taken at 5 K and 300 K show the typical hysteresis loops for ferro-/ferrimagnetic materials for each sample. For the $Co_xFe_{3-x}O_4$ film with $x = 1.1$, the saturation magnetization of (3.63 ± 0.20) μ_B/f.u. at 5 K exceeds the theoretical value of 3 μ_B/f.u. of stoichiometric bulk $CoFe_2O_4$ [9] (dashed lines). Enhanced saturation magnetization was also reported for thinner $CoFe_2O_4$ [254, 281] and $NiFe_2O_4$ [282, 283] films, and was attributed to a partial inverse cation distribution with divalent cations occupying both octahedral B sites and tetrahedral A sites. According to our CTM calculations of the XAS/XMCD measurements and the resulting overall magnetic moments based solely on the determined cation distribution and the spin moment of each individual cation, the enhanced saturation magnetization in our case can also be ascribed to the partial inverse spinel structure.

For the $Co_xFe_{3-x}O_4$ film with $x = 1.4$, the saturation magnetization of (3.18 ± 0.20) μ_B/f.u. at 5 K is lower compared to the $Co_xFe_{3-x}O_4$ film with $x = 1.1$. It has been shown that the amount of Co in $Co_xFe_{3-x}O_4$ films strongly affects the net magnetization [239,240,266]. It was demonstrated that for Co concentrations of $1 < x < 2$, the saturation magnetization of the $Co_xFe_{3-x}O_4$ films decreases with increasing x [239, 240]. The lower saturation magnetization with a higher concentration of Co cations in the cobalt ferrite film was also found to be related to a partial inverse spinel structure in combination with the presence of Co^{3+} cations at octahedral B sites in the low-spin state, both of which are in accordance with our XAS/XMCD results. Since the spin-related magnetic moment of Co^{3+} cations in its low-spin state is 0 μ_B/f.u. at octahedral B sites [cf. Fig. 7.5 (a)], an increase in the amount of Co^{3+} at these lattice sites would consequently reduce the net magnetization.

Additionally, the magnetization curve for $Co_{1.1}Fe_{1.9}O_4$ recorded at 5 K exhibits a large jump in the magnetization at low magnetic fields. A similar but weaker jump can also be seen for the $Co_{1.4}Fe_{1.6}O_4$ film. Similar observations have been reported in the literature for cobalt ferrite films deposited on several substrates – e.g., MgO(001) or $SrTiO_3$(001) [238, 254, 284–286] – and their origins are still under discussion. Substrate induced strain effects [286], the presence of antiphase boundaries [238], and a second magnetic phase [254, 285] are commonly considered to be the reason for this behavior of the magnetization.

One may assume that a very thin Fe_3O_4 interlayer between cobalt ferrite film and $SrTiO_3$ substrate acts as a second magnetic phase, contributing also to the magnetization curves. Since the AR-HAXPES results indicate a homogeneous distribution of both Fe and Co cations [22], a very thin existing Fe_3O_4 film is unlikely but cannot be ruled out completely.

Furthermore, the crystallographic Co–Fe oxide rock-salt phase can be excluded as being responsible for this behavior of the magnetization. Since this second crystallographic phase is present exclusively in the $Co_{1.4}Fe_{1.6}O_4$ film, the magnetization curve of the $Co_{1.4}Fe_{1.6}O_4$ film should be the most pinched, assuming the second crystallographic phase is the culprit. However, the contrary is the case, and the magnetization curve of the $Co_{1.1}Fe_{1.9}O_4$ film is instead more pinched, which just does not contain this phase.

Rigato *et al.* [254] reported that a second ferrimagnetic phase, in their case, stemmed from the existence of pyramidal-shaped cobalt ferrite hut clusters, emerging from the surface, which dominate the magnetization curves more with decreasing film thickness of the cobalt ferrite film. According to the AFM results of both samples studied here (cf. Fig. 7.3), it is possible that the jump in the magnetic moment in Fig. 7.7 might also be attributed to this second magnetic phase due to pyramidal hut clusters at the surface of the ferrite film. Due to an increased volume fraction of the pyramidal-shaped cobalt ferrite hut clusters relative to the total film volume at lower film thicknesses, the second phase has a stronger contribution to the magnetization curves compared to cobalt ferrite films with higher film thicknesses (15 % volume fraction for the $Co_{1.1}Fe_{1.9}O_4$ film and 10 % volume fraction for the $Co_{1.4}Fe_{1.6}O_4$ film according to the AFM results). This may explain that the jump of the magnetic moment for the $Co_{1.1}Fe_{1.9}O_4$ film is more evident due to the larger fraction of the second hut cluster phase at the surface of the ferrite film, which is in accordance with the observations of Rigato *et al.* [254] and Coll *et al.* [238].

Compared to the saturation magnetization at 5 K the saturation magnetization at 300 K decreases from $(3.63 \pm 0.20)\ \mu_B$/f.u. to $(2.88 \pm 0.20)\ \mu_B$/f.u. for the $Co_{1.1}Fe_{1.9}O_4$ film and from $(3.18 \pm 0.20)\ \mu_B$/f.u. to $(2.28 \pm 0.20)\ \mu_B$/f.u. for the $Co_{1.4}Fe_{1.6}O_4$ film. Both saturation magnetizations at 300 K are in good agreement with the overall magnetic moments derived from the XAS/XMCD results also recorded at 300 K, confirming our analysis based on the CTM model. Comparing also the saturation magnetizations at 5 K of both samples with the overall magnetic moments based on the corresponding cation distribution and the theoretical spin moment of each cation species, the latter is larger than the measured value for the $Co_{1.4}Fe_{1.6}O_4$ film. The values of the $Co_{1.1}Fe_{1.9}O_4$ film agree nicely here as well. The deviation of the $Co_{1.4}Fe_{1.6}O_4$ film might very likely be related to the Co–Fe oxide precipitates mentioned earlier. In order to match the total magnetic moment of the film with the saturation magnetization of the SQUID results at 5 K, roughly 8 % of all Co^{2+} cations from the cation distribution need to be assigned to the Co–Fe oxide precipitates (a pure CoO rock-salt phase was assumed for simplicity). This value is slightly smaller than obtained from our consideration before, assuming that precipitates are build if the Co content exceeds $x = 1.1$.

Further, a temperature dependence of the saturation magnetization was also observed in other studies of cobalt ferrite thin films [238, 256, 285], cobalt ferrite nanoparticles [287–289], and cobalt ferrite single crystals [290]. In fact, the theoretical works of Bercoff and Bertorello [291] and Srivastava *et al.* [292] also showed a decrease of the magnetization of CFO with increasing temperatures, which is in accordance with the decrease in saturation magnetization of the $Co_xFe_{3-x}O_4$ films presented in this case study. Consequently, we can most plausibly ascribe the decrease in saturation magnetization as observed in our Co ferrite films to the general dependence of magnetization on temperature.

7.4 Conclusions

We prepared two Co-rich $Co_xFe_{3-x}O_4$ ultrathin films with stoichiometries $x = 1.1$ and $x = 1.4$ by means of intermixing epitaxial CoO/Fe_3O_4 bilayers on Nb-doped $SrTiO_3(001)$ via RSPE [22]. We performed a comprehensive analysis of the electronic and magnetic properties, employing both surface and bulk specific approaches. XAS and XMCD measurements across the Co $L_{2,3}$ and Fe $L_{2,3}$ edges in combination with charge-transfer multiplet calculations revealed the presence of Co^{3+} cations in the low-spin state at octahedral B sites and partial inverse spinel structures for both samples. A higher amount of low-spin Co^{3+} cations was found for the $Co_xFe_{3-x}O_4$ film with higher Co content x, resulting in a decreased Co spin moment per ion and a lower overall magnetic moment. The SQUID measurements revealed enhanced saturation magnetizations at 5 K, which can be explained by the partial inverse spinel structure. A second soft magnetic phase in the magnetization loops might be explained by islands present on the surfaces of both samples, as observed by AFM measurements.

7.5 Acknowledgments

The preparation of the Co ferrite films was performed on the beamline BM25-SpLine at the ESRF, Grenoble, France. We are grateful to Juan Rubio-Zuazo and G. Castro at the ESRF for providing assistance with using the beamline BM25-SpLine. We also acknowledge DESY (Hamburg, Germany), a member of the Helmholtz Association HGF, for the provision of experimental facilities. Parts of this research were carried out at PETRA III, and we would like to thank A. Gloskovskii and C. Schlüter for their excellent support during the beamtime. Furthermore, this research used resources of the Advanced Light Source, a DOE Office of Science User Facility under contract number DE-AC02-05CH11231. In addition, we thank Paul Steadman at DLS for giving us access to their SQUID magnetometer for the SQUID measurements. Financial support from the Deutsche Forschungsgemeinschaft and from the Open Access Publishing Fund of Osnabrück University is gratefully acknowledged.

Co Depending Strain Accumulation and Relief during Growth of Ultrathin $Co_xFe_{3-x}O_4$ Films

J. Thien[1], J. Rodewald[1], T. Pohlmann[1,2], K. Ruwisch[1], R. Fan[3], P. Steadman[3], F. Bertram[2], K. Küpper[1], and J. Wollschläger[1]

[1]*Department of Physics, Osnabrück University, 49076 Osnabrück, Germany*
[2]*Deutsches Elektronen-Synchrotron (DESY), Photon Science, 22607 Hamburg, Germany*
[3]*Diamond Light Source, Didcot OX11 0DE, United Kingdom*

Abstract

$Co_xFe_{3-x}O_4$ single thin films of high structural quality and with different Co content ($x = 0.6 - 1.2$) have been prepared by reactive molecular beam epitaxy on MgO(001) substrates. Their stoichiometry is confirmed by subsequent hard X-ray photoelectron spectroscopy measurements, which also reveal increasing Fe^{3+}/Fe^{2+} cation ratios for a higher Co content. The film growth of each film is extensively monitored by means of time-resolved (operando) specular X-ray diffraction measurements, demonstrating highly crystalline ordering and smooth film interfaces for each film independent of the Co content. Furthermore, all $Co_xFe_{3-x}O_4$ films exhibit enhanced compressive out-of-plane strain for the early growth stages, which partly releases with increasing film thickness. Additionally, the $Co_xFe_{3-x}O_4$ films with higher Co content show increasing vertical layer distances but also slightly increasing film roughnesses, which is supported by surface sensitive low-energy electron diffraction measurements on the final films. On the contrary, the substrate-film interface roughness decreases with increasing Co content, which is confirmed by X-ray reflectivity measurements. Moreover, saturation magnetization of these $Co_xFe_{3-x}O_4$ films as observed by superconducting quantum interference device measurements reduce significantly for higher Co contents.

8.1 Introduction

Among other transition metal (TM) ferrites, the TM ferrite $CoFe_2O_4$ (CFO, lattice constant $a_{\mathrm{CFO}} = 8.392\,\text{Å}$) is a key material in the field of spintronics. Deposited on a substrate with different lattice constant (heteroepitaxy), the strain induced by the lattice mismatch between the ferrite lattice and the substrate lattice is quite capable of leaving a great impact on the electronic, structural and magnetic properties of the ferrite film [254, 281, 293–295]. In particular, it has been reported that the strain in thinner ferrite films can modify the cationic distribution on different lattice sites [212], which in turn significantly affects, e.g., the electronic and magnetic properties of the ferrite films [282, 293, 296]. Therefore, substrate-induced strain can be specifically used for strain-engineering of ultrathin ferrite films to hugely improve the performance of ferrites for spintronic applications such as, e.g., spin-filters, where highly spin-polarized electrons are generated due to spin-dependent tunneling through ferrimagnetic barriers [9, 230, 297, 298]. However, in order to tailor the properties of these ultrathin ferrite films using strain, it is important to know the details of strain accumulation, especially during the very early stages of growth as well as strain relief during later growth stages [299]. Moreover, the initial growth stages as well as the interface of the films are also crucial for the quality of devices based on spin Hall magnetoresistance [300].

Hence, this work focuses on time-resolved (operando) X-ray diffraction (XRD) [209,299] to study the growth behavior and evolving strain of $Co_xFe_{3-x}O_4$ thin films with varying Co content $x = 0.6-1.2$ and a final total film thickness of (30 ± 2) nm prepared by reactive molecular beam epitaxy (RMBE). The $Co_xFe_{3-x}O_4$ films were grown on MgO(001) substrates (lattice constant $a_{\mathrm{MgO}} = 4.212\,\text{Å}$) due to the small lattice mismatch of about $-0.37\,\%$ (comparing two unit cells of MgO with a single unit cell of CFO), which provides almost perfect growth conditions for $Co_xFe_{3-x}O_4$ thin films on these substrates.

In addition, for a more conclusive and comprehensive analysis, further structural characterization by means of X-ray reflection (XRR) and low-energy electron diffraction (LEED) as well as electronic and magnetic characterization by means of hard X-ray photoelectron spectroscopy (HAXPES) and superconducting quantum interference device (SQUID), respectively, were performed.

8.2 Experimental details

Both the preparation and the *in situ* characterization of the $Co_xFe_{3-x}O_4$ films were carried out in an ultra high vacuum chamber with a base pressure of 1×10^{-10} mbar at beamline I07 [301] of the Diamond Light Source (DLS). Prior to film deposition, the MgO(001) substrates were cleaned at a temperature of 400 °C in a diluted O_2 atmosphere of 5×10^{-5}mbar to remove unwanted adsorbates (e.g. carbon) from the surfaces and to get well-defined surfaces [302]. Effectiveness of the cleaning process was examined by LEED. The $Co_xFe_{3-x}O_4$ films were grown by evaporation of metals from pure Co and Fe rods in a diluted O_2 atmosphere of 5×10^{-6}mbar, while keeping the substrates at a temperature of 250 °C, which was demonstrated to ensure good growth conditions for Fe_3O_4 thin films deposited on MgO(001) [194]. In order to steer the stoichiometry of the resulting $Co_xFe_{3-x}O_4$ films, the Co flux was varied, whereas the Fe flux was kept constant. Additionally, one Fe_3O_4 film ($Co_xFe_{3-x}O_4$ with $x = 0$) was grown under same conditions for comparison.

During film growth, XRD measurements were carried out in specular ($\theta - 2\theta$) geometry close to the (002) and (004) Bragg condition of MgO and $Co_xFe_{3-x}O_4$, respectively, to monitor the growth behavior of the ferrite films of different stoichiometry. Immediately after film deposition, LEED measurements and XRR measurements were performed at room temperature to examine the surface structure and crystallinity of the prepared $Co_xFe_{3-x}O_4$ film surfaces and to determine their final film thicknesses, respectively. For the XRD and XRR measurements, a photon energy of 21 keV and a two-dimensional Pilatus 100K detector was used.

Using a photon energy of 6 keV, HAXPES experiments were conducted at beamline P22 [303] of PETRA III at Deutsches Elektronen-Synchrotron (DESY) and at 7-ID [304] of the National Synchrotron Light Source II (NSLS-II) to examine the electronic structure and to determine the chemical composition of the $Co_xFe_{3-x}O_4$ films, having finished film growth, by means of Co $2p$, Fe $2p$, and O $1s$ core-level spectra. The spectra were calibrated according to the O $1s$ core-level at 530 eV [216, 305]. The stoichiometry x of each film was determined by evaluating relative intensity ratios of the Co $2p$ and Fe $2p$ spectra. The intensities were corrected by subtracting a Shirley background and normalized to the corresponding photoionization cross-sections from Scofield [306] as well as to the corresponding inelastic mean free paths calculated by the Tanuma, Powell, and Penn formula (TPP-2M) [90]. In addition, the O content was obtained analogously by including also the normalized intensities of the respective O $1s$ spectra in the relative intensity ratios. For all films, the obtained O stoichiometries match with the expected O stoichiometry in $Co_xFe_{3-x}O_4$, indicating negligible anionic and/or cationic defects.

The SQUID measurements were conducted at room temperature at the Diamond Light Source (DLS) to probe the integral magnetic properties of the $Co_xFe_{3-x}O_4$ films using a Quantum Design MPMS system. The magnetization curves recorded from $-5\,T$ to $5\,T$ were corrected with respect to the diamagnetic background, originating from the MgO substrates as well as from the sample holder.

8.3 Results and discussion

8.3.1 XRD

Fig. 8.1 shows the XRD scans along the $(00L)$ rod and across the (002) Bragg reflection of MgO during film deposition of the $Co_{0.9}Fe_{2.1}O_4$ film, serving as a representative also for the other $Co_xFe_{3-x}O_4$ films ($x = 0.6$ and $x = 1.2$).

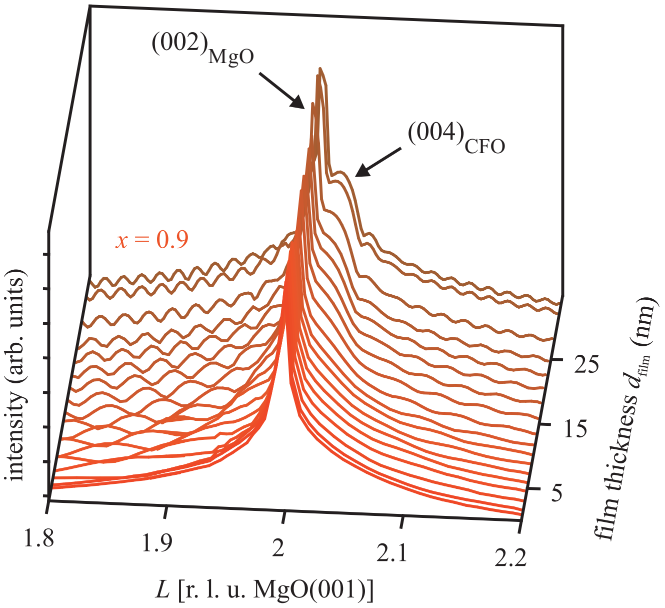

Fig. 8.1: XRD scans in specular ($\theta - 2\theta$) geometry close to the (002) Bragg peak of MgO. The (004) Bragg peak of the $Co_{0.9}Fe_{2.1}O_4$ film evolves during film deposition. Clear Laue oscillations are visible due to homogeneous film thickness and smooth interfaces.

The XRD scan of the pristine MgO(001) substrate shows exclusively a sharp and intense Bragg peak located at $L = 2$ corresponding to the (002) Bragg reflection of MgO with rock-salt structure. After the first few monolayers of $Co_{0.9}Fe_{2.1}O_4$ ($\sim 2\,nm$) are deposited on the MgO substrate, an initially very broad additional Bragg reflection at slightly larger L values becomes apparent as a shoulder of the (002) Bragg reflection of MgO. This can be ascribed to the increasing size of the (004) Bragg reflection of $Co_{0.9}Fe_{2.1}O_4$ due to its (inverse) spinel structure and vertical layer distance c_{vert} smaller than the MgO layer distance. With increasing coverage, the (004) Bragg reflection of $Co_{0.9}Fe_{2.1}O_4$ gains intensity and the peak width decreases constantly since more material contributes to coherent diffraction. Moreover, Laue fringes emerge due to the homogeneous and highly crystalline ordering of the film, which is consistent for the whole growth process.

Each XRD scan has been analyzed in the framework of kinematical diffraction theory to determine the vertical layer distance c_{vert}. The temporal evolution of the vertical layer distance c_{vert} is depicted in Fig. 8.2 for each $Co_xFe_{3-x}O_4$ film with $x > 0$ during film deposition.

The temporal evolution of the vertical layer distances c_{vert} in Fig. 8.2 shows that they are smaller than the layer distance $c^{250}_{CFO} = 2.103\,Å$ of bulk CFO at 250 °C considering thermal expansion [307] for all $Co_xFe_{3-x}O_4$ films during the entire growth process. As a consequence, each $Co_xFe_{3-x}O_4$ film is vertically compressively strained from the very first growth stages. Generally, this kind of

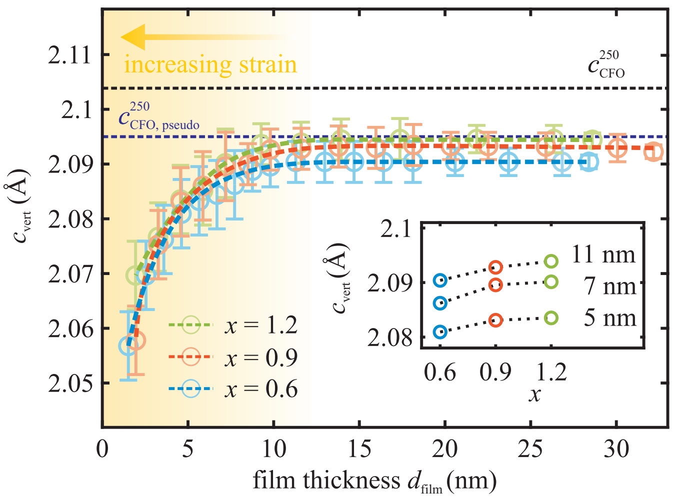

Fig. 8.2: Temporal evolutions of the vertical layer distance c_{vert} during growth of $Co_xFe_{3-x}O_4$ films. The corresponding dashed lines serve as guides to the eye. The vertical layer distance c^{250}_{CFO} of bulk CFO at 250 °C and the vertical layer distance $c^{250}_{CFO,\ pseudo}$ of pseudomorphic grown CFO at 250 °C are displayed for reference (dashed horizontal lines). The inset shows the dependence of the layer distances of the $Co_xFe_{3-x}O_4$ films representative at three different $Co_xFe_{3-x}O_4$ film thicknesses.

compressive strain in vertical direction is caused by lateral tensile strain, which can be expected, e.g., considering lateral adaptation of the $Co_xFe_{3-x}O_4$ unit cell to the slightly larger unit cell of MgO(001) (pseudomorphic growth). The vertical induced strain $\Delta c_{vert}/c_{vert}$ caused by the lateral distortion Δa_{lat} of the $Co_xFe_{3-x}O_4$ unit cells can be determined quantitatively according to Hashimoto *et al.* [52] via

$$\frac{\Delta c_{vert}}{c_{vert}} = \frac{2\nu}{\nu - 1}\frac{\Delta a_{lat}}{a_{lat}} \tag{8.1}$$

with the in-plane film lattice constant a_{lat} and $\nu = 0.367$ as the Poisson ration of CFO [54]. Assuming indeed a complete lateral adaptation of the $Co_xFe_{3-x}O_4$ lattice to the MgO(001) lattice and taking also into account the thermal expansion of both materials [307, 308], a lateral strain of $\Delta a_{lat}/a^{250}_{CFO} = 0.35\,\%$ is expected, resulting in a vertical compressive strain of $\Delta c_{vert}/c^{250}_{CFO} = -0.41\,\%$.

The expected vertical compression of the films is observed during late stages of growth (film thickness > 12 nm). For the early growth stages ($d_{film} < 12$ nm), however, the $Co_xFe_{3-x}O_4$ films show a significantly larger vertical compressive strain. Quite similar behavior has recently been observed in $Ni_xFe_{3-x}O_4$ ultrathin films ($0 \leq x \leq 1.5$) [299] and has been attributed as an effect arising from antiphase boundaries (APBs), which were reported to have a non-negligible influence on strain itself [190, 191]. APBs in the films lead to an increased lateral expansion and, consequently, to additional compressive vertical strain [cf. Eq. (8.1)]. With increasing film coverage, the compressive out-of-plane strain in each film diminishes constantly as the APB density decreases [192, 193] until, finally, only a constant residual strain of $(-0.5 \pm 0.1)\,\%$ remains at >12 nm film thickness, which is in accordance with the expected vertical strain assuming pseudomorphic growth.

Due to the small lattice mismatch, the incorporation of strain-releasing misfit dislocations in the films would not be presumed to occur until a critical film thickness of ~ 87 nm according to the model of Matthews and Blakeslee [58] for stoichiometric CFO on MgO(001), which is well above the thicknesses of all films prepared. Furthermore, we would like to point out that a tendential lower vertical compressive strain is observed the higher the Co content x in the $Co_xFe_{3-x}O_4$ films is (cf. inset of Fig. 8.2).

Figure 8.3 presents the experimental XRD data for each $Co_xFe_{3-x}O_4$ film recorded directly after film growth. For comparison, XRD diffractograms calcuated via kinematial diffraction theory

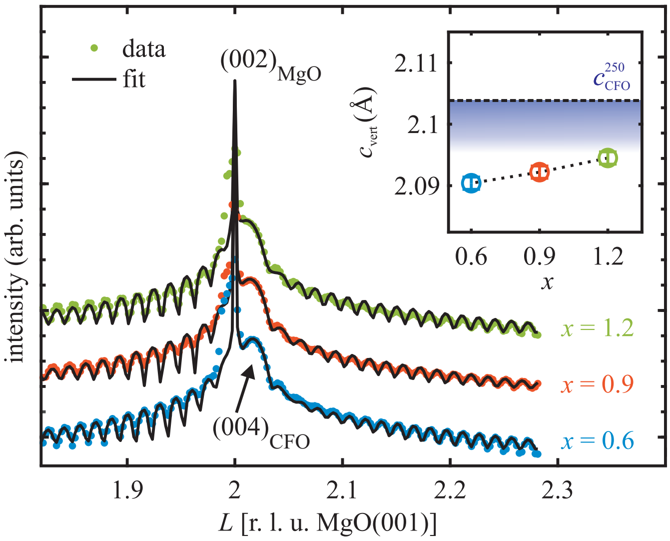

Fig. 8.3: XRD scans (dots) of each $Co_xFe_{3-x}O_4$ film ($x > 0$) recorded after deposition at 250 °C. Corresponding diffractograms calculated by kinematic diffraction theory (black solid lines) are also shown. The obtained vertical layer distances c_{vert} are presented in the inset. The dashed line in the inset marks the vertical layer distance c^{250}_{CFO} of bulk CFO at 250 °C considering thermal expansion. All films are vertically compressed with decreasing compression for increasing Co content.

are also shown, having optimized structural parameters as, e.g., vertical layer distance c_{vert} as well as roughnesses $\sigma_{\mathrm{f}}^{\mathrm{XRD}}$ and $\sigma_{\mathrm{s/f}}^{\mathrm{XRD}}$ of the film surface and substrate-film interface, respectively. The calculated diffractograms agree well with the experimental data. The respective structural parameters are shown in Table 8.1.

Tab. 8.1: Structural parameters of the prepared $Co_xFe_{3-x}O_4$ films ($x > 0$). The final $Co_xFe_{3-x}O_4$ film thickness $d_{\mathrm{film}}^{\mathrm{XRR}}$ has been determined by XRR, while the vertical layer distance c_{vert}, the film surface roughness $\sigma_{\mathrm{f}}^{\mathrm{XRD}}$, and the substrate-film interface roughness $\sigma_{\mathrm{s/f}}^{\mathrm{XRD}}$ of each final $Co_xFe_{3-x}O_4$ film were determined from the XRD analysis based on kinematic diffraction theory.

x	$d_{\mathrm{film}}^{\mathrm{XRR}}$ (nm)	c_{vert} (Å)	$\sigma_{\mathrm{f}}^{\mathrm{XRD}}$ (Å)	$\sigma_{\mathrm{s/f}}^{\mathrm{XRD}}$ (Å)
0.6	28.2 ± 0.2	2.090 ± 0.001	0.6 ± 0.2	7.1 ± 0.3
0.9	32.1 ± 0.2	2.092 ± 0.001	0.7 ± 0.2	6.7 ± 0.3
1.2	28.6 ± 0.2	2.095 ± 0.001	0.7 ± 0.2	6.3 ± 0.3

The (004) Bragg reflections of the $Co_xFe_{3-x}O_4$ films shift closer to the (002) Bragg reflection of MgO as the Co content increases, indicating a continuously increasing vertical layer distance with increasing Co content. All films are nearly atomically flat as demonstrated from the well-developed Laue fringes and deduced from the very small film surface roughnesses. Nevertheless, the roughness of the substrate-film interface is slightly enhanced for lower Co content in the $Co_xFe_{3-x}O_4$ films.

8.3.2 LEED

LEED images recorded at 150 eV electron energy directly after film growth are displayed for each $Co_xFe_{3-x}O_4$ film in Fig. 8.4. A typical LEED image of the pristine MgO(001) substrate after the cleaning procedure is displayed as well.

The diffraction pattern of the cleaned MgO(001) substrate features a clear square (1 × 1) surface unit cell (reciprocal unit vectors point in [110] and [$\bar{1}$10] directions) with sharp reflections and low background intensity, indicating a well-ordered and crystalline MgO(001) surface with low defect density.

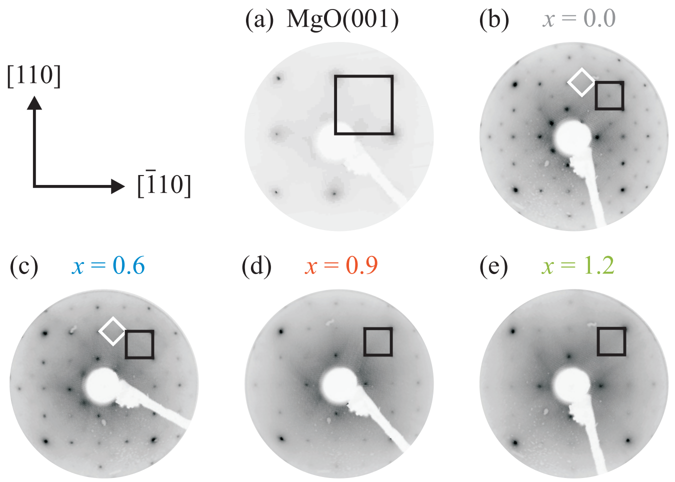

Fig. 8.4: LEED pattern of the cleaned MgO(001) substrate and each $Co_xFe_{3-x}O_4$ film recorded at an electron energy of 150 eV. The black squares indicate the respective (1×1) surface unit cells of substrate and film. The white squares indicate the $(\sqrt{2} \times \sqrt{2})R45°$ superstructure unit cells.

For the $Co_xFe_{3-x}O_4$ film with $x = 0$ (Fe_3O_4), the LEED pattern also shows a clear square fundamental (1×1) surface unit cell (reciprocal unit vectors also point in [110] and [$\bar{1}$10] directions), which is approximately two times smaller than the surface unit cell of MgO(001) due to the almost doubled size of the surface unit cell in real space. Additionally, a $(\sqrt{2} \times \sqrt{2})R45°$ superstructure is visible, which is typical for well-ordered Fe_3O_4 surfaces [18, 309, 310].

As the Co content x in the $Co_xFe_{3-x}O_4$ films increases, the intensity of the $(\sqrt{2} \times \sqrt{2})R45°$ superstructure diffraction spots decreases until they vanish completely for $x > 0.6$. The diffraction pattern of the fundamental (1×1) structure, however, shows intense and sharp diffraction peaks. Furthermore, a marginal increase of the background intensity with increasing Co content is observable, pointing to film surfaces with more defects for the $Co_xFe_{3-x}O_4$ films with a higher Co content. This is in accordance with the reported XRD results above (cf. film surface roughnesses σ_f^{XRD} in Table 8.1).

8.3.3 XRR

The X-ray reflectivity scans of all $Co_xFe_{3-x}O_4$ films recorded directly after film deposition are depicted in Fig. 8.5 dependent on the vertical scattering vector q. Each reflectivity curve has been analyzed according to the Parratt algorithm [128] and the Névot-Croce roughness model [130]. For comparison, corresponding calculated reflectivity curves are shown in Fig. 8.5 as well. The fits are based on a basic one-film-plus-substrate model, in which film thickness, interface roughnesses, and refractive indices have been used as free fitting parameters. For the refractive index of the substrate, literature values [311] were used, whereas for refractive indices of the the $Co_xFe_{3-x}O_4$ films a deviation of ±5 % from the literature value [311] of stoichiometric $CoFe_2O_4$ was allowed.

All reflectivity curves exhibit clear intensity oscillations (Kiessig-Fringes) due to interference of the beams reflected from smooth film surface and substrate-film interfaces. In each reflectivity curve, the intensity oscillations show only one periodicity, indicating the formation of single $Co_xFe_{3-x}O_4$ films, which is in accordance with the assumed model. Moreover, the calculated reflectivity curves agree well with the experimental data for all samples. This confirms the used model and the formation of single $Co_xFe_{3-x}O_4$ films.

In comparison to the $Co_xFe_{3-x}O_4$ film with $x = 0$, the films with a Co content of $x > 0$ feature a damping of the intensity oscillations due to an increased interface roughness $\sigma_{s/f}^{XRR}$ between MgO substrate and $Co_xFe_{3-x}O_4$ film. This effect is somewhat more pronounced for the $Co_xFe_{3-x}O_4$ films with less Co content (cf. inset Fig. 8.5), indicating a steadily rougher substrate-film interface

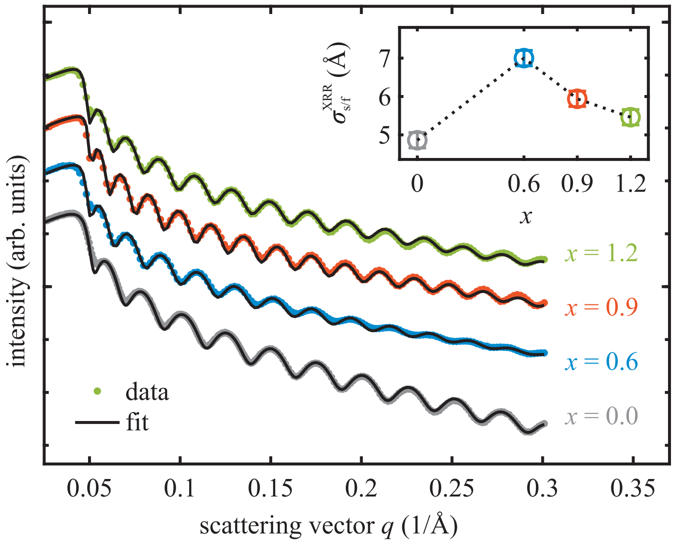

Fig. 8.5: Reflectivity curves and respective fits (black solid lines) of all prepared $\mathrm{Co}_x\mathrm{Fe}_{3-x}\mathrm{O}_4$ films with different Co content ($0 \leq x \leq 1.2$). The inset shows the interface roughness $\sigma_{\mathrm{s/f}}^{\mathrm{XRR}}$ between MgO substrate and each $\mathrm{Co}_x\mathrm{Fe}_{3-x}\mathrm{O}_4$ film extracted from the respective fits.

the lower the amount of Co in the films, which is also confirmed by the XRD analysis based on kinematic diffraction theory (cf. Table 8.1). Compared to XRD, XRR is more sensitive to interfacial roughness, meaning the XRR roughness results will be more reliable. Overall, the surface and interface roughnesses obtained from the fits of the XRR curves agree well with the corresponding roughnesses derived from the kinematic diffraction theory simulations of the XRD measurements.

8.3.4 HAXPES

The Co 2*p* and Fe 2*p* core-level spectra of the HAXPES measurements of all prepared $\mathrm{Co}_x\mathrm{Fe}_{3-x}\mathrm{O}_4$ films recorded after deposition are shown in Fig. 8.6. Both spectra show $2p_{1/2}$ and $2p_{3/2}$ photoelectron peaks as a result of spin-orbit coupling.

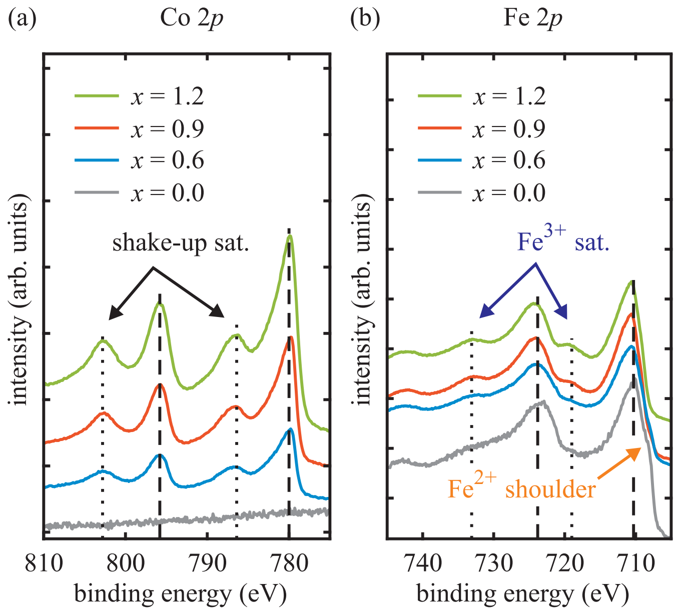

Fig. 8.6: (a) Co 2*p* and (b) Fe 2*p* core-level spectra of all prepared $\mathrm{Co}_x\mathrm{Fe}_{3-x}\mathrm{O}_4$ films with different Co content. Dotted black lines indicate the positions of Co^{2+} shake-up satellites in (a) and the positions of the Fe^{3+} charge-transfer satellite peaks in (b). Dashed black lines indicate the positions of the respective main peaks in (a) and in (b) for $\mathrm{Fe}_3\mathrm{O}_4$ ($x = 0$).

All Co 2*p* core-level spectra of the $\mathrm{Co}_x\mathrm{Fe}_{3-x}\mathrm{O}_4$ films with $x > 0$ show two main peaks (Co $2p_{1/2}$ and Co $2p_{3/2}$), which are located at binding energies of about 795.8 eV and 780.0 eV. Each main peak is accompanied by one (shake-up) satellite peak at $\sim 6\,\mathrm{eV}$ higher binding energies characteristic for divalent Co cations [242, 252, 312]. The shape of the presented Co $2p$ spectra is therefore consistent with Co^{2+} incorporated in ferrite films [242].

The Fe $2p$ core-level spectrum of the $Co_xFe_{3-x}O_4$ film with $x = 0$ (magnetite) reveals two main peaks of Fe $2p_{1/2}$ and Fe $2p_{3/2}$ at binding energies of about $723.8\,\mathrm{eV}$ and $710.3\,\mathrm{eV}$, respectively. The Fe $2p_{3/2}$ peak shows a shoulder at its lower binding energy side due to the presence of Fe^{2+} cations [313]. Furthermore, no apparent (charge-transfer) satellite can be observed between the Fe $2p_{1/2}$ and Fe $2p_{3/2}$ peaks due to mixed Fe^{3+} and Fe^{2+} valence states as known well from magnetite [216].

As the Co content in the $Co_xFe_{3-x}O_4$ films increases ($x > 0$), both the Fe $2p_{1/2}$ peak and Fe $2p_{3/2}$ peak shift to higher binding energies. In addition, the Fe^{2+} related shoulder vanishes for higher Co content and Fe^{3+} charge-transfer satellites at $\sim 719.0\,\mathrm{eV}$ and $\sim 733.0\,\mathrm{eV}$ arise, which become more pronounced with increasing Co content. All three observations point to increasing Fe^{3+}/Fe^{2+} ratios and are expected for cobalt ferrite films with increasing Co content [257].

8.3.5 SQUID

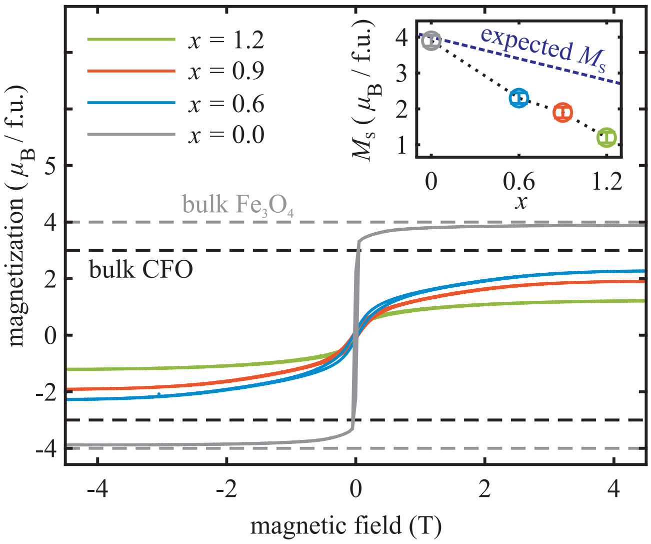

Fig. 8.7: SQUID magnetization curves at room temperature of each $Co_xFe_{3-x}O_4$ film. Dashed gray and black lines denote literature values of the saturation magnetization for stoichiometric bulk Fe_3O_4 ($x = 0$) and CFO ($x = 1$), respectively, considering solely spin magnetic moments [9]. The inset shows the saturation magnetization M_s of each film dependent on the Co amount. Here, the dashed line indicates expected M_s, where a gradual substitution of Fe^{2+} cations by Co^{2+} cations on octahedral sites in a perfect inverse spinel structure has been assumed without taking into account cationic orbital magnetic moments.

Fig. 8.7 presents the room temperature SQUID magnetization curves of all $Co_xFe_{3-x}O_4$ films. All films feature the expected typical ferrimagnetic behavior. With a saturation magnetization of about $3.9\,\mu_B$/f.u., the saturation magnetization of the Fe_3O_4 film ($Co_xFe_{3-x}O_4$ with $x = 0$) coincides well with its literature bulk value [9] considering experimental uncertainties. As the amount of Co in the films increases, an almost linear decrease of the saturation magnetization is observed. Generally, reducing of saturation magnetization with increasing Co content is expected due to the lower spin magnetic moment of Co^{2+} ($3\,\mu_B$) compared to Fe^{2+} ($4\,\mu_B$) and assuming the same inversion of the spinel crystal structure, where Co^{2+} cations replace only for Fe^{2+} cations on octahedral sites (cf. dashed line in Fig. 8.7). However, the experimentally determined values drastically undercut these expectations, which has also been reported before for $Co_xFe_{3-x}O_4$ thin films on MgO substrates [180, 242, 257, 314] and cannot be explained by the lower spin magnetic moment of Co^{2+} cations alone. However, since the magnetite film does not exhibit such discrepancies, it is reasonable to assume that the unanticipated strong decrease in saturation magnetization is mainly due to the incorporation of Co cations and does not originate, e.g., from APBs, which can potentially be present in all $Co_xFe_{3-x}O_4$ films, due to similar lattice mismatches with respect to the MgO(001) substrates. For example, the observed decrease could be related to an altered magnetostriction of the samples (magnetostriction constant $\lambda_{Fe_3O_4} = -25\,\mathrm{ppm}$ for Fe_3O_4 [315] compared to $\lambda_{CFO} = -245\,\mathrm{ppm}$ for $CoFe_2O_4$ [315]), which in turn would also affect the magnetization [314].

8.4 Summary and conclusions

In summary, the growth behavior and evolving strain of $Co_xFe_{3-x}O_4$ single thin films with stoichiometries $x = 0.6 - 1.2$ grown on MgO(001) have been monitored by operando time-resolved specular XRD measurements, which were analyzed using full kinematic diffraction theory. For each film, highly crystalline ordering is observed throughout the whole film growth. However, up to a film thickness of $\sim 12\,\mathrm{nm}$, all $Co_xFe_{3-x}O_4$ films exhibit enhanced vertical compressive strain, which partly releases with increasing film thickness. The residual constant vertical strain for film thicknesses above 12 nm is reconcilable with the model of pseudomorphic growth on MgO substrates. Furthermore, the vertical layer distance of the $Co_xFe_{3-x}O_4$ films increases with increasing Co content, while all films exhibit overall very small surface roughnesses. Nevertheless, LEED measurements point to a slight increase of surface defects with increasing Co content. In contrast to this, the roughness of the substrate-film interface decreases for increasing Co content as indicated by XRR measurements. HAXPES experiments confirm the underlying stoichiometry of the $Co_xFe_{3-x}O_4$ films and reveal a reduced amount of Fe^{2+} cations for higher x due to the expected gradual replacement of Fe^{2+} by Co^{2+}. As can be seen from the SQUID measurements, this cationic replacement has a great impact on the magnetic properties of the films and leads to a significantly reduced saturation magnetization.

Finally, considering the evolving strain of the different $Co_xFe_{3-x}O_4$ films produced, our results may open up new perspectives for strain engineering physical properties of ultrathin $Co_xFe_{3-x}O_4$ films depending on the amounts of Co. Accurate knowledge of the strain accumulation in the films provided here allows specific physical (magnetic or electronic) properties to be targeted to meet or even surpass the criteria required for the films to be used in spintronics, e.g., as spin-filters.

8.5 Acknowledgements

We acknowledge Diamond Light Source for time on I07 under proposal SI20857. We also acknowledge DESY (Hamburg, Germany), a member of the Helmholtz Association HGF, for the provision of experimental facilities. Parts of this research were carried out at PETRA III and we would like to thank A. Gloskovskii and C. Schlüter for their excellent support during the beamtime. This research also used resources of the National Synchrotron Light Source II, a U.S. Department of Energy (DOE) Office of Science User Facility operated for the DOE Office of Science by Brookhaven National Laboratory under Contract No. DE-SC0012704. Furthermore, we gratefully acknowledge financial support from the Deutsche Forschungsgemeinschaft (DFG, grant nos. KU2321/6-1 and WO533/20-1).

9 Summary and outlook

This work deals with the growth of some specially selected ferrites, namely magnetite and cobalt ferrite, and their thorough structural, electronic, and magnetic characterization to further advance their potential use in spintronic applications. With respect to the presented results, the work at hand can be divided into four principle parts.

The first part is primarily concerned with the structural properties of epitaxially grown Fe_3O_4 films of different thicknesses grown on Nb-doped $SrTiO_3(001)$ substrates by RMBE (cf. Chap. 5). The comprehensive structural characterization of the films is carried out by the complementary characterization methods HRTEM, GIXRD, XRD, and LEED, while the film stoichiometries are verified by (soft) XPS. It is found that each film is subject to strong compressive strain in the vertical direction with simultaneous rather negligible tensile strain in the lateral direction. Here, the formation of misfit dislocations at the atomically sharp and well-defined interface between the film and substrate leads to an almost complete relaxation of the lateral film lattice constants toward literature bulk value. The observed compressive strain in the vertical direction, however, contradicts both the assumption of pseudomorphic growth and the expected strain associated with the incorporation of dislocations. Further investigations need to be carried out with a larger number of samples, whose film thicknesses span a much wider range, to find the definitive cause for this behavior. In particular, in order to identify a possible influence of the interfacial dislocations, sample thicknesses in the monolayer range are required that are below the critical thickness at which dislocation incorporation begins.

In the second part, additional CoO films of different film thicknesses are deposited on top of such $Fe_3O_4/SrTiO_3(001)$ heterostructures with the Fe_3O_4 film thickness kept constant (cf. Chap. 6). Afterward, the effects of PDA on the bilayer stacks are studied *in situ* in a dilute molecular oxygen atmosphere, aiming to demonstrate an improved synthesis technique for the formation of $CoFe_2O_4$ films by thermally mediated interdiffusion without any residual CoO top layer. After each PDA step, (soft) XPS, HAXPES, GIXRD, and XRD measurements are performed to monitor the electronic and structural variations, indicating the onset of interdiffusion of both oxide films for annealing temperatures exceeding 350 °C. As the annealing temperature increases, a gradual replacement of Fe^{2+} cations by Co^{2+} cations is observed both in the near-surface regions and in deeper layers accompanied by a transition from Fe^{2+} to Fe^{3+}. These observations can be ascribed to the successful formation of cobalt ferrite ($Co_xFe_{3-x}O_4$) films. Both the PDA temperature required for the full interdiffusion and the resulting stoichiometry x of the final $Co_xFe_{3-x}O_4$ films are strongly dependent on the initial CoO film thickness relative to the Fe_3O_4 film thickness, i.e., for a larger initial CoO film thickness, a higher PDA temperature is required and larger will also be the Co content in the film. Complete intermixing of the respective bilayer stacks as well as the formation of single $Co_xFe_{3-x}O_4$ films with stoichiometries $x = 0.6 - 1.4$ and without additional CoO film on top is confirmed by AR-HAXPES and XRR after the last PDA steps. Moreover, the final cobalt ferrite films demonstrate high structural quality comparable with cobalt ferrite films prepared by conventional film preparation methods. Additionally, they exhibit high compressive strain in the vertical direction and high tensile strain in the lateral direction. Hence, the $Co_xFe_{3-x}O_4$ films produced show the same inverted behavior as Fe_3O_4 thin films directly grown on $SrTiO_3(001)$ substrates, which therefore also needs further systematic investigation and elucidation. Regardless, a secondary rock-salt phase of Co–Fe oxide precipitates is also observed along with the ferrite spinel phase in the $Co_{1.4}Fe_{1.6}O_4$ film, which was prepared from the bilayer stack with the initially thickest CoO film. This secondary phase is formed from a solid dispersion of FeO in CoO due to the initial excess of CoO provided with respect to the Fe_3O_4 film and the formation of $Co_xFe_{3-x}O_4$. The Co–Fe oxide precipitates are arranged as columnar grown microstructures in the vertical direction.

The impact of the specific cationic ordering as well as this additional Co–Fe oxide phase on the magnetic properties of the two Co-richest cobalt ferrite thin films ($x = 1.1$ and $x = 1.4$) prepared by this novel synthesis technique is the subject of the next part (cf. Chap. 7). Therefore, XAS, XMCD, and SQUID measurements are performed to examine the individual cationic moments and the cation distribution, as well as to probe the integral magnetic properties of the (Co-rich) cobalt ferrite films. The findings are supported by CTM calculations, showing excellent agreement with the experimental data. Both cobalt ferrite films exhibit partially inverse spinel structure with Co^{3+} cations in low-spin state on octahedral lattice sites. However, for the cobalt ferrite film with higher Co content ($x = 1.4$), a drastically lower averaged magnetic moment of the Co ions is obtained, resulting in an overall lower film magnetization. This can be attributed to a significantly increased fraction of Co^{3+} cations being in the low-spin state in the (inverse) spinel crystal structure in combination with the additionally observed Co–Fe oxide phase. Though, compared to the reduction of magnetic moment per Co atom caused by the Co^{3+} cations, the effect due to the Co–Fe oxide phase is expected to be much smaller and hence less significant. Furthermore, a second soft (ferri)magnetic phase in the M vs H curves of the SQUID measurements is observed, which is more pronounced for the $Co_{1.1}Fe_{1.9}O_4$ film than it is for the $Co_{1.4}Fe_{1.6}O_4$ film. It is suspected that this soft (ferri)magnetic phase is related to cobalt ferrite islands at the surface, as suggested by AFM measurements of the surface morphology of the films.

This alternative approach of preparing cobalt ferrite (ultra)thin films by solid-phase reactive epitaxy of CoO/Fe_3O_4 bilayer stacks yields very promising results that compete very well with conventional film preparation methods such as sputter deposition or reactive molecular beam epitaxy. However, this method should be further applied also to the synthesis of other transition metal ferrites such as $MnFe_2O_4$ and $ZnFe_2O_4$ to verify its general validity for the ferrite film preparation. Moreover, the discovery of the second additional rock-salt phase, which is presumed to be antiferromagnetic just below room temperature and paramagnetic at room temperature, in the otherwise ferrimagnetic film could be of great interest to spintronics, where antiferromagnets are often used to pin the magnetization of a ferro-/ferrimagnet. The lateral coexistence of both phases could unify AFM/FM bilayers into one layer, where both magnetic phases are present. Therefore, future plans are to use this novel synthesis technique to prepare even more Co-rich cobalt ferrite films in order to push the formation of the second phase and to study its influence on the electronic and magnetic film properties in more detail.

In the last part, single-phase $Co_xFe_{3-x}O_4$ thin films of different stoichiometries x are grown epitaxially by RMBE on MgO(001) substrates to explore the growth behavior of these films in relation to Co content when deposited on a substrate that inherently provides them with growth conditions less favorable for defect formation compared to $SrTiO_3$ substrates (cf. Chap. 8). The growth of each film is monitored *in situ* and in real-time by (operando) specular XRD measurements during the growth process. These measurements demonstrate the growth of highly crystalline ordered cobalt ferrite films with smooth film interfaces independent of the film stoichiometry. Yet, with increasing Co content, the surface roughness of the films increases slightly, while the roughness of the substrate-film interface decreases, which is also confirmed by LEED and XRR. In addition, all films up to a film thickness of about 12 nm show a significantly larger vertical compressive strain compared to the expected strain when assuming pseudomorphic growth and taking into account the corresponding bulk lattice constants. This effect is even more pronounced at thinner film thicknesses than it is at thicker ones and can be explained by an increased density of APBs, entailing an enhanced lateral expansion of the film. For film thicknesses above 12 nm, the vertical compressive strain then agrees very well with the expected strain behavior, corresponding to the lateral adaptation of the films to the underlying substrate, due to the negligible effect of APBs for higher film thicknesses. Furthermore, HAXPES measurements reveal a gradual substitution of Fe^{2+} cations by Co^{2+} cations in the spinel crystal structure with increasing Co content, which is also consistent with the anticipated behavior when film stoichiometry is progressively increased above $x = 0$. This cationic replacement, in turn, has a noticeable effect on the magnetic properties of the films, such that their saturation magnetization is greatly reduced, which might be related to altered film magnetostriction constants. The latter could be verified by additional magnetostriction measurements, e.g., with a conventional strain gauge. Additionally, XAS/XMCD measurements are planned in combination with CTM calculations and HRTEM measurements to correlate the obtained saturation magnetizations of the films with their cationic distribution and to evaluate the density of APBs in the films as they might also be responsible for the lower saturation magnetizations as reported in the works of other research groups.

In conclusion, both conventional and rather non-conventional film preparation techniques were successfully employed in this work to study high-quality ultrathin magnetite and cobalt ferrite films. Using a multi-technique approach, comprehensive and valuable information on the respective structural, chemical, electronic, and magnetic film properties could be gathered, leading to a rather thorough and conclusive picture that is also well consistent with corresponding model calculations. However, for these films to be considered at all for their application in spintronic devices, further studies are required that shed light on the transport properties and, in the case of cobalt ferrite, ensure its insulating character.

10 List of publications

1. T. Pohlmann, M. Hoppe, J. Thien, A. B. Dey, A. Alexander, K. Ruwisch, O. Gutowski, J. Röh, A. Gloskovskii, C. Schlueter, K. Küpper, and J. Wollschläger, F. Bertram
   "Time-resolved x-ray diffraction and photoelectron spectroscopy investigation of the reactive molecular beam epitaxy of Fe_3O_4 ultrathin films"
   Physical Review B **105**, 045412 (2022);
   doi:10.1103/PhysRevB.105.045412
2. J. Thien, J. Bahlmann, A. Alexander, K. Ruwisch, J. Rodewald, T. Pohlmann, M. Hoppe, F. Alarslan, M. Steinhart, B. Altuncevahir, P. Shafer, C. Meyer, F. Bertram, J. Wollschläger, and K. Küpper
   "Cationic Ordering and Its Influence on the Magnetic Properties of Co-Rich Cobalt Ferrite Thin Films Prepared by Reactive Solid Phase Epitaxy on Nb-Doped $SrTiO_3(001)$"
   Materials **15**, 46 (2022);
   doi:10.3390/ma15010046
3. L. Guo, J. Klein, J. Thien, M. Philippi, M. Haase, J. Wollschläger, and M. Steinhart
   "Phenolic Resin Dual-Use Stamps for Capillary Stamping and Decal Transfer Printing"
   ACS Applied Materials & Interfaces **13**, 49567–49579 (2021);
   doi:10.1021/acsami.1c17904
4. T. Pohlmann, T. Kuschel, J. Rodewald, J. Thien, K. Ruwisch, F. Bertram, E. Weschke, P. Shafer, J. Wollschläger, and K. Küpper
   "Cation- and lattice-site-selective magnetic depth profiles of ultrathin $Fe_3O_4(001)$ films"
   Physical Review B **102**, 220411(R) (2020);
   doi:10.1103/PhysRevB.102.220411
5. J. Thien, J. Bahlmann, A. Alexander, M. Hoppe, T. Pohlmann, K. Ruwisch, C. Meyer, F. Bertram, K. Küpper, and J. Wollschläger
   "Effects of Post-deposition Annealing on Epitaxial CoO/Fe_3O_4 Bilayers on $SrTiO_3(001)$ and Formation of Thin High-Quality Cobalt Ferrite-like Films"
   The Journal of Physical Chemistry C **124**, 23895–23904 (2020);
   doi:10.1021/acs.jpcc.0c05503
6. J. Rodewald, J. Thien, T. Pohlmann, M. Hoppe, F. Bertram, K. Kuepper, and J. Wollschläger
   "Real-time monitoring the growth of strained off-stoichiometric $Ni_xFe_{3-x}O_4$ ultrathin films on MgO(001)"
   Applied Physics Letters **117**, 011601 (2020);
   doi:10.1063/5.0013925
7. J. Rodewald, J. Thien, K. Ruwisch, F. Bertram, K. Kuepper, and J. Wollschläger
   "Enhanced magnetization of ultrathin $NiFe_2O_4$ films on $SrTiO_3(001)$ related to cation disorder and anomalous strain"
   Physical Review Materials **4**, 064404 (2020);
   doi:10.1103/PhysRevMaterials.4.064404

8. J. Rodewald, J. Thien, T. Pohlmann, M. Hoppe, F. Timmer, F. Bertram, K. Kuepper, and J. Wollschläger
   ”Formation of ultrathin cobalt ferrite films by interdiffusion of Fe_3O_4/CoO bilayers”
   Physical Review B **100**, 155418 (2019);
   doi:10.1103/PhysRevB.100.155418
9. M. Philippi, C. You, C. P. Richter, M. Schmidt, J. Thien, D. Liße, J. Wollschläger, J. Piehler, and M. Steinhart
   ”Close-packed silane nanodot arrays by capillary nanostamping coupled with heterocyclic silane ring opening”
   RSC Advances **9**, 24742–24750 (2019);
   doi:10.1039/C9RA03440D
10. R. Silber, O. Stejskal, L. Beran, P. Cejpek, R. Antoš, T. Matalla-Wagner, J. Thien, O. Kuschel, J. Wollschläger, M. Veis, T. Kuschel, and J. Hamrle
    ”Quadratic magneto-optic Kerr effect spectroscopy of Fe epitaxial films on MgO(001) substrates”
    Physical Review B **100**, 064403 (2019);
    doi:10.1103/PhysRevB.100.064403

Literature

[1] S. Bhatti, R. Sbiaa, A. Hirohata, H. Ohno, S. Fukami and S. N. Piramanayagam. "Spintronics based random access memory: a review". *Mater. Today*, 20, 530–548, 2017. doi:10.1016/j.mattod.2017.07.007.

[2] S. A. Wolf, A. Y. Chtchelkanova and D. M. treger. "Spintronics - A retrospective and perspective". *IBM J. Res. Dev.*, 50, 101–110, 2006. doi:10.1147/rd.501.0101.

[3] A. Hirohata, K. Yamada, Y. Nakatani, I.-L. Prejbeanu, B. Diény, P. Pirro and B. Hillebrands. "Review on spintronics: Principles and device applications". *J. Magn. Magn. Mater.*, 509, 166711, 2020. doi:10.1016/j.jmmm.2020.166711.

[4] R. Mattana, N. Locatelli and V. Cros. "Spintronics and Synchrotron Radiation". In H. Bulou, L. Joly, J.-M. Mariot and F. Scheurer (Editors), "Magnetism and Accelerator-Based Light Sources", volume 262 of *Springer Proceedings in Physics*, pages 131–163. Springer, Cham, 2021. doi:10.1007/978-3-030-64623-3_5.

[5] B. Dieny, I. L. Prejbeanu, K. Garello, P. Gambardella, P. Freitas, R. Lehndorff, W. Raberg, U. Ebels, S. O. Demokritov, J. Akerman, A. Deac, P. Pirro, C. Adelmann, A. Anane, A. V. Chumak, A. Hirohata, S. Mangin, S. O. Valenzuela, M. C. Onbasli, M. d'Aquino, G. Prenat, G. Finocchio, L. Lopez-Diaz, R. Chantrell, O. Chubykalo-Fesenko and P. Bortolotti. "Opportunities and challenges for spintronics inthe microelectronics industry". *Nat. Electron.*, 3, 446–459, 2020. doi:10.1038/s41928-020-0461-5.

[6] S. Fukami and H. Ohno. "Perspective: Spintronic synapse for artificial neural network". *J. Appl. Phys.*, 124, 151904, 2018. doi:10.1063/1.5042317.

[7] M. N. Baibich, J. M. Broto, A. Fert, F. N. V. Dau, F. Petroff, P. Etienne, G. Creuzet, A. Friederich and J. Chazelas. "Giant Magnetoresistance of (001)Fe/(001)Cr Magnetic Superlattices". *Phys. Rev. Lett.*, 61, 2472–2475, 1988. doi:10.1103/PhysRevLett.61.2472.

[8] G. Binasch, P. Grünberg, F. Saurenbach and W. Zinn. "Enhanced magnetoresistance in layered magnetic structures with antiferromagnetic interlayer exchange". *Phys. Rev. B*, 39, 4828–4830, 1989. doi:10.1103/PhysRevB.39.4828.

[9] J.-B. Moussy. "From epitaxial growth of ferrite thin films to spin-polarized tunnelling". *J. Phys. D: Appl. Phys.*, 46, 143001, 2013. doi:10.1088/0022-3727/46/14/143001.

[10] T. Miyazaki and N. Tezuka. "Spin polarized tunneling in ferromagnet/insulator/ferromagnet junctions". *J. Magn. Magn. Mater.*, 151, 403–410, 1995. doi:10.1016/0304-8853(95)00563-3.

[11] J. S. Moodera, L. R. Kinder, T. M. Wong and R. Meservey. "Large Magnetoresistance at Room Temperature in Ferromagnetic Thin Film Tunnel Junctions". *Phys. Rev. Lett.*, 74, 3273–3276, 1995. doi:10.1103/PhysRevLett.74.3273.

[12] M. Jullière. "Tunneling between ferromagnetic films". *Phys. Lett. A*, 54, 225–226, 1975. doi:10.1016/0375-9601(75)90174-7.

[13] G. S. Parkinson, U. Diebold, J. Tang and L. Malkinski. "Tailoring the Interface Properties of Magnetite for Spintronics". In L. Malkinski (Editor), "Adv. Magn. Mater.", chapter 3. IntechOpen, Rijeka, 2012. doi:10.5772/39101.

[14] J. S. Moodera, G.-X. Miao and T. S. Santos. “Frontiers in spin-polarized tunneling”. *Phys. Today*, 63, 46–51, 2010. doi:10.1063/1.3397043.

[15] X. W. Li, A. Gupta, G. Xiao, W. Qian and V. P. Dravid. “Fabrication and properties of heteroepitaxial magnetite (Fe_3O_4) tunnel junctions”. *Appl. Phys. Lett.*, 73, 3282–3284, 1998. doi:10.1063/1.122745.

[16] P. J. van der Zaag, P. J. H. Bloemen, J. M. Gaines, R. M. Wolf, P. A. A. van derHeijden, R. J. M. van de Veerdonk and W. J. M. de Jonge. “On the construction of an Fe_3O_4-based all-oxide spin valve”. *J. Magn. Magn. Mater.*, 211, 301–308, 2000. doi:10.1016/S0304-8853(99)00751-9.

[17] F. Greullet, E. Snoeck, C. Tiusan, M. Hehn, D. Lacour, O. Lenoble, C. Magen and L. Calmels. “Large inverse magnetoresistance in fully epitaxial Fe/Fe_3O_4/MgO/Co magnetic tunnel junctions”. *Appl. Phys. Lett.*, 92, 053508, 2008. doi:10.1063/1.2841812.

[18] R. Bliem, E. McDermott, P. Ferstl, M. Setvin, O. Gamba, J. Pavelec, M. A. Schneider, M. Schmid, U. Diebold, P. Blaha, L. Hammer and G. S. Parkinson. “Subsurface cation vacancy stabilization of the magnetite (001) surface”. *Science*, 346, 1215–1218, 2014. doi:10.1126/science.1260556.

[19] M. Hoppe. *Magnetic, structural, and electronic properties of $NiFe_2O_4$ ultrathin films*. Ph.D. thesis, Forschungszentrum Jülich, 2016.

[20] J. S. Moodera, T. S. Santos and T. Nagahama. “The phenomena of spin-filter tunnelling”. *J. Phys.: Condens. Matter*, 19, 165202, 2007. doi:10.1088/0953-8984/19/16/165202.

[21] J. S. Moodera, X. Hao, G. A. Gibson and R. Meservey. “Electron-Spin Polarization in Tunnel Junctions in Zero Applied Field with Ferromagnetic EuS Barriers”. *Phys. Rev. Lett.*, 61, 637–639, 1988. doi:10.1103/PhysRevLett.61.637.

[22] J. Thien, J. Bahlmann, A. Alexander, M. Hoppe, T. Pohlmann, K. Ruwisch, C. Meyer, F. Bertram, K. Küpper and J. Wollschläger. “Effects of Post-deposition Annealing on Epitaxial CoO/Fe_3O_4 Bilayers on $SrTiO_3$(001) and Formation of Thin High-Quality Cobalt Ferrite-like Films”. *J. Phys. Chem. C*, 124, 23895–23904, 2020. doi:10.1021/acs.jpcc.0c05503.

[23] J. Thien, J. Bahlmann, A. Alexander, K. Ruwisch, J. Rodewald, T. Pohlmann, M. Hoppe, F. Alarslan, M. Steinhart, B. Altuncevahir, P. Shafer, C. Meyer, F. Bertram, J. Wollschläger and K. Küpper. “Cationic Ordering and Its Influence on the Magnetic Properties of Co-Rich Cobalt Ferrite Thin Films Prepared by Reactive Solid Phase Epitaxy on Nb-Doped $SrTiO_3$(001)”. *Materials*, 15, 46, 2022. doi:10.3390/ma15010046.

[24] C. Kittel. *Introduction to Solid State Physics*. John Wiley & Sons, Inc., New Caledonia, eighth edition, 2002.

[25] G. Gottstein. *Physical Foundations of Materials Science*. Springer, Berlin, Heidelberg, first edition, 2004. doi:10.1007/978-3-662-09291-0.

[26] R. Gross and A. Marx. *Festkörperphysik*. De Gruyter Oldenbourg, München, second edition, 2014. doi:10.1524/9783110358704.

[27] K. Kopitzki and P. Herzog. *Einführung in die Festkörperphysik*. Vieweg+Teubner Verlag, Wiesbaden, sixth edition, 2007. doi:10.1007/978-3-8351-9127-3.

[28] H. Lüth and H. Ibach. *Festkörperphysik: Einführung in die Grundlagen*. Springer-Lehrbuch. Springer, Berlin, Heidelberg, seventh edition, 2009. doi:10.1007/978-3-540-85795-2.

[29] K. Oura, V. G. Lifshits, A. Saranin, A. V. Zotov and M. Katayama. *Surface Science: An Introduction*. Advanced Texts in Physics. Springer, Berlin, Heidelberg, first edition, 2003. doi:10.1007/978-3-662-05179-5.

[30] S. Blundell. *Magnetism in Condensed Matter*. Oxford University Press, Oxford, first edition, 2001.

[31] J. M. D. Coey. *Magnetism and Magnetic Materials*. Cambridge University Press, Cambridge, first edition, 2009. doi:10.1017/CBO9780511845000.

[32] J. Stöhr and H. C. Siegmann. *Magnetism: From Fundamentals to Nanoscale Dynamics*, volume 152 of *Springer Series in Solid-State Sciences*. Springer, Berlin, Heidelberg, first edition, 2006. doi:10.1007/978-3-540-30283-4.

[33] J. Clarke. "SQUIDs". *Scientific American*, 271, 46–53, 1994.

[34] J. Clarke and A. I. Braginski (Editors). *The SQUID Handbook: Fundamentals and Technology of SQUIDs and SQUID Systems*, volume 1. Wiley-VCH Verlag GmbH & Co. KGaA, Weinheim, first edition, 2004. doi:10.1002/3527603646.

[35] R. L. Fagaly. "Superconducting quantum interference device instruments and applications". *Rev. Sci. Instrum.*, 77, 101101, 2006. doi:10.1063/1.2354545.

[36] H. Weinstock (Editor). *SQUID Sensors: Fundamentals, Fabrication and Applications*, volume 329 of *NATO ASI Series (Series E: Applied Sciences)*. Springer, Dordrecht, first edition, 1996. doi:10.1007/978-94-011-5674-5.

[37] F. de Groot and A. Kotani. *Core Level Spectroscopy of Solids*. Advances in Condensed Matter Science. CRC Press, Boca Raton, first edition, 2008. doi:10.1201/9781420008425.

[38] S. Hüfner. *Photoelectron Spectroscopy: Principles and Applications*. Advanced Texts in Physics. Springer, Berlin, Heidelberg, third edition, 2003. doi:10.1007/978-3-662-09280-4.

[39] V. I. Nefedov. *X-ray photoelectron spectroscopy of solid surfaces*. VSP, Utrecht, first edition, 1988.

[40] C. S. Fadley. "Basic concepts of X-ray photoelectron spectroscopy". In C. R. Brundle and A. D. Baker (Editors), "Electron Spectroscopy: Theory, Techniques and Applications", volume 2, pages 1–156. Academic Press, London, 1978.

[41] I. K. Robinson. "Crystal truncation rods and surface roughness". *Phys. Rev. B*, 33, 3830–3836, 1986. doi:10.1103/PhysRevB.33.3830.

[42] R. Feidenhans'l. "Surface structure determination by X-ray diffraction". *Surf. Sci. Rep.*, 10(3), 105–188, 1989. doi:10.1016/0167-5729(89)90002-2.

[43] I. K. Robinson and D. J. Tweet. "Surface x-ray diffraction". *Rep. Prog. Phys.*, 55, 599, 1992. doi:10.1088/0034-4885/55/5/002.

[44] M. Tolan. *X-Ray Scattering from Soft-Matter Thin Films: Materials Science and Basic Research*, volume 148 of *Springer Tracts in Modern Physic*. Springer, Berlin, Heidelberg, first edition, 1999. doi:10.1007/BFb0112834.

[45] J. Als-Nielsen and D. McMorrow. *Elements of Modern X-ray Physics*. John-Wiley & Sons, Ltd, Chichester, second edition, 2011.

[46] T. L. Alford, L. C. Feldman and J. W. Mayer. *Fundamentals of Nanoscale Film Analysis*. Springer, Boston, MA, first edition, 2007. doi:10.1007/978-0-387-29261-8.

[47] B. Voigtländer. *Scanning Probe Microscopy: Atomic Force Microscopy and Scanning Tunneling Microscopy*. NanoScience and Technology. Springer, Berlin, Heidelberg, first edition, 2015. doi:10.1007/978-3-662-45240-0.

[48] D. B. Williams and C. B. Carter. *Transmission Electron Microscopy: A Textbook for Materials Science*. Springer, Boston, MA, second edition, 2009. doi:10.1007/978-0-387-76501-3.

[49] N.-T. H. Kim-Ngan, A. G. Balogh, J. D. Meyer, J. Brötz, M. Zajac, T. Ślezak and J. Korecki. "Thermal and irradiation induced interdiffusion in magnetite thin films grown on magnesium oxide (001) substrates". *Surf. Sci.*, 603, 1175–1181, 2009. doi:10.1016/j.susc.2009.02.028.

[50] J. Rodewald. *Advancement of growth and characteristics of ultrathin ferrite films.* Ph.D. thesis, Osnabrück University, 2020.

[51] K.-N. Tu, J. W. Mayer and L. C. Feldman. *Electronic Thin Film Science: For Electrical Engineers and Materials Scientists.* Macmillian Publishing Company, New York, first edition, 1992.

[52] S. Hashimoto, J. L. Peng and W. M. Gibson. "Strain measurement of epitaxial CaF_2 on Si(111) by MeV ion channeling". *Appl. Phys. Lett.*, 47, 1071–1073, 1985. doi:10.1063/1.96383.

[53] M. Valant, A.-K. Axelsson, F. Aguesse and N. M. Alford. "Molecular Auxetic Behavior of Epitaxial Co-Ferrite Spinel Thin Film". *Adv. Funct. Mater.*, 20, 644–647, 2010. doi:10.1002/adfm.200901762.

[54] M. Foerster, M. Iliev, N. Dix, X. Martí, M. Barchuk, F. Sánchez and J. Fontcuberta. "The Poisson Ratio in $CoFe_2O_4$ Spinel Thin Films". *Adv. Funct. Mater.*, 22, 4344–4351, 2012. doi:10.1002/adfm.201200257.

[55] A. G. Every and A. K. McCurdy. *Second and higher order elastic constants.* Springer-Verlag Berlin Heidelberg, 1992.

[56] J. H. V. D. Merwe and N. G. V. D. Berg. "Misfit dislocation energy in epitaxial overgrowths of finite thickness". *Surf. Sci.*, 32, 1–15, 1972. doi:10.1016/0039-6028(72)90117-3.

[57] J. Zou and D. J. H. Cockayne. "Theoretical consideration of misfit dislocation nucleation by partial dislocations in [001] strained-layer heterostructures". *J. Appl. Phys.*, 74, 925–930, 1993. doi:10.1063/1.354860.

[58] J. W. Matthews and A. E. Blakeslee. "Defects in epitaxial multilayers: I. Misfit dislocations". *J. Cryst. Growth*, 27, 118, 1974. doi:10.1016/S0022-0248(74)80055-2.

[59] F. C. Frank and J. H. V. D. Merwe. "One-dimensional dislocations. II. Misfitting monolayers and oriented overgrowth". *Proc. R. Soc. Lond. A*, 198, 216–225, 1949. doi:10.1098/rspa.1949.0096.

[60] W. Heisenberg. "Zur Theorie des Ferromagnetismus". *Z. Phys.*, 49, 619–636, 1928. doi:10.1007/BF01328601.

[61] M. C. Gutzwiller. "Effect of Correlation on the Ferromagnetism of Transition Metals". *Phys. Rev. Lett.*, 10, 159–162, 1963. doi:10.1103/PhysRevLett.10.159.

[62] J. Kanamori. "Electron Correlation and Ferromagnetism of Transition Metals". *Prog. Theor. Phys.*, 30, 275–289, 1963. doi:10.1143/PTP.30.275.

[63] J. Hubbard. "Electron correlations in narrow energy bands". *Proc. R. Soc. Lond. A*, 276, 238–257, 1963. doi:10.1098/rspa.1963.0204.

[64] H. A. Kramers. "L'interaction Entre les Atomes Magnétogènes dans un Cristal Paramagnétique". *Physica*, 1, 182–192, 1934. doi:10.1016/S0031-8914(34)90023-9.

[65] P. W. Anderson. "Antiferromagnetism. Theory of Superexchange Interaction". *Phys. Rev.*, 79, 350–356, 1950. doi:10.1103/PhysRev.79.350.

[66] C. Zener. "Interaction between the *d*-Shells in the Transition Metals. II. Ferromagnetic Compounds of Manganese with Perovskite Structure". *Phys. Rev.*, 82, 403–405, 1951. doi:10.1103/PhysRev.82.403.

[67] T. Pohlmann. *Structural and magnetic properties of ultrathin Fe_3O_4 films: cation- and lattice-site-selective studies by synchrotron radiation based techniques.* Ph.D. thesis, Osnabrück University, 2021.

[68] J. M. D. Coey, M. Venkatesan and H. Xu. *Introduction to Magnetic Oxides*, chapter 1, pages 1–49. John Wiley & Sons, Ltd, Weinheim, first edition, 2013. doi:10.1002/9783527654864.ch1.

[69] J. B. Goodenough. *Magnetism and the chemical bond.* Interscience Publishers, New York, London, first edition, 1963.

[70] J. Kanamori. "Superexchange interaction and symmetry properties of electron orbitals". *J. Phys. Chem. Solids*, 10, 87–98, 1959. doi:10.1016/0022-3697(59)90061-7.

[71] P. W. Anderson. "2 - Exchange in Insulators: Superexchange, Direct Exchange, and Double Exchange". In G. T. Rado and H. Suhl (Editors), "Magnetism", pages 25–83. Academic Press, New York, 1963. doi:10.1016/B978-0-12-575301-2.50009-2.

[72] R. Carey and E. D. Isaac. *Magnetic Domains and Techniques for their Observation.* The English Universities Press Ltd, London, first edition, 1966.

[73] F. London. *Superfluids: Macroscopic Theory of Superconductivity*, volume 1. John-Wiley & Sons, Inc., New York, first edition, 1950.

[74] B. D. Josephson. "Possible new effects in superconductive tunnelling". *Phys. Lett.*, 1, 251–253, 1962. doi:10.1016/0031-9163(62)91369-0.

[75] L. N. Cooper. "Bound Electron Pairs in a Degenerate Fermi Gas". *Phys. Rev.*, 104, 1189–1190, 1956. doi:10.1103/PhysRev.104.1189.

[76] J. Bardeen, L. N. Cooper and J. R. Schrieffer. "Theory of Superconductivity". *Phys. Rev.*, 108, 1175–1204, 1957. doi:10.1103/PhysRev.108.1175.

[77] Y. Aharonov and D. Bohm. "Significance of Electromagnetic Potentials in the Quantum Theory". *Phys. Rev.*, 115, 485–491, 1959. doi:10.1103/PhysRev.115.485.

[78] B. S. Deaver and W. M. Fairbank. "Experimental Evidence for Quantized Flux in Superconducting Cylinders". *Phys. Rev. Lett.*, 7, 43–46, 1961. doi:10.1103/PhysRevLett.7.43.

[79] R. Doll and M. Näbauer. "Experimental Proof of Magnetic Flux Quantization in a Superconducting Ring". *Phys. Rev. Lett.*, 7, 51–52, 1961. doi:10.1103/PhysRevLett.7.51.

[80] P. W. Anderson and J. M. Rowell. "Probable Observation of the Josephson Superconducting Tunneling Effect". *Phys. Rev. Lett.*, 10, 230–232, 1963. doi:10.1103/PhysRevLett.10.230.

[81] A. H. Silver and J. E. Zimmerman. "Quantum States and Transitions in Weakly Connected Superconducting Rings". *Phys. Rev.*, 157, 317–341, 1967. doi:10.1103/PhysRev.157.317.

[82] J. Clarke, W. M. Goubau and M. B. Ketchen. "Tunnel junction dc SQUID: Fabrication, operation, and performance". *J. Low Temp. Phys.*, 25, 99–144, 1976. doi:10.1007/BF00654826.

[83] H. Hertz. "Ueber einen Einuss des ultravioletten Lichtes auf die electrische Entladung". *Ann. Phys.*, 267, 983–1000, 1887. doi:10.1002/andp.18872670827.

[84] A. Einstein. "Über einen die Erzeugung und Verwandlung des Lichtes betreffenden heuristischen Gesichtspunkt". *Ann. Phys.*, 322, 132–148, 1905. doi:10.1002/andp.19053220607.

[85] C. M. Schneider. "Photoelectron Emission Spectroscopy". In M. Angst, T. Brückel, D. Richter and R. Zorn (Editors), "Scattering Methods for Condensed Matter Research: Towards Novel Applications at Future Sources", volume 33 of *Schriften des Forschungszentrums Jülich / Reihe Schlüsseltechnologien / Key Technologies*, pages F3.1–F3.45. Forschungszentrum Jülich GmbH, JCNS, PGI, ICS, IAS, Jülich, 2012.

[86] S. D. Kevan and E. Rotenberg. "Many body effects at surfaces and interfaces". *J. Electron Spectrosc. Relat. Phenom.*, 117-118, 57–70, 2001. doi:10.1016/S0368-2048(01)00245-6.

[87] G. Borstel. "Theoretical aspects of photoemission". *Appl. Phys. A*, 38, 193–204, 1985. doi:10.1007/BF00616497.

[88] T. Koopmans. "Über die Zuordnung von Wellenfunktionen und Eigenwerten zu den Einzelnen Elektronen Eines Atoms". *Physica*, 1, 104–113, 1934. doi:10.1016/S0031-8914(34)90011-2.

[89] C. J. Powell and A. Jablonski. "Surface sensitivity of X-ray photoelectron spectroscopy". *Nucl. Instrum. Methods Phys. Res., Sect. A*, 601, 54–65, 2009. doi:10.1016/j.nima.2008.12.103.

[90] S. Tanuma, C. J. Powell and D. R. Penn. "Calculation of electron inelastic mean free paths (IMFPs) VII. Reliability of the TPP2M IMFP predictive equation". *Surf. Interface Anal.*, 35, 268–275, 2003. doi:10.1002/sia.1526.

[91] M. P. Seah and W. A. Dench. "Quantitative electron spectroscopy of surfaces: A standard data base for electron inelastic mean free paths in solids". *Surf. Interface Anal.*, 1, 2–11, 1979. doi:10.1002/sia.740010103.

[92] D. A. Shirley. "High-resolution x-ray photoemission spectrum of the valence bands of gold". *Phys. Rev. B*, 5, 4709–4714, 1972. doi:10.1103/PhysRevB.5.4709.

[93] J. W. Cooper and S. T. Manson. "Photo-Ionization in the Soft X-Ray Range: Angular Distributions of Photoelectrons and Interpretation in Terms of Subshell Structure". *Phys. Rev.*, 177, 157–163, 1969. doi:10.1103/PhysRev.177.157.

[94] J. Cooper and R. N. Zare. "Angular Distribution of Photoelectrons". *J. Chem. Phys.*, 48, 942–943, 1968. doi:10.1063/1.1668742.

[95] J. W. Cooper. "Photoelectron-angular-distribution parameters for rare-gas subshells". *Phys. Rev. A*, 47, 1841–1851, 1993. doi:10.1103/PhysRevA.47.1841.

[96] J. W. Cooper. "Multipole corrections to the angular distribution of photoelectrons at low energies". *Phys. Rev. A*, 42, 6942–6945, 1990. doi:10.1103/PhysRevA.42.6942.

[97] P. J. Cumpson and M. P. Seah. "Elastic scattering corrections in AES and XPS. II. Estimating attenuation lengths and conditions required for their valid use in overlayer/substrate experiments". *Surf. Interface Anal.*, 25, 430–446, 1997. doi:10.1002/(SICI)1096-9918(199706)25:6<430::AID-SIA254>3.0.CO;2-7.

[98] J. T. Newberg, D. E. Starr, S. Yamamoto, S. Kaya, T. Kendelewicz, E. R. Mysak, S. Porsgaard, M. B. Salmeron, G. E. B. Jr., A. Nilsson and H. Bluhm. "Formation of hydroxyl and water layers on MgO films studied with ambient pressure XPS". *Surf. Sci.*, 605, 89–94, 2011. doi:10.1016/j.susc.2010.10.004.

[99] J. L. Erskine and E. A. Stern. "Calculation of the M_{23} magneto-optical absorption spectrum of ferromagnetic nickel". *Phys. Rev. B*, 12, 5016–5024, 1975. doi:10.1103/PhysRevB.12.5016.

[100] G. Schütz, P. Fischer, E. Goering, K. Attenkofer, D. Ahlers and W. Rößl. "X-ray magnetic circular dichroism". *Synchrotron Radiation News*, 10, 13–26, 1997. doi:10.1080/08940889708260897.

[101] J. Stöhr and Y. Wu. *X-Ray Magnetic Circular Dichroism: Basic Concepts and Theory for 3D Transition Metal Atoms*, volume 254 of *NATO ASI Series (Series E: Applied Sciences)*, pages 221–250. Springer, Dordrecht, first edition, 1994. doi:10.1007/978-94-011-0868-3_9.

[102] U. Fano. "Spin Orientation of Photoelectrons Ejected by Circularly Polarized Light". *Phys. Rev.*, 178, 131–136, 1969. doi:10.1103/PhysRev.178.131.

[103] U. Fano. "Spin Orientation of Photoelectrons: Erratum and Addendum". *Phys. Rev.*, 184, 250–251, 1969. doi:10.1103/PhysRev.184.250.

[104] B. T. Thole, P. Carra, F. Sette and G. van der Laan. "X-ray circular dichroism as a probe of orbital magnetization". *Phys. Rev. Lett.*, 68, 1943–1946, 1992. doi:10.1103/PhysRevLett.68.1943.

[105] P. Carra, B. T. Thole, M. Altarelli and X.Wang. "X-ray circular dichroism and local magnetic fields". *Phys. Rev. Lett.*, 70, 694–697, 1993. doi:10.1103/PhysRevLett.70.694.

[106] C. T. Chen, Y. U. Idzerda, H.-J. Lin, N. V. Smith, G. Meigs, E. Chaban, G. H. Ho, E. Pellegrin and F. Sette. "Experimental Confirmation of the X-Ray Magnetic Circular Dichroism Sum Rules for Iron and Cobalt". *Phys. Rev. Lett.*, 75, 152–155, 1995. doi:10.1103/PhysRevLett.75.152.

[107] F. de Groot. "X-ray absorption and dichroism of transition metals and their compounds". *J. Electron Spectrosc. Relat. Phenom.*, 67, 529–622, 1994. doi:10.1016/0368-2048(93)02041-J.

[108] J. C. Vickerman and I. S. Gilmore (Editors). *Surface Analysis: The Principal Techniques*. John Wiley & Sons, Ltd, Chichester, second edition, 2009. doi:10.1002/9780470721582.

[109] O. Sakata and M. Nakamura. *Grazing Incidence X-Ray Diffraction*, volume 51 of *Springer Series in Surface Sciences*, pages 165–190. Springer, Berlin, Heidelberg, first edition, 2013. doi:10.1007/978-3-642-34243-1_6.

[110] W. H. Bragg and W. L. Bragg. "The reflection of x-rays by crystals". *Proc. R. Soc. Lond. A*, 88, 428, 1913. doi:10.1098/rspa.1913.0040.

[111] W. Friedrich, P. Knipping and M. Laue. "Interferenzerscheinungen bei Röntgenstrahlen". *Ann. Phys.*, 346, 971, 1913. doi:10.1002/andp.19133461004.

[112] D. P. Woodruff and T. A. Delchar. *Modern Techniques of Surface Science*. Cambridge University Press, Cambridge, second edition, 1994. doi:10.1017/CBO9780511623172.

[113] J. D. Jackson. *Classical Electrodynamics*. John Wiley & Sons, Inc., New York, second edition, 1975.

[114] R. W. James. *The Optical Principles of the Diffraction of X-rays*, volume 2 of *Crystalline state*. Ox Bow Press, Woodbridge, first edition, 1982.

[115] B. E. Warren. *X-ray diffraction*. Dover Publications, Inc., New York, first edition, 1990.

[116] *International tables for x-ray crystallography*. Kynoch Press for the International Union of Crystallography, Birmingham, 1952-1974. doi:10.1107/97809553602060000001.

[117] E. R. Wölfel. *Die Beugung von Röntgenstrahlen an Kristallgittern (wellenkinematische Theorie)*, pages 50–97. Vieweg+Teubner Verlag, Wiesbaden, third edition, 1987. doi:10.1007/978-3-663-07787-9_3.

[118] P. Scherrer. "Bestimmung der Größe und der inneren Struktur von Kolloidteilchen mittels Röntgenstrahlen". *Nachrichten von der Gesellschaft der Wissenschaften zu Göttingen, Mathematisch-Physikalische Klasse*, 1918, 98–100, 1918.

[119] J. I. Langford and A. J. C. Wilson. "Scherrer after sixty years: A survey and some new results in the determination of crystallite size". *J. Appl. Cryst.*, 11, 102–113, 1978. doi:10.1107/S0021889878012844.

[120] F. Bertram. *The structure of ultrathin iron oxide films studied by x-ray diffraction*. Ph.D. thesis, Osnabrück University, 2012.

[121] A. Munkholm, S. Brennan and E. C. Carr. "A comparison of surface roughness as measured by atomic force microscopy and x-ray scattering". *J. Appl. Phys.*, 82, 2944–2953, 1997. doi:10.1063/1.366129.

[122] I. K. Robinson. "X-ray Crystallography of Surfaces and Interfaces". *Acta Cryst.*, A54, 772–778, 1998. doi:10.1107/S0108767398008125.

[123] I. Arnay, J. Rubio-Zuazo and G. R. Castro. “Impact of cleaning methods on the structural properties and morphology of $SrTiO_3$ surface”. *Appl. Surf. Sci.*, 427, 561–565, 2018. doi:10.1016/j.apsusc.2017.09.025.

[124] G. Ju, D. Xu, C. Thompson, M. J. Highland, J. A. Eastman, W. Walkosz, P. Zapol and G. B. Stephenson. “Crystal truncation rods from miscut surfaces with alternating terminations”. *Phys. Rev. B*, 103, 125402, 2021. doi:10.1103/PhysRevB.103.125402.

[125] C. Deiter. *Röntgenstrukturanalyse von Halbleiter-Isolator-Schichtsystemen.* Ph.D. thesis, Osnabrück Bremen, 2005.

[126] M. Henzler and W. Göpel. *Oberflächenphysik des Festkörpers.* Vieweg+Teubner Verlag, Stuttgart, second edition, 1991. doi:10.1007/978-3-322-84875-8.

[127] S. Macke and E. Goering. “Magnetic reflectometry of heterostructures”. *J. Phys.: Condens. Matter*, 26, 363201, 2014. doi:10.1088/0953-8984/26/36/363201.

[128] L. G. Parratt. “Surface Studies of Solids by Total Reflection of X-Rays”. *Phys. Rev.*, 95, 359–369, 1954. doi:10.1103/PhysRev.95.359.

[129] F. Bertram. *Röntgenreflektometrie an ultradünnen Schichten.* Bachelor’s thesis, Osnabrück University, 2007.

[130] L. Névot and P. Croce. “Caractérisation des surfaces par réflexion rasante de rayons X. Application à l’étude du polissage de quelques verres silicates”. *Rev. Phys. Appl. (Paris)*, 15, 761–779, 1980. doi:10.1051/rphysap:01980001503076100.

[131] Y. Seo and W. Jhe. “Atomic force microscopy and spectroscopy”. *Rep. Prog. Phys*, 71, 016101, 2008. doi:10.1088/0034-4885/71/1/016101.

[132] F. Genz. *Atomare Struktur von phosphidbasierten Halbleiternanostrukturen.* Diploma thesis, Technische Universität Berlin, 2009.

[133] J. Heggemann. *HRTEM-Strukturuntersuchungen an überwachsenen Seltenerd-Silizid-Nanodrähten.* Master’s thesis, Technische Universität Berlin, 2017.

[134] G. Binnig, C. F. Quate and C. Gerber. “Atomic Force Microscope”. *Phys. Rev. Lett.*, 56, 930–934, 1986. doi:10.1103/PhysRevLett.56.930.

[135] M. Tortonese, R. C. Barrett and C. F. Quate. “Atomic resolution with an atomic force microscope using piezoresistive detection”. *Appl. Phys. Lett.*, 62, 834–836, 1993. doi:10.1063/1.108593.

[136] F. J. Giessibl and B. M. Trafas. “Piezoresistive cantilevers utilized for scanning tunneling and scanning force microscope in ultrahigh vacuum”. *Rev. Sci. Instrum.*, 65, 1923–1929, 1994. doi:10.1063/1.1145232.

[137] S. C. Minne, S. R. Manalis and C. F. Quate. “Parallel atomic force microscopy using cantilevers with integrated piezoresistive sensors and integrated piezoelectric actuators”. *Appl. Phys. Lett.*, 67, 3918–3920, 1995. doi:10.1063/1.115317.

[138] S. R. Manalis, S. C. Minne and C. F. Quate. “Atomic force microscopy for high speed imaging using cantilevers with an integrated actuator and sensor”. *Appl. Phys. Lett.*, 68, 871–873, 1996. doi:10.1063/1.116528.

[139] Y. Martin, C. C. Williams and H. K. Wickramasinghe. “Atomic force microscope-force mapping and profiling on a sub 100-Å scale”. *J. Appl. Phys.*, 61, 4723–4729, 1987. doi:10.1063/1.338807.

[140] Q. Zhong, D. Inniss, K. Kjoller and V. B. Elings. “Fractured polymer/silica fiber surface studied by tapping mode atomic force microscopy”. *Surf. Sci.*, 290, L688–L692, 1993. doi:10.1016/0039-6028(93)90582-5.

[141] M. Knoll and E. Ruska. "Das Elektronenmikroskop". *Z. Phys.*, 78, 318–339, 1932. doi:10.1007/BF01342199.

[142] M. Knoll and E. Ruska. "Beitrag zur geometrischen Elektronenoptik. I". *Ann. Phys.*, 404, 607–640, 1932. doi:10.1002/andp.19324040506.

[143] M. Knoll and E. Ruska. "Beitrag zur geometrischen Elektronenoptik. II". *Ann. Phys.*, 404, 641–661, 1932. doi:10.1002/andp.19324040602.

[144] M. Haider, S. Uhlemann, E. Schwan, H. Rose, B. Kabius and K. Urban. "Electron microscopy image enhanced". *Nature*, 392, 768–769, 1998. doi:10.1038/33823.

[145] X. Zou. "On the phase problem in electron microscopy: the relationship between structure factors, exit waves, and HREM images". *Microsc. Res. Techniq.*, 46, 202–219, 1999. doi:10.1002/(SICI)1097-0029(19990801)46:3<202::AID-JEMT4>3.0.CO;2-8.

[146] X. Zou, S. Hovmöller and P. Oleynikov. *Electron Crystallography: Electron Microscopy and Electron Diffraction*. Oxford University Press, Oxford, first edition, 2011. doi:10.1093/acprof:oso/9780199580200.001.0001.

[147] H. Rose. "Outline of a spherically corrected semiaplanatic medium-voltage transmission electron microscope". *Optik*, 85, 19–24, 1990.

[148] M. Haider, H. Rose, S. Uhlemann, E. Schwan, B. Kabius and K. Urban. "A spherical-aberration-corrected 200 kV transmission electron microscope". *Ultramicroscopy*, 75, 53–60, 1998. doi:10.1016/S0304-3991(98)00048-5.

[149] M. H. F. Overwijk, A. J. Bleeker and A. Thust. "Correction of three-fold astigmatism for ultra-high-resolution TEM". *Ultramicroscopy*, 67, 163–170, 1997. doi:10.1016/S0304-3991(96)00096-4.

[150] E. J. Kirkland. "Improved high resolution image processing of bright field electron micrographs: I. Theory". *Ultramicroscopy*, 15, 151–172, 1984. doi:10.1016/0304-3991(84)90037-8.

[151] P. Schiske. "Image reconstruction by means of focus series". *J. Microscopy*, 207, 154–154, 2002. doi:https://doi.org/10.1046/j.1365-2818.2002.01042.x.

[152] C. Kübel and A. Thust. "TrueImage: A Software Package for Focal-Series Reconstruction in HRTEM". In T. E. Weirich, J. L. Lábár and X. Zou (Editors), "Electron Crystallography", volume 211 of *NATO Science Series II: Mathematics, Physics and Chemistry*, pages 373–392. Springer, Dordrecht, 2006. doi:10.1007/1-4020-3920-4_23.

[153] W. Coene, G. Janssen, M. O. de Beeck and D. V. Dyck. "Phase retrieval through focus variation for ultra-resolution in field-emission transmission electron microscopy". *Phys. Rev. Lett.*, 69, 3743–3746, 1992. doi:10.1103/PhysRevLett.69.3743.

[154] A. Thust, W. M. J. Coene, M. O. de Beeck and D. V. Dyck. "Focal-series reconstruction in HRTEM: simulation studies on non-periodic objects". *Ultramicroscopy*, 64, 211–230, 1996. doi:https://doi.org/10.1016/0304-3991(96)00011-3.

[155] A. Thust, M. H. F. Overwijk, W. M. J. Coene and M. Lentze. "Numerical correction of lens aberrations in phase-retrieval HRTEM". *Ultramicroscopy*, 64, 249–264, 1996. doi:10.1016/0304-3991(96)00022-8.

[156] A. Thust. "Theory and Applications of Focal-Series Reconstruction in HRTEM". *Microscopy and Microanalysis*, 11, 602–603, 2005. doi:10.1017/S1431927605503520.

[157] G. Möllenstedt and H. Düker. "Beobachtungen und Messungen an Biprisma-Interferenzen mit Elektronenwellen". *Z. Phys.*, 145, 377–397, 1956. doi:10.1007/BF01326780.

[158] A. Orchowski, W. D. Rau and H. Lichte. "Electron Holography Surmounts Resolution Limit of Electron Microscopy". *Phys. Rev. Lett.*, 74, 399–402, 1995. doi:10.1103/PhysRevLett.74.399.

[159] S. Kret, P. Ruterana, A. Rosenauer and D. Gerthsen. "Extracting Quantitative Information from High Resolution Electron Microscopy". *phys. stat. sol. (b)*, 227, 247–295, 2001. doi:10.1002/1521-3951(200109)227:1<247::AID-PSSB247>3.0.CO;2-F.

[160] D. M. Roessler and W. C. Walker. "Electronic Spectrum and Ultraviolet Optical Properties of Crystalline MgO". *Phys. Rev.*, 159, 733–738, 1967. doi:10.1103/PhysRev.159.733.

[161] M. Bass (Editor). *Handbook of Optics: Devices, Measurements, and Properties*, volume 2. McGraw-Hill, Inc., New York, second edition, 1995.

[162] M. Cardona. "Optical Properties and Band Structure of $SrTiO_3$ and $BaTiO_3$". *Phys. Rev.*, 140, A651–A655, 1965. doi:10.1103/PhysRev.140.A651.

[163] J. M. D. Coey, M. Venkatesan and P. Stamenov. "Surface magnetism of strontium titanate". *J. Phys.: Condens. Matter*, 28, 485001, 2016. doi:10.1088/0953-8984/28/48/485001.

[164] T. Tomio, H. Miki, H. Tabata, T. Kawai and S. Kawai. "Control of electrical conductivity in laser deposited $SrTiO_3$ thin films with Nb doping". *J. Appl. Phys.*, 75, 5886–5890, 1994. doi:10.1063/1.358404.

[165] F. B. Lewis and N. H. Saunders. "The thermal conductivity of NiO and CoO at the Neel temperature". *J. Phys. C: Solid State Phys.*, 6, 2525–2532, 1973. doi:10.1088/0022-3719/6/15/012.

[166] J. B. Goodenough. "Metallic oxides". *Prog. Solid State Chem.*, 5, 145–399, 1971. doi:10.1016/0079-6786(71)90018-5.

[167] V. I. Anisimov, M. A. Korotin and E. Z. Kurmaev. "Band-structure description of Mott insulators (NiO, MnO, FeO, CoO)". *J. Phys.: Condens. Matter*, 2, 3973–3987, 1990. doi:10.1088/0953-8984/2/17/008.

[168] W. Jauch and M. Reehuis. "Electron density distribution in paramagnetic and antiferromagnetic CoO: A γ-ray diffraction study". *Phys. Rev. B*, 65, 125111, 2002. doi:10.1103/PhysRevB.65.125111.

[169] R. M. Cornell and U. Schwertmann. *The iron oxides: Structure, properties, reactions, occurencesand uses*. Wiley-VCH Verlag GmbH & Co. KGaA, Weinheim, second edition, 2003. doi:10.1002/3527602097.

[170] J. F. Anderson, M. Kuhn, U. Diebold, K. Shaw, P. Stoyanov and D. Lind. "Surface structure and morphology of Mg-segregated epitaxial Fe_3O_4(001) thin films on MgO(001)". *Phys. Rev. B*, 56, 9902–9909, 1997. doi:10.1103/PhysRevB.56.9902.

[171] Z. Szotek, W. M. Temmerman, D. Ködderitzsch, A. Svane, L. Petit and H. Winter. "Electronic structures of normal and inverse spinel ferrites from first principles". *Phys. Rev. B*, 74, 174431, 2006. doi:10.1103/PhysRevB.74.174431.

[172] Z. Li, E. S. Fisher, J. Z. Liu and M. V. Nevitt. "Single-crystal elastic constants of Co-Al and Co-Fe spinels". *J. Mater. Sci.*, 26, 2621–2624, 1991. doi:10.1007/BF02387728.

[173] G. A. Sawatzky, F. van der Woude and A. H. Morrish. "Mössbauer Study of Several Ferrimagnetic Spinels". *Phys. Rev.*, 187, 747–757, 1969. doi:10.1103/PhysRev.187.747.

[174] L. Braicovich, A. Tagliaferri, G. van der Laan, G. Ghiringhelli and N. B. Brookes. "Sum Rules in X-Ray Resonant Raman Scattering: Recovering the Co Ground State Information in $CoFe_2O_4$ as a Test Case". *Phys. Rev. Lett.*, 90, 117401, 2003. doi:10.1103/PhysRevLett.90.117401.

[175] S. J. Kim, C. S. Kim and E. J. Hahn. "Mössbauer Studies on Superexchange Interactions in Fe_3O_4". *J. Kor. Phys. Soc.*, 64, 852–856, 2014. doi:10.3938/jkps.64.852.

[176] S. J. Kim, S. W. Lee and C. S. Kim. “Mössbauer Studies on Exchange Interactions in $CoFe_2O_4$”. *Jpn. J. Appl. Phys.*, 40, 4897–4902, 2001. doi:10.1143/JJAP.40.4897.

[177] S. Celotto, W. Eerenstein and T. Hibma. “Characterization of anti-phase boundaries in epitaxial magnetite films”. *Eur. Phys. J. B*, 36, 271–279, 2003. doi:10.1140/epjb/e2003-00344-7.

[178] D. T. Margulies, F. T. Parker, F. E. Spada, R. S. Goldman, J. Li, R. Sinclair and A. E. Berkowitz. “Anomalous moment and anisotropy behavior in Fe_3O_4 films”. *Phys. Rev. B*, 53, 9175–9187, 1996. doi:10.1103/PhysRevB.53.9175.

[179] D. T. Margulies, F. T. Parker, M. L. Rudee, F. E. Spada, J. N. Chapman, P. R. Aitchison and A. E. Berkowitz. “Origin of the Anomalous Magnetic Behavior in Single Crystal Fe_3O_4 Films”. *Phys. Rev. Lett.*, 79, 5162–5165, 1997. doi:10.1103/PhysRevLett.79.5162.

[180] G. Hu, V. G. Harris and Y. Suzuki. “Microstructure and Magnetic Properties of Cobalt Ferrite Thin Films”. *IEEE Trans. Magn.*, 37, 2347–2349, 2001. doi:10.1109/20.951168.

[181] W. Eerenstein, T. Hibma and S. Celotto. “Mechanism for superparamagnetic behavior in epitaxial Fe_3O_4 films”. *Phys. Rev. B*, 70, 184404, 2004. doi:10.1103/PhysRevB.70.184404.

[182] J.-B. Moussy, S. Gota, A. Bataille, M.-J. Guittet, M. Gautier-Soyer, F. Delille, B. Dieny, F. Ott, T. D. Doan, P. Warin, P. Bayle-Guillemaud, C. Gatel and E. Snoeck. “Thickness dependence of anomalous magnetic behavior in epitaxial Fe_3O_4(111) thin films: Effect of density of antiphase boundaries”. *Phys. Rev. B*, 70, 174448, 2004. doi:10.1103/PhysRevB.70.174448.

[183] R. J. M. van de Veerdonk, M. A. M. Gijs, P. A. A. van der Heijden, R. M. Wolf and W. J. M. de Jonge. “Study of the Verwey Transition of Fe_3O_4 Films and Fe_3O_4/MgO Multilayers Grown by Mbe”. *Mat. Res. Soc. Symp. Proc.*, 401, 455–460, 1996. doi:10.1557/PROC-401-455.

[184] J. M. D. Coey, A. E. Berkowitz, L. Balcells, F. F. Putris and F. T. Parker. “Magnetoresistance of magnetite”. *Appl. Phys. Lett.*, 72, 734–736, 1998. doi:10.1063/1.120859.

[185] W. Eerenstein, T. T. M. Palstra, T. Hibma and S. Celotto. “Origin of the increased resistivity in epitaxial Fe_3O_4 films”. *Phys. Rev. B*, 66, 201101(R), 2002. doi:10.1103/PhysRevB.66.201101.

[186] M. Ziese and H. J. Blythe. “Magnetoresistance of magnetite”. *J. Phys.: Condens. Matter*, 12, 13–28, 1999. doi:10.1088/0953-8984/12/1/302.

[187] W. Eerenstein, L. Kalev, L. Niesen, T. T. M. Palstra and T. Hibma. “Magneto-resistance and superparamagnetism in magnetite films on MgO and $MgAl_2O_4$”. *J. Magn. Magn. Mater.*, 258–259, 73–76, 2003. doi:10.1016/S0304-8853(02)01109-5.

[188] R. Arras, L. Calmels and B. Warot-Fonrose. “Electronic structure near an antiphase boundary in magnetite”. *Phys. Rev. B*, 81, 104422, 2010. doi:10.1103/PhysRevB.81.104422.

[189] P. A. A. van der Heijden, P. J. H. Bloemen, J. M. Gaines, J. T. W. M. van Eemeren, R. M. W. P. J. van der Zaag and W. J. M. de Jonge. “Magnetic interface anisotropy of MBE-grown ultra-thin (001) Fe_3O_4 layers”. *J. Magn. Magn. Mater.*, 159, L293–L298, 1996. doi:10.1016/0304-8853(96)00376-9.

[190] K. Balakrishnan, S. K. Arora and I. V. Shvets. “Strain relaxation studies of the Fe_3O_4/MgO(100) heteroepitaxial system grown by magnetron sputtering”. *J. Phys.: Condens. Matter*, 16, 5387–5393, 2004. doi:10.1088/0953-8984/16/30/001.

[191] S. K. Arora, R. G. S. Sofin, I. V. Shvets and M. Luysberg. “Anomalous strain relaxation behavior of Fe_3O_4/MgO(100) heteroepitaxial system grown using molecular beam epitaxy”. *J. Appl. Phys.*, 100, 073908, 2006. doi:10.1063/1.2349468.

[192] W. Eerenstein, T. T. M. Palstra, T. Hibma and S. Celotto. "Diffusive motion of antiphase domain boundaries in Fe_3O_4 films". *Phys. Rev. B*, 68, 014428, 2003. doi:10.1103/PhysRevB.68.014428.

[193] A. V. Ramos, J.-B. Moussy, M.-J. Guittet, A. M. Bataille, M. Gautier-Soyer, M. Viret, C. Gatel, P. Bayle-Guillemaud and E. Snoeck. "Magnetotransport properties of Fe_3O_4 epitaxial thin films: Thickness effects driven by antiphase boundaries". *J. Appl. Phys.*, 100, 103902, 2006. doi:10.1063/1.2386927.

[194] F. Bertram, C. Deiter, T. Schemme, S. Jentsch and J. Wollschläger. "Reordering between tetrahedral and octahedral sites in ultrathin magnetite films grown on MgO(001)". *J. Appl. Phys.*, 113, 184103, 2013. doi:10.1063/1.4803894.

[195] J. Thien. *Bildung und Charakterisierung von Cobaltferritschichten durch Interdiffusion von Cobaltoxid- und Magnetitschichten.* Master's thesis, Osnabrück University, 2017.

[196] J. Treacy. *Synchrotron studies of TiO_2 single crystal surfaces.* Ph.D. thesis, Manchester University, 2014.

[197] A. Greuling. *Röntgenstrukturanalyse von Isolatorschichten.* Master's thesis, Osnabrück University, 2007.

[198] S. Hahne. *Strukturanalyse von Praseodymoxidschichten mit Röntgenbeugung.* Bachelor's thesis, Osnabrück University, 2008.

[199] F. Bertram. *Röntgenstrukturanalyse von Oxidschichten.* Master's thesis, Osnabrück University, 2009.

[200] F. de Groot. "Multiplet effects in X-ray spectroscopy". *Coord. Chem. Rev.*, 249, 31–63, 2005. doi:10.1016/j.ccr.2004.03.018.

[201] E. Stavitski and F. M. F. de Groot. "The CTM4XAS program for EELS and XAS spectral shape analysis of transition metal L edges". *Micron*, 41, 687–694, 2010. doi:10.1016/j.micron.2010.06.005.

[202] G. van der Laan. "Theory of simple spectra". *J. Electron Spectrosc. Relat. Phenom.*, 86, 41–47, 1997. doi:10.1016/S0368-2048(97)00047-9.

[203] A. Strecker, U. Bäder, M. Kelsch, U. Salzberger, M. Sycha, M. Gao, G. Richter and K. van Benthem. "Progress in the Preparation of Cross-Sectional TEM Specimens by Ion-Beam Thinning". *Z. Metallkd.*, 94, 290–297, 2003. doi:10.3139/146.030290.

[204] K. Gramm, L. Lundgren and O. Beckman. "SQUID Magnetometer for Mangetization Measurements". *Phys. Scr.*, 13, 93–95, 1976. doi:10.1088/0031-8949/13/2/004.

[205] M. Buchner, K. Höfler, B. Henne, V. Ney and A. Ney. "Tutorial: Basic principles, limits of detection, and pitfalls of highly sensitive SQUID magnetometry for nanomagnetism and spintronics". *J. Appl. Phys.*, 124, 161101, 2018. doi:10.1063/1.5045299.

[206] J. Cibert, J.-F. Bobo and U. Lüders. "Development of new materials for spintronics". *C. R. Physique*, 6, 977–996, 2005. doi:10.1016/j.crhy.2005.10.008.

[207] R. Ramos, T. Kikkawa, K. Uchida, H. Adachi, I. Lucas, M. H. Aguirre, P. Algarabel, L. Morellón, S. Maekawa, E. Saitoh and M. R. Ibarra. "Observation of the spin Seebeck effect in epitaxial Fe_3O_4 thin films". *Appl. Phys. Lett.*, 102, 072413, 2013. doi:10.1063/1.4793486.

[208] J. García and G. Subías. "The Verwey transition - a new perspective". *J. Phys.: Condens. Matter*, 16, R145–R178, 2004. doi:10.1088/0953-8984/16/7/R0.

[209] O. Kuschel, W. Spiess, T. Schemme, J. Rubio-Zuazo, K. Kuepper and J. Wollschläger. "Real-time monitoring of the structure of ultrathin Fe_3O_4 films during growth on Nb-doped $SrTiO_3$(001)". *Appl. Phys. Lett.*, 111, 041902, 2017. doi:10.1063/1.4995408.

[210] X. S. Gao, D. H. Bao, B. Birajdar, T. Habisreuther, R. Mattheis, M. A. Schubert, M. Alexe and D. Hesse. “Switching of magnetic anisotropy in epitaxial $CoFe_2O_4$ thin films induced by $SrRuO_3$ buffer layer”. *J. Phys. D: Appl. Phys.*, 42, 175006, 2009. doi:10.1088/0022-3727/42/17/175006.

[211] M. Hoppe, S. Döring, M. Gorgoi, S. Cramm and M. Müller. “Enhanced ferrimagnetism in auxetic $NiFe_2O_4$ in the crossover to the ultrathin-film limit”. *Phys. Rev. B*, 91, 054418, 2015. doi:10.1103/PhysRevB.91.054418.

[212] J. Rodewald, J. Thien, K. Ruwisch, F. Bertram, K. Kuepper and J. Wollschläger. “Enhanced magnetization of ultrathin $NiFe_2O_4$ films on $SrTiO_3$(001) related to cation disorder and anomalous strain”. *Phys. Rev. Mater.*, 4, 064404, 2020. doi:10.1103/PhysRevMaterials.4.064404.

[213] E. Ferreiro-Vila, L. Iglesias, I. L. del Pozo, N. Varela-Dominguez, C. T. Bui, B. Rivas-Murias, J. M. Vila-Fungueiriño, P. Jimenez-Cavero, C. Magen, L. Morellon, V. Pardo and F. Rivadulla. “Apparent auxetic to non-auxetic crossover driven by Co^{2+} redistribution in $CoFe_2O_4$ thin films”. *Apl. Mater.*, 7, 031109, 2019. doi:10.1063/1.5087559.

[214] E. Martin, F. Roulland, S. Grenier, F. Appert, J. Juraszek, M. Trassin, C. Bouillet, E. Chikoidze, C. Arnold, B. Berini, Y. Dumont, S. Colis, S. Barre, G. Versini, D. Preziosi, C. Leuvrey, N. Blanc, N. Boudet, G. Pourroy, N. Viart and C. Lefèvre. “Non-auxetic/auxetic transitions inducing modifications of the magnetic anisotropy in $CoFe_2O_4$ thin films”. *J. Alloys Compd.*, 836, 155425, 2020. doi:10.1016/j.jallcom.2020.155425.

[215] O. Kuschel, N. Pathé, T. Schemme, K. Ruwisch, J. Rodewald, R. Buss, F. Bertram, T. Kuschel, K. Kuepper and J. Wollschläger. “Impact of Strain and Morphology on Magnetic Properties of Fe_3O_4/NiO Bilayers Grown on Nb:$SrTiO_3$(001) and MgO(001)”. *Materials*, 11, 1122, 2018. doi:10.3390/ma11071122.

[216] T. Yamashita and P. Hayes. “Analysis of XPS spectra of Fe^{2+} and Fe^{2+} ions in oxide materials”. *Appl. Surf. Sci.*, 254, 2441–2449, 2008. doi:10.1016/j.apsusc.2007.09.063.

[217] T. Fujii, F. M. F. de Groot, G. A. Sawatzky, F. C. Voogt, T. Hibma and K. Okada. “In situ XPS analysis of various iron oxide films grown by NO_2-assisted molecular-beam epitaxy”. *Phys. Rev. B*, 59, 3195–3202, 1999. doi:10.1103/PhysRevB.59.3195.

[218] S. A. Chambers and S. A. Joyce. “Surface termination, composition and reconstruction of Fe_3O_4(001) and γ-Fe_2O_3(001)”. *Surf. Sci.*, 420, 111–122, 1999. doi:10.1016/S0039-6028(98)00657-8.

[219] Y. J. Kim, Y. Gao and S. A. Chambers. “Selective growth and characterization of pure, epitaxial α-Fe_2O_3(0001) and Fe_3O_4(001) films by plasma-assisted molecular beam epitaxy”. *Surf. Sci.*, 371, 358–370, 1997. doi:10.1016/S0039-6028(96)00999-5.

[220] Y. Gao and S. A. Chambers. “Heteroepitaxial growth of α-Fe_2O_3, γ-Fe_2O_3 and Fe_3O_4 thin films by oxygen-plasma-assisted molecular beam epitaxy”. *J. Cryst. Growth*, 174, 446–454, 1997. doi:10.1016/S0022-0248(96)01141-4.

[221] T. E. Mitchell, L. Hwang and A. H. Heuer. “Deformation in spinel”. *J. Mater. Sci.*, 11, 264–272, 1976. doi:10.1007/BF00551437.

[222] Q.-X. Zhu, M. Zheng, M.-M. Yang, R.-K. Zheng, Y. Wang, X.-M. Li and X. Shi. “Interface correlated exchange bias effect in epitaxial Fe_3O_4 thin films grown on $SrTiO_3$ substrates”. *Appl. Phys. Lett.*, 105, 241604, 2014. doi:10.1063/1.4904471.

[223] F. Bertram, C. Deiter, O. Hoefert, T. Schemme, F. Timmer, M. Suendorf, B. Zimmermann and J. Wollschläger. “X-ray diffraction study on size effects in epitaxial magnetite thin films on MgO(001)”. *J. Phys. D: Appl. Phys.*, 45, 395302, 2012. doi:10.1088/0022-3727/45/39/395302.

[224] G. W. Leung, M. E. Vickers, R. Yu and M. G. Blamire. “Epitaxial growth of Fe_3O_4 (111) on $SrTiO_3$ (001) substrates”. *J. Cryst. Growth*, 310, 5282–5286, 2008. doi:10.1016/j.jcrysgro.2008.07.126.

[225] R. Takahashi, H. Misumi and M. Lippmaa. “Self-Template Growth of Orientation-Controlled Fe_3O_4 Thin Films”. *Cryst. Growth Des.*, 12, 2679–2683, 2012. doi:10.1021/cg300287r.

[226] A. V. Ramos, M.-J. Guittet, J.-B. Moussy, R. Mattana, C. Deranlot, F. Petroff and C. Gatel. “Room temperature spin filtering in epitaxial cobalt-ferrite tunnel barriers”. *Appl. Phys. Lett.*, 91, 122107, 2007. doi:10.1063/1.2787880.

[227] S. Matzen, J.-B. Moussy, R. Mattana, K. Bouzehouane, C. Deranlot and F. Petroff. “Nanomagnetism of cobalt ferrite-based spin filters probed by spin-polarized tunneling”. *Appl. Phys. Lett.*, 101, 042409, 2012. doi:10.1063/1.4738790.

[228] N. M. Caffrey, D. Fritsch, T. Archer, S. Sanvito and C. Ederer. “Spin-filtering efficiency of ferrimagnetic spinels $CoFe_2O_4$ and $NiFe_2O_4$”. *Phys. Rev. B*, 87, 024419, 2013. doi:10.1103/PhysRevB.87.024419.

[229] M. Foerster, F. Rigato, K. Bouzehouane and J. Fontcuberta. “Tunnel transport through $CoFe_2O_4$ barriers investigated by conducting atomic force microscopy”. *J. Phys. D: Appl. Phys.*, 43, 295001, 2010. doi:10.1088/0022-3727/43/29/295001.

[230] Y. K. Takahashi, S. Kasai, T. Furubayashi, S. Mitani, K. Inomata and K. Hono. “High spin-filter efficiency in a Co ferrite fabricated by a thermal oxidation”. *Appl. Phys. Lett.*, 96, 072512, 2010. doi:10.1063/1.3318297.

[231] E.-J. Guo, A. Herklotz, A. Kehlberger, J. Cramer, G. Jakob and M. Kläui. “Thermal generation of spin current in epitaxial $CoFe_2O_4$ thin films”. *Appl. Phys. Lett.*, 108, 022403, 2016. doi:10.1063/1.4939625.

[232] T. Niizeki, T. Kikkawa, K.-I. Uchida, M. Oka, K. Z. Suzuki, H. Yanagihara, E. Kita and E. Saitoh. “Observation of longitudinal spin-Seebeck effect in cobalt-ferrite epitaxial thin films”. *AIP Adv.*, 5, 053603, 2015. doi:10.1063/1.4916978.

[233] K.-I. Uchida, H. Adachi, T. Kikkawa, A. Kirihara, M. Ishida, S. Yorozu, S. Maekawa and E. Saitoh. “Thermoelectric Generation Based on Spin Seebeck Effects”. *Proc. IEEE*, 104, 1946–1973, 2016. doi:10.1109/JPROC.2016.2535167.

[234] M. Valvidares, N. Dix, M. Isasa, K. Ollefs, F. Wilhelm, A. Rogalev, F. Sánchez, E. Pellegrin, A. Bedoya-Pinto, P. Gargiani, L. E. Hueso, F. Casanova and J. Fontcuberta. “Absence of magnetic proximity effects in magnetoresistive Pt/$CoFe_2O_4$ hybrid interfaces”. *Phys. Rev. B*, 93, 214415, 2016. doi:10.1103/PhysRevB.93.214415.

[235] S. Y. Huang, W. G. Wang, S. F. Lee, J. Kwo and C. L. Chien. “Intrinsic Spin-Dependent Thermal Transport”. *Phys. Rev. Lett.*, 107, 216604, 2011. doi:10.1103/PhysRevLett.107.216604.

[236] S. Zhu, J. Li, X. Deng, C. He, E. Liu, F. He, C. Shi and N. Zhao. “Ultrathin-Nanosheet-Induced Synthesis of 3D Transition Metal Oxides Networks for Lithium Ion Battery Anodes”. *Adv. Funct. Mater.*, 27, 1605017, 2017. doi:10.1002/adfm.201605017.

[237] X.-F. Lu, L.-F. Gu, J.-W. Wang, J.-X. Wu, P.-Q. Liao and G.-R. Li. “Bimetal-Organic Framework Derived $CoFe_2O_4$/C Porous Hybrid Nanorod Arrays as High-Performance Electrocatalysts for Oxygen Evolution Reaction”. *Adv. Mater.*, 29, 1604437, 2017. doi:10.1002/adma.201604437.

[238] M. Coll, J. M. M. Moreno, J. Gazquez, K. Nielsch, X. Obradors and T. Puig. “Low Temperature Stabilization of Nanoscale Epitaxial Spinel Ferrite Thin Films by Atomic Layer Deposition”. *Adv. Funct. Mater.*, 24, 5368–5374, 2014. doi:10.1002/adfm.201400517.

[239] I. C. Nlebedim, A. J. Moses and D. C. Jiles. "Non-stoichiometric cobalt ferrite, $Co_xFe_{3-x}O_4$ (x=1.0 to 2.0): Structural, magnetic and magnetoelastic properties". *J. Magn. Magn. Mater.*, 343, 49–54, 2013. doi:10.1016/j.jmmm.2013.04.063.

[240] H. L. Trong, L. Presmanes, E. D. Grave, A. Barnabé, C. Bonningue and P. Tailhades. "Mössbauer characterisations and magnetic properties of iron cobaltites $Co_xFe_{3-x}O_4$ ($1 \leq x \leq 2.46$) before and after spinodal decomposition". *J. Magn. Magn. Mater.*, 334, 66–73, 2013. doi:10.1016/j.jmmm.2013.01.007.

[241] A. K. Sinha, M. N. Singh, S. N. Archary, A. Sagdeo, D. K. Shukla and D. M. Phase. "Crystal field splitting and spin states of Co ions in cobalt ferrite with composition $Co_{1.5}Fe_{1.5}O_4$ using magnetization and X-ray absorption spectroscopy measurements". *J. Magn. Magn. Mater.*, 435, 87–95, 2017. doi:10.1016/j.jmmm.2017.03.070.

[242] S. A. Chambers, R. F. C. Farrow, S. Maat, M. F. Toney, L. Folks, J. G. Catalano, T. P. Trainor and G. E. B. Jr. "Molecular beam epitaxial growth and properties of $CoFe_2O_4$ on MgO(001)". *J. Magn. Magn. Mater.*, 246, 124–139, 2002. doi:10.1016/S0304-8853(02)00039-2.

[243] F. Eskandari, S. B. Porter, M. Venkatesan, P. Kameli, K. Rode and J. M. D. Coey. "Magnetization and anisotropy of cobalt ferrite thin films". *Phys. Rev. Mater.*, 1, 074413, 2017. doi:10.1103/PhysRevMaterials.1.074413.

[244] J. Rodewald, J. Thien, T. Pohlmann, M. Hoppe, F. Timmer, F. Bertram, K. Kuepper and J. Wollschläger. "Formation of ultrathin cobalt ferrite films by interdiffusion of Fe_3O_4/CoO bilayers". *Phys. Rev. B*, 100, 155418, 2019. doi:10.1103/PhysRevB.100.155418.

[245] D. Fritsch and C. Ederer. "Epitaxial strain effects in the spinel ferrites $CoFe_2O_4$ and $NiFe_2O_4$ from first principles". *Phys. Rev. B*, 82, 104117, 2010. doi:10.1103/PhysRevB.82.104117.

[246] D. Fritsch and C. Ederer. "Effect of epitaxial strain on the cationdistribution in spinel ferrites $CoFe_2O_4$ and $NiFe_2O_4$: A density functional theory study". *Appl. Phys. Lett.*, 99, 081916, 2011. doi:10.1063/1.3631676.

[247] Y. Z. Chen, J. R. Sun, Y. N. Han, X. Y. Xie, J. Shen, C. B. Rong, S. L. He and B. G. Shen. "Microstructure and magnetic properties of strained Fe_3O_4 films". *J. Appl. Phys.*, 103, 07D703, 2008. doi:10.1063/1.2832305.

[248] M. Monti, M. Sanz, M. Oujja, E. Rebollar, M. Castillejo, F. J. Pedrosa, A. Bollero, J. Camarero, J. L. F. Cunado, N. M. Nemes, F. J. Mompean, M. Garcia-Hernández, S. Nie, K. F. McCarty, A. T. N'Diaye, G. Chen, A. K. Schmid, J. F. Marco and J. de la Figuera. "Room temperature in-plane $\langle 100 \rangle$ magnetic easy axis for $Fe_3O_4/SrTiO_3(001)$:Nb grown by infrared pulsed laser deposition". *J. Appl. Phys.*, 114, 223902, 2013. doi:10.1063/1.4837656.

[249] G. A. Sawatzky, F. van der Woude and A. H. Morrish. "Cation Distributions in Octahedral and Tetrahedral Sites of the Ferrimagnetic Spinel $CoFe_2O_4$". *J. Appl. Phys.*, 39, 1204–1206, 1968. doi:10.1063/1.1656224.

[250] G. Hu, J. H. Choi, C. B. Eom, V. G. Harris and Y. Suzuki. "Structural tuning of the magnetic behavior in spinel-structure ferrite thin films". *Phys. Rev. B*, 62, R779–R782, 2000. doi:10.1103/PhysRevB.62.R779.

[251] R. D. Cowan. *The Theory of Atomic Structure and Spectra*. University of California Press, Berkeley, first edition, 1981. doi:10.1525/9780520906150.

[252] N. S. McIntyre and M. G. Cook. "X-ray photoelectron studies on some oxides and hydroxides of cobalt, nickel, and copper". *Anal. Chem.*, 47, 2208–2213, 1975. doi:10.1021/ac60363a034.

[253] P. C. J. Graat and M. A. J. Somers. “Simultaneous determination of composition and thickness of thin iron-oxide films from XPS Fe 2p spectra”. *Appl. Surf. Sci.*, 100–101, 36–40, 1996. doi:10.1016/0169-4332(96)00252-8.

[254] F. Rigato, J. Geshev, V. Skumryev and J. Fontcuberta. “The magnetization of epitaxial nanometric $CoFe_2O_4$ (001) layers”. *J. Appl. Phys.*, 106, 113924, 2009. doi:10.1063/1.3267873.

[255] G. van der Laan, E. Arenholz, R. V. Chopdekar and Y. Suzuki. “Influence of crystal field on anisotropic x-ray magnetic linear dichroism at the Co^{2+} $L_{2,3}$ edges”. *Phys. Rev. B*, 77, 064407, 2008. doi:10.1103/PhysRevB.77.064407.

[256] J. A. Moyer, C. A. F. Vaz, D. P. Kumah, D. A. Arena and V. E. Henrich. “Enhanced magnetic moment in ultrathin Fe-doped $CoFe_2O_4$ films”. *Phys. Rev. B*, 86, 174404, 2012. doi:10.1103/PhysRevB.86.174404.

[257] J. A. Moyer, C. A. F. Vaz, E. Negusse, D. A. Arena and V. E. Henrich. “Controlling the electronic structure of $Co_{1-x}Fe_{2+x}O_4$ thin films through iron doping”. *Phys. Rev. B*, 83, 035121, 2011. doi:10.1103/PhysRevB.83.035121.

[258] J. P. Crocombette, M. Pollak, F. Jollet, N. Thromat and M. Gautier-Soyer. “X-ray-absorption spectroscopy at the Fe $L_{2,3}$ threshold in iron oxides”. *Phys. Rev. B*, 52, 3143–3150, 1995. doi:10.1103/PhysRevB.52.3143.

[259] P. Kuiper, B. G. Searle, P. Rudolf, L. H. Tjeng and C. T. Chen. “X-ray magnetic dichroism of antiferromagnet Fe_2O_3: The orientation of magnetic moments observed by Fe $2p$ x-ray absorption spectroscopy”. *Phys. Rev. Lett.*, 70, 1549–1552, 1993. doi:10.1103/PhysRevLett.70.1549.

[260] C. Piamonteze, P. Miedema and F. M. F. de Groot. “Accuracy of the spin sum rule in XMCD for the transition-metal L edges from manganese to copper”. *Phys. Rev. B*, 80, 184410, 2009. doi:10.1103/PhysRevB.80.184410.

[261] Y. Teramura, A. Tanaka and T. Jo. “Effect of Coulomb Interaction on the X-Ray Magnetic Circular Dichroism Spin Sum Rule in $3d$ Transition Elements”. *J. Phys. Soc. Jpn.*, 65, 1053–1055, 1996. doi:10.1143/JPSJ.65.1053.

[262] H. L. Trong, A. Barnabé, L. Presmanes and P. Tailhades. “Phase decomposition study in $Co_xFe_{3-x}O_4$ iron cobaltites: Synthesisand structural characterization of the spinodal transformation”. *Solid State Sci.*, 10, 550–556, 2008. doi:10.1016/j.solidstatesciences.2007.10.004.

[263] P. J. Murray and (the late) J. W. Linnett. “Cation distribution in the spinels $Co_xFe_{3-x}O_4$”. *J. Phys. Chem. Solids*, 37, 1041–1042, 1976. doi:10.1016/0022-3697(76)90128-1.

[264] D. H. Lee, H. S. Kim, J. Y. Lee, C. H. Yo and K. H. Kim. “Characterization of the magnetic properties and transport mechanisms of $Co_xFe_{3-x}O_4$ spinel”. *Solid State Commun.*, 96, 445–449, 1995. doi:10.1016/0038-1098(95)00491-2.

[265] N. Kita, N. Shibuichi and S. Sasaki. “X-ray magnetic circular dichroism in cobalt-iron spinels and electronic states of Co ions”. *J. Synchrotron Radiat.*, 8, 446–448, 2001. doi:10.1107/s0909049500018409.

[266] M. Takahashi and M. E. Fine. “Magnetic behavior of quenched and aged $CoFe_2O_4$-Co_3O_4 alloys”. *J. Appl. Phys.*, 43, 4205–4216, 1972. doi:10.1063/1.1660897.

[267] P. A. Smith, C. D. Spencer and R. P. Stillwell. “Co^{57} and Fe^{57} mössbauer studies of the spinels $FeCo_2O_4$ and $Fe_0.5Co_2.5O_4$”. *J. Phys. Chem. Solids*, 39, 107–111, 1978. doi:10.1016/0022-3697(78)90208-1.

[268] G. H. Jonker. “Analysis of the semiconducting properties of cobalt ferrite”. *J. Phys. Chem. Solids*, 9, 165–175, 1959. doi:10.1016/0022-3697(59)90206-9.

[269] J. J. Beltrán, J. A. Osorio, C. A. Barrero, C. B. Hanna and A. Punnoose. “Magnetic properties of Fe doped, Co doped, and Fe+Co co-doped ZnO”. *J. Appl. Phys.*, 113, 17C308, 2013. doi:10.1063/1.4799778.

[270] J. H. Kim, H. Kim, D. Kim, Y. E. Ihm and W. K. Choo. “The origin of room temperature ferromagnetism in cobalt-doped zinc oxide thin films fabricated by PLD”. *J. Eur. Ceram. Soc.*, 24, 1847–1851, 2004. doi:10.1016/S0955-2219(03)00447-3.

[271] N. M. Basith, J. J. Vijaya, L. J. Kennedy and M. Bououdina. “Structural, morphological, optical, and magnetic properties of Ni-doped CuO nanostructures prepared by a rapid microwave combustion method”. *Mater. Sci. Semicond. Process.*, 17, 110–118, 2014. doi:10.1016/j.mssp.2013.09.013.

[272] Y. Li, M. Xu, L. Pan, Y. Zhang, Z. Guo and C. Bi. “Structural and room-temperature ferromagnetic properties of Fe-doped CuO nanocrystals”. *J. Appl. Phys.*, 107, 113908, 2010. doi:10.1063/1.3436573.

[273] D. S. Negi, B. Loukya, K. Dileep, R. Sahu, K. K. Nagaraja, N. Kumar and R. Datta. “Robust room temperature ferromagnetism in epitaxial CoO thin film”. *Appl. Phys. Lett.*, 103, 242407, 2013. doi:10.1063/1.4847775.

[274] M. Gheisari, M. Mozafari, M. Niyaifar, J. Amighian and R. Soleimani. “Observation of Small Exchange Bias in Defect WÃ¼stite ($Fe_{0.93}O$) Nanoparticles”. *J. Supercond. Nov. Magn.*, 26, 237–242, 2013. doi:10.1007/s10948-012-1821-9.

[275] H. Qin, Z. Zhang, X. Liu, Y. Zhang and J. Hu. “Room-temperature ferromagnetism in CuO sol-gel powders and films”. *J. Magn. Magn. Mater.*, 322, 1994–1998, 2010. doi:10.1016/j.jmmm.2010.01.021.

[276] Q. Xu, H. Schmidt, S. Zhou, K. Potzger, M. Helm, H. Hochmuth, M. Lorenz, A. Setzer, P. Esquinazi, C. Meinecke and M. Grundmann. “Room temperature ferromagnetism in ZnO films due to defects”. *Appl. Phys. Lett.*, 92, 082508, 2008. doi:10.1063/1.2885730.

[277] N. Jedrecy, T. Aghavnian, J.-B. Moussy, H. Magnan, D. Stanescu, X. Portier, M.-A. Arrio, C. Mocuta, A. Vlad, R. Belkhou, P. Ohresser and A. Barbier. “Cross-Correlation between Strain, Ferroelectricity, and Ferromagnetism in Epitaxial Multiferroic $CoFe_2O_4/BaTiO_3$ Heterostructures”. *ACS Appl. Mater. Interfaces*, 10, 28003–28014, 2018. doi:10.1021/acsami.8b09499.

[278] O. Kuschel, R. Buß, W. Spiess, T. Schemme, J. Wöllermann, K. Balinski, A. T. N’Diaye, T. Kuschel, J. Wollschläger and K. Kuepper. “From Fe_3O_4/NiO bilayers to $NiFe_2O_4$-like thin films through Ni interdiffusion”. *Phys. Rev. B*, 94, 094423, 2016. doi:10.1103/PhysRevB.94.094423.

[279] E. Arenholz, G. van der Laan, R. V. Chopdekar and Y. Suzuki. “Anisotropic x-ray magnetic linear dichroism at the Fe $L_{2,3}$ edges in Fe_3O_4”. *Phys. Rev. B*, 74, 094407, 2006. doi:10.1103/PhysRevB.74.094407.

[280] K. Kuepper, O. Kuschel, N. Pathé, T. Schemme, J. Schmalhorst, A. Thomas, E. Arenholz, M. Gorgoi, R. Ovsyannikov, S. Bartkowski, G. Reiss and J. Wollschläger. “Electronic and magnetic structure of epitaxial Fe_3O_4(001)/NiO heterostructures grown on MgO(001) and Nb-doped $SrTiO_3$(001)”. *Phys. Rev. B*, 94, 024401, 2016. doi:10.1103/PhysRevB.94.024401.

[281] T. Tainosho, J. ichiro Inoue, S. Sharmin, M. Takeguchi, E. Kita and H. Yanagihara. “Large negative uniaxial magnetic anisotropy in highly distorted Co-ferrite thin films”. *Appl. Phys. Lett.*, 114, 092408, 2019. doi:10.1063/1.5064845.

[282] U. Lüders, M. Bibes, J.-F. Bobo, M. Cantoni, R. Bertacco and J. Fontcuberta. “Enhanced magnetic moment and conductive behavior in $NiFe_2O_4$ spinel ultrathin films”. *Phys. Rev. B*, 71, 134419, 2005. doi:10.1103/PhysRevB.71.134419.

[283] F. Rigato, S. Estradé, J. Arbiol, F. Peiró, U. Lüders, X. Martí, F. Sánchez and J. Fontcuberta. “Strain-induced stabilization of new magnetic spinel structures in epitaxial oxide heterostructures”. *Mater. Sci. Eng. B*, 144, 43–48, 2007. doi:10.1016/j.mseb.2007.07.102.

[284] H. Yanagihara, K. Uwabo, M. Minagawa, E. Kita and N. Hirota. “Perpendicular magnetic anisotropy in $CoFe_2O_4$(001) films epitaxially grown on MgO(001)”. *J. Appl. Phys.*, 109, 07C122, 2011. doi:10.1063/1.3566079.

[285] L. Horng, G. Chern, M. C. Chen, P. C. Kang and D. S. Lee. “Magnetic anisotropic properties in Fe_3O_4 and $CoFe_2O_4$ ferrite epitaxy thin films”. *J. Magn. Magn. Mater.*, 270, 389–396, 2004. doi:10.1016/j.jmmm.2003.09.005.

[286] Y. Zhang, C. Deng, J. Ma, Y. Lin and C.-W. Nan. “Enhancement in magnetoelectric response in $CoFe_2O_4$-$BaTiO_3$ heterostructure”. *Appl. Phys. Lett.*, 92, 062911, 2008. doi:10.1063/1.2841048.

[287] X. Zeng, J. Zhang, S. Zhu, X. Deng, H. Ma, J. Zhang, Q. Zhang, P. Li, D. Xue, N. J. Mellors, X. Zhang and Y. Peng. “Direct observation of cation distributions of ideal inverse spinel $CoFe_2O_4$ nanofibres and correlated magnetic properties”. *Nanoscale*, 9, 7493–7500, 2017. doi:10.1039/C7NR02013A.

[288] A. Franco, F. L. A. Machado and V. S. Zapf. “Magnetic properties of nanoparticles of cobalt ferrite at high magnetic field”. *J. Appl. Phys.*, 110, 053913, 2011. doi:10.1063/1.3626931.

[289] K. C. Verma, V. P. Singh, M. Ram, J. Shah and R. K. Kotnala. “Structural, microstructural and magnetic properties of $NiFe_2O_4$, $CoFe_2O_4$ and $MnFe_2O_4$nanoferrite thin films”. *J. Magn. Magn. Mater.*, 323, 3271–3275, 2011. doi:10.1016/j.jmmm.2011.07.029.

[290] M. Guillot, J. Ostorero and A. Marchand. “High magnetic field magnetization study in cadmium-cobalt ferrite single crystals”. *Z. Phys. B*, 71, 193–197, 1988. doi:10.1007/BF01312789.

[291] P. G. Bercoff and H. R. Bertorello. “Exchange constants and transfer integrals of spinel ferrites”. *J. Magn. Magn. Mater.*, 169, 314–322, 1997. doi:10.1016/S0304-8853(96)00748-2.

[292] C. M. Srivastava, G. Srinivasan and N. G. Nanadikar. “Exchange constants in spinel ferrites”. *Phys. Rev. B*, 19, 499–508, 1979. doi:10.1103/PhysRevB.19.499.

[293] J. A. Moyer, D. P. Kumah, C. A. F. Vaz, D. A. Arena and V. E. Henrich. “Epitaxial strain-induced changes in the cation distribution and resistivity of Fe-doped $CoFe_2O_4$”. *Appl. Phys. Lett.*, 101, 021907, 2012. doi:10.1063/1.4735233.

[294] J. J. Wisser, L. J. Riddiford, A. Altman, P. Li, S. Emori, P. Shafer, C. Klewe, A. T. N’Diaye, E. Arenholz and Y. Suzuki. “The role of iron in magnetic damping of $Mg(Al,Fe)_2O_4$ spinel ferrite thin films”. *Appl. Phys. Lett.*, 116, 142406, 2020. doi:10.1063/5.0003628.

[295] S. Regmi, Z. Li, A. Srivastava, R. Mahat, S. KC, A. Rastogi, Z. Galazka, R. Datta, T. Mewes and A. Gupta. “Structural and magnetic properties of $NiFe_2O_4$ thin films grown on isostructural lattice-matched substrates”. *Appl. Phys. Lett.*, 118, 152402, 2021. doi:10.1063/5.0047865.

[296] V. Zviagin, Y. Kumar, I. Lorite, P. Esquinazi, M. Grundmann and R. Schmidt-Grund. “Ellipsometric investigation of $ZnFe_2O_4$ thin films in relation to magnetic properties”. *Appl. Phys. Lett.*, 108, 131901, 2016. doi:10.1063/1.4944898.

[297] P. V. Lukashev, J. D. Burton, A. Smogunov, J. P. Velev and E. Y. Tsymbal. “Interface states in $CoFe_2O_4$ spin-filter tunnel junctions”. *Phys. Rev. B*, 88, 134430, 2013. doi:10.1103/PhysRevB.88.134430.

[298] N. Tezuka. “New materials research for high spin polarized current”. *J. Magn. Magn. Mater.*, 324, 3588–3592, 2012. doi:10.1016/j.jmmm.2012.02.097.

[299] J. Rodewald, J. Thien, T. Pohlmann, M. Hoppe, F. Bertram, K. Kuepper and J. Wollschläger. “Real-time monitoring the growth of strained off-stoichiometric $Ni_xFe_{3-x}O_4$ ultrathin films on MgO(001)”. *Appl. Phys. Lett.*, 117, 011601, 2020. doi:10.1063/5.0013925.

[300] M. Althammer, A. V. Singh, T. Wimmer, Z. Galazka, H. Huebl, M. Opel, R. Gross and A. Gupta. “Role of interface quality for the spin Hall magnetoresistance in nickel ferrite thin films with bulk-like magnetic properties”. *Appl. Phys. Lett.*, 115, 092403, 2019. doi:10.1063/1.5097600.

[301] C. Nicklin, T. Arnold, J. Rawle and A. Warne. “Diamond beamline I07: a beamline for surfaceand interface diffraction”. *J. Synchrotron Radiat.*, 23, 1245–1253, 2016. doi:10.1107/S1600577516009875.

[302] T. Schemme, A. Krampf, F. Bertram, T. Kuschel, K. Kuepper and J. Wollschläger. “Modifying magnetic properties of ultra-thin magnetite films by growth on Fe pre-covered MgO(001)”. *J. Appl. Phys.*, 118, 113904, 2015. doi:10.1063/1.4930998.

[303] C. Schlueter, A. Gloskovskii, K. Ederer, I. Schostak, S. Piec, I. Sarkar, Y. Matveyev, P. Lömker, M. Sing, R. Claessen, C. Wiemann, C. M. Schneider, K. Medjanik, G. Schönhense, P. Amann, A. Nilsson and W. Drube. “The new dedicated HAXPES beamline P22 at PETRAIII”. *AIP Conf. Proc.*, 2054, 040010, 2019. doi:10.1063/1.5084611.

[304] C. Weiland, C. Jaye, N. F. Quackenbush, E. Gann, Z. Fu, J. P. Kirkland, B. A. Karlin, B. Ravel, J. C. Woicik and D. A. Fischer. “NIST HAXPES at NSLS and NSLS-II”. *Synch. Rad. News*, 31, 23–28, 2018. doi:10.1080/08940886.2018.1483654.

[305] G. C. Allen, M. T. Curtis, A. J. Hooper and P. M. Tucker. “X-Ray photoelectron spectroscopy of iron-oxygen systems”. *J. Chem. Soc., Dalton Trans.*, pages 1525–1530, 1974. doi:10.1039/DT9740001525.

[306] J. H. Scofield. “Theoretical photoionization cross sections from 1 to 1500 keV”. Technical Report UCRL-51326, California University, Livermore; Lawrence Livermore Laboratory, USA, 1973. doi:10.2172/4545040.

[307] L. Iyengar, B. R. Prasad and B. Qadri. “Thermal Expansion of Cobalt Ferrite and Cobalt-Zinc Ferrite”. *Curr. Sci.*, 42, 534–535, 1973.

[308] M. A. Durand. “The Coefficient of Thermal Expansion of Magnesium Oxide”. *Physics*, 7, 297–298, 1936. doi:10.1063/1.1745396.

[309] J. Korecki, B. Handke, N. Spiridis, T. Ślezak, I. Flis-Kabulska and J. Haber. “Size effects in epitaxial films of magnetite”. *Thin Solid Films*, 412, 14–23, 2002. doi:10.1016/S0040-6090(02)00306-1.

[310] R. Pentcheva, W. Moritz, J. Rundgren, S. Frank, D. Schrupp and M. Scheffler. “A combined DFT/LEED-approach for complex oxide surface structure determination: $Fe_3O_4(001)$”. *Surf. Sci.*, 602, 1299–1305, 2008. doi:10.1016/j.susc.2008.01.006.

[311] B. L. Henke, E. M. Gullikson and J. C. Davis. “X-Ray Interactions: Photoabsorption, Scattering, Transmission, and Reflection at $E = 50 - 30000$ eV, $Z = 1 - 92$”. *At. Data. Nucl. Data Tables*, 54, 181–342, 1993. doi:10.1006/adnd.1993.1013.

[312] Z.-X. Shen, J. W. Allen, P. A. P. Lindberg, D. S. Dessau, B. O. Wells, A. Borg, W. Ellis, J. S. Kang, S.-J. Oh, I. Lindau and W. E. Spicer. “Photoemission study of CoO”. *Phys. Rev. B*, 42, 1817–1828, 1990. doi:10.1103/PhysRevB.42.1817.

[313] M. C. Biesinger, B. P. Payne, A. P. Grosvenor, L. W. M. Lau, A. R. Gerson and R. S. C. Smart. “Resolving surface chemical states in XPS analysis of first row transition metals, oxides and hydroxides: Cr, Mn, Fe, Co and Ni”. *Appl. Surf. Sci.*, 257, 2717–2730, 2011. doi:10.1016/j.apsusc.2010.10.051.

[314] S. Xie, J. Cheng, B. W. Wessels and V. P. Dravid. “Interfacial structure and chemistry of epitaxial $CoFe_2O_4$ thin films on $SrTiO_3$ and MgO substrates”. *Appl. Phys. Lett.*, 93, 181901, 2008. doi:10.1063/1.3006060.

[315] D. Odkhuu, P. Taivansaikhan, W. S. Yun and S. C. Hong. “A first-principles study of magnetostrictions of Fe_3O_4 and $CoFe_2O_4$”. *J. Appl. Phys.*, 115, 17A916, 2014. doi:10.1063/1.4863811.

Danksagung

Zu guter Letzt möchte ich noch ein großes Dankeschön aussprechen an jene Personen, die mir durch ihr Zutun und ihre Unterstützung eine große Hilfe während der Promotion und beim Gelingen dieser Arbeit waren.

Hierbei ist an erster Stelle mein Mentor und Doktorvater Prof. Dr. Joachim Wollschläger zu nennen. Vielen Dank für deine fortwährende Zuversicht und dein Vertrauen in mich und meine Arbeit, deine fachlichen Ratschläge sowie für die zahlreichen und aufschlussreichen Diskussionen, die wir aufgrund der teils schwierigen Interpretation der Daten geführt haben.

Außerdem bedanke ich mich bei Dr. Karsten Küpper, nicht nur, dass er sich bereit erklärt hat die Position des Zweitprüfers zu bekleiden, sondern auch dafür, dass er sein umfangreiches Wissen über XAS/XMCD und (charge-transfer) Multiplett-Berechnungen mit mir geteilt hat. In diesem Kontext sei auch Prof. Dr. Robin Steinigeweg und Dr. Philipp Rahe gedankt, die ohne zu zögern einverstanden waren ebenfalls als Teil der Promotionskommission zu fungieren.

Des Weiteren gilt mein Dank – auch wenn ich viele nicht explizit hier erwähne – allen ehemaligen und aktuellen Mitgliedern der Arbeitsgruppe "Dünne Schichten und Grenzflächen", die ich während meiner Zeit kennenlernen durfte. Durch euch war die Arbeitsatmosphäre im Büro, im Labor, während Synchrotronmesszeiten und auch während aller außeruniversitärer Veranstaltungen stets angenehm und entspannt, vielen Dank dafür! Hier sei besonders meinen lieben Bürokollegen Kevin Ruwisch, Jascha Bahlmann und Andreas Alexander gedankt sowie auch Jari Rodewald, Tobias Pohlmann, Martin Hoppe und Olga Kuschel. Zusätzlich danke ich explizit noch einmal Jari Rodewald und Tobias Pohlmann für die stets amüsanten Abende bei unseren gemeinsam abgehaltenen Online-Treffen und Kevin Ruwisch für die sehr schöne Zeit in New York. Auch danke ich Florian Bertram, Timo Kuschel und Baki Altuncevahir für die hilfreichen Diskussionen, immer dann, wenn ich spezielle Fragen zum Thema Beugung und Magnetismus hatte. Darüber hinaus bedanke ich mich noch bei Gregor Steinhoff für die jahrelange tatkräftige Unterstützung bei Arbeiten, die im Labor angefallen sind und bei sonstigen technischen Problemen. Stets hattest du die richtige Lösung parat und hattest auch sonst immer ein offenes Ohr für mich. Danke! An dieser Stelle sei auch Alexander Weißbach gedankt für seine Unterstützung im Labor während der letzten Züge meiner Promotion sowie Eugenia Miller für die Hilfe bei allen bürokratischen Angelegenheiten.

Ebenfalls gebührt mein Dank der feinmechanischen Werkstatt und der Werkstatt für Elektronik für die ausgezeichnete Reparatur von defekten Gerätschaften sowie allen anderen Arbeiten, die sie für mich erledigt haben.

Und ganz besonders bedanke ich mich noch bei meinen Freunden für die tolle Ablenkung, wenn ich mal etwas Abstand von der Uni brauchte.

Vor allem aber danke ich von ganzem Herzen meinem Vater und meiner Mutter, meinem Bruder Joscha und meiner Freundin Toni für eure unerschöpfliche Geduld mit mir, eure unersetzliche Unterstützung und euer absolutes Verständnis in stressigen Zeiten meiner Promotion. Ihr seid immer eine wahnsinnige Stütze für mich gewesen, ohne die all dies nicht möglich gewesen wäre. Danke für eure Liebe und dass ihr immer für mich da gewesen seid!